



**HAL**  
open science

# Evaluation of lipid nanocapsules for oral absorption using new quantitative FRET technique

Norraseth Kaeokhamloed

► **To cite this version:**

Norraseth Kaeokhamloed. Evaluation of lipid nanocapsules for oral absorption using new quantitative FRET technique. Human health and pathology. Université d'Angers, 2022. English. NNT : 2022ANGE0080 . tel-04749741

**HAL Id: tel-04749741**

**<https://theses.hal.science/tel-04749741v1>**

Submitted on 23 Oct 2024

**HAL** is a multi-disciplinary open access archive for the deposit and dissemination of scientific research documents, whether they are published or not. The documents may come from teaching and research institutions in France or abroad, or from public or private research centers.

L'archive ouverte pluridisciplinaire **HAL**, est destinée au dépôt et à la diffusion de documents scientifiques de niveau recherche, publiés ou non, émanant des établissements d'enseignement et de recherche français ou étrangers, des laboratoires publics ou privés.

# THESE DE DOCTORAT DE

L'UNIVERSITE D'ANGERS

ECOLE DOCTORALE N° 605  
*Biologie Santé*  
Spécialité : NANOMÉDECINES

Par

**Norraseth KAEOKHAMLOED**

## **Evaluation of lipid nanocapsules (LNCs) for oral absorption using new quantitative FRET technique**

Thèse présentée et soutenue à Angers, le 21 octobre 2022

Unité de recherche : Micro et Nanomédecines Translationnelles, INSERM U1066 – CNRS 6021

Thèse N° :

### **Rapporteurs avant soutenance :**

Bruno SARMENTO      Professeur, Université de Porto  
Gilles PONCHEL      Professeur, Université Paris-Saclay

### **Composition du Jury :**

Président :	Sandrine MARCHAND	PU-PH, Université de Poitiers
Examineurs :	Ana BELOQUI GARCIA	Chercheuse qualifiée FNRS, Université catholique de Louvain
	Gilles PONCHEL	Professeur, Université Paris-Saclay
	Bruno SARMENTO	Professeur, Université de Porto

Dir. de thèse : Emilie ROGER  
Co-dir. de thèse : Samuel LEGEAY

Maître de conférences, HDR, Université d'Angers  
Maître de conférences, Université d'Angers

**L'auteur du présent document vous autorise à le partager, reproduire, distribuer et communiquer selon les conditions suivantes :**



- Vous devez le citer en l'attribuant de la manière indiquée par l'auteur (mais pas d'une manière qui suggérerait qu'il approuve votre utilisation de l'œuvre).
- Vous n'avez pas le droit d'utiliser ce document à des fins commerciales.
- Vous n'avez pas le droit de le modifier, de le transformer ou de l'adapter.

**Consulter la licence creative commons complète en français :**  
**<http://creativecommons.org/licences/by-nc-nd/2.0/fr/>**



# ACKNOWLEDGEMENTS

I would like to express my deepest gratitude to:

Professor Emilie ROGER, the director of the thesis, for accepting me as the thesis candidate and for the great supports and guidance throughout the 3 years of the thesis. I wish you and your family a good health and all the best.

Professor Samuel LEGEAY, the co-director of the thesis, for accepting me as the thesis candidate and as the Master student, for the great supports, guidance, and training in cell culture and animal experiments. I wish you and your family the happiness and all the best.

Professor Patrick SAULNIER, the director the MINT Laboratory, for welcoming me to the MINT laboratory since my Master internship.

Professor Ana BELOQUI GARCIA, Professor Sandrine MARCHAND, Professor Gilles PONCHEL, and Professor Bruno SARMENTO for accepting the invitation to be a member of the jury and dedicating time to evaluate this thesis.

Professor Maxime MAHE for accepting to be a member of the CSI committee and scientific advice on the project.

All the members of the MINT Laboratory, for the warm welcome, the great support, and the all the help.

Ligue Contre le Cancer, Mine-et-Loire department, for funding of the project.

The European Union and the Erasmus+ Program NANOMED EMJMD for contributing the fund and resources to the project *via* the student internship program.

University of Angers for funding the remuneration of my PhD candidate position.

The FRENCH Republic for an opportunity to peruse the PhD.

I am deeply grateful to:

Vincent LEBRETON, my project partner throughout the thesis and during the time of the pandemic. This endeavor would not have been possible without your contribution. I wish you and your family all the best.

Professor Florence GATTACCECA for the pharmacokinetics analysis and scientific advice on pharmacokinetics.

Jérôme BEJAUD for synthesizing FRET dyes and performing other technical works. I wish you all the best.

Nolwenn LAUTRAM for the technical assistants, HPLC, and administrative works. I wish you all the best.

# ACKNOWLEDGEMENTS

Adélie MELLINGER for the development of the LNCs extraction technique and the technical assistants on cell culture during the early period of my thesis.

Florence MANERO and Rodolph PERROT of SCIAM for confocal microscopy and TEM analyses.

Chadi ABBARA and Marie BRIET of CRPV, CHU Angers for HPLC analyses of drugs in the *in vitro* coculture model experiment.

Thomas BENNETT, Anastasiia VASYLAKI, Rana ELFATAIRI, and other Master or Undergraduate students, for the works contributing to this thesis during their internships. I wish you all the bright future.

I am sincerely thankful to:

Professor Jean-Christophe GIMEL, Professor Camille SAVARY, Professor Guillaume BASTIAT, Florence DUMAS, Laurent LAMAIRE, Olivier THOMAS, Isabelle VERDU, and Audrey GRIVEAU for the technical and scientific advice.

Jeremy ROUX and other members of the animal facility (SCAHU) for their facility and a great care of the animal.

Edith GRELEAU and Marie GUILLON, the secretaries of MINT laboratory, for all the help with the administrative matters.

Many thanks for the warm support, the help, and the advises from Friends and Colleagues at the MINT laboratory: Flavien DELAPORTE, Milad BAROUD, Pierre IDLAS, Valentin PLATEL, Jaspe CHEN, Abdallah LADAYCIA, Heba NEAMEH, Claire GAZAILLE, Kevin MATHA, Ting Chithdavone HER, Marie-Anne JOURDAIN, Nicola ROLLEY, and Pierre LEGOUT. I wish you all a bright future and happiness.

All the (not so) little rats in the lab will be in my memories for their sacrifice to science.

Many thanks for my friends in Thailand: Nakky, J'Mint, Tiera, Teddy, Cathy, Fai. I would have not survived through the dark time of the pandemic and everything without the support from you guys.

And finally, all the love and gratitude for my parents, my grandparents, my family who always give me love and supports throughout this hardest time.

# ENGAGEMENT DE NON PLAGIAT

Je, soussigné(e) **Norraseth KAEOKHAMLOED**  
déclare être pleinement conscient(e) que le plagiat de documents ou d'une  
partie d'un document publiée sur toutes formes de support, y compris l'internet,  
constitue une violation des droits d'auteur ainsi qu'une fraude caractérisée.  
En conséquence, je m'engage à citer toutes les sources que j'ai utilisées  
pour écrire ce rapport ou mémoire.

signé par l'étudiant(e) le **21 / 10 / 2022**

**Cet engagement de non plagiat doit être signé et joint  
à tous les rapports, dossiers, mémoires.**

Présidence de l'université  
40 rue de rennes – BP 73532  
49035 Angers cedex  
Tél. 02 41 96 23 23 | Fax 02 41 96 23 00



# Table of Contents

<b>List of Abbreviations</b> .....	<b>8</b>
<b>List of Tables</b> .....	<b>10</b>
<b>List of Figures</b> .....	<b>11</b>
<b>Introduction</b> .....	<b>13</b>
<b>1. Oral drug delivery &amp; oral nanomedicines</b> .....	<b>13</b>
<b>2. Parameters and tools for evaluating oral absorption</b> .....	<b>16</b>
2.1 Membrane permeability model.....	16
2.2 <i>In vivo</i> oral bioavailability .....	19
<b>3. Lipid nanocapsule by phase inversion temperature (PIT) method</b> .....	<b>21</b>
<b>4. Lipid nanocapsules for oral absorption</b> .....	<b>23</b>
<b>5. <i>In vivo</i> lipid nanocapsules behavior</b> .....	<b>28</b>
<b>6. Objectives of the thesis</b> .....	<b>29</b>
<b>Bibliographic study</b> .....	<b>31</b>
Review : FRET as the tool for <i>in vivo</i> nanoparticle tracking.....	32
<b>Chapter 1: <i>In vitro</i> oral absorption of intact LNCs</b> .....	<b>50</b>
<b>New <i>in vitro</i> coculture model for evaluating intestinal absorption of different lipid nanocapsules</b> .....	<b>51</b>
Supplementary data .....	67
<b>Chapter 2: Quantitative FRET for determining intact LNCs in blood</b> .....	<b>69</b>
<b>Pharmacokinetics of intact lipid nanocapsules using new quantitative FRET technique</b> .....	<b>70</b>
Supplementary data .....	81
Unpublished Supplementary data .....	87
<b>Chapter 3: <i>In vivo</i> oral absorption of intact LNCs</b> .....	<b>91</b>
<b>Evidence from quantitative FRET suggests intact lipid nanocapsules not absorbing via rat's GI</b> .....	<b>93</b>
1. Introduction.....	94
2. Materials and methods .....	95

3. Results and discussion .....	103
4. Conclusion.....	111
Supplementary data .....	112
<b>Chapter 4: General discussion .....</b>	<b>116</b>
<b>1. <i>In vitro</i> oral absorption of intact LNCs.....</b>	<b>116</b>
1.1 Development of the new <i>in vitro</i> Caco-2/HMEC-1 coculture model .....	116
1.2 <i>In vitro</i> oral absorption of intact LNCs.....	118
<b>2. <i>In vivo</i> oral absorption of intact LNCs .....</b>	<b>121</b>
2.1 Quantitative FRET for blood sample.....	121
2.2 Quantitative FRET for hepatic portal system's organs.....	123
2.3 Lack of intact LNCs oral absorption.....	126
<b>Conclusion .....</b>	<b>132</b>
<b>Reference .....</b>	<b>133</b>



## List of Abbreviations

AUC	Area under the curve (of plasma drug concentration–time profile)
BCS	Biopharmaceutics classification system
Caco-2	Human colon adenocarcinoma cells
C <sub>max</sub>	Peak plasma drug/particle concentration
CS-LNCs	Chitosan coating lipid nanocapsules
CTAB	Cetrimonium bromide
DCP-LNCs	Dicetyl phosphate coating lipid nanocapsules
DiD	1,1'-dioctadecyl-3,3,3',3'-tetramethylindo-dicarbocyanine perchlorate
DiI	1,10-dioctadecyl-3,3,30,30-tetramethyl-indocarbocyanine perchlorate
DNA	Deoxyribonucleic acid
DPEG	DSPE-PEG-2000-NH <sub>2</sub>
FRET	Förster resonance energy transfer
FRET-LNCs	lipid nanocapsules coloaded with FRET dyes
GI	Gastrointestinal
HIV	Human immunodeficiency virus
HMEC-1	Human microvascular endothelium-1 cells
IEC-18	Rat intestinal epithelium cells
IVIS	<i>In vivo</i> imaging system
LLC-PK1	Pig kidney epithelial cells
LNC	Lipid nanocapsules
LNC-50	50-nm lipid nanocapsules
LNC-50-PEG	50-nm LNCs with DSPE-PEG-2000 surface added
LNC-50-SA	50-nm LNCs with stearylamine surface added
LNC-85	85-nm lipid nanocapsules
LNC-85-PEG	85-nm LNCs with DSPE-PEG-2000 surface added
LNC-85-SA	85-nm LNCs with stearylamine surface added
LNCs	Lipid nanocapsules
M-cells	Microfold cells
MDCK	Madin-Darby's canine kidney cells
miRNA	MicroRNA
NTA	Nanoparticle tracking analysis
OA	Oleic acid
PAMPA	Parallel artificial membrane permeability assay
P <sub>app</sub>	Apparent permeability coefficient
PBS	Phosphate-buffered saline

PEG	Polyethylene glycol
PIT	Phase inversion temperature
PR	Proximity ratio
RNA	Ribonucleic acid
SD	Standard curve
siRNA	Small interfering RNA
SLN	Solid lipid nanoparticles
T <sub>max</sub>	Time of the peak plasma drug/particle concentration
TPB	Tetraphenylborate

## List of Tables

<b>Table 1.</b> BCS class and drug examples.....	14
<b>Table 2.</b> Summary of different cell lines used in the oral absorption cell culture model.	18
<b>Table 3.</b> Example of drugs loaded to LNCs with PIT method.....	22
<b>Table 4.</b> Summary of the studies on oral absorption of LNCs formulations. ....	25
<b>Table 5.</b> Compositions of different FRET-LNCs formulations .....	96
<b>Table 6.</b> Experimental condition for the selection of the fiber removal method.....	100
<b>Table 7.</b> Experimental condition for the volumetric yield of Büchner filtration .....	100
<b>Table 8.</b> Experimental condition for the mortar and pestle method .....	101
<b>Table 9.</b> Experimental conditions for biodistribution studies after oral gavage .....	102
<b>Table 10.</b> FRET-LNCs Characterization (mean $\pm$ SD) .....	103
<b>Table 11.</b> LNCs intestinal extraction results.....	104
<b>Table 12.</b> Result of the test on the selection of fiber removal method .....	106
<b>Table 13.</b> Result of the test on volumetric yield after filtration via porcelain Büchner + paper filter .....	107
<b>Table 14.</b> Result of the test on the mortar and pestle method.....	108
<b>Table 15.</b> Experiment results of intact LNCs in the hepatic portal system and feces. .	109

## List of Figures

- Figure 1** An example of plasma drug concentration–time curve of an imaginary drug administrated by the oral route.  $C_{max}$  is the peak plasma concentration.  $T_{max}$  is the time of the peak plasma concentration ( $C_{max}$ ). AUC is the area under the curve which represents the total amount of drug in the systemic circulation over the measuring period. Reprinted from Boussey et al. [87].....20
- Figure 2.** Schematic representation of a lipid nanocapsules. ....21
- Figure 3.** Composition and structure of LNCs utilized throughout this thesis. From left to right 1) classical LNCs, 2) PEGylated LNCs with long PEG chain DSPE-mPEG-2000 (abv. LNC-PEG), and 3) cationic LNCs with stearylamine coating (abv. LNC-SA). ....30
- Figure 4.** Illustration of the Caco-2 model and the new coculture model Caco-2/HMEC-1 in Transwell®. The characteristic of the new coculture model is that the HMEC-1 endothelium is contact Caco-2 epithelium imitating the cellular structure of the gut-blood barrier. ....50
- Figure 5.** The Illustrations show the similarity between the hepatic portal system of (left) human and (right) rat (the animal model used in this thesis). Drugs and xenobiotics are absorbed through the intestinal tissue entering the mesenteric vein, portal vein, and liver before the systemic circulation [135,136]. Reprinted form DeSesso et al. [20].....92
- Figure 6.** Schematic illustration showing the location of FRET-LNCs in the rat's GI system at 0, 2.5, 4, and 24 hours after oral gavage (above). Quantity of intact LNCs in rat's GI system, hepatic portal vein, liver, feces, and systemic circulation, quantified by quantitative FRET (below). .... 110
- Figure 7.** Transport efficiency of six FRET-LNCs formulations after 2 hours in the blank Transwell® (purple, n = 4), and HMEC-1 monolayer (green, n = 4). F1 = 50-nm FRET-LNCs, F2 = 85-nm FRET-LNCs. The (+) symbols represent the arithmetic mean, and the whiskers represent a 95% confidence interval (Kruskal-Wallis: \* p ≤ 0.05). .... 119
- Figure 8.** % Remaining of six FRET-LNCs formulations after 2 hours in the Caco-2 model (blue, n = 4-8), and the Caco-2/HMEC-1 coculture model (red, n = 4-6). F1 = 50-nm FRET-LNCs, F2 = 85-nm FRET-LNCs. The (+) symbols represent the arithmetic mean, and the whiskers represent a 95% confidence interval ..... 120
- Figure 9.** Illustration shows the density gradient separation of rat blood sample containing FRET-LNCs (in a 200-µL polycarbonate tube) after ultracentrifugation with 400,000 G force for 120 min. Density information of plasma and neutrophil obtained from Zipursky et al. [169]. .... 122
- Figure 10.** Real example of FRET-LNCs separated from blood of the rat injected with FRET-LNCs after ultracentrifugation. The purple layer of FRET-LNCs on the top is clearly visible due to high injected dose ( $2 \times 10^{14}$  particles/100 g rat). The clear layer in the middle indicates blood plasma and polysucrose solution. Red layer at the bottom (partially observable over the rack) indicates the red blood cell pellet. A thin white layer of neutrophile can also be observed as a boundary between the red layer and clear layer (not clearly visible in the photo). .... 122
- Figure 11.** Schematic illustration summarizing the thesis project. .... 126

**Figure 12.** Absorption pathway of digested lipid-type nanoparticles. FA = fatty acid. MG = medium chain triglycerides. C = carbon atom. TG = triglycerides. ER = endoplasmic reticuli. Lipoproteins = chylomicrons. Reprinted from Wang et al. [173]. ..... 127

**Figure 13.** Lymphatic pathway of lipid absorption *via* intestinal lumen. Lipid molecules (hydrophobic) are absorbed through the lymphatic system *via* chylomicron transport. Reprinted from Miao et al. [175]. ..... 129

**Figure 14.** Chylomicron transport from lymphatic system to liver. Reprinted from Engelking L. R. [176]. ..... 130

## **Manuscript: Evidence from quantitative FRET suggests intact lipid nanocapsules not absorbing via rat's GI**

### **Supplementary**

**Figure S3-1.** Intestinal sample prepared in 5-mL water (control) after the ultracentrifugation with  $4 \times 10^5$  G force for 2 hours. Thick mucus layer was observed on the top of the supernatant, blocking the separation of LNC-50. .... 112

**Figure S3-2.** Intestinal sample prepared in 5-mL of 3% L-cysteine after the ultracentrifugation with  $4 \times 10^5$  G force for 2 hours. Thick mucus layer was observed on the top of the supernatant with a crystalized L-cysteine at the bottom and the wall of the tube, blocking the separation of LNC-50. .... 112

**Figure S3-3.** Intestinal sample prepared in 5-mL of acetate buffer pH 5.0 after the ultracentrifugation with  $4 \times 10^5$  G force for 2 hours. No separation was clearly observed, indicating a failure to separate LNC-50. .... 112

**Figure S3-4.** Example of feces quantitative FRET calibration curve of LNC-50-PEG between FRET acceptor intensity and particle concentration per gram of feces. .... 113

**Figure S3-5.** Rat autopsy at 24 hours after the gavage of LNC-50-PEG with the dose  $2 \times 10^{14}$  particle/100 g rat. FRET-LNCs were not observed in any part of the GI tract. 113

**Figure S3-6.** Rat autopsy at 2.5 hours after the gavage of LNC-50 with the dose  $2 \times 10^{14}$  particle/100 g rat. FRET-LNCs were not observed in the intestine yet. .... 114

**Figure S3-7.** Rat autopsy at 4 hours after the gavage of LNC-50 with the dose  $2 \times 10^{14}$  particle/100 g rat. FRET-LNCs were observed in all parts of the GI tract. .... 114

**Figure S3-8.** Rat autopsy at 4 hours after the gavage of LNC-85 with the dose  $5 \times 10^{13}$  particle/100 g rat. FRET-LNCs were observed in all parts of the GI tract. .... 115

# Introduction

## 1. Oral drug delivery & oral nanomedicines

Oral medication is one of the most popular route of administration that contributes up to 52% of the pharmaceutical market share in 2013 [1]. Due to the ease of use, availability for self-medication, and flexibility for pediatric and geriatric uses, oral medication was reported to be the patient's preferred choice over injectables [2,3]. Injectable dosage form has benefits for its fast onset and its capability to deliver a precise dose, but due to its invasiveness it could reduce patient's adherence to the medication [3,4]. For example, one of the main reasons for poor adherence among diabetes patient practicing daily insulin self-injection were the difficulty to inject and the pain on the injection site [5,6]. Patient's medication adherence is one of the most important aspect of clinical pharmacotherapy [3]. Increase in drug adherence leads to better treatment outcomes [7] while the lack of the adherence could post the risk of avoidable hospitalization, poor treatment outcomes, and overall higher medical cost [4,8–10]. Non-adherence problems stem from various factors either from the patient's side or the medication side [11]. Availability of an oral medication could be one strategy to improve patient's adherence to the treatment by allowing for more flexible medication regimen that better suits different patients in different scenarios, moving forward beyond the failure of the one-size-fits-all approach [3,12–14]. For example, oral anticancer drug such as imatinib allows for the chronic dosing regimen (long-term and low-level dosing) which can reduce the medical cost and the patient's financial burden due to less need for the conventional in-patient infusion chemotherapy session [12,15]. Oral medication can also act as a complement to the standard parenteral regimen. For example, oral antibiotics can be used as a combination with the parenteral antibiotics giving a benefits of the patient's early discharge from hospital as well as reducing the risk of canula-related infection [16–18]. Clearly, oral drug delivery provides the advantages both clinically and financially.

However, not all drugs are capable for oral administration because drug oral bioavailability is a complex process relying on both physicochemical and biological mechanisms [12,19–21]. Most drug absorption occurs in the small intestine [20]. The intestinal barrier (also called the gut-blood barrier) consists of three main barriers: the mucus layer, the epithelium layer, and the vascular endothelium layer [20,22]. Drug intestinal absorption is highly dependent on drug stability in GI, drug aqueous solubility and membrane permeability [23,24]. The biopharmaceutics classification system (BCS) is established to classify drugs bioavailability based on these two parameters [23,25] (**Table 1**).

**Table 1.** BCS class and drug examples

BCS class	Aqueous solubility	Membrane permeability	GI absorption	Example drugs
I	High	High	High absorption	metoprolol tartrate, propranolol HCl [26]
II	Low	High	Limited by dissolution rate	carbamazepine, cephalexin [26]
III	High	Low	Limited by permeation rate	atenolol, cimetidine [26]
IV	Low	Low	Poor absorption	furosemide, amphotericin B, paclitaxel, lopinavir [26,27]

High aqueous solubility = The highest therapeutic dose is completely soluble in 250 mL or less of the aqueous buffer with pH range of 1.2–6.8 at 37 °C.

High membrane permeability = at least 85% absolute bioavailability or permeability in the *in vitro* Caco-2 cell membrane model.

There are various ways to determine drug's solubility and permeability. The main criteria provided by the United States Food and Drug Administration (U.S. FDA) suggest that a drug is classified as "high solubility" if its highest therapeutic dose is completely soluble in 250 mL or less of the aqueous buffer with pH range of 1.2–6.8 at 37 °C; while a "high permeability" drug should have at least 85% absolute bioavailability or permeability in the *in vitro* Caco-2 cell membrane model [25]. BCS class I drugs are high solubility–high permeability drugs and thus have high intestinal absorption. BCS class II drugs are low solubility–high permeability so their absorption is limited by the solubility. BCS class III drugs are high solubility–low permeability so their absorption is limited by its permeability. BCS class IV drugs are low solubility–low permeability so they have poor bioavailability and high absorption variability [23]. It is reported that poorly soluble drugs contribute up to one third of drugs in the US pharmacopeia and the number could be as high as 90% for new chemical entities [28]. These drugs belong to either the BCS class II or IV and some of them are a widely used drug that is available only in the injectable dosage form. For example, paclitaxel is widely used in the chemotherapy regimen treating various cancers. It belongs to the BCS class IV and only has round 7% of oral bioavailability, making it only approved by the U.S. FDA for intravenous use [27,29]. Besides, a small number of widely use BCS class IV drugs, around 5%, is approved for oral administration but with some degree of absorption problem or precaution [24,27]. For example, furosemide, a commonly used diuretics, shows a highly variability in oral bioavailability from 10-90% and thus dosing adjustment is required for each patient with different health conditions [30–32]. Lopinavir, a standard antiviral drug for HIV, is another BCS class IV drug with several oral formulations available. However, due to its poor bioavailability (around 25%), the drug can only be orally administrated as a combination with ritonavir (lopinavir/ritonavir combined pill) [33,34], causing the incremental medical cost that leads to the affordability problem to the people in developing countries where

the prevalence of HIV infection is relatively high [35]. Indeed, poor drug absorption problem can be a factor attributing to the problem not only for the pharmaceutical industry but also the public health system. In addition, one should keep in mind that the BCS classification system still has the limitations that it does not include other parameters affecting oral absorption such as drug stability in GI, GI diseases, and the variability among the population.

Several strategies have been developed to enhance oral absorption of poorly soluble drugs based on 1) the chemical approach such as prodrug or salt form; and 2) the formulation approach such as solid dispersion, self-emulsifying drug delivery systems (SEDDS), cyclodextrin, etc. [36–38]. In recent years, nanotechnology gains a lot of interest for its application in pharmaceutical science. The term “nanomedicine” is coined for drug delivery system based on nanotechnology [39]. In the literature, lots of evidence suggest that general benefits of nanomedicines for oral delivery are 1) to improve drug GI stability by the protection against harsh GI environment, 2) to increase the absorption of poorly soluble drugs, and 3) to control drug release [40–43]. Notable drugs with poor absorption such as amphotericin B, exenatide, and insulin were also reported to have an improved oral bioavailability in an animal model after being encapsulated in the polymeric-type nanocarriers [43]. Especially insulin, the polymeric nanoparticles was found to protect the encapsulated insulin against the enzymatic degradation in the GI [44], showing the superiority of nanomedicine over the classical delivery system such as SEDDS that is not capable. Nano Lipid-type nanomedicines are known to improve the oral bioavailability of various drugs such as clozapine, paclitaxel, lopinavir, etc. [45,46]. Nanomedicine seems to be one of the promising solution for oral delivery of poor absorption drugs [22,47].

However, among 1,450 drugs and more than 20,000 drug products approved by the U.S. FDA [48,49], only around 70 nanomedicines drug products reach the market globally as of 2022, of which only 13 drug products are available for oral administration [50,51]. Almost all of the approved oral nanomedicines is nanocrystals, which mainly aimed for increasing drug dissolution rate by increasing drug surface area [36,51,52]. Lipid-based and polymer-based nanomedicines contributed to a very large part of the approved nanomedicines but no products in these groups are aimed for improving oral absorption [50,51]. Lack of nanomedicines products may suggest that there is a problem on the clinical translation between the preclinical study in the literature and the clinical trials, the problem that even nanomedicines in general suffer from [42]. That root cause may stem from the fact that nanomedicines are inherently different from classical drug formulation in many aspects. While drug molecules have chemical properties, nanomedicines also have extra aspects such as size, shape, surface modification, organ targeting property, etc. [53,54]. However, these aspects of nanomedicine are often ignored as they are still treated like the classical formulation [42]. For example, preclinical



pharmacokinetics study of nanomedicines still focuses on the encapsulated drug level alone and ignores the fate of the nanomedicine as the nanocarrier, despite the fact that the effects such as specific organ targeting, controlled release, and prolonged circulation actually rely on the property of the nanocarrier itself rather than the drug as in the classical formulation [42,55]. It is clear that better understanding on the biofate of nanomedicines is needed and many aspects of the nanomedicine should not be ignored in order that the benefits the nanomedicine will finally come to fruition.

## 2. Parameters and tools for evaluating oral absorption

In order to explore the oral absorption of nanomedicines, the first important thing to consider is the parameters and tools to evaluate oral absorption. There are two main parameters to evaluate oral absorption: the intestinal permeability (either *in vitro* or *ex vivo*) and the *in vivo* bioavailability. Tools are developed around these two parameters. However, when studying the oral absorption of nanomedicine, there are two aspects to consider: 1) the absorption of the encapsulated drugs as in the conventional approach; and 2) the absorption of the intact nanomedicine itself. It is important to investigate the absorption of the intact nanomedicine to determine the location of drug release: whether in the intestinal lumen or in the systemic circulation (after intact nanoparticle being absorbed); and to better predict drug absorption [56]. This is because the drugs encapsulated in the nanoparticles must be released in order to have therapeutic efficacy, similar to the analogy of drug release from the conventional capsules or tablets.

### 2.1 Membrane permeability model

There are various *in vitro* and *ex vivo* models for evaluating drug intestinal absorption, but all the models are actually based on the same basic structure. All the models consists of two compartments called the apical and the basolateral compartment (also called the donor and the acceptor chamber) with a permeable membrane in-between separating the two compartments [57]. Drug absorption in the *in vitro* model can also be called *drug permeability* since it is determined by the drug transport rate across the membrane (from apical to basolateral) per time and area, called the apparent permeability coefficient ( $P_{app}$ ) which is represented by the following equation:

$$P_{app} = \frac{dQ}{dt} \times \frac{1}{A \cdot C_0}$$

Where  $dQ/dt$  is the rate of drug content to the basolateral compartment over time;  $A$  is the area of the permeable membrane;  $C_0$  is the drug content in the apical compartment at time zero [57].

For the intestinal model, the apical and basolateral compartments are the representations of the intestinal lumen and the systemic circulation, respectively. The variation and the advancement of each model depends on the difference in the type of the permeable membrane. Types of the membrane can be grouped in 3 types: 1) artificial membrane, 2) cell culture membrane, and 3) *ex vivo* membrane.

### **2.1.1 Artificial membrane**

Parallel artificial membrane permeability assay (PAMPA) is a static model with an artificial membrane made of phospholipid [57]. It is useful for studying passive diffusion and for screening test because it is easily prepared using only chemicals. The disadvantage of this model is that it cannot be used to study biological process and is not specific for oral absorption. The model can be used to represent non-specific diffusion through any type of barrier [58]. PAMPA was found to be used to evaluate the permeability of solid lipid nanoparticles (SLN), which SLN could increase the permeability of phytochemicals [59,60]. The use of this model with nanomedicine was intended only for specifically evaluating the passive diffusion (solely chemical process) of the encapsulated drugs with the absence of all biological factors (from cell culture model) [60].

### **2.1.2 Cell culture membrane**

Various cell lines are used for constructing the *in vitro* intestinal absorption cell culture model. The use of cell culture models allow for absorption *via* biological process such as active transport or receptor mediated transport to be evaluated [61]. Cell lines can be derived from either human or animal sources. **Table 2** gives a summary on different cell lines used in the intestinal cell culture model.

**Table 2.** Summary of different cell lines used in the oral absorption cell culture model.

Cell lines	Source	Cell types	Remarks	Ref.
<b>Human cell lines</b>				
Caco-2	Human colon	enterocytes	Standard cell line	[62]
HT-29	Human colon	enterocytes, goblet cells	Subtype of Caco-2 that can differentiate to mucus-producing goblet cell	[63,64]
HT-29-MTX	Human colon	enterocytes, goblet cells	Subtype of HT-29 but they are resistant to methotrexate	[65]
TC-7	Human colon	enterocytes	Subtype of Caco-2	[66]
HIEC	Human small intestine	enterocytes		[67]
M-cells	Human	intestinal immune cells	Allowing for passage of drug absorption.	[68]
Raji-B	Human	intestinal immune cells	Immune cells inducing the differentiation of HT-29 to M-cells	[69]
<b>Animal cell lines</b>				
MDCK	Canine kidney	kidney epithelium	Caco-2 analogous	[57,70]
LLC-PK1	Pig kidney	kidney epithelium	Caco-2 analogous	[71]
2/4/A1	Rat intestine (fetal)	enterocytes		[72]
IEC-18	Rat small intestine	enterocytes		[73]

Caco-2 = Human colon adenocarcinoma

M-cells = Microfold cells

MDCK = Madin-Darby's Canine Kidney

LLC-PK1 = Pig kidney epithelial cells

IEC-18 = Rat intestinal epithelium cells

The most commonly used cell line is the Caco-2 (Human colon adenocarcinoma) cell line due to its well-established correlation with *in vivo* absorption [62,74]. For oral nanomedicines, Caco-2 model was also widely used to evaluate the *in vitro* oral permeability, including the test for various encapsulated drugs such as decitabine [75], paclitaxel [61], dexamethasone [76], amphotericin B [77]; as well as for intact nanoparticle absorption of various polymeric nanoparticles, SLN, LNCs, and liposomes [78]. However, more advanced models are rarely used for studying oral absorption of nanomedicines [78]. The model such as Caco-2/HT-29 coculture provides a benefits of the mucus layer due to the fact that HT-29 (as well as HT-29-MTX) is the goblet cell producing mucus [56,79–81]. For example, a study by Prego *et al.* [82] using this coculture model could reveal that chitosan nanoparticles having a mucoadhesive property. This result could not be obtained with the Caco-2 model. To date, one of the most sophisticated *in vitro* model for intestinal absorption is the triple-coculture Caco-2/HT-29/Raji-B model by Antunes *et al.* [83,84]. This model, while Caco-2 and HT-29 are seeded together on the apical side of the Transwell®, a lymphoblast like cell "Raji-B" is seeded in the basolateral side. Raji-B does not attach to the surface and it will migrate to the Caco-2/HT-29 layer to induce Caco-2 to differentiate to M-cell [83,85], the cell which can facilitate nanoparticle transcytosis [78]. A study by Schimpel *et al.* [85] gave evidence that presence of the M-cell in this model really increased the absorption of polystyrene nanoparticles, and thus

suggested that nanoparticle transcytosis *via* M-cell could be another viable strategy for oral nanomedicine absorption.

Despite the great development in the oral absorption cell culture model during the past few years, the cell lines used in these models still compose mainly of the enterocyte's epithelium and, at best, the mucus layer. Indeed, the intestinal barrier consists of the mucus layer, the epithelium layer, and also the endothelium layer. The current existing *in vitro* oral absorption models clearly lack the cooperation of the endothelium cell line, and this is the limitation of the models.

### **2.1.3 Ex vivo membrane**

The *ex vivo* model has the benefits of using the actual intestinal membrane obtained from animal models which include the natural mucus layer. The model also allows for the use of pig intestinal membrane which is morphologically similar to human intestine [86]. One of the prominent *ex vivo* model is the Ussing chamber, which was used by Schimpel *et al.* [85] for evaluating the permeability of polystyrene nanoparticles through the pig intestinal membrane. In this study, they found that the *ex vivo* permeability of the polystyrene nanoparticles highly correlated to the Caco-2/HT-29/Raji-B cell culture models.

## **2.2 In vivo oral bioavailability**

In the *in vivo* study, after a drug is administrated into a body, the amount of drug that reaches the systemic circulation can be measured as the plasma drug concentration–time curve (**Figure 1**). The area under the curve (AUC) can be calculated to represent the total amount of drug in the systemic circulation over the measuring time period (often abbreviated as  $AUC_{0 \rightarrow t}$ ) [87].

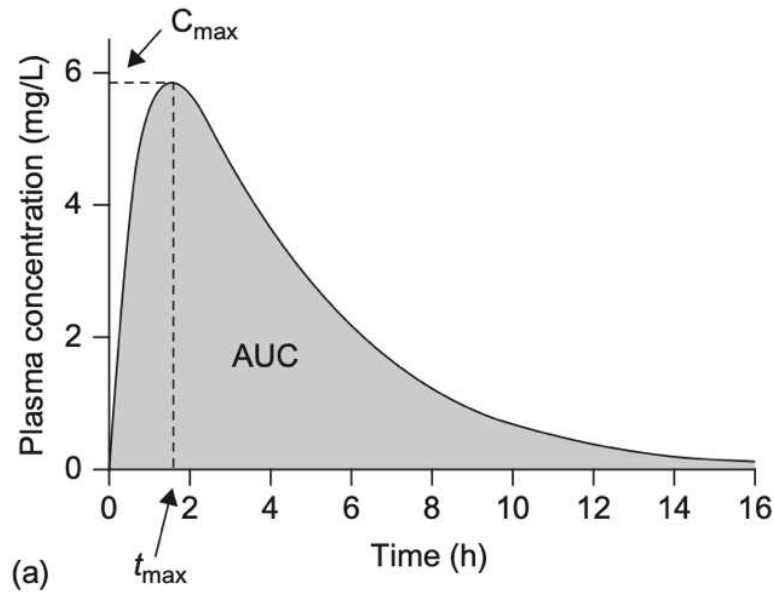


**Figure 1** An example of plasma drug concentration–time curve of an imaginary drug administered by the oral route.  $C_{max}$  is the peak plasma concentration.  $T_{max}$  is the time of the peak plasma concentration ( $C_{max}$ ). AUC is the area under the curve which represents the total amount of drug in the systemic circulation over the measuring period. Reprinted from Boussey et al. [87].

Bioavailability is a standard pharmacokinetic parameter for drug absorption which is calculated with the AUC [88]. An increase in oral bioavailability generally correlates with a higher therapeutic efficacy of the drug, making it a crucial predictive parameter in the pre-clinical study [42]. The principle of bioavailability is to measure the amount of drug that reaches the systemic circulation after the absorption compared to scenario without the absorption [87,89,90]. Bolus intravenous administration is considered the scenario with no absorption since the drug is directly administered to the systemic circulation. Therefore, the so-called absolute bioavailability can be calculated as the ratio between the AUC of the drug going through absorption vs. the AUC of the drug administered by intravenous injection. For the oral absorption [87], the absolute oral bioavailability can be calculated by the equation:

$$\text{Absolute Oral Bioavailability } (F_{abs, PO}) = \frac{AUC_{PO} \cdot D_{IV}}{AUC_{IV} \cdot D_{PO}}$$

Where  $F_{abs,PO}$  is the absolute oral bioavailability;  $AUC_{PO}$  is the AUC of drug administered orally;  $AUC_{IV}$  is the AUC of drug administered intravenously;  $D_{PO}$  is the dose of drug administered orally;  $D_{IV}$  is the dose of drug administered intravenously. Following the equation, the absolute bioavailability of intravenously administered drug is always  $F_{abs} = 1$  (or 100%) while orally administered drug will always has the  $F_{abs} \leq 1$  (or  $\leq 100\%$ )

due to the loss during absorption process [87,90]. Moreover, the oral bioavailability of drug with different dosage forms or different formulations can also be compared to each other using the relative bioavailability as the following equation:

$$\text{Relative Oral Bioavailability } (F_{\text{rel,PO}}) = \frac{\text{AUC}_{\text{test}} \cdot D_{\text{ref}}}{\text{AUC}_{\text{ref}} \cdot D_{\text{test}}}$$

Where  $F_{\text{rel,PO}}$  is the relative oral bioavailability;  $\text{AUC}_{\text{test}}$  is the AUC of the test drug;  $\text{AUC}_{\text{ref}}$  is the AUC of the reference drug;  $D_{\text{test}}$  is the dose of the test drug;  $D_{\text{ref}}$  is the dose of the reference drug. Relative bioavailability is a useful parameter to evaluate the efficiency of the formulation or the dosage form to improve drug absorption as a comparison to the reference formulation [87].

### 3. Lipid nanocapsule by phase inversion temperature (PIT) method

Lipid nanocapsules (LNCs), developed by the MINT laboratory, is one of the nanomedicines showing a benefit to improve oral bioavailability of several drugs e.g. paclitaxel [29,91,92], albendazole [93,94], praziquantel [95], etc. LNCs is prepared with the phase inversion temperature (PIT) method developed by Heurtault et al. [96]. The structure of LNC is described as an oily lipid core made of medium-chained triglyceride surrounded by a monolayer shell of short-chained pegylated surfactant and lecithin (phosphatidylcholine) (**Figure 2**) [96,97].

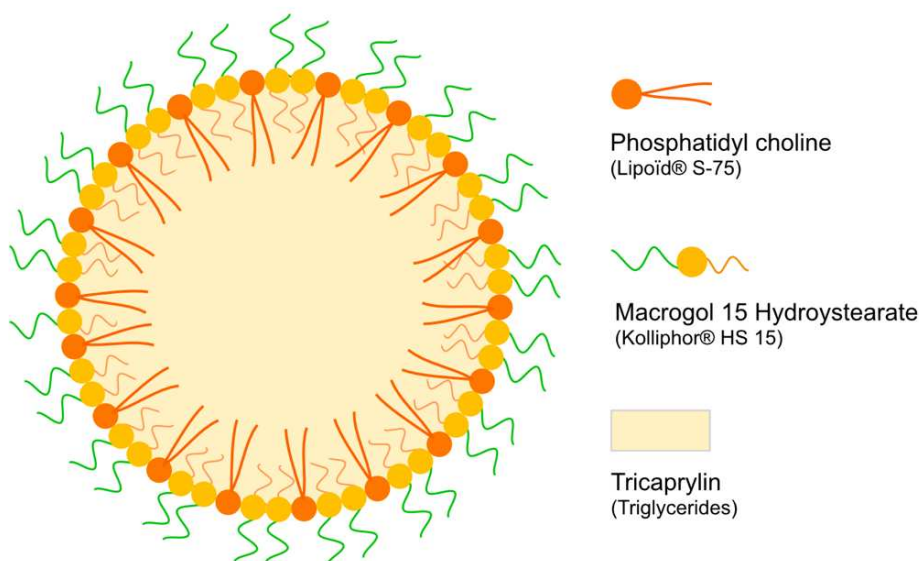


**Figure 2.** Schematic representation of a lipid nanocapsules.

PIT technique is based on the principle that the modification of hydrophilic–lipophilic balance of nonionic surfactant such as polyoxythelene-type surfactants changes according to the temperature. At low temperature, the surfactant is more hydrophilic as it can form a hydrogen bond with the aqueous phase creating the oil-in-water emulsion (O/W). On the contrary, at high temperature, the hydrogen bond between water and polyoxythelene chain will break reversing the phase of the emulsion to water-in-oil (W/O). The transitional phase between O/W and W/O is called the phase inversion zone (PIZ). During the PIZ, surfactant and lipid phase will rearrange in the bicontinuous (sponge-like) structure. LNC can be formed by the addition of cold water (0-2°C) to irreversibly break this lipid bicontinuous structure [46,98,99].

PIT method can produce LNCs in the size ranging from around 20-150 nm and is monodispersed. LNCs has the advantages of using the biocompatible excipients and not using toxic organic solvents during the formulation process. LNC are physical stable for up to 18 months [46,96]. LNCs is proved to be versatile for encapsulating or surface loading of chemical drugs, peptides, monoclonal antibodies, DNA, RNA, etc. (**Table 3**).

**Table 3.** Example of drugs loaded to LNCs with PIT method.

Types of drugs	Loading system	Example of drug loaded to LNCs
Hydrophobic drug	Encapsulation	paclitaxel [91], sorafenib [100], ropivacaine [101], miltefosine [102–104], albendazole [93,94,105], ibuprofen [106], deferasirox [107], rapamycin [108]
Hydrophilic drug	Encapsulation	decitabine [75], cisplatin [109]
Macrolides	Encapsulation	cyclosporin [110]
Polysaccharides	Surface loading	fondaparinux [111]
Peptides	Surface loading	salmon calcitonin [112], antimicrobial peptides [113]
	Encapsulation	antimicrobial peptides [113]
Monoclonal antibody	Surface loading	bevacizumab [114]
DNA	Encapsulation	DNA [115,116], plasmid DNA [117]
RNA	Surface loading	siRNA [118,119]
	Encapsulation	miRNA [120,121]

## 4. Lipid nanocapsules for oral absorption

Several drugs were encapsulated into lipid nanocapsules (LNCs) for oral administration. LNCs could increase the oral bioavailability of many encapsulated drugs namely paclitaxel [29,91,92], albendazole [93,94], praziquantel [95], fondaparinux [111], tetrandrone [122], and tanshinone IIA [123].

*In vitro* studies in Caco-2 epithelium cells also showed that LNCs could improve the permeability of paclitaxel [61], Sn38 [124] and decitabine [75]. The *in vitro* studies also revealed that the main absorption process of drug-loaded LNCs occurred *via* the active transport transcytosis process namely the clathrin-dependent and caveolin-dependent transcytosis and these processes were size-independent [61]. In contrast, passive transport of LNCs was found to be size-dependent as it increased when the size decreased. Intact LNCs particles were also found to cross the Caco-2 epithelium by around 0.3% of initial quantity of LNCs after 2 hours of incubation on Caco-2 cells model [61,124]. Moreover, LNCs were stable in the GI mucus and had a mucopenetrative effect that improved drug permeability across the mucus layer [125]. Besides, it was reported by Tran *et al.* [92] that LNCs also elevated paclitaxel absorption through the lymphatic system in rat model. The amount of paclitaxel in the mesenteric lymph node was significantly higher for rat administered with paclitaxel-LNCs compared to the paclitaxel oral solution at any time points from 4–24 hours.

On the other hand, LNCs did not increase the oral bioavailability of ibuprofen [106], (R)-CE3F4 [126], and miltefosine [102]. However, it was observed that LNCs interestingly improved the therapeutic efficacy of ibuprofen and miltefosine. In the case of ibuprofen, it was suggested that the sustained release effect in the ibuprofen-LNCs formulation might contribute to this phenomenon because the prolonged pharmacokinetics profile was observed compared to ibuprofen oral solution [106]. However, for miltefosine, the cause of this phenomenon was unclear because both the miltefosine-LNCs and the oral miltefosine solution had similar oral bioavailability and pharmacokinetic profile but only the oral solution did not have therapeutic effect. It was hypothesized by the article's author that this effect was a result of the absorption of intact LNCs because the suspect nano-objects were found at the therapeutic site (fluke worm *Schistosoma mansoni*) [102].

Different LNCs were formulated into the size ranging from 20-150 nm for oral administration. Size of LNCs did not seem to have a strong effect on 1) *in vitro* drug permeation across Caco-2 epithelium [61], 2) mucopenetrating ability [125], and 3) oral bioavailability [29,91,92]. An increase in size may lower the oral bioavailability as it was observed that 90-nm paclitaxel-LNCs increased the oral bioavailability of paclitaxel only by 2 folds [92] compared to the 3-fold increase by 60-nm paclitaxel-LNCs [29,91].



LNCs coated with DSEP-PEG-2000-NH<sub>2</sub> (DPEG-LNCs) increased oral bioavailability of paclitaxel by 11 folds in a rat model, compared to 3 folds by the classical LNCs, and 4 folds by the cationic LNCs [29,91]. However, the Paclitaxel-DPEG-LNCs did not improve *in vivo* antitumor efficacy of paclitaxel in rat model when given orally. The classical Paclitaxel-LNCs, on the other hand, still maintained high antitumor efficacy after oral administration [91]. The pegylated LNCs seemed to highly increase oral bioavailability of the encapsulated drugs but surprisingly failed to improve any therapeutic effect of the drug in the case of paclitaxel. The classical LNCs still successfully improved the therapeutic effect despite elevating the oral bioavailability not as high as the pegylated LNCs. The cause of this discrepancy was still unclear and could not be explained by the classical pharmacokinetics model of plasma drug concentration and bioavailability as in the classical pharmacokinetic model, an increase in oral bioavailability (plasma drug concentration and AUC) always correlates with a higher therapeutic efficacy of the drug [42].

On the other hand, anionic dicetyl phosphate coating LNCs (DCP-LNCs) loaded with miltefosine had poor anthelmintic against a fluke worm *Schistosoma mansoni*. However, their pharmacokinetic profile has not yet been attested [102].

Finally, cationic coating of oral LNCs includes cetrimonium bromide (CTAB), chitosan, and stearylamine. Coating with stearylamine on LNCs (SA-LNCs) prolonged the plasma concentration half-life and increased oral bioavailability of the encapsulated fondaparinux by 15 folds, higher than CTAB-LNCs (7 folds). It was also hypothesized that this was a result of SA-LNCs having lower surface charge than CTAB-LNCs as this was the only difference property between the two types of coating. However, the study did not compare the two cationic LNCs with classical LNCs in this regard [111]. In another study by Groo *et al.* [91], chitosan-LNCs (CS-LNCs) increased the oral bioavailability of paclitaxel by 4 folds but this was not significantly different from classical LNCs. However, they did not investigate the therapeutic efficacy of this cationic LNCs further. Later, Eissa *et al.* [102] found that CS-LNCs and CTAB-LNCs encapsulating miltefosine had higher anthelmintic efficacy against a fluke worm *Schistosoma mansoni* than the classical LNCs, despite the fact that all cationic LNCs and classical LNCs had the same oral bioavailability and pharmacokinetic profile. This result was also confirmed in another study [103], in which cationic LNCs seemed to have a similar oral bioavailability to classical LNCs but surprisingly gave a significantly higher therapeutic efficacy. As previously explained for the case of miltefosine, it was hypothesized that this was the result of the absorption of intact LNCs into the systemic circulation. **Table 4** summarizes the studies on oral absorption of LNCs formulations.

**Table 4.** Summary of the studies on oral absorption of LNCs formulations.

Encapsulated drugs / substances	Lipid core	Particle size (nm)	Surface modification	Study	Model	Discoveries	Ref.
<b>Anticancer</b>							
Paclitaxel	Captex® 8000	60	n/a	V	Rat	3-fold increase in bioavailability of paclitaxel observed in LNCs formulation compared to oral solution of Taxol®.	[29]
	Captex® 8000	25, 50, 100, 130	n/a	T	Caco-2 cells	<ul style="list-style-type: none"> <li>Increase in paclitaxel permeability across Caco-2 observed in LNCs formulations.</li> <li>Intact LNCs found in basolateral media.</li> <li>LNCs absorption mechanisms occurs via clathrin-dependent &amp; caveolin dependent transcytosis.</li> </ul>	[61]
	Captex® 8000	25, 55, 110	n/a	T	GI Mucus (Transwell)	<ul style="list-style-type: none"> <li>LNCs formulation is stable in GI mucus and do no change mucus rheology.</li> <li>Paclitaxel diffusion is not size-dependent (for &lt;110 nm).</li> <li>Mucus layer reduces paclitaxel permeability in LNCs formulations.</li> <li>2-fold increase in permeability of paclitaxel observed in 55-nm LNCs formulation compared to oral solution.</li> </ul>	[125]
	Captex® 8000	50-70	Chitosan (cationic), DSEP-PEG-2000-NH <sub>2</sub> (anionic)	V	Rat	<ul style="list-style-type: none"> <li>3-fold increase in bioavailability of paclitaxel observed in LNCs formulation compared to oral solution. Highest antitumor effect (tumor size reduction).</li> <li>11-fold increase in bioavailability of paclitaxel observed in DPEG-LNCs formulation compared to oral solution. Fails to have antitumor effect.</li> <li>4-fold increase in bioavailability of paclitaxel observed in Chitosan-LNCs compared to oral solution. No different to normal LNCs formulation.</li> </ul>	[91]
	Captex® 8000	90	n/a	V	Rat	<ul style="list-style-type: none"> <li>2-fold increase in bioavailability of paclitaxel observed in LNCs formulation compared to oral solution.</li> <li>Increase of paclitaxel level in lymphatic system observed for LNCs formulation.</li> </ul>	[92]
Sn38	Transcutol® HP, Labrafil® M1944, Labrafac®	40	n/a	T	Caco-2	<ul style="list-style-type: none"> <li>5-fold increase in Sn38 permeability across Caco-2 observed in LNCs formulation in comparison free Sn38.</li> <li>No paracellular effect of LNCs observed.</li> </ul>	[124]
Decitabine	Transcutol® HP + Tween 80	30	n/a	T	Caco-2	30-fold increase in decitabine permeability across Caco-2 observed in LNCs formulation compared to oral solution.	[75]

Encapsulated drugs / substances	Lipid core	Particle size (nm)	Surface modification	Study	Model	Discoveries	Ref.
<b>Anthelmintic</b>							
Miltefosine	Labrafac® WL 1349 ± OA	40-60	CTAB (cationic), Chitosan (cationic), DCP (anionic)	V	Mouse	<ul style="list-style-type: none"> <li>Cationic LNCs has high anthelmintic effect against <i>S. mansoni</i> (fluke worm), CTAB is the strongest with 8-fold increase compared to oral solution.</li> <li>Anionic LNCs has poor anthelmintic effect.</li> <li>Bioavailability of miltefosine is similar for free drug, LNCs, and all cationic LNCs formulations.</li> <li>Nano-objects found on fluke worm treated with LNCs formulations.</li> </ul>	[102]
	Labrafac® WL 1349 ± OA	40-50	CTAB (cationic)	V	Mouse	<ul style="list-style-type: none"> <li>CTAB-LNCs or OA-LNCs has better anthelmintic effect against <i>S. mansoni</i> (fluke worm) than miltefosine oral solution.</li> </ul>	[103]
Albendazole	Labrafac® WL 1349 + OA	50	n/a	V	Mouse	<ul style="list-style-type: none"> <li>2-fold increase of albendazole in plasma and <i>E. granulosus</i> cyst (tapeworm) observed in LNCs formulation compared to oral solution.</li> <li>2-fold increase in anthelmintic effect against <i>E. granulosus</i> compared to oral solution.</li> <li>Increase in therapeutic effect correlates with AUC</li> </ul>	[93]
	Captex® 8000, Labrafac® WL 1349 ± OA	50	n/a	V	Mouse	(new) LNCs formulation has higher anthelmintic efficacy against <i>E. granulosus</i> cyst, compared to albendazole oral solution.	[105]
	Labrafac® WL 1349 + OA	50	n/a	V	Mouse brain	2 to 3-fold increase of albendazole level in mouse brain by Albendazole-LNCs formulation compared to oral solution.	[94]
Praziquantel	Labrafac® WL 1349 ± OA	50-60	n/a	V	Rat	<ul style="list-style-type: none"> <li>2.5-fold increase in bioavailability of praziquantel observed in LNCs and LNCs-OA formulations compared to oral solution.</li> <li>3-fold increase in MRT suggesting prolonged release compared to oral solution.</li> <li>20% increase of anthelmintic effect against <i>S. mansoni</i> (fluke worm) compared to oral solution.</li> </ul>	[95]
<b>NSAIDs</b>							
Ibuprofen	Labrafac® CC	50-60	n/a	V	Rat	<ul style="list-style-type: none"> <li>Prolonged half-life and antinociceptive effect observed in LNCs formulation.</li> <li>No significant increase in bioavailability observed.</li> </ul>	[106]

Encapsulated drugs / substances	Lipid core	Particle size (nm)	Surface modification	Study	Model	Discoveries	Ref.
<b>Anticoagulant</b>							
Fondaparinux	Labrafac® WL 1349	50	CTAB, Stearylamine (cationic)	V	Rat	<ul style="list-style-type: none"> <li>• 15-fold increase in bioavailability of fondaparinux observed in Stearylamine-LNCs formulation compared to oral solution.</li> <li>• 7-fold increase in bioavailability of fondaparinux observed in CTAB-LNCs formulation compared to oral solution.</li> <li>• Prolonged half-life observed in all LNCs formulations.</li> </ul>	[111]
<b>Antiviral</b>							
Efavirenz	Labrafac®	60	n/a	E	Rat jejunum	2-fold increase in permeability observed in LNCs formulation compared to oral solution.	[127]
<b>Antiarrhythmic</b>							
(R)-CE3F4	Miglyol® 812	30	n/a	V	Mouse	LNCs formulation improve ( <i>in vitro</i> ) GI stability of the drug but do not increase the bioavailability.	[126]
<b>Phytochemicals</b>							
Tetrandrine	Labrafil® M1944 CS	40	n/a	V	Rat	2-fold increase in AUC observed in LNCs formulation, compared to tetrandrine tablet.	[122]
Tanshinone IIA	Labrafac® WL 1349	70	n/a	V	Rat	3.6-fold increase in bioavailability of the drug observed in LNCs formulation, with prolonged half-life and MRT, compared to oral solution.	[123]
<b>Other</b>							
FRET dyes	Captex® 8000	60	n/a	T	Caco-2	0.3% intact LNCs found crossing Caco-2 after 2 hours.	[128]

V = *in vivo*

T = *in vitro*

E = *ex vivo*

FRET = Förster resonance energy transfer

OA = Oleic acid

CTAB = Cetyltrimonium bromide

DCP = Dicapryl phosphate

DPEG = DSPE-PEG-2000-NH<sub>2</sub>

Captex® 8000 = Tricaprylin

Transcutol® HP = Diethylene glycol monoethyl ether

Tween 80 = Polysorbate 80

Labrafac® = Medium chain triglycerides

Labrafac® WL 1349 = Medium chain triglycerides

Labrafac® CC = Caprylic/Capric Triglyceride

Labrafil® M1944 CS = Oleoyl polyoxyl-6 glycerides

Miglyol® 812 = Medium chain triglycerides

## 5. *In vivo* lipid nanocapsules behavior

From the last section, the *in vivo* oral absorption of LNCs formulation was investigated only with the conventional approach to follow the level of the encapsulated drug alone. The absorption of the intact LNCs particles itself was only investigated in the *in vitro* model and none in the *in vivo* model. It was clear that investigating only the drug level was inadequate to explain the behavior of drug-loaded LNCs such as miltefosine [102] and paclitaxel [91]. The lack of *in vivo* studies on the biofate of intact LNCs is possibly due to the fact that *in vivo* tracking of the intact nanomedicine is difficult [129].

*Förster resonance energy transfer* (FRET) is a tool for tracking intact nanoparticle either in the *in vitro* or the *in vivo* settings. In brief, FRET is the distance-dependent phenomenon (not occurring if the distance >10 nm) that can be used to monitor the dissociation of LNCs. Details are explained in the **Bibliographic Study** section.

## 6. Objectives of the thesis

LNCs is the nanomedicine that provide the benefits on either the flexibility to encapsulate wide ranges of drugs and the capability to increase the oral bioavailability of many drugs. However, there exists the unresolved discrepancy between the correlation of oral bioavailability and therapeutic efficacy in the case of drug-loaded cationic and anionic LNCs [91,102]. That means classical pharmacokinetics model using plasma drug concentration is inadequate to explain the behavior of nanomedicine formulation. Many studies hypothesize that this discrepancy is a result of intact LNCs being able to cross the intestinal membranes into the systemic circulation and thus alters the *in vivo* pharmacological efficacy of the drug [75,91,93,94,102]. However, this has not yet been proven and the bioavailability of intact LNCs is also still unknown due to lack of an appropriate tool. Hence, before the correlation between the oral bioavailability and the therapeutic efficacy of the encapsulated drugs in LNCs will be drawn, it is necessary that the oral absorption of intact LNCs must be more precisely characterized. As such, the main objective of this thesis is:

- 1) To develop appropriate tools *in vitro* and *in vivo* to study intact LNCs oral absorption.
- 2) To characterize the oral absorption of intact LNCs both *in vitro* and *in vivo*.

The first chapter explains the development of the new *in vitro* co-culture model of Caco-2 epithelium and HMEC-1 endothelium. The addition of HMEC-1 endothelium could improve the model to be closer to the physiology of the intestinal barriers.

The second chapter describes the development of a new quantitative FRET technique used for quantifying the particle concentration in biological media both *in vitro* and *in vivo*. This new technique was successfully employed for pharmacokinetic study and pharmacokinetic modelling of LNCs with different sizes (50 and 85 nm) and surface modifications (cationic, anionic, classical LNCs).

The third chapter is the development of quantitative FRET to quantify the particle concentration of intact LNCs in rat intestine, and feces in order to evaluate the oral bioavailability and biodistribution of intact LNCs with different sizes and surface modifications in the hepatic portal system

Moreover, six formulations of LNCs with different size (50-nm and 85-nm) and surface modifications (DSPE-mPEG-2000, Stearylamine, and unmodified) were developed namely LNC-50, LNC-50-PEG, LNC-50-SA, LNC-85, LNC-85-PEG, LNC-85-SA, and then

encapsulated by FRET dyes DiI-TPB and DiD-TPB (**Figure 3**). These six formulations were used throughout the thesis as the standard formulations.

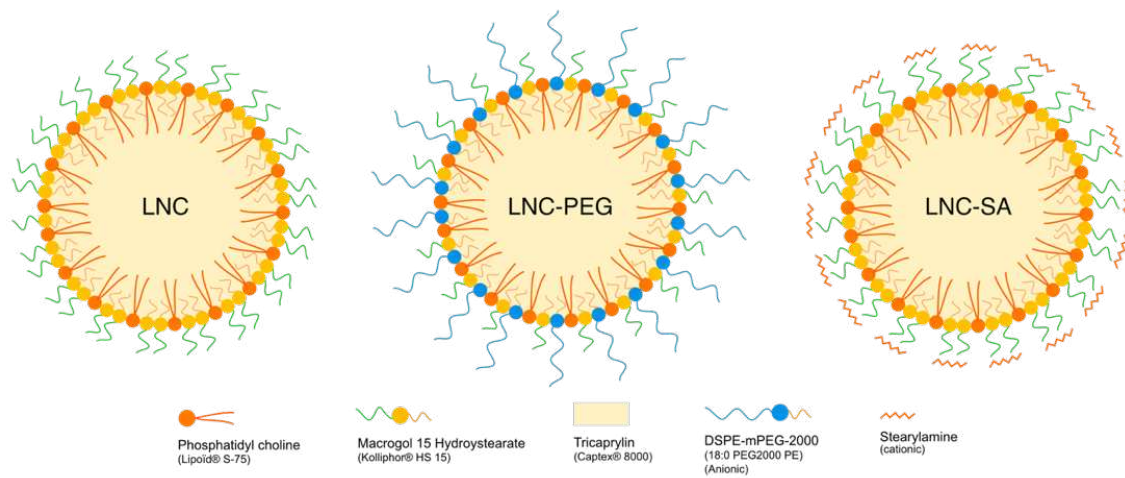


**Figure 3.** Composition and structure of LNCs utilized throughout this thesis. From left to right 1) classical LNCs, 2) PEGylated LNCs with long PEG chain DSPE-mPEG-2000 (abv. LNC-PEG), and 3) cationic LNCs with stearylamine coating (abv. LNC-SA).

## Bibliographic study

The following article details the basic knowledge of FRET, discussing the importance of particle integrity in pharmacokinetic study (including drug absorption), reviewing the use of FRET in various nanosystems with different types of equipment, and finally pointing out the lack of true quantitative FRET which is necessary for advance pharmacokinetics studies. It has been published in the *Journal of Controlled Release* in 2022, entitled "FRET as the tool for *in vivo* nanomedicine tracking".





## Review article

FRET as the tool for *in vivo* nanomedicine tracking

Norraseth Kaeokhamloed, Samuel Legeay, Emilie Roger\*

MINT, INSERM U1066, CNRS 6021, SFR-ICAT, University of Angers, 49333 Angers, France



## ARTICLE INFO

## Keywords:

FRET  
Pharmacokinetics  
Nanomedicine  
*In vivo* fluorescence imaging  
Confocal microscopy

## ABSTRACT

Advanced drug delivery system utilizing a nanocarrier is the major application of nanotechnology on pharmaceuticals. However, despite the promising benefits and a leading trend in pharmaceutical research, nanomedicine development suffers from a poor clinical translation problem as only a handful of nanomedicine products reach the market yearly. The conventional pharmacokinetic study generally focuses only on monitoring the level of a free drug but ignores the nanocarrier's role in pharmacokinetics. One hurdle is that it is difficult to directly track intact nanocarriers *in vivo* to explore their pharmacokinetics. Although several imaging techniques such as radiolabeling, nuclear imaging, fluorescence imaging, etc., have been developed over the past few years, currently, one method that can successfully track the intact nanocarriers *in vivo* directly is by Förster resonance energy transfer (FRET). This review summarizes the application of FRET as the *in vivo* nanoparticle tracker for studying the *in vivo* pharmacokinetics of the organic nanocarriers and gives elaborative details on the techniques utilized.

## 1. Introduction

The European Medicine Agency (EMA) defines ‘nanomedicine’ as the application of nanotechnology aiming for clinical diagnosis and therapeutic use [1]. Advanced drug delivery system utilizing a nanocarrier is the major application of nanotechnology on pharmaceuticals [2]. The main benefits of the nanocarrier delivery system include targeted drug delivery, reducing side effects, enhancing bioavailability, and controlling drug release. With the versatility to carry either large or small molecule drugs, biologics, and genetic materials, the nanocarrier delivery system provides a viable solution for the delivery problem encountered in conventional drug formulation [1–3]. However, despite the promising benefits and a leading trend in pharmaceutical research, nanomedicine development suffers from a poor clinical translation problem as only a handful of nanomedicine products reach the market yearly [4,5]. The lack of a complete understanding of nanomedicine's pharmacokinetics contributes to the cause of this failure. The conventional pharmacokinetic study generally focuses only on monitoring drug levels but ignores the nanocarrier's role in pharmacokinetics. This approach is certainly inadequate for the overall understanding of a drug's pharmacokinetics because the interaction that a body acts upon a nanocarrier also directly affects the pharmacokinetics, the therapeutic efficacy, and the safety of the loading drug [6,7]. Moreover, there are many more aspects of pharmacokinetics in the context of nanomedicine,

for example, particle integrity, drug release, particle internalization, etc., which are difficult to be explained using the classical ADME (absorption, distribution, metabolism, and elimination) model alone. Therefore, to obtain a complete view of the pharmacokinetics of the nanomedicine, the pharmacokinetics of the intact nanocarriers is as important and needs to be investigated [8,9].

Up until now, the advanced pharmacokinetic analysis on the nanocarriers is still limited, especially for the organic nanomedicine [8,9]: lipid-based and polymer-based nanoparticles [3]. Despite making up the largest group of nanomedicine in the market [10], the organic nanoparticles are difficult to be directly characterized *in vivo*, in tissue, and in biological fluid. Several imaging techniques have been developed over the past few years, trying to directly characterize the nanocarriers *in vivo*. Nuclear imaging using the radiolabel is one of the conventional techniques with high sensitivity for monitoring biodistribution and elimination. It can indirectly give quantitative information about the nanocarriers. However, radiolabeling needs to be strongly conjugated to the nanocarrier's structure, risking modifying the nanocarrier's physicochemical properties. The technique also gives a poor resolution and involves radioactive materials. Other imaging techniques such as computed tomography (CT) and magnetic resonance imaging (MRI) are also employed with the advantage of a higher resolution for organic nanoparticles. However, their operation cost is high, and those methods are not appropriate for organic nanoparticles detection. Thus, a simpler

\* Corresponding author.

E-mail address: [emilie.roger@univ-angers.fr](mailto:emilie.roger@univ-angers.fr) (E. Roger).<https://doi.org/10.1016/j.jconrel.2022.06.048>

Received 25 April 2022; Received in revised form 20 June 2022; Accepted 25 June 2022

Available online 7 July 2022

0168-3659/© 2022 The Authors. Published by Elsevier B.V. This is an open access article under the CC BY-NC-ND license (<http://creativecommons.org/licenses/by-nc-nd/4.0/>).

and less expensive technique such as the fluorescence method is preferably used [9,11], particularly with the emergence of carbocyanine fluorescence dyes. The commercialized carbocyanine dyes have emission spectra covering the near-infrared (NIR) range (650–900 nm) which is the sweet spot for the *in vivo* fluorescence imaging due to less interference from the *in vivo* environment. This greatly improves fluorescence's specificity and tissue penetration. The dyes are biocompatible and can be encapsulated into the nanocarriers, rendering them ideal for tracing organic nanocarriers [12]. However, whole-body fluorescence imaging still gives a relatively low resolution, but this can be compensated by using the confocal fluorescence microscopy (CFM) technique in parallel. The technique acts as a fluorescence magnifying glass zooming into a small area of interest. It gives a very high resolution but loses the tissue penetration capability so that it is more suitable for imaging *ex vivo* tissue or organs [9,13].

Nevertheless, all of the techniques mentioned earlier have the same crucial problem that they cannot directly determine the particle integrity of organic nanoparticles. Currently, the only method that can characterize the particle integrity of organic nanoparticles is by Förster resonance energy transfer (FRET) [9,14,15]. It is a subset of the fluorescence technique often dubbed the 'nano-ruler' since the technique is very sensitive to the distance change in nanoscale and is thus proved to be useful for monitoring the association or the dissociation of organic nanoparticles [16]. Another advantage of FRET is that the commonly used carbocyanine dyes can be utilized, making it easier for the existing fluorescence imaging techniques to be upgraded to FRET [16,17]. Therefore, it is obvious that FRET can be an ideal tool for studying the pharmacokinetics of nanomedicine in the future. This review summarizes the application of FRET as the *in vivo* nanoparticle tracker for studying the *in vivo* pharmacokinetics of the organic nanocarriers and gives elaborative details on the techniques utilized.

## 2. General overview on FRET

Förster resonance energy transfer (FRET), a.k.a. the fluorescence resonance energy transfer, was discovered by Theodor Förster. [18,19] FRET is a non-radiative near-field resonance phenomenon originating from the dipole-dipole interaction between two fluorophore molecules, which can only occur at a very close distance (<10 nm). When one fluorophore is excited and in close proximity with another fluorophore whose absorption spectrum overlaps the first fluorophore's emission spectrum, the energy can be transferred from the first fluorophore to the second one (Fig. 1). The fluorophore that transfers the energy is called the donor, and the one receiving the energy is called the acceptor. The amount of energy absorbed by the donor that is transferred to the

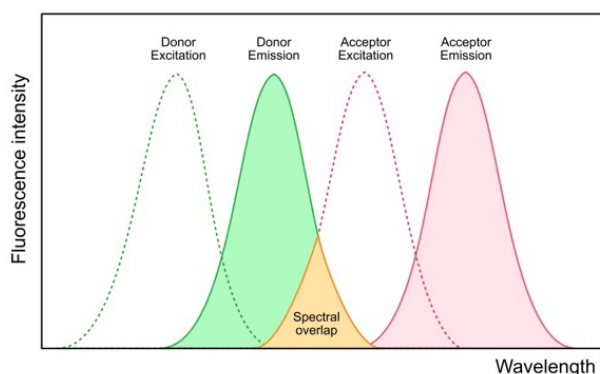


Fig. 1. FRET occurs when the donor emission spectrum overlaps the acceptor excitation spectrum (yellow area). (For interpretation of the references to colour in this figure legend, the reader is referred to the web version of this article.)

acceptor is the FRET efficiency ( $E_{FRET}$ ), which is highly dependent on the distance ( $r$ ) between the donor and acceptor by the factor of  $r^{-6}$ . FRET transfer rate is in equilibrium with the decay rate at  $E_{FRET} = 50\%$ , and as such, the corresponding  $r$  distance is defined as  $R_0$  (Fig. 2). Thus, the  $E_{FRET}$  can be defined by the relationship with  $R_0$  and  $r$  as the equation below [16,20,21].

$$E_{FRET} = \frac{R_0^6}{R_0^6 + r^6}$$

There are several ways to measure  $E_{FRET}$  based on the quantum yield, the fluorescence intensity, or the fluorescence lifetime, of which their details can be found elsewhere [20,22]. Herein, only the most commonly used techniques of FRET measurement are explained.

### 2.1. FRET proximity-based measurement

Proximity-based FRET measurement focuses on measuring  $E_{FRET}$  relating to the distance between the donor-acceptor ( $r$ ). The  $E_{FRET}$  rapidly increases to 98% at the distance of  $0.5R_0$  and conversely plummets to 1% at  $2R_0$  (Fig. 2). Therefore, the distance range between  $0.5R_0$  and  $2R_0$  is very useful for the proximity measurement [16,23]. However, directly measuring  $E_{FRET}$  and  $R_0$  is a complex task. Therefore, for practicality,  $E_{FRET}$  is simplified by correlating to the donor and acceptor intensity, giving a practical parameter called FRET proximity ratio (PR) as shown in the equation:

$$PR = \frac{I_{AD}}{(I_{AD} + I_{DA})}$$

Where  $I_{AD}$  and  $I_{DA}$  are the emission intensity of the FRET acceptor and the donor, respectively [24–28]. Sometimes,  $E_{FRET}$  is simplified to FRET intensity ratio, which is seldomly found in the literature [29,30].

$$Ratio = \frac{I_{AD}}{I_{DA}}$$

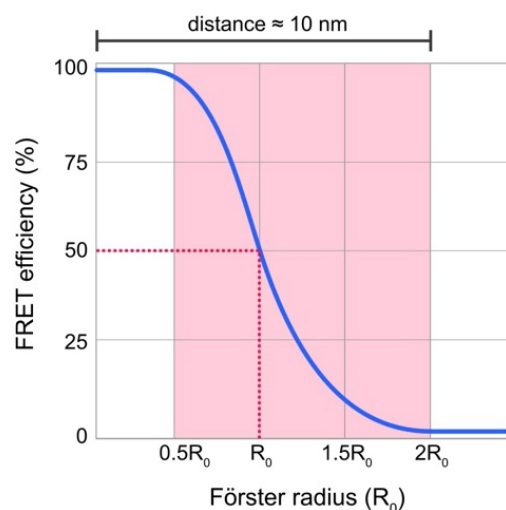


Fig. 2. Relationship between FRET efficiency ( $E_{FRET}$ ) and Förster radius ( $R_0$ ). FRET transfer rate is in equilibrium with the decay rate at  $E_{FRET} = 50\%$ , and as such, the corresponding donor-acceptor distance ( $r$ ) is defined as  $R_0$  (red dash line).  $E_{FRET}$  is highly dependent on  $r$  as it rapidly increases to 98% at the distance of  $0.5R_0$  and conversely plummets to 1% at  $2R_0$ . Therefore, the distance range between  $0.5R_0$  and  $2R_0$  is very useful for the proximity measurement. Generally, the distance of  $2R_0$  is approximately 10 nm, which is why FRET occurs only at a nanoscale. Adapted from [23]. Copyright 2014, with permission from John Wiley and Sons. (For interpretation of the references to colour in this figure legend, the reader is referred to the web version of this article.)

Proximity-based FRET has the main application for monitoring the structural and conformational change of macromolecules at a molecular level. It can be used as a biosensor for either qualitative analysis for the spatial interaction as the on/off switch (FRET vs. No-FRET situations) or quantitative analysis as a nanoscale ruler [21,22,31].

## 2.2. FRET lifetime-based measurement

Fluorescence lifetime ( $\tau$ ) is the time interval that the fluorophore stays at the excited state before radiating the photon. Generally, it is around  $10^{-9}$  s and follows the exponential decay as in the equation:

$$\frac{F(t)}{F(0)} = e^{-t/\tau}$$

Where  $F(t)$  is the photon count at the time  $t$ . Thus, the lifetime  $\tau$  is defined as  $F(0)/e \approx 37\%$  of the initial photon count [32,33]. For FRET application, the donor will transfer the energy to the acceptor via a non-radiating process resulting in the donor emission quenching and a decrease in  $\tau$ . Thereby,  $E_{FRET}$  can be monitored from donor quenching as in the equation:

$$E_{FRET} = 1 - \left( \frac{\tau_{DA}}{\tau_D} \right) = 1 - \left( \frac{I_{DA}}{I_D} \right)$$

Where  $\tau_{DA}$  is the donor lifetime with FRET,  $\tau_D$  is the donor lifetime without FRET, and likewise for the donor intensity ( $I$ ) [20,22,33]. This FRET donor quenching technique is useful for dynamic fluorescence measurement, such as live-cell image analysis. The technique referred to as FRET Fluorescence lifetime imaging (FRET-FILM) is the combination of lifetime measurement and cellular imaging with FRET donor quenching. Indeed, the use of FRET helps to discriminate the endogenous molecules against the autofluorescence. FRET-FILM allows for live monitoring of several dynamic interactions such as receptor-ligand binding, protease activity, protein folding, hybridization of genetic materials [33].

## 3. FRET-nanomedicine applied to *in vivo* nanoparticles tracking

Generally, FRET proximity-based measurement is applied to nanomedicine to monitor the nanoparticle's structural change, including particle association, particle integrity, cargo release, and particle interaction with cells [15]. In the context of the pharmacokinetics of nanomedicine, especially the organic nanoparticles, FRET is usefully employed as the *in vivo* nanoparticle tracking technique because it is the technique that can determine nanoparticle's integrity both *in vivo* and *in vitro* [9]. Particle integrity is crucial for the pharmacokinetics of nanoparticles because the integrity defines the existence of the nanoparticle and the clinical benefits thereof, such as the protective effect to the encapsulated drugs, the organ targeting effect, the extravasation and membrane transport effect, etc. [1,2]. An ability to determine the intact nanoparticles *in vivo* will help to elucidate the *in vivo* pharmacokinetics of the nanocarriers, which is essential for clinical translation [4–7].

*In vivo* nanoparticle tracking requires a pair of FRET dyes (often called a FRET pair) to be integrated into the nanoparticle's structure rendering the FRET-nanoparticles. The FRET dyes of choice are the carbocyanine dyes with the emission spectra in the near-infrared (NIR) range (650–900 nm) to obtain high tissue penetration by avoiding autofluorescence from cells and tissues [12]. These dyes include, for example, non-sulfonated cyanines: Cy3, Cy5, Cy5.5, Cy7, Cy7.5, indocyanine green (ICG); and dialkylcarbocyanines (Di): DiO, DiR, DiI, DiD (Fig. 3) [34].

Despite following the same FRET principle, techniques to integrate the FRET dyes to make the system of FRET-nanoparticles vary by the structural and chemical differences of each type of the organic nanoparticles.

## 3.1. Polymeric micelles

Polymeric micelles are one of the most diverse groups in terms of chemical composition. However, they do share structural similarities. They have a property of self-assembling and structurally consist of the hydrophobic moiety (not entirely hydrophobic but less hydrophilic than the other part) resembling a core and the hydrophilic moiety resembling an outer shell. Carbocyanine dyes are mainly used as a FRET pair in this type of nanoparticle, and they can either be loaded into the hydrophobic core or be conjugated to the polymer itself, in order to reflect or mimic how drugs can actually be loaded to the nanocarrier. Therefore, it can be classified into a group of dye-loading FRET system and dye-conjugating FRET system (Fig. 4). In the dye-loading FRET system, carbocyanine dyes can be loaded into the hydrophobic core of the micelles. Besides, in the dye-conjugating FRET system, hydrophobic fluorescence dyes could be conjugated to the hydrophobic moiety of the polymer. Donor and acceptor FRET dyes are conjugated separately and then mixed together while forming a micelle consisting of a FRET pair. So, when the micelles dissociate, the conjugated-FRET pair will disperse out, resulting in the disappearance of the FRET signal. These different FRET systems imply different aspects of micelles stability and pharmacokinetics. The dye-loading FRET system implies cargo release. The dye-conjugating FRET system implies the dissociation of the micelles. This is useful for monitoring the pharmacokinetics of drugs loaded inside the micelle core. However, in terms of pharmacokinetic study of nanomedicine, those aspects are not practically different since the focus is on the nanoparticles' integrity rather than the loaded drugs.

## 3.2. Lipid nanocapsules and liposomes

Nanocapsules are a class of nanoparticles that contains a shell-like structure and a core resembling a capsule or a vesicle. Lipid nanocapsules and lipid nanoemulsions contain a monolayer shell of surfactant surrounding a lipid core. Liposomes are a vesicle with phospholipid bilayer shell. Carbocyanine dyes are utilized in this type of nanoparticles by the co-encapsulation inside the nanoparticle's core or void. All the FRET systems of lipid nanocapsules and liposomes are summarized in Fig. 5.

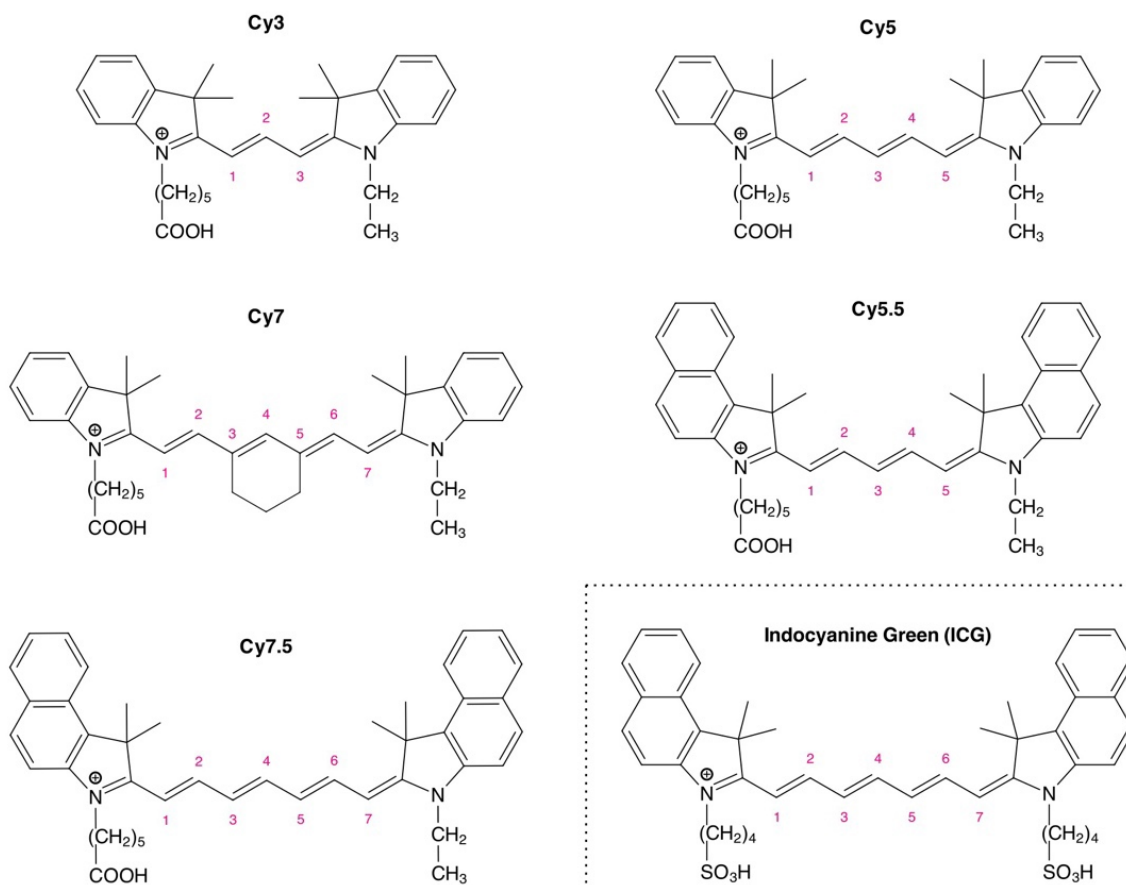
## 3.3. Nanospheres

Nanospheres are a class of nanoparticles that has a matrix structure. It is called nanospheres, although it does not need to be spherical in shape. It can be made of various organic and inorganic materials. However, FRET was only utilized in organic lipid or polymeric nanospheres for studying their *in vivo* pharmacokinetics. Nanospheres seem to be uniquely developed for delivering a specific drug. All three types of nanospheres have different strategies to incorporate FRET pairs. For the squalene-gemcitabine bioconjugate nanoparticles (SQGem nanospheres) [38], the FRET pair was conjugating to the matrix structure. For the c(CRGDKGPDC) peptide (iRGD) modified hyaluronic acid–deoxycholic acid conjugate (iRGD-PEG-HA-DOCA) a.k.a. IPHD nanoparticles [49], the FRET pair was simply dispersed in the polymer matrix. On the other hand, for the polymeric  $\gamma$ PGA-EGTA nanoparticles [50,51], the FRET system is firstly conjugated to insulin before being loaded into the polymer matrix. The study also focused on the stability of the insulin in the GI tracts rather than the stability of the polymer matrix [50]. Fig. 6 summarizes all the FRET systems of nanospheres.

## 3.4. Nanocrystals

Nanocrystal is a crystal in the nanometer range formulated by nanoprecipitation of poorly water-soluble organic substances. There are two nanocrystals with FRET described: coumarin-6 nanocrystals [52] and curcumin nanocrystals (Fig. 7) [53]. While coumarin-6 nanocrystal can be paired with DiI to create a FRET system, curcumin nanocrystal loses

## Non-sulfonated Cyanines



## Dialkylcarbocyanines

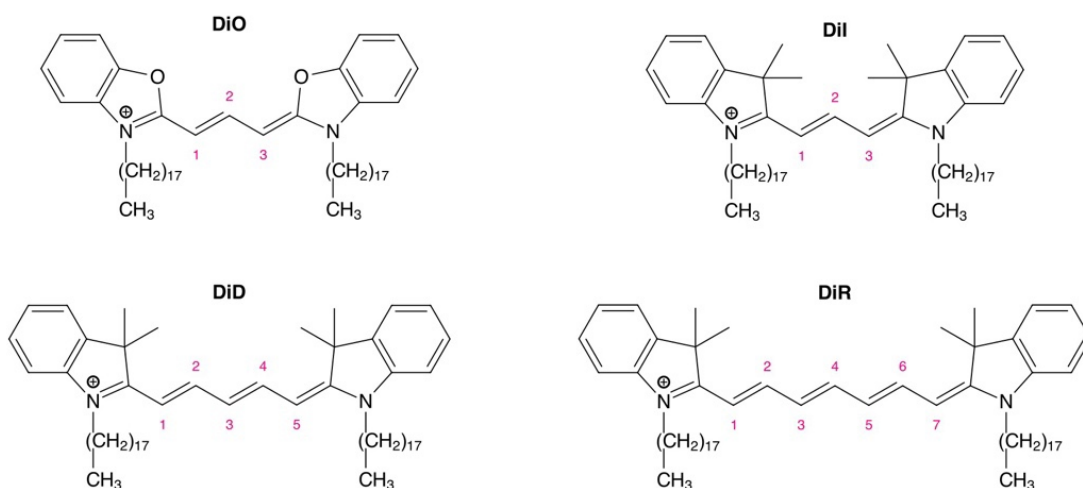


**Fig. 3.** Example of commonly used carbocyanine dyes for FRET with the emission spectrum in the range from 500 to 900 nm. Non-sulfonated cyanine dyes include Cy3 [35], Cy5 [36], Cy7 [37], Cy5.5 [38], Cy7.5 [38], and ICG [39]. Dialkylcarbocyanine dyes include DiO, DiI, DiD, DiR [34]. There are structural similarities between Cy3/DiI, Cy5/DiD, Cy7/DiR, and Cy7.5/ICG. A longer polymethine chain (marked by carbon number) red-shifts the excitation and emission wavelengths towards the near-infrared region. (For interpretation of the references to colour in this figure legend, the reader is referred to the web version of this article.)

**Table 1**  
Summary of the instrumental technique of FRET for *in vivo* pharmacokinetic study.

Instruments	Fluorometer/ microplate reader	Confocal Microscopy (CFM)	<i>In vivo</i> imaging system (IVIS)
Samples	<ul style="list-style-type: none"> <li>Plasma extract</li> <li>Blood</li> </ul>	<ul style="list-style-type: none"> <li>Tissue slice</li> <li>Cells</li> <li>Mouse's earlobe and liver vasculatures (<i>in vivo</i> intravital)</li> <li>Zebrafish larva (whole-body)</li> </ul>	<ul style="list-style-type: none"> <li>Mouse or rat (whole-body, live)</li> <li><i>Ex vivo</i> organs</li> <li>Blood</li> <li>Plasma extract</li> </ul>
Assay technique	Semi-quantitative particle concentration and chemical assay	Qualitative & Semi-quantitative imaging assay	<ul style="list-style-type: none"> <li>Qualitative &amp; Semi-quantitative imaging assay (live)</li> <li>Semi-quantitative particle assay</li> </ul>
Pharmacokinetic study	<ul style="list-style-type: none"> <li>Plasma particle concentration (SQT)</li> <li>Particle stability in plasma (SQT)</li> </ul>	<ul style="list-style-type: none"> <li>Particle stability in organ (QL, SQT)</li> <li>Biodistribution (SQT)</li> <li>Oral absorption (QL)</li> <li>Cargo release (QL)</li> </ul>	<ul style="list-style-type: none"> <li>Particle stability in organ or whole-body (QL, SQT)</li> <li>Biodistribution (QL, SQT)</li> <li>Plasma particle concentration (SQT)</li> <li>Oral absorption (SQT)</li> <li>Cargo release (SQT)</li> </ul>
Advantages	<ul style="list-style-type: none"> <li>Gives a high-resolution fluorescence spectrum</li> <li>True chemical assay</li> <li>Potential for true quantitative analysis if done with proper calibration curves</li> </ul>	<ul style="list-style-type: none"> <li>High image resolution (microscopic level)</li> <li>More practical for qualitative imaging analysis</li> </ul>	<ul style="list-style-type: none"> <li>Live animal whole-body image</li> <li>Wide range of samples</li> </ul>
Limitations	<ul style="list-style-type: none"> <li>Limited to plasma or blood sample</li> <li>Non-imaging analysis</li> </ul>	<ul style="list-style-type: none"> <li>Practical only for microscopic sample</li> <li>Less practical for live animal imaging</li> </ul>	<ul style="list-style-type: none"> <li>Signal interferences for whole-body imaging</li> <li>Requires complex signal calibration procedures for FRET</li> </ul>

QL = Qualitative assay.

SQT = Semi-quantitative assay.

its fluorochrome property and thus needs another FRET system from the pair of perylene and H<sub>2</sub>TPyP.

### 3.5. Dendrimers

Dendrimers consisting of an inner core and a peripheral shell are the well-designed branching architectures macromolecules with abundant terminal groups allowing for dye conjugation. Dyes can also be loaded into the inner core.

PEG<sup>5k</sup>-CA<sub>8</sub> telodendrimers were a class of dendrimer developed by Li et al. [54]. The basic structure of the telodendrimers consists of the PEG<sup>5k</sup> moiety and the dendritic oligomer of cholic acid (CA<sub>8</sub>). It is a self-assembly system in which cholic acid telodendrimers coalesce together as a hydrophobic core and the PEG<sup>5k</sup> moiety facing outward as a hydrophilic shell. Carbocyanine dye DiO as the FRET donor was

encapsulated in the core, while rhodamine B as the FRET acceptor was conjugated to the telodendrimer (Fig. 8).

## 4. *In vivo* pharmacokinetic studies using FRET-nanomedicine

Pharmacokinetic study involves collecting the animal's blood sample, tissues, organs, or even full-body imagery. In these different samples, FRET measurement can be performed by common fluorescence imaging tools, namely microplate reader, fluorometer, confocal microscopy (CFM), or *in vivo* imaging system (IVIS). All the instruments can perform the semi-quantitative assay, while only CFM and IVIS can perform qualitative and semi-quantitative imaging analysis. The advantages and limitations of each instrumental technique are summarized in Table 1. The following sections will detail these FRET techniques used as the *in vivo* nanoparticle tracker exemplified with some nanoparticles described before. Table 2 summarizes all the FRET system and their application for the *in vivo* pharmacokinetics of the nanomedicine.

### 4.1. FRET *in vivo* nanoparticle tracking by confocal microscopy (CFM)

CFM is used for the tissue slides or organ samples. CFM may also be used for live imaging of the superficial veins of rodents, or the whole body of zebrafish larvae.

#### 4.1.1. Live-imaging of the vasculature by intravital FRET-CFM

Live-imaging of the vasculature by intravital FRET-CFM was only performed on micelles nanoparticles.

Chen et al. [40] were the first to utilize FRET as the *in vivo* nanoparticle tracker. The technique was to perform the qualitative imagery assay and the semi-quantitative assay on the *in vivo* particle stability of the PED-b-PPLG micelles (PPMs) in a mouse model. Then the FRET-PPMs were intravenously injected into the mice. The fluorescence image of the vasculature on the mouse's ear lobe was taken by the confocal microscope. The intensity of the signals from the photo was recorded, and the FRET proximity ratio could be calculated to estimate the plasma particle concentration of the micelles. The proximity ratio (called the FRET ratio) was also compared with the positive standard of the fully intact micelles in water and the negative standard of the dissociated micelles in acetone. The result showed the fast *in vivo* dissociation of FRET-PPMs in the mouse's circulatory system, as the PR dropped from 0.90 to 0.46 (negative control's PR = 0.30) within 15 min. Further *in vitro* particle stability study using the FRET method revealed that  $\alpha$ - and  $\beta$ -globulins in blood were the probable cause of the PPMs' fast dissociation.

Later, by Ishizawa et al. [42], the *in vivo* live FRET imaging of FRET-PPMs in the mouse's ear and the liver vasculature was conducted by confocal microscopy for up to 4 h (Fig. 9.). The particle stability in the vasculature was observed qualitatively and found that FRET-PPMs extravasated to a hepatic tissue and dissociated. Further *in vitro* FRET experiment also revealed that FRET-PPMs might dissociate while interacting with the hepatic cell membrane.

A derivative of PEG-PDLLA was developed by Lee et al. [41] as the disulfide-bonded mPEG-(Cys)4-PDLLA micelles (DS-PPMs) for the delivery of doxorubicin, aiming for strengthening the particle integrity and for the targeting release in the glutathione (GSH) rich environment of the cancer tumor. Confocal microscopy was also utilized to record the vasculature on the mice's ear lobe. The *in vivo* particle stability of PPMs and DS-PPMs in the circulation system was semi-quantitatively analyzed by the proximity ratio (PR). The result was clear that the PR of DS-PPMs was always higher than the PPMs up to 12 h, meaning that DS-PPMs retained higher particle stability than PPMs. Next, the biodistribution and the particle stability of DS-PPMs (alone) in the tumor were studied using the same FRET confocal microscopy technique. M109 tumor grafted mice were intravenously injected with DS-PPMs with the tumor and internal organs harvested after 6 h. The particle integrity of the DS-

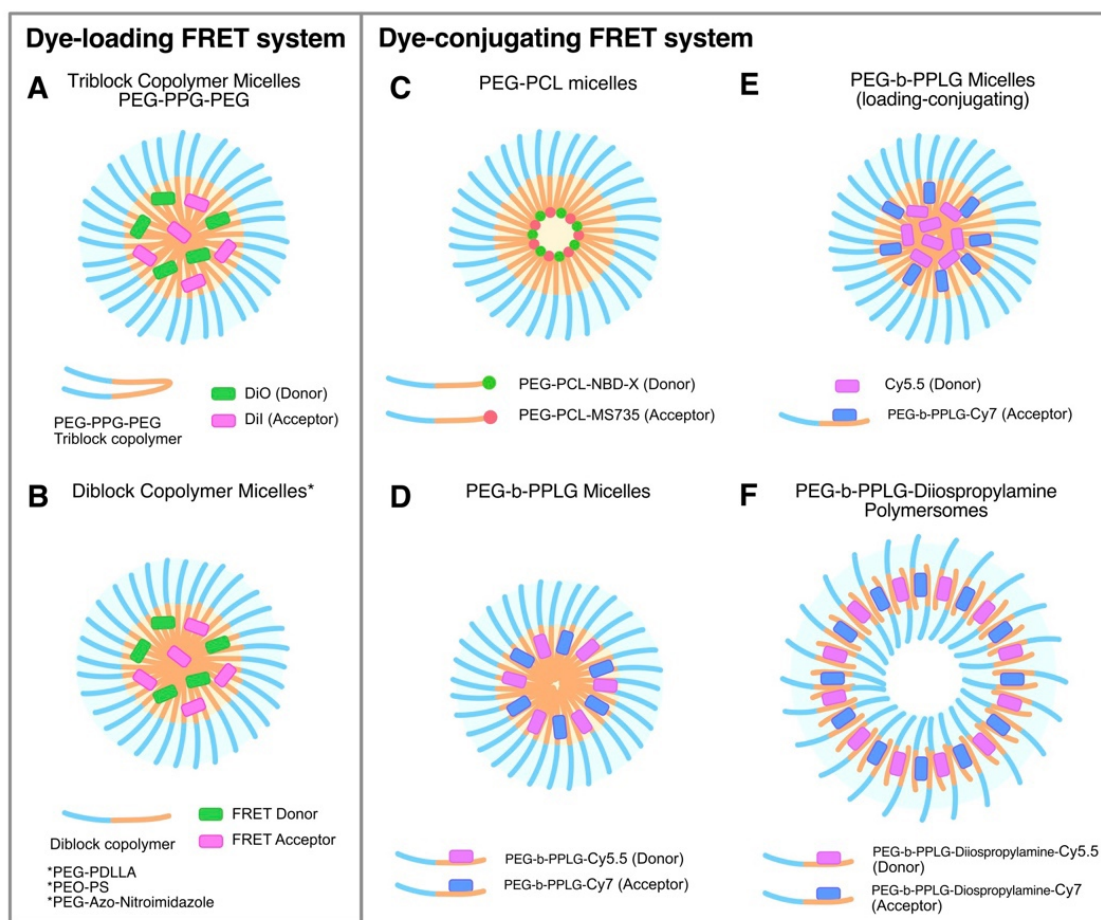


**Fig. 4.** Schematic illustration summarizing the FRET system of polymeric micelles. Nanoparticles with dye-loading FRET system include A) Triblock copolymer micelles PEG-PPG-PEG, B) Diblock copolymer micelles including PEG-PDLLA, PEO-PS, PEG-Azo-Nitroimidazole. Nanoparticles with dye-conjugating FRET system include C) PEG-PCL micelles, D) PEG-b-PPLG micelles with Cy5.5 and Cy7 conjugation, E) PEG-b-PPLG micelles with Cy5.5 loading and Cy7 conjugation, F) PEG-b-PPLG polymersomes with Cy5.5 and Cy7 conjugation.

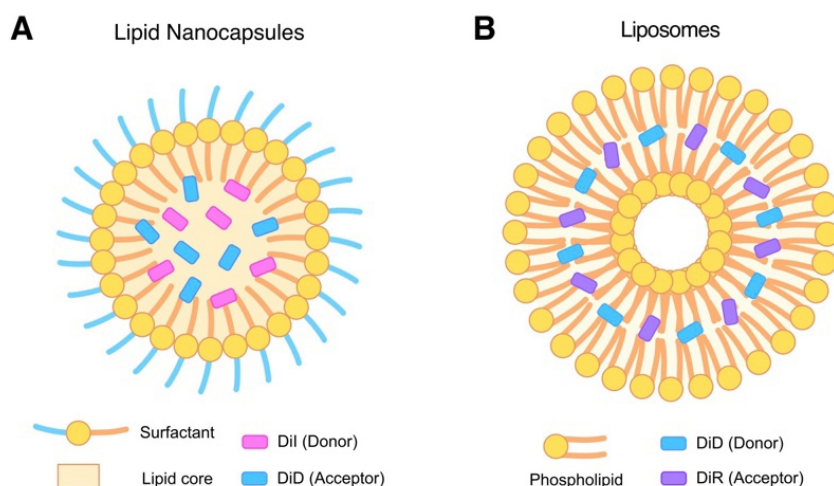


**Fig. 5.** Schematic illustration summarizing the published FRET system of lipid nanocapsules and liposomes. A) Lipid nanocapsules with the FRET system of DiI and DiD from Gravier et al. [29] as an example. B) Liposomes with the FRET system of DiD and DiR from Liu et al. [48] as an example. FRET dyes are co-encapsulated inside the lipid compartment of the nanoparticles.

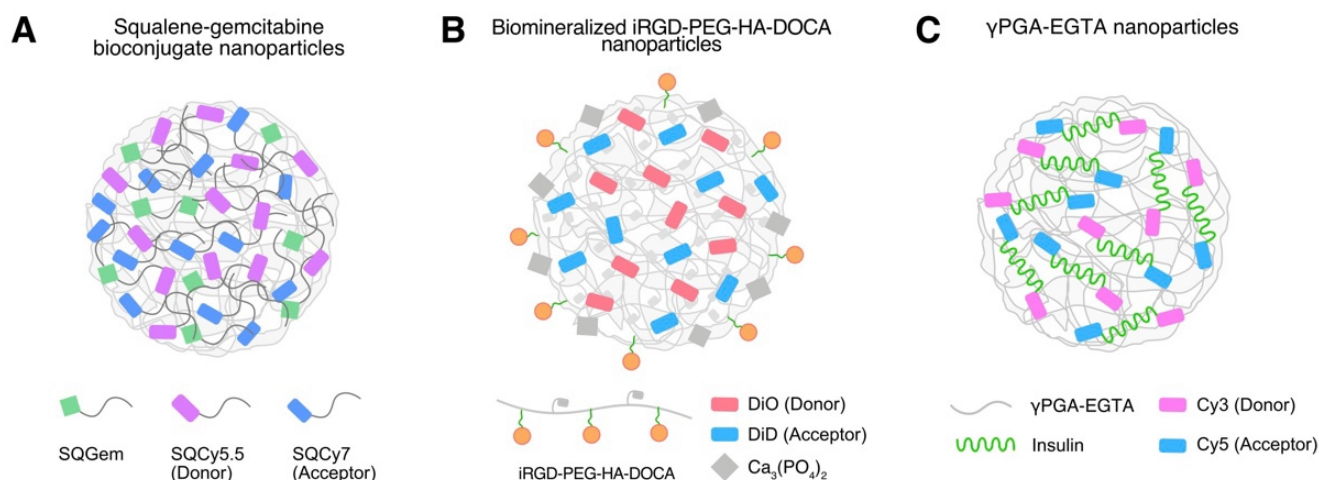


**Fig. 6.** Schematic illustration summarizing the published FRET system of the nanospheres. A) Squalene-gemcitabine bioconjugate nanoparticles with the FRET dye Cy5.5 and Cy7 conjugating to squalene. B) Biom mineralized iRGD-PEG-HA-DOCA nanoparticles with the FRET dyes DiO and DiD loading inside the polymer matrix. C)  $\gamma$ PGA-EGTA nanoparticles with the FRET dyes Cy3 and Cy5 conjugating to insulin and then loaded inside the polymer matrix.

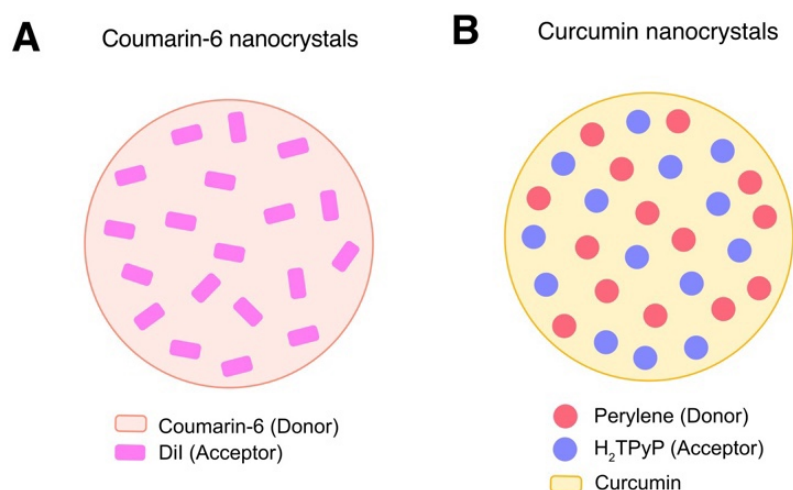


**Fig. 7.** Schematic illustration summarizing the published FRET system of the nanocrystals, in which FRET dyes are dispersed inside the nanocrystal. A) Coumarin-6 nanocrystals, which coumarin-6 itself acts as FRET donor to the acceptor DiI. B) Curcumin nanocrystal with the FRET system of perylene and  $\text{H}_2\text{TPyP}$  (porphyrin derivative).

PPMs was analyzed semi-quantitatively by FRET in the tumor vasculature vs. the tumor cells. DS-PPMs retained their integrity in the tumor vasculature ( $\text{PR} = 0.66$ ) while dissociated in the tumor cell ( $\text{PR} = 0.31$ ). FRET images from other *ex vivo* organs (liver, spleen, lungs, kidney) were analyzed qualitatively, and a strong FRET acceptor signal was visually observed. This means that DS-PPMs have a highly targeting release in the tumor. Further study on the efficacy of doxorubicin encapsulated DS-PPMs (DOX-DS-PPMs) showed a 7-times increase of doxorubicin accumulation in the tumor and higher tumor suppression efficacy, compared with the conventional non-disulfide doxorubicin encapsulated PPMs (DOX-PPMs), which had poorer *in vivo* particle stability. This study really demonstrated that the *in vivo* particle integrity of the nanocarrier really has an effect on drug efficacy and delivery, and FRET is proved as a very practical tool to investigate it.

These studies really demonstrated a series of technical development of FRET application for the live *in vivo* test using confocal microscopy. However, the intravital imaging of liver vasculature is rather complicating and invasive to the animal (an advanced surgical procedure to open a living rat's liver and keep them alive for an extended period of

time).

#### 4.1.2. Imaging of *ex vivo* tissue slides by FRET-CFM

For this technique, only liposome systems were described. Firstly, Tang et al. [55] performed the FRET semi-quantitative assay to investigate the particle stability of liposomes (LPs) vs. D-self-peptide-labeled liposomes (DSL) in the mouse's liver. DSL was designed to have a high adsorption affinity to the cell membrane of the various hepatic cells, blocking the hepatic cell's endocytosis and the hepatic clearance of the actual therapeutic nanoparticles that would be administrated later. As such, DSL was expected to have long particle stability on the liver cell membrane surface. For the FRET assay, carbocyanine dyes DiO (donor) and DiI (acceptor) were co-encapsulated inside the liposomes (LPs) voids. Mice were intravenously injected with the FRET-LPs and FRET-DSL. They were then sacrificed after 0.5, 4, 24 h with their liver harvested and sliced by a microtome. The FRET fluorescence image of the sliced liver sample was taken using a microplate reader. The fluorescence intensity was retrieved from the image allowing for the FRET proximity ratio to be calculated and normalized to the time zero (called

## Telodendrimers nanoparticles

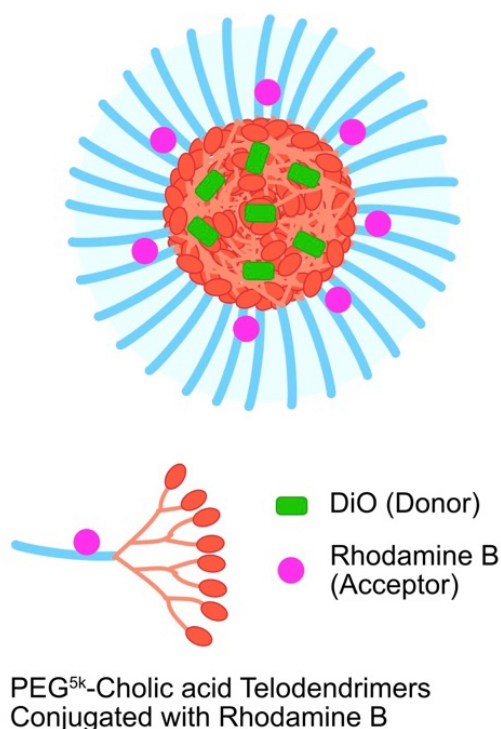


**Fig. 8.** Schematic illustration summarizing the FRET system of telodendrimers nanoparticles. DiO was loaded to the cholic acid core, and rhodamine B was covalently conjugated to telodendrimers. Adapted with permission from [54], Copyright 2012 American Chemical Society.

% relative FRET ratio). FRET-DSL was found to be more stable than FRET-LPs in the mouse's liver after 24 h, suggesting a slower elimination of DSL from the liver. DLS was later verified to be more effective than the conventional LPs to block the hepatic clearance of the amphotericin B encapsulated PLGA-Nanoparticles. This resulted in a prolonged circulation of amphotericin B and the increase in its effectiveness against the brain's fungal infection in a mouse model. This research again shows the usefulness of FRET to analyze the *in vivo* particle stability of LPs.

Liu et al. [48] also used the qualitative FRET imaging by confocal microscopy to study the oral absorption of liposomes (LPs). The jejunum section was selected for the *in vivo* intestinal epithelial uptake experiment. Male Sprague-Dawley rats were anesthetized, and the FRET-LPs were directly injected into the jejunum and ileum where the Peyer's patches were situated. After 2 h, the said intestinal section was harvested, immobilized, frozen, and further stained with DAPI for revealing tissue structure. Then, the intestinal sample was sliced and put under the CFM for magnified imaging. Its visible presence signified the intact FRET-LPs that migrated through the epithelium layer of jejunum and ileum. However, the FRET signal could not be quantifiable with the confocal microscopy, making this only the qualitative assay. It was observed that the intact cationic LPs and PEGylated LPs had a higher FRET intensity throughout the jejunum's epithelium, suggesting their better uptake.

### 4.1.3. FRET-CFM with zebrafish larva

#### 4.1.3.1. Nanocrystals.

Li et al. [52] demonstrated the use of qualitative

FRET with the zebrafish larva model for the first time for investigating the particle stability of FRET-nanocrystal. The *in vivo* particle stability was qualitatively studied by exposing zebrafishes (*Danio rerio*) and their larvae with the FRET-nanocrystals using the incubation method. After a specific time period, fluorescence images of the fishes and the larvae were taken using confocal microscopy. The presence of the FRET acceptor signals in the imagery determines the presence of stable nanocrystals in the zebrafish larvae. Imaging results found the increase in FRET intensity signal over time 60 min indicating that the nanocrystal absorbed into the larva gradually. Unfortunately, FRET was only used qualitatively and briefly in this research, and only coumarin-6 (FRET donor) was further analyzed for their accumulation in organs regardless of the particle integrity.

4.1.3.2. *Micelles.* Another study using FRET with a zebrafish larva model was performed by Tao et al. [43]. The semi-quantitative FRET technique was employed to study the *in vivo* particle stability and the cargo release of the ordinary PEG-PPG-PEG micelles (OPMs) and the disulfide bond cross-link PMs (CPMs). The FRET-micelles were injected into the circulatory system of the zebrafish's larva using a microneedle. Over specific time points, the live fluorescence images of the fishes were taken by confocal microscopy. At first, the image was qualitatively analyzed by determining the presence of the FRET acceptor signal in the caudal veins and caudal arteries. Then, both the FRET donor and the FRET acceptor signals were quantified by the software (Fig. 10.). In this case, the FRET donor (DiO) signal means the released core content, and the FRET acceptor (DiI) signal determines the relative amount of the intact micelles. Then, the FRET proximity ratio was calculated and normalized to 100% (called % integrity), being used as another integrity parameter. CPMs were found to be more stable than PMs. After 1 h, CPMs retained 60% integrity in contrast to 30% integrity of OPMs. Next, in order to investigate the cargo release dynamic, the fluorescence intensity of the donor channel and FRET channel were directly compared in their arbitrary unit. In this article, the donor signal from DiO was considered the signal of the free DiO released from the OPMs, meaning that it was the measurement of the dequenching of DiO. Despite the fact that the donor dequenching may imply the release of the free donor dye, the donor (de)quenching intensity alone is not adequate as the proof of FRET [22], i.e., not the proof of integrity or content release. As such, the donor intensity can be, at best, a qualitative parameter for the cargo release. Generally, the FRET proximity ratio is adequate for the determination of the cargo release dynamics.

### 4.2. FRET *in vivo* nanoparticle tracking by *in vivo* imaging system (IVIS)

For animals such as rats or mice, the IVIS allows for live imaging of either whole-body animals, *ex vivo* organs, or even blood samples. It also comes with the quantification software to quantify the emission intensity from the area of interest in the image allowing both qualitative imagery and semi-quantitative assay.

#### 4.2.1. FRET-IVIS for live whole-body and *ex vivo* organs imaging

4.2.1.1. *Micelles.* Zou et al. [44] demonstrated the use of a semi-quantitative FRET assay for the first time using IVIS to study the cargo release of PEO-PS micelles. For this experiment, FRET was measured from two perspectives. The first perspective is like an ordinary FRET system in which DiD and DiR were co-loaded into the micelles and administered to the test subject. Then, decreasing FRET signals signifies the cargo release or the micelle dissociation. Nevertheless, to focus on the released content, this conventional co-loaded system has a drawback. Because, if the released dyes still accumulate together, they will still give too bright a FRET signal that makes it very difficult to be distinguished from the FRET of the intact micelle. Therefore, the second perspective was developed to fix this problem. This time, DiD and DiR



**Table 2**  
Summary of the FRET system used for pharmacokinetic studies of nanomedicine.

Nanoparticle type	FRET system		FRET Excitation (nm)	Donor Emission (nm)	Acceptor Emission (nm)	Instrument	Animal model	Area of Interest	Pharmacokinetics study	Level of assay	Reference
	Donor/ Acceptor pair	FRET									
Nanospheres SQGem iRGD-PEG-HA-DOCA	Cy5.5/Cy7.5	640	695–770	810–875		IVIS	Mouse	Liver	Particle stability in liver	Semi-quantitative	[38]
	DIO/DID	484	501	565		Fluorimeter	Rat	Plasma extract	Plasma particle concentration, particle stability	Semi-quantitative	[49]
	Cy3/Cy5	535	570	680		IVIS	Rat	Duodenum	Protective effect of the nanoparticle against the intestinal enzyme	Qualitative, Semi-quantitative	[50,51]
Nanocapsules LNCs, LNEs	DID/FC730-C18	590	660	764		IVIS	Mouse	Whole-body (live), <i>ex vivo</i> organs	<i>In vivo</i> particle stability, Biodistribution	Qualitative	[56]
	DII/DID	535	640	680		IVIS	Mouse	Liver, Tumor	<i>In vivo</i> particle stability, Biodistribution	Semi-quantitative	[29]
						CFM	Mouse	Tumor	<i>In vivo</i> particle stability, Biodistribution	Semi-quantitative	[29]
	Cy5.5TPB/Cy7.5TPB	640	700	820		IVIS	Mouse	Whole-body (live), Tumor	<i>In vivo</i> particle stability, Biodistribution	Semi-quantitative	[57]
Liposomes	DID/DIR	640	n/a	780		IVIS	Mouse	Intestines, hearts, liver, spleen, kidney, lungs ( <i>ex vivo</i> )	Particle stability in the GI, oral absorption, biodistribution	Semi-quantitative	[48]
Liposomes	DIO/DII	435–460	470–515	515–580		CFM	Rat	Intestines	Oral absorption	Qualitative	[48]
Liposomes						CFM	Mouse	Liver	Particle stability in liver	Semi-quantitative	[55]
Nanocrystals Coumarin-6 nanocrystals Curcumin nanocrystals	Coumarin-6/DII	488	490–540	555–675		CFM	Zebrafish larva	Whole-body (intravital)	<i>In vivo</i> particle stability	Qualitative	[52]
	Perylene/H <sub>2</sub> TPP	n/a	n/a	635		Microplate reader	Mouse	Plasma extract	Plasma particle concentration	Semi-quantitative	[53]
						IVIS	Mouse	<i>Ex vivo</i> organs and tumor	Biodistribution	Semi-quantitative	[53]
Polymeric micelles (dye-loading FRET system) PEG-PPG-PEG	DIO/DII	488	508	578		CFM	Zebrafish larva	Cauda (intravital)	<i>In vivo</i> particle stability	Semi-quantitative	[43]
	DIO/DII	488	501	565		CFM	Mouse	Ear vasculature (intravital)	Cargo release Particle stability in blood circulation	Qualitative Qualitative, Semi-quantitative	[43] [40]
	DID/DIR	640	680	809		CFM	Mouse	Ear and liver vasculature ( <i>in vivo</i> intravital)	<i>In vivo</i> particle stability	Qualitative	[42]
mPEG-(Cys) <sub>4</sub> -PDLLA	DIO/DII	488	500–530	555–655		IVIS	Mouse	Whole-body (live), <i>ex vivo</i> organs	<i>In vivo</i> particle stability, Biodistribution	Qualitative, Semi-quantitative	[42]
						CFM	Mouse	Ear vasculature	<i>In vivo</i> particle stability in blood circulation	Qualitative, Semi-quantitative	[41]
						CFM	Mouse	<i>Ex vivo</i> tumor & organs	Biodistribution, Particle stability	Qualitative, Semi-quantitative	[41]
PEO-PS	DID/DIR	640	680	780		IVIS	Mouse	Whole-body (live)	Cargo release (reversed FRET), Particle stability	Semi-quantitative	[44]
	Cy5/Cy7	640	670–730	730–790		IVIS	Mouse	Tumor	Cargo release	Semi-quantitative	[30]

(continued on next page)

Table 2 (continued)

Nanoparticle type	FRET system		Instrument	Animal model	Area of Interest	Pharmacokinetics study	Level of assay	Reference
	Donor/ Acceptor pair	FRET Excitation (nm)						
PEG-Azo-Nitroimidazole								
Polymeric micelles (dye-conjugating FRET system)								
PEG-PCL	NBD-X/MS735	475	Fluorimeter	Mouse	Plasma extract	Plasma particle concentration	Semi-quantitative	[47]
PEG-b-PPLG	Cy5.5/Cy7	640	IVIS	Mouse	Whole-body (live), blood, ex vivo organs	Plasma particle concentration, Biodistribution	Semi-quantitative	[45,46]
Dendrimers								
TEMPO-PEGSk-CA8 telodendrimer	DIO/Rhodamine B	480	Microplate reader	Mouse	Blood	In vivo particle stability, Plasma particle concentration	Semi-quantitative	[54]

CFM = confocal fluorescence microscopy.

IVIS = *In vivo* imaging system.

DiO = DiOC<sub>18</sub>(3) 3,3'-Dioctadecyloxacarbocyanine perchlorate.

DiI = DiIC<sub>18</sub>(3) 1,1'-Dioctadecyl-3,3',3'-Tetramethylindocarbocyanine perchlorate.

DiD = DiIC<sub>18</sub>(5) 1,1'-Dioctadecyl-3,3',3'-Tetramethylindocarbocyanine perchlorate.

DiR = DiIC<sub>18</sub>(7) 1,1'-Dioctadecyl-3,3',3'-Tetramethylindocarbocyanine iodide.

FC730-C18 = Interchim FluoroProbes® 730 conjugated with octadecylamine.

TPB = tetraphenyl borate.

H<sub>2</sub>TPyP = 5,10,15,20-tetra(4-pyridyl)porphyrin.

NBD-X = NBD-X, SE, Succinimidyl 6-(N-(7-Nitrobenz-2-Oxa-1,3-Diazol-4-yl)Amino)Hexanoate.

MS735 = Azide MegaStokes dye 735, 1-(3-Azidopropyl)-4-{2-[6-(diethylamino)-2-benzofuranyl]ethenyl}-3-sulfo-pyridinium inner salt.

were separately loaded into the micelles, making the DiD-micelles and the DiR-micelles. Then they were mixed with the same proportion and administered to the test subject. Thus, this is like a reversed FRET measurement that there is no FRET at the beginning. And then, the increase in FRET signals would only signify the released content, making it more sensitive than the co-loaded FRET system in studying the release dynamics. These techniques could be used for either *in vitro* or *in vivo* release studies. For the *in vivo* study, mice were divided into two groups, with one injected with the FRET-PEO-PS (the ordinary FRET system) and the other with the DiD-PEO-PS and DiR-PEO-PS mixture (the reversed FRET system). IVIS was used to obtain the full-body image and the fluorescence intensity value for calculating the FRET proximity ratio (PR, called FRET ratio in the article). The PR from the ordinary FRET system would decrease while the PR from the reversed FRET would increase. Thus, over time, the PR from the two FRET perspectives would meet and become equal, from which it indicates the end of the cargo release (Fig. 11). The difference between the ordinary PR and the reversed FRET PR could be calculated giving the release kinetics value, where the release half-life of FRET-PEO-PS was found to be 9.2 min in a mouse model. However, this release kinetic was too fast and inefficient for drug delivery to the tumor site. Thus, the oleic acid-coated iron oxide nanoparticles (IONPs) were incorporated into FRET-PEO-PS (becoming FRET-PEO-PS-IONP) to increase the lipophilicity of the nanocarriers. This strategy was proved to be successful as the release kinetics half-life measured by the same FRET-IVIS technique was found to be 50.8 min. Increasing lipophilicity of PEO-PS could slow down the premature release and hence improves drug delivery to the tumor. Thus, this study successfully demonstrated an advanced application of the semi-quantitative FRET technique to determine the cargo release kinetics with the benefit of live imagery using IVIS. It would be very interesting to develop further the quantitative technique based on this approach because this technique really allows both particle stability and release kinetics of the nanoparticles to be determined.

Morton and Quadir et al. [46] demonstrated the use of FRET semi-quantitative assay on the particle stability, biodistribution, and cargo release of PEG-b-PPLG micelles (PPMs). Basically, the dye-conjugating FRET system was used as a standard as Cy5.5 and Cy7 were both conjugated to PPLG and then mixed together to form the co-conjugated FRET-micelles (FRET-CPPMs), which represents blank-micelles. Moreover, the mixed system was employed, as Cy5.5 (donor) was loaded into the Cy7-conjugating micelles (FRET-PPM-Cy7) representing drug loading-micelles. Technically, the co-conjugated dye system determined only the dissociation of the micelles, while the mixed system allowed the determination of both dissociation and cargo release. However, in the pharmacokinetics study, they practically gave the same information of micelles stability since micelles dissociation and cargo release occur at the same time. For this experiment, the FRET assay was performed on a mouse model using both FRET dye systems in comparison to each other. Mice were intravenously injected with FRET-CPPM and FRET-PPM-Cy7. The relative plasma particle concentration of FRET-CPPMs and FRET-PPM-Cy7 was determined by two methods, both using IVIS. The first was by the FRET intensity obtained from the live full-body image (Fig. 12A). The FRET proximity ratio (PR) was calculated and normalized to the percentage called % FRET efficiency (Fig. 12C). The second was by the FRET intensity from the blood sample (Fig. 12B). PR was then normalized to the percentage of the initial PPMs concentration called % injected dose (%ID) (Fig. 12D). The result suggested that both the % FRET efficiency and the %ID were correlated and in accordance. The information from the %ID was more accurate because it came directly from blood with less signal interference from skin or other organs. As such, the blood clearance half-life of the micelles was obtained (Fig. 12D). In addition, the biodistribution was also studied using IVIS. Internal organs, including the mice's blood, were harvested for FRET intensity measurement. The result indicated a high accumulation of the intact micelles in the liver. This study really showed the flexibility and utility of IVIS with different experimental techniques to semi-

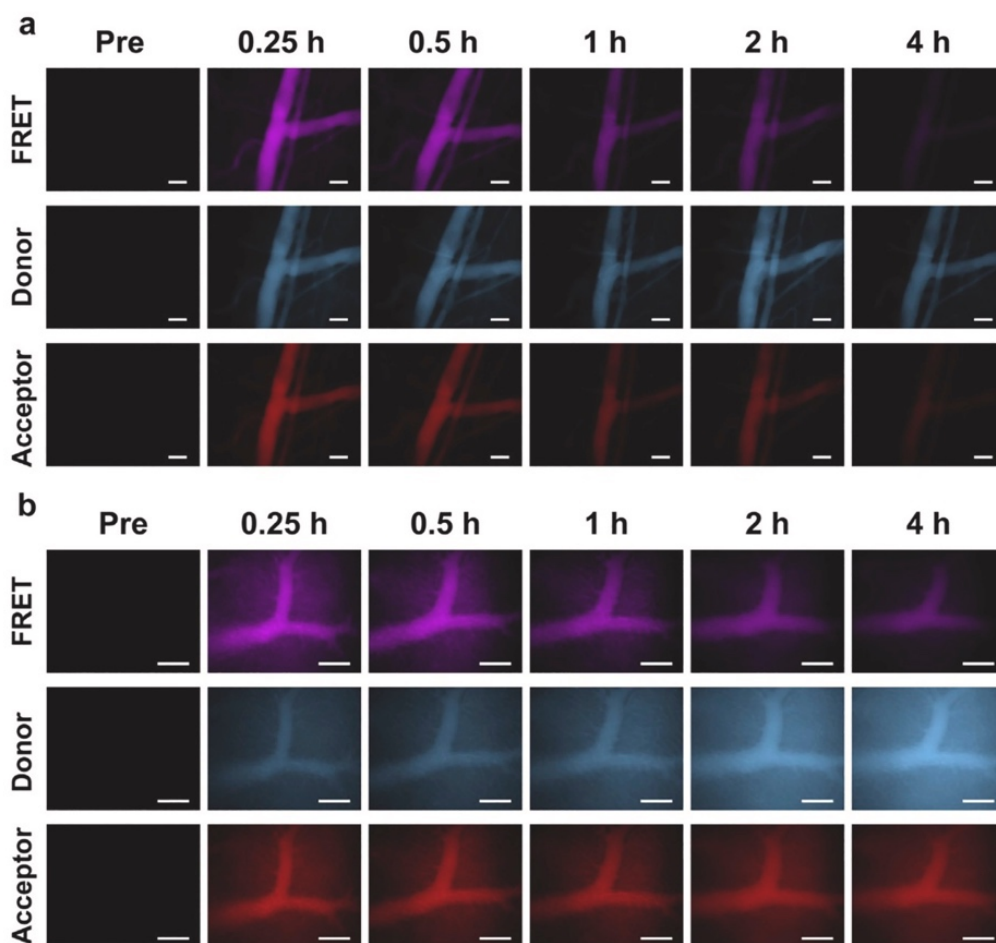


**Fig. 9.** An example of qualitative live *in vivo* FRET imaging analysis using confocal microscopy, by Ishizawa et al. [42]. PEG-PDLLA micelles were analyzed for the *in vivo* particle stability and biodistribution to the liver. A) FRET images of mouse's earlobe vasculatures. B) FRET images of mouse's liver vasculatures. The Figure shows that the FRET signal of FRET-PEG-PDLLA was found outside liver vasculature suggesting the intact nanoparticle's extravasation to liver cells. A drop in FRET signal and increase in donor signal in liver cells at 4 h also indicates nanoparticle's dissociation in liver cells. Reprinted from [42], Copyright 2020, with permission from Elsevier and American Pharmacist Association.

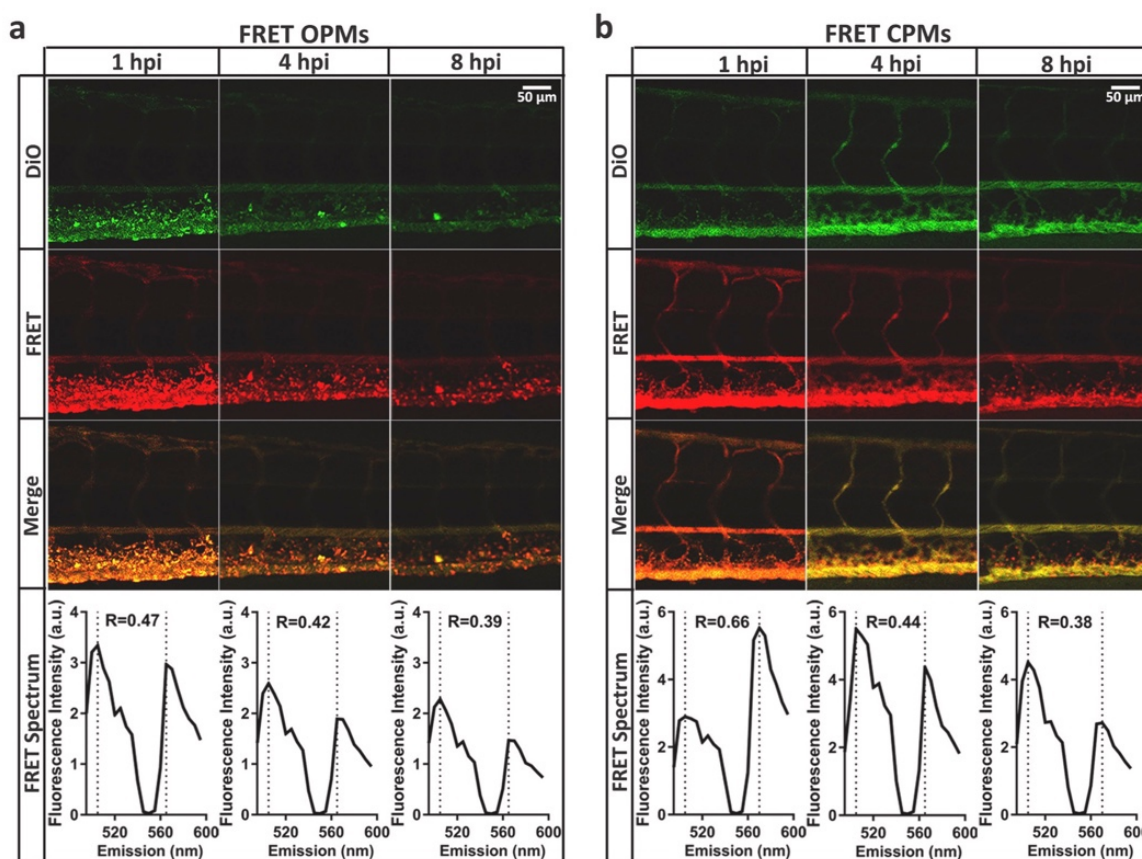
quantitatively analyze the plasma particle concentration and biodistribution by FRET.

Then, Ishizawa et al. [42] improved the semi-quantitative FRET technique used for PEG-PDLLA by using IVIS to capture the live full-body image of a mouse. DiD/DiR FRET system has a FRET acceptor emission spectrum closer to the near-infrared range than DiO/DiI system providing a higher tissue penetration ability, which is more suitable for the live full-body imagery. Mice were injected with FRET-PPMs. The FRET fluorescence signals were taken from the mice's chest and abdomen area, as well as the *ex vivo* organs at several time points up to 8 h. With the quantification software, IVIS gave the average intensity value. Thus, the FRET proximity ratio (called FRET ratio in the article) of the whole-body and *ex vivo* organs image signals was calculated. Then, the particle stability and the biodistribution were semi-quantitatively determined. The proximity ratio was calibrated with FRET-PPMs in PBS as the positive control and the one in ethanol as the negative control of the integrity. FRET-PPMs were found to dissociate over time with high accumulation in the liver and the lungs.

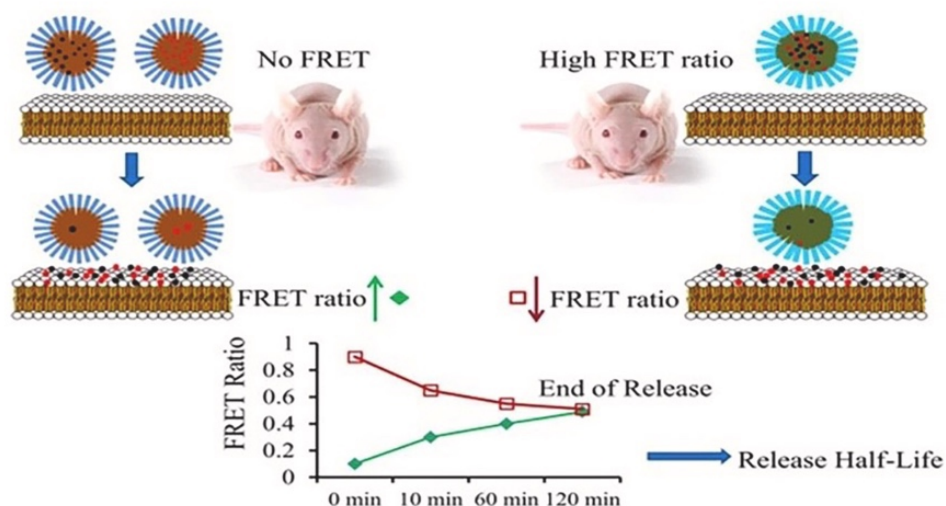
Finally, PEG-Azo-Nitroimidazole is a hypoxia-responsive micelle developed by Guo et al. [30] for drug delivery to the hypoxic environment of a tumor. Tumor-bearing mice were used in this experiment, and the FRET-micelles were directly administrated into the tumor. After specific time points, the IVIS was employed to take the live fluorescence

image of the tumor. The ratio between the intensity of the FRET acceptor and the donor was calculated and used as the semi-quantitative parameter for the cargo release. The intensity ratio of the nitroimidazole micelles was found to have a greater decrease when compared to the nitroimidazole-free micelles (control), suggesting a better cargo release of the nitroimidazole micelles in the tumor environment. The *in vivo* FRET technique helped to prove the hypoxia-responsive efficacy of the nitroimidazole micelles, which was one of the most important aims of this study.

**4.2.1.2. Polymersomes.** Quadir and Morton et al. [45], developed PEG5k-b-PPLG-Diisopropylamine (PPD) polymersomes developed. Unlike the normal PEG-b-PPLG, this polymer rearranges into a bilayer and becomes polymersomes with PEG to form an outer shell. The PPD-polymersomes are also designed to be acid pH-responsive dissociation, aiming for drug release in the acidic environment of a cancer tumor. The FRET intensity from *ex vivo* organs and blood samples was measured by IVIS and normalized with that of the injected dose to become the % injected dose (%ID). Thus, the semi-quantitative biodistribution data and the relative particle concentration of the intact FRET-PPD-polymersomes in a tumor-bearing mouse model were provided. The intact FRET-PPD-polymersomes were found to accumulate in the liver at 21%ID and in the tumor at 3%ID after 24 h. Doxorubicin-loaded PPD-



**Fig. 10.** An example of a semi-quantitative FRET live imaging assay in zebrafish larva model using confocal microscopy, by Tao et al. [43]. PEG-PPG-PEG micelles (PMs) were analyzed for the *in vivo* particle stability. A) Live FRET imaging of the ordinary PMs (OPMs) and B) Live FRET imaging of the disulfide bond cross-link PMs (CPMs). FRET signal of FRET-CPMs was stronger than FRET-OPMs after 1 h, suggesting higher stability of FRET-OPMs due to the disulfide bond cross-link. The bottom row shows the FRET spectra in terms of proximity ratio, which was semi-quantified as %integrity. Reprinted from [43], Copyright 2020, with permission from Elsevier.



**Fig. 11.** Schematic illustration summarizes the released dynamic study using the reversed FRET technique developed by Zou et al. [44]. Reprinted with permission from [44], Copyright 2013 American Chemical Society.

polymersomes also showed a tumor suppression effect in mice when compared to the untreated group.

4.2.1.3. *Lipid nanoparticles.* Lainé et al. [56] developed the FRET technique to qualitatively study the biodistribution of lipid nanocapsules (LNCs), DSPE-mPEG-2000 lipid nanocapsules (DPEG-LNCs),

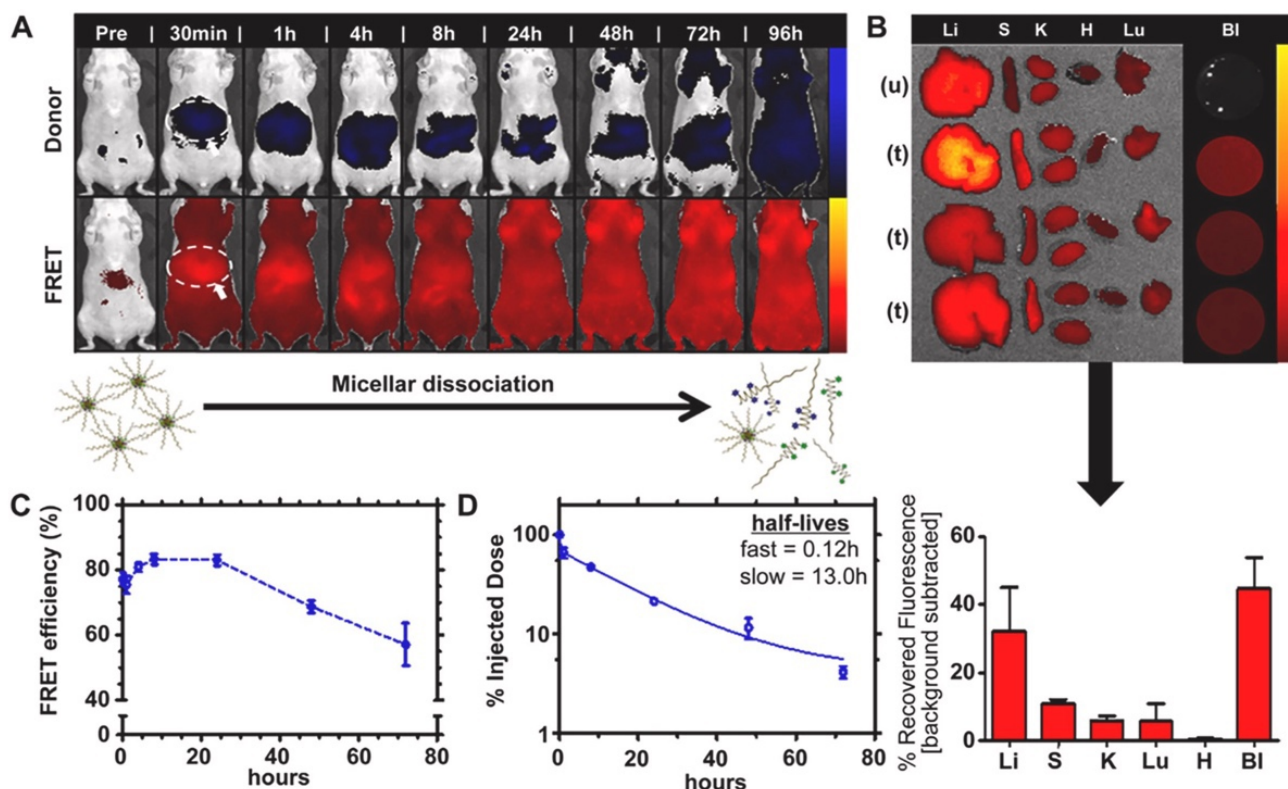


**Fig. 12.** An example of semi-quantitative FRET imaging analysis in a wide range of samples from mouse model using IVIS, by Morton et al. [46]. PED-b-PPLG micelles (PPMs) were analyzed for the *in vivo* plasma particle concentration and biodistribution. A) Live whole-body FRET IVIS image analysis showing the biodistribution of intact micelles. B) FRET IVIS image analysis of *ex vivo* organs: liver (Li), spleen (S), kidney (K), heart (H), lungs (Lu), and blood (BI) showing the organ biodistribution and particle stability in the circulatory system. C) PR (called % FRET efficiency in the article) of the blood sample analyzed by IVIS. D) PR normalized to the percentage of the initial PPMs concentration called % injected dose (%ID) with the blood clearance half-life calculated following the two-compartment pharmacokinetics model. Reprinted from [46], Copyright 2014, with permission from Elsevier.

and lipid nanoemulsions (LNEs). The pair of FRET dyes were co-encapsulated inside the LNCs, DPEG-LNCs, and LNEs. These FRET nanoparticles were intravenously injected into nude mice. Using IVIS, the fluorescence image of the mice was recorded over time from the FRET channel and free FP730-C18 (acceptor dye) channel. The image deconvolution technique was employed to differentiate the three emission signals from each other by calibrating each signal with the signal from FRET-LNCs vs. the mixture of DiD-LNCs FP730-C18-LNCs (likewise for LNEs); and then converting them to pseudocolors. The visible presence of FRET pseudocolors over the area of the mice's body signified the accumulation of FRET nanoparticles in the internal organ beneath the area. As such, the biodistribution of FRET-LNCs, FRET-DPEG-LNCs, and FRET-LNEs to the organs could be identified qualitatively. Image results of the whole rat body showed that FRET-DPEG-LNCs and FRET-LNEs had a different biodistribution from the conventional FRET-LNCs. However, the whole-body image alone can only give an approximative and inconclusive result for the particle's biodistribution because the superficial signals from the skin can obscure the signal from deeper organs. As a result, IVIS images of the *ex vivo* organs and the blood were taken to detail the biodistribution. Then, it was revealed that the intact FRET-DPEG-LNCs had better particle stability in blood at 3 h and less accumulation in the liver after 24 h when compared with FRET-LNCs. In conclusion, this IVIS FRET technique could give a qualitative study of the biodistribution and particle stability of the LNCs and LNEs. However, even though the IVIS is a quick and non-invasive technique for the qualitative assay, the obtained result is inadequate. As such, *ex vivo* organ imaging is still needed for meaningful interpretation. Finally, a more complex semi-quantitative FRET technique using the IVIS was also

used by Gravier et al. [29] for the particle stability and the biodistribution of LNCs in the liver and the breast carcinoma tumors. The FRET dyes were also co-encapsulated inside LNCs or LNEs. The FRET nanoparticles were intravenously injected into nude mice with TS/A-pc breast carcinoma tumors. Using the IVIS, FRET was recorded around the liver and the tumor area. The signals were corrected for the autofluorescence background prior to the injection. Then, the FRET ratio between the acceptor and the donor signals could be calculated from the image as  $FRET\ Ratio = DiD\ (Acceptor)\ signal / DiI\ (donor)\ signal$  and then converted to the percentage of intact FRET nanoparticles (called % intact LNCs) via the calibration curve. The calibration curve of the % intact FRET nanoparticles could be constructed by mixing FRET nanoparticles with various concentrations of DiI-LNCs and DiD-LNCs mixture ranging from 100% FRET to 0% FRET (100% of DiI-LNCs and DiD-LNCs mixture). This DiI-LNCs and DiD-LNCs mixture simulated the remnants of FRET-LNCs when the FRET dyes DiI and DiD were far apart and yielded no FRET. As such, the % intact LNCs in the liver and the tumor was obtained. Around 45% of intact LNCs were founded both in the liver and the tumor after 1 h and then dropped in half after 5 h. After 24 h, around 5% of the intact LNCs were detected in the tumor but 0% in the liver, indicating that LNCs were less stable in the liver than in the tumor. Furthermore, the % intact LNCs of the *ex vivo* tumor was determined using the same method but with confocal microscopy. A similar result was obtained, confirming the results from IVIS. Summarily, this research demonstrated the use of FRET by both the IVIS and the confocal microscopy to semi-quantitatively study the biodistribution and the particle stability in mice's liver and tumor.

**4.2.1.4. Nanocrystals.** FRET-curcumin nanocrystals were also developed by Zhang et al. [53] (called the co-doped curcumin nanoparticles in the article), aiming for their theragnostic application. Curcumin is a fluorophore, but in a nanocrystal form, it does not emit fluorescence. Therefore, FRET was instead employed as the nanocrystal tracker. As such, the FRET pair of perylene (donor) and 5,10,15,20-tetra(4-pyridyl) porphyrin ( $H_2TPyP$ , acceptor) was dissolved inside the curcumin nanocrystal. However, free curcumin dissolved from the nanocrystals can still give a fluorescence emission at 520 nm, and that can also be used as a direct parameter of free curcumin. By using IVIS, it allowed for the semi-quantitative assay of the biodistribution in a mouse model. The FRET-curcumin nanocrystal was intravenously injected into xenografted mice daily for 14 days. Then, the mice were sacrificed with their internal organs, including a xenografted tumor harvested. The FRET signal from  $H_2TPyP$  was then recorded by IVIS. However, the article does not clearly specify the excitation or the emission wavelength. Besides, the mean FRET intensity from each organ was obtained and compared with each other, revealing the relative amount of FRET-curcumin nanocrystal in each organ. The accumulation of the FRET-nanocrystal was found mainly in the liver and the tumor.

#### 4.2.2. FRET-IVIS with pseudocolors technique

**4.2.2.1. Lipid nanoparticles.** Another similar IVIS technique was

developed by Bouchaala et al. for lipid nanoemulsions (LNEs) [57]. This time, the FRET pair used was the carboxyanine Cy5.5 and Cy7.5 with a bulky counterion tetraphenylborate (TPB) added to increase their lipophilicity, making them Cy5.5TPB and Cy7.5TPB, which were employed as the donor and the acceptor respectively. By increasing the lipophilicity, the TPB-dye had a higher encapsulation capacity in the LNEs. In this study, FRET-LNEs were injected into the tumor-bearing mice. IVIS was employed for live whole-body imagery with the excitation at 640 nm, the FRET donor at 700 nm, and the FRET acceptor at 820 nm. FRET proximity ratio (PR) was calculated from the area of interest, which is the tumor and the liver areas, and then other *ex vivo* organs dissected from the mouse after 24 h. Several mixtures of donor-LNEs and acceptor-LNEs were used to calibrate the PR to the pseudocolors and then converted it to the % integrity that could overlay on the IVIS image (Fig. 13). So, unlike the previous technique, this technique not only showed the plain FRET intensity but showed the pseudocolors of the particle integrity itself on the image. The result indicated that the new TPB-dye gave a higher spatial resolution for IVIS, allowing for the semi-quantitative % integrity of the FRET-LNEs in the liver and the tumor area to be determined over time. The biodistribution from the *ex vivo* organs also showed a high accumulation of the intact FRET-LNEs and the in the liver and the tumor. This last study really demonstrated an impressive improvement in the FRET system for lipid-nanoparticles.

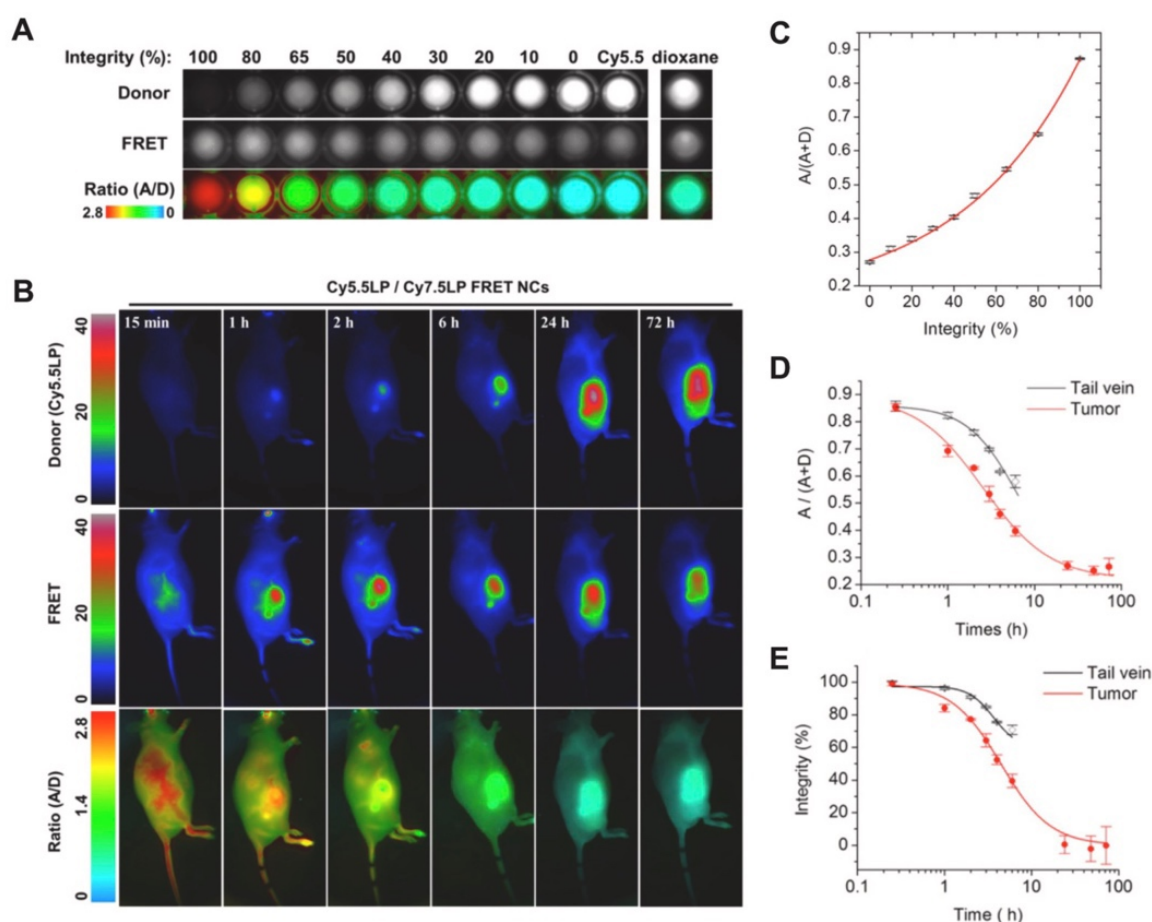


**Fig. 13.** An example of a semi-quantitative FRET assay in a tumor-bearing mouse model using IVIS, by Bouchaala et al. [57]. LNEs were analyzed on the *in vivo* particle stability and biodistribution. A) and C) The calibration curves between proximity ratio (PR), % integrity, and pseudocolors for the conversion of the FRET signal to %integrity. B) The IVIS image of the rats injected with FRET-LNEs over 72 h; the last row shows the PR being converted to pseudocolors of the particle integrity overlaying the tumor-bearing mouse images. D) The proximity ratio information obtained from the tail vein and tumor area expressed as a function of time and then converted to E) % integrity by the calibration curve in graph C). Adapted from [57]. Copyright 2016, Elsevier under a Creative Commons CC-BY license.

**4.2.2.2. Nanospheres.** Later, Cayre et al. [38] demonstrated the application of a semi-quantitative FRET assay for the particle stability of squalene-gemcitabine bioconjugate nanoparticles (SQGem) in mouse liver. A pair of FRET dyes, Cy5.5 (donor) and Cy7.5 (acceptor), were conjugated to squalene moiety turning into squalene-Cy5.5 (SQCy5.5) and squalene-Cy7.5 (SQCy7.5). Then SQGem, SQCy5.5, and SQCy7.5 were all mixed and put to precipitate to form FRET-SQGem nanoparticles. The nanoparticles were intravenously injected into mice, and the fluorescence images around the liver area were taken using the IVIS. The fluorescent intensity was converted to the numerical value using Living Image software (PerkinElmer). Then, the FRET proximity ratio was calculated to determine the particle integrity. With this method, the authors hypothesized that the FRET proximity ratio could be correlated to the proportion of intact FRET-SQGem nanoparticles and dissociated FRET-SQGem remnants (separated SQCy5.5 and SQCy7.5 moieties) accumulating in fatty tissues of the liver. Therefore, the proximity ratio could be converted to the relative percentage of the intact FRET-SQGem, called %integrity, via the calibration curve. The %integrity calibration curve was constructed by mixing the fully intact FRET-SQGem nanoparticles with various percentages of the nanoparticles purely made of the SQCy5.5 or SQCy7.5. The proximity ratio closing to 1.0 was converted to 100% of intact nanoparticles, and a decrease in the proximity ratio meant a decrease in the population of the intact nanoparticle and loss of particle stability. The image from IVIS around the mouse's liver area revealed for the first time that intact FRET-SQGem could be observed in the liver for 56% at 35 min after the injection and then dropped to lower than 10% after 2 h, indicating the dissociation of SQGem in the liver with no persistent accumulation, which is desirable for reducing liver toxicity. This FRET system allowed for the semi-quantitative assay of intact FRET-SQGem in the mouse's liver with the advantage that this technique is non-invasive and can be performed in live animals. The author suggested that the method could be used for a future study on the biodistribution of SQGem in other areas of the rat body. However, this FRET system still had low signal penetration (<1 cm), and the new FRET system with the emission in the NIR-II region (1000–1700 nm) may need to be developed for a future experiment.

#### 4.2.3. FRET-IVIS for oral nanomedicine

**4.2.3.1. Nanospheres.** EGTA-conjugated nanoparticles are the polymeric-based nanoparticles developed by Chuang et al. [50,51] to deliver insulin via the oral route. It is a pH-responsive nanoparticle consisting of chitosan and poly( $\gamma$ -glutamic acid) conjugated with ethylene glycol tetra-acetic acid (CS/ $\gamma$ PGA-EGTA) in which insulin can be loaded. The nanoparticles themselves can facilitate paracellular absorption of insulin as well as protect the insulin from gastrointestinal enzymes. Therefore, to test the protective effect of the  $\gamma$ PGA-EGTA nanoparticles, insulin stability was investigated in rats by comparing the naked insulin and the insulin with  $\gamma$ PGA-EGTA nanoparticles. FRET was used for the semi-quantitative assay of insulin stability relating to the protective effect of  $\gamma$ PGA-EGTA nanoparticles. The FRET donor and acceptor were conjugated to insulin on the opposite end of the amino chain before being loaded into the nanoparticles (Fig. 4C). Rat's duodenum was cut open and tied up to make a closed loop. Then, the FRET-insulin-loading nanoparticles and naked FRET-insulin were directly injected into the lumen of the said loop. After specific time points, live FRET imagery of the duodenum loop was taken over time using IVIS. FRET acceptor intensity signal was quantified by the software with their maximum values normalized to 100%. The amount of stable FRET-insulin was semi-quantitatively estimated. The comparison between the amount of the naked FRET-insulin and the loading insulin allowed for the protective effect of the  $\gamma$ PGA-EGTA nanoparticles to be determined. The results found that, in 2 h, the % normalized acceptor intensity of naked insulin plummeted to 40%, while the encapsulated insulin remained at 80%, meaning that  $\gamma$ PGA-EGTA nanoparticles had a

good protective effect for insulin against the intestinal enzyme. Besides, the nanoparticle also increased the oral bioavailability of insulin to 18% when compared to 0.1% by the orally given free-form insulin powder. The orally given nano-encapsulated insulin significantly reduced plasma glucose during the oral glucose tolerance test compared to the control group. This research is the most unique among all since FRET is implemented to study the stability of the encapsulated insulin rather than the integrity of the nanoparticles.

**4.2.3.2. Liposomes.** Semi-quantitative and qualitative FRET application in the *in vivo* oral absorption study of the liposomes (LPs) with various sizes (conventional LPs at 100, 200, 500 nm) and surface modifications (conventional, anionic, cationic, PEGylated LPs at 200 nm) were also developed by Liu et al. [48]. Similar to the nanocapsules, carbocyanine dyes could be directly co-encapsulated inside the LPs voids making the FRET-LPs. The semi-quantitative FRET technique was developed at first and employed in the *in vitro* particle stability experiment, in which FRET-LPs were incubated in various gastrointestinal fluids. FRET acceptor signal could be retrieved by using the IVIS. With the quantification software, the FRET intensity was converted to the % total radiant efficiency, which is then normalized to the percentage implying the number of intact LPs. Thereafter, the same technique could be utilized for the study of the *in vivo* particle stability in the gastrointestinal (GI) tract and biodistribution. Firstly, mice were orally given the FRET-LPs and then sacrificed at several time points with their GI tract and internal organs harvested. Then, IVIS was utilized with the whole *ex vivo* GI tract image taken, and the FRET intensity was quantified into the % total radiant efficiency. Thus, the percentage amount of intact FRET-LPs over 4 h in each part of the GI tract (stomach, duodenum, jejunum, etc.) and other intestinal organs could be estimated. The result indicated that smaller size conventional LPs, (200 nm) cationic LPs, and (200 nm) PEGylated LPs were more stable as they could be retained longer in the GI tract. Besides, no fluorescence signals were found in the *ex vivo* internal organs meaning that the intact LPs did not absorb into the circulatory system. Further study on the oral bioavailability of doxorubicin-encapsulated LPs also had the exact correlation. It confirmed that better particle stability and longer GI retention of the small-sized LPs, the cationic LPs, and the PEGylated LPs resulted in the increase in oral bioavailability of doxorubicin, despite no intact LPs found in the circulatory system. This article demonstrates that the semi-quantitative FRET technique could help to elucidate the association between the LPs particle integrity and the increase in oral bioavailability of the encapsulated drug, by which it could pave the way to a better LP design in the future.

#### 4.3. FRET fluorometry of blood and plasma

For the small liquid *in vitro* samples such as blood, plasma, and small tissue, a microplate reader or a fluorometer are adequate for obtaining the fluorescence spectrum and the intensity values of FRET.

##### 4.3.1. Micelles

Semi-quantitative FRET fluorimetry was developed to investigate and compare the *in vivo* particle stability and plasma particle concentration of the ordinary non-cross-linked PEG<sup>5k</sup>-CA<sub>8</sub> micelles (NCMN) and the disulfide cross-linked PEG<sup>5k</sup>-Cys<sub>4</sub>-CA<sub>8</sub> micelles (DCMN) [54]. The FRET-NCMN and FRET-DCMN were injected intravenously into nude mice with blood collected over time. The samples were then analyzed for FRET by the microplate reader. The FRET proximity ratio (PR) was calculated and normalized to the percentage (called % FRET ratio), allowing for the semi-quantitative assay of the relative plasma particle concentration (Fig. 14). The result showed that FRET-DCMN was more stable over 24 h in blood than the FRET-NCMN. Further FRET *in vitro* assay was able to evidence that lipoproteins caused the rapid dissociation of FRET-NCMN.

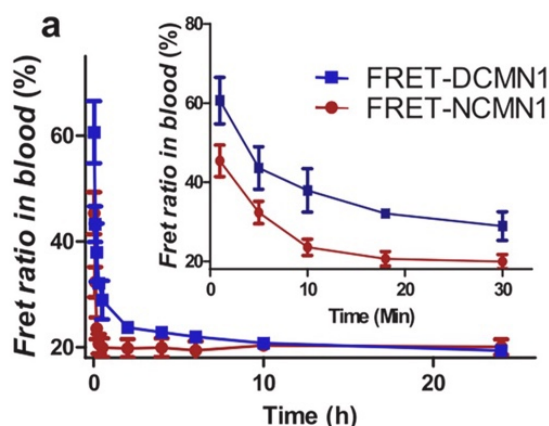


Fig. 14. An example of semi-quantitative FRET fluorimetry for particle concentration assay in a mouse model using microplate reader, by Li et al. [54]. Telodendrimers nanoparticles (DCMN and NCMN) were analyzed for the *in vivo* plasma particle concentration. The PR was obtained from mouse blood and then normalized as a relative percentage (called % FRET ratio in the article). Reprinted with permission from [54], Copyright 2012 American Chemical Society.

Zhang et al. [47] also performed the semi-quantitative assay for analyzing the plasma particle concentration of PEG-PCL micelles. The FRET-micelles were intravenously injected into mice with blood collected over time. The plasma was then extracted, and the sample was analyzed by the fluorimeter. The intensity was converted to the % integrity via the calibration curve developed specifically for this FRET system. Similar to the technique of Cayre et al. [38] in the SQGem nanoparticles, the calibration curve was built by mixing various concentrations of the co-conjugated FRET micelles (with NBD-X and MS735 together) with the mixture of NBD-X micelles and MS735 micelles. The co-conjugated FRET-micelles represent the percentage of the intact micelles, while the mixture of NBD-X micelles and MS735 micelles simulate the signals of the dissociated FRET remnants. The % integrity was considered as a semi-quantitative parameter since it provided only the relative percentage, not the true particle numbers. The % integrity of the micelles in plasma declined gradually and reached 60% after 72 h. The study successfully demonstrated the new FRET pair and the semi-quantitative FRET technique for determining the plasma particle concentration of the micelles in mice.

#### 4.3.2. Nanocrystals

Zhang et al. [53] also utilized semi-quantitative FRET fluorimetry to determine the plasma particle concentration of FRET-curcumin nanocrystals. Mice were intravenously injected with the FRET-curcumin nanocrystal, and the blood was collected for up to 24 h. The plasma was extracted from the blood sample thereafter and then analyzed for FRET using the microplate reader. The FRET signal was recorded at 635 nm and converted to the concentration of the FRET-curcumin nanocrystal expressed in mass concentration (ng/ $\mu$ L). The curcumin nanocrystals were found in plasma for up to 4 h after a single-dose intravenous injection (15 mg/kg). However, neither the FRET excitation wavelength nor the quantification calibration curve was elaborated.

#### 4.3.3. Nanospheres

c(CRGDKGPDC) peptide (iRGD) modified hyaluronic acid–deoxycholic acid conjugate (iRGD-PEG-HA-DOCA, IPHD) is a self-assembly polymeric nanosphere developed by Liu et al. [49] to deliver dasatinib to a solid tumor. Dasatinib and FRET pair dyes were loaded together into the nanoparticles' matrix allowing for the semi-quantitative FRET assay of the plasma particle concentration and *in vivo* particle integrity. The nanoparticles were also further

biomineralized by calcium phosphate, called  $\text{Ca}_3(\text{PO}_4)_2$ -iRGD-PEG-HA-DOCA (CIPHD), by coating with calcium phosphate, aiming for the pH-responsive property. The FRET-IPHD/Dasatinib and the FRET-CIPHD/Dasatinib were injected into rats, and blood samples were collected after several time points. The plasma was separated from the sample and then analyzed for FRET by the fluorimeter. FRET proximity ratio (called FRET ratio in the article) was calculated and normalized to a percentage. This value was interpreted as the relative percentage of the nanoparticle's plasma concentration, inferring the *in vivo* particle integrity of the FRET-IPHD and FRET-CIPHD.

These FRET experiments aimed at proving whether biomineralization increases particle stability or not. The result found that the non-mineralized FRET-IPHD/Dasatinib was less stable than the mineralized FRET-CIPHD in the rat's blood circulation. The normalized PR of FRET-CIPHD/Dasatinib in blood stayed at around 60% up to 24 h, while the normalized PR value from FRET-IPHD/Dasatinib dropped from 77% to 50% just in 30 min. The higher blood particle stability of CIPHD/Dasatinib also resulted in a higher AUC and half-life of plasma dasatinib (analyzed by HPLC, thus indistinguishable between the free drug or the encapsulated drugs). This also resonated with the *in vivo* result of CIPHD/Dasatinib having higher efficacy than IPHD/Dasatinib to increase the survival of tumor-bearing mice. This article is an example that the FRET semi-quantitative assay helped to prove that higher particle stability due to biomineralization (not by other processes) contributed to a better anti-tumor efficacy for this type of nanoparticle.

## 5. Conclusion

Currently, most of the FRET *in vivo* nanoparticle tracking techniques are the qualitative imagery and the semi-quantitative assay on *in vivo* particle stability, biodistribution, cargo release, and plasma particle concentration. Some unique techniques were also developed, such as the FRET study on the protective effect of the nanoparticle against the intestinal enzyme on insulin [50,51], oral absorption [48], and the reversed FRET for determining the cargo release [44]. It is clear that FRET is still mainly employed for *in vivo* particle stability and biodistribution study. There are only two *in vivo* FRET studies on oral absorption and none from other absorption routes nor the excretion pathway. It is also obvious that there is a lack of quantitative assay, which also leads to the lack of advanced pharmacokinetics of the nanoparticles.

Different instruments were used for the FRET assay, namely CFM, IVIS, fluorimeter, and microplate reader. All the instruments are capable of performing the semi-quantitative assay, while only CFM and IVIS can perform qualitative and semi-quantitative imaging analysis. IVIS has the advantages of being a non-invasive technique and having high flexibility to analyze various kinds of samples ranging from a well-plate, *ex vivo* organs, and live full-body imagery. It turns out that the spatial resolution of IVIS is rather low due to high signal interference and low tissue penetration. Therefore, for the biodistribution study, only large organs such as the liver can give a relatively high resolution for FRET whole-body live imaging. For other smaller organs, it really needs validation and correlation from the invasive *ex vivo* organs imaging or other techniques such as CFM. Besides, IVIS also requires complex signal calibration procedures such as the pseudocolors technique in order to be semi-quantitative. These hurdles make it difficult to obtain the true quantitative assay on particle numbers to be obtained from IVIS. However, IVIS is still the popular instrument of choice as being mostly employed in much recent literature, possibly due to its versatility and benefits in giving both live imagery and semi-quantitative % intact nanoparticles. In addition, CFM is less flexible for the use than IVIS. It was mainly used for analyzing the *ex vivo* tissue samples or a very small animal model like zebrafish larva [43,52]. The zebrafish larva as an animal model is adapted for quickly demonstrating the FRET system as the larva is transparent and tiny, but one must take into consideration that the evidence for the clinical translation of this animal model in



terms of pharmacokinetics is still extremely limited. A rodent model is still preferential as it has more solid evidence to support its pharmacokinetics translation to humans [58,59] and is also considered a goal standard in the preclinical stage [60]. Besides, CFM is also utilized for live FRET imaging on the mouse's earlobe vasculature [41,42]. This earlobe technique was one of the earliest to be developed using FRET, but it is limited only to micelles and was overshadowed by the development of IVIS. Moreover, the FRET fluorimetry is used only for analyzing blood samples to obtain the semi-quantitative plasma particle concentration, as the fluorimeter is not an imaging instrument. Despite being very specific to the plasma particle concentration, this technique has the highest potentiality to be developed into a true quantitative assay, which requires the construction of a proper calibration curve to link the intensity value or FRET proximity ratio to the particle number. However, due to the fact that the technique involves extracting nanoparticles from plasma, an extraction method that can ensure the stability of nanoparticles during the process needs to be implemented.

To conclude, true quantitative *in vivo* tracking of nanomedicine is important. Without the information on the intact nanoparticle number in plasma and organs, it is not possible to perform any advanced pharmacokinetics such as the physiologically based pharmacokinetic modeling (PBPK). Thus, this is one of the reasons for the lack of pharmacokinetic models on the nanomedicine [8], causing a problem in the translation to the clinical trial. Despite its necessity, there is a lack of quantitative assay for nanomedicine, even for the *in vitro* experiments, as researchers still focus on the pharmacokinetics of the encapsulated drugs, ignoring the fact that the nanocarriers also have their own fate that can greatly affect the drug efficacy. In brief, FRET is an effective tool for *in vivo* tracking the nanomedicine to investigate the pharmacokinetics of nanomedicine, especially the *in vivo* particle stability and bio-distribution. However, it still has a limitation for not reaching the level of true quantitative assay yet. And as such, the advanced pharmacokinetic analysis could not be completely achieved.

#### Declaration of Competing Interest

The authors declare that they have no known competing financial interests or personal relationships that could have appeared to influence the work reported in this paper.

#### Acknowledgements

This work was supported by the Ligue Contre le Cancer, Maine-et-Loire Committee (49), Angers, France (#JPB/FP – 223/12.2020).

#### References

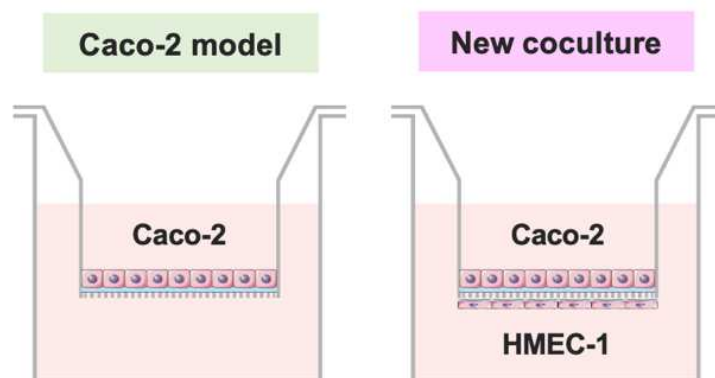
- [1] B. Flühmann, I. Ntai, G. Borchard, S. Simoens, S. Mühlebach, Nanomedicines: the magic bullets reaching their target? *Eur. J. Pharm. Sci.* 128 (2019) 73–80, <https://doi.org/10.1016/j.ejps.2018.11.019>.
- [2] F. Farjadian, A. Ghasemi, O. Gohari, A. Rooiantan, M. Karimi, M.R. Hamblin, Nanopharmaceuticals and nanomedicines currently on the market: Challenges and opportunities, 2019, <https://doi.org/10.2217/nmm-2018-0120>.
- [3] M.J. Mitchell, M.M. Billingsley, R.M. Haley, M.E. Wechsler, N.A. Peppas, R. Langer, Engineering precision nanoparticles for drug delivery, *Nat. Rev. Drug Discov.* 20 (2021) 101–124, <https://doi.org/10.1038/s41573-020-0090-8>.
- [4] K. Greish, A. Mathur, M. Bakhtiet, S. Taurin, Nanomedicine: is it lost in translation? *Ther. Deliv.* 9 (2018) 269–285, <https://doi.org/10.4155/tde-2017-0118>.
- [5] H.L. Jang, Y.S. Zhang, A. Khademhosseini, Boosting clinical translation of nanomedicine, *Nanomedicine* 11 (2016) 1495–1497, <https://doi.org/10.2217/nmm-2016-0133>.
- [6] D. Sun, S. Zhou, W. Gao, What went wrong with anticancer nanomedicine design and how to make it right, *ACS Nano* 14 (2020) 12281–12290, <https://doi.org/10.1021/acsnano.9b09713>.
- [7] V. Agrahari, V. Agrahari, Facilitating the translation of nanomedicines to a clinical product: challenges and opportunities, *Drug Discov. Today* 23 (2018) 974–991, <https://doi.org/10.1016/j.drudis.2018.01.047>.
- [8] V. Lebreton, S. Legeay, P. Saulnier, F. Lagarce, Specificity of pharmacokinetic modeling of nanomedicines, *Drug Discov. Today* 26 (2021) 2259–2268, <https://doi.org/10.1016/j.drudis.2021.04.017>.
- [9] S. Bonnet, R. Elfatairi, F. Franconi, E. Roger, S. Legeay, Organic nanoparticle tracking during pharmacokinetic studies, *Nanomedicine* 16 (2021), <https://doi.org/10.2217/nmm-2021-0155>, 2539–2536.
- [10] M. Germain, F. Caputo, S. Metcalfe, G. Tosi, K. Spring, A.K.O. Åslund, A. Pottier, R. Schiffelers, A. Ceccaldi, R. Schmid, Delivering the power of nanomedicine to patients today, *J. Control. Release* 326 (2020) 164–171, <https://doi.org/10.1016/j.jconrel.2020.07.007>.
- [11] C. Pérez-Medina, A.J.P. Teunissen, E. Kluzka, W.J.M. Mulder, R. van der Meel, Nuclear imaging approaches facilitating nanomedicine translation, *Adv. Drug Deliv. Rev.* 154–155 (2020) 123–141, <https://doi.org/10.1016/j.addr.2020.07.017>.
- [12] Marcin Ptaszek, Chapter three – rational design of fluorophores for *in vivo* applications, in: M.C. Morris (Ed.), *Fluorescence-Based Biosensors*, Academic Press, 2013, pp. 59–108, <https://doi.org/10.1016/B978-0-12-386932-6.00003-X>.
- [13] T. Etrych, O. Janoušková, P. Chytil, Fluorescence imaging as a tool in preclinical evaluation of polymer-based nano-DDS systems intended for cancer treatment, *Pharmaceutics* 11 (2019), <https://doi.org/10.3390/pharmaceutics11090471>.
- [14] D.M. Charron, G. Zheng, Nanomedicine development guided by FRET imaging, *Nano Today* 18 (2018) 124–136, <https://doi.org/10.1016/j.nantod.2017.12.006>.
- [15] T. Chen, B. He, J. Tao, Y. He, H. Deng, X. Wang, Y. Zheng, Application of Förster Resonance Energy Transfer (FRET) technique to elucidate intracellular and *in vivo* biofate of nanomedicines, *Adv. Drug Deliv. Rev.* 143 (2019) 177–205, <https://doi.org/10.1016/j.addr.2019.04.009>.
- [16] H. Sahoo, Förster resonance energy transfer - a spectroscopic nanoruler: principle and applications, *J. Photochem. Photobiol. C. Photochem. Rev.* 12 (2011) 20–30, <https://doi.org/10.1016/j.jphotochemrev.2011.05.001>.
- [17] A.S. Klymchenko, F. Liu, M. Collet, N. Anton, Dye-loaded nanoemulsions: biomimetic fluorescent Nanocarriers for bioimaging and nanomedicine, *Adv. Healthcare Mater.* 10 (2021) 1–27, <https://doi.org/10.1002/adhm.202001289>.
- [18] T. Förster, Energy migration and fluorescence, *J. Biomed. Opt.* 17 (2012), 011002, <https://doi.org/10.1117/1.jbo.17.1.011002>.
- [19] R.M. Clegg, The history of FRET: from conception through the labors of birth, *Rev. Fluoresc.* 3 (2006) 1–45.
- [20] B.W. van der Meer, Förster Theory, in: *FRET – Förster Resonance Energy Transfer*, John Wiley & Sons, Ltd, 2013, pp. 23–62, <https://doi.org/10.1002/9783527656028.ch03>.
- [21] A. Kaur, P. Kaur, S. Ahuja, Förster resonance energy transfer (FRET) and applications thereof, *Anal. Methods* 12 (2020) 5532–5550, <https://doi.org/10.1039/D0AY01961E>.
- [22] N. Hildebrandt, How to apply FRET: from experimental design to data analysis, in: *FRET – Förster Resonance Energy Transfer*, John Wiley & Sons, Ltd, 2013, pp. 105–163, <https://doi.org/10.1002/9783527656028.ch05>.
- [23] J.R. Lakowicz, Energy transfer, in: *Principles of Fluorescence Spectroscopy*, Springer US, Boston, MA, 2006, pp. 443–475, [https://doi.org/10.1007/978-0-387-46312-4\\_13](https://doi.org/10.1007/978-0-387-46312-4_13).
- [24] M. Dahan, A.A. Deniz, T. Ha, D.S. Chemla, P.G. Schultz, S. Weiss, Ratiometric measurement and identification of single diffusing molecules, *Chem. Phys.* 247 (1999) 85–106.
- [25] B. Wallace, P.J. Atzberger, Förster resonance energy transfer: role of diffusion of fluorophore orientation and separation in observed shifts of FRET efficiency, *PLoS One* (2017) 1–22, <https://doi.org/10.1371/journal.pone.0177122> May.
- [26] E. Nir, X. Michalet, K.M. Hamadani, T.A. Laurence, D. Neuhauser, Shot-noise limited single-molecule FRET histograms: comparison between theory and experiments, *J. Phys. Chem. B* 110 (2006) 22103–22124, <https://doi.org/10.1021/jp063483n>.
- [27] J.J. McCann, U.B. Choi, L. Zheng, K. Weninger, M.E. Bowen, Optimizing methods to recover absolute FRET efficiency from immobilized single molecules, *Biophys. J.* 99 (2010) 961–970, <https://doi.org/10.1016/j.bpj.2010.04.063>.
- [28] J.P. Torella, S.J. Holden, Y. Santoso, J. Hohlbein, A.N. Kapanidis, Identifying molecular dynamics in single-molecule FRET experiments with burst variance analysis, *Biophys. J.* 100 (2011) 1568–1577, <https://doi.org/10.1016/j.bpj.2011.01.066>.
- [29] J. Gravier, L. Sancey, S. Hirsjärvi, E. Rustique, C. Passirani, J.P. Benoît, J.L. Coll, I. Texier, FRET imaging approaches for *in vitro* and *in vivo* characterization of synthetic lipid nanoparticles, *Mol. Pharm.* 11 (2014) 3133–3144, <https://doi.org/10.1021/mp500329z>.
- [30] X. Guo, F. Liu, J. Deng, P. Dai, Y. Qin, Z. Li, B. Wang, A. Fan, Z. Wang, Y. Zhao, Electron-accepting micelles deplete reduced nicotinamide adenine dinucleotide phosphate and impair two antioxidant cascades for ferroptosis-induced tumor eradication, *ACS Nano* 14 (2020) 14715–14730, <https://doi.org/10.1021/acsnano.0c00764>.
- [31] P.J. Robinson, C.A. Woolhead, Implementation of FRET technologies for studying the folding and conformational changes in biological structures, in: *FRET – Förster Resonance Energy Transfer*, John Wiley & Sons, Ltd, 2013, pp. 357–396, <https://doi.org/10.1002/9783527656028.ch09>.
- [32] K. Suhling, L.M. Hirvonen, J.A. Levitt, P.-H. Chung, C. Tregidgo, A. le Marois, D. A. Rusakov, K. Zheng, S. Ameer-Beg, S. Poland, S. Coelho, R. Henderson, N. Krstajic, Fluorescence lifetime imaging (FLIM): basic concepts and some recent developments, *Med. Photon.* 27 (2015) 3–40, <https://doi.org/10.1016/j.medpho.2014.12.001>.
- [33] R. Datta, T.M. Heaster, J.T. Sharick, A.A. Gillette, M.C. Skala, Fluorescence lifetime imaging microscopy: fundamentals and advances in instrumentation, analysis, and applications, *J. Biomed. Opt.* 25 (2020) 1–43, <https://doi.org/10.1117/1.JBO.25.7.071203>.
- [34] Thermo Fisher Scientific, Fluorescent tracers derivatives of cell morphology and fluid flow, in: *The Molecular Probes Handbook*, 2010, pp. 588–648.

- [35] National Center for Biotechnology Information, PubChem Compound Summary for CID 126455658, Cy3 Carboxylic acids, (n.d.). <https://pubchem.ncbi.nlm.nih.gov/compound/Cy3-Carboxylic-acids> (accessed March 4, 2022).
- [36] National Center for Biotechnology Information, PubChem Compound Summary for CID 86276410, Cy5 Carboxylic acids, (n.d.). <https://pubchem.ncbi.nlm.nih.gov/compound/Cy5-Carboxylic-acids> (accessed March 4, 2022).
- [37] National Center for Biotechnology Information, PubChem Compound Summary for CID 91757848, Cy7-carboxylic acid chloride, (n.d.). <https://pubchem.ncbi.nlm.nih.gov/compound/Cy7-carboxylic-acid-chloride> (accessed March 4, 2022).
- [38] F. Cayre, S. Mura, B. Andreiuk, D. Sobot, S. Gouazou, D. Desmaële, A. S. Klymchenko, P. Couvreur, In vivo FRET imaging to predict the risk associated with hepatic accumulation of squalene-based prodrug nanoparticles, *Adv. Healthc. Mater.* 7 (2018), <https://doi.org/10.1002/adhm.201700830>.
- [39] National Center for Biotechnology Information, PubChem Compound Summary for CID 5282412, Indocyanine green, (n.d.). <https://pubchem.ncbi.nlm.nih.gov/compound/Indocyanine-green> (accessed March 4, 2022).
- [40] H. Chen, S. Kim, W. He, H. Wang, P.S. Low, K. Park, J.X. Cheng, Fast release of lipophilic agents from circulating PEG-PDLLA micelles revealed by in vivo Förster resonance energy transfer imaging, *Langmuir*. 24 (2008) 5213–5217, <https://doi.org/10.1021/la703570m>.
- [41] S.Y. Lee, S. Kim, J.Y. Tyler, K. Park, J.X. Cheng, Blood-stable, tumor-adaptable disulfide bonded mPEG-(Cys)4-PDLLA micelles for chemotherapy, *Biomaterials*. 34 (2013) 552–561, <https://doi.org/10.1016/j.biomaterials.2012.09.065>.
- [42] K. Ishizawa, K. Togami, H. Tada, S. Chono, Multiscale live imaging using Förster Resonance Energy Transfer (FRET) for evaluating the biological behavior of nanoparticles as drug carriers, *J. Pharm. Sci.* 109 (2020) 3608–3616, <https://doi.org/10.1016/j.xphs.2020.08.028>.
- [43] J. Tao, Z. Wei, Y. He, X. Yan, S. Ming-Yuen Lee, X. Wang, W. Ge, Y. Zheng, Toward understanding the prolonged circulation and elimination mechanism of crosslinked polymeric micelles in zebrafish model, *Biomaterials*. 256 (2020) 1–17, <https://doi.org/10.1016/j.biomaterials.2020.120180>.
- [44] P. Zou, H. Chen, H.J. Paholak, D. Sun, Noninvasive fluorescence resonance energy transfer imaging of in vivo premature drug release from polymeric nanoparticles, *Mol. Pharm.* 10 (2013) 4185–4194, <https://doi.org/10.1021/mp4002393>.
- [45] M.A. Quadir, S.W. Morton, Z.J. Deng, K.E. Shopsowitz, R.P. Murphy, T.H. Epps, P. T. Hammond, PEG-polypeptide block copolymers as pH-responsive endosome-solubilizing drug nanocarriers, *Mol. Pharm.* 11 (2014) 2420–2430, <https://doi.org/10.1021/mp500162w>.
- [46] S.W. Morton, X. Zhao, M.A. Quadir, P.T. Hammond, FRET-enabled biological characterization of polymeric micelles, *Biomaterials*. 35 (2014) 3489–3496, <https://doi.org/10.1016/j.biomaterials.2014.01.027>.
- [47] H. Zhang, H. Li, Z. Cao, J. Du, L. Yan, J. Wang, Investigation of the in vivo integrity of polymeric micelles via large Stokes shift fluorophore-based FRET, *J. Control. Release* 324 (2020) 47–54, <https://doi.org/10.1016/j.jconrel.2020.04.046>.
- [48] W. Liu, D. Li, Z. Dong, K. Liu, H. He, Y. Lu, W. Wu, Q. Li, L. Gan, J. Qi, Insight into the in vivo translocation of oral liposomes by fluorescence resonance energy transfer effect, *Int. J. Pharm.* 587 (2020), <https://doi.org/10.1016/j.ijpharm.2020.119682>.
- [49] Y. Liu, L. Li, J. Liu, M. Yang, H. Wang, X. Chu, J. Zhou, M. Huo, T. Yin, Biomaterialization-inspired dasatinib nanodrug with sequential infiltration for effective solid tumor treatment, *Biomaterials*. 267 (2021), 120481, <https://doi.org/10.1016/j.biomaterials.2020.120481>.
- [50] E.Y. Chuang, K.J. Lin, F.Y. Su, F.L. Mi, B. Maiti, C.T. Chen, S.P. Wey, T.C. Yen, J. H. Juang, H.W. Sung, Noninvasive imaging oral absorption of insulin delivered by nanoparticles and its stimulated glucose utilization in controlling postprandial hyperglycemia during OGTT in diabetic rats, *J. Control. Release* 172 (2013) 513–522, <https://doi.org/10.1016/j.jconrel.2013.05.006>.
- [51] E.-Y. Chuang, K.-J. Lin, F.-Y. Su, H.-L. Chen, B. Maiti, Y.-C. Ho, T.-C. Yen, N. Panda, H.-W. Sung, Calcium depletion-mediated protease inhibition and apical-junctional-complex disassembly via an EGTA-conjugated carrier for oral insulin delivery, *J. Control. Release* 169 (2013) 296–305, <https://doi.org/10.1016/j.jconrel.2012.11.011>.
- [52] Y. Li, X. Miao, T. Chen, X. Yi, R. Wang, H. Zhao, S.M.Y. Lee, X. Wang, Y. Zheng, Zebrafish as a visual and dynamic model to study the transport of nanosized drug delivery systems across the biological barriers, *Colloids Surf. B: Biointerfaces* 156 (2017) 227–235, <https://doi.org/10.1016/j.colsurfb.2017.05.022>.
- [53] J. Zhang, Y.C. Liang, X. Lin, X. Zhu, L. Yan, S. Li, X. Yang, G. Zhu, A.L. Rogach, P.K. N. Yu, P. Shi, L.C. Tu, C.C. Chang, X. Zhang, X. Chen, W. Zhang, C.S. Lee, Self-monitoring and self-delivery of photosensitizer-doped nanoparticles for highly effective combination cancer therapy in vitro and in vivo, *ACS Nano* 9 (2015) 9741–9756, <https://doi.org/10.1021/acs.nano.5b02513>.
- [54] Y. Li, M.S. Budamagunta, J. Luo, W. Xiao, J.C. Voss, K.S. Lam, Probing of the assembly structure and dynamics within nanoparticles during interaction with blood proteins, *ACS Nano* 6 (2012) 9485–9495, <https://doi.org/10.1021/nn302317j>.
- [55] Y. Tang, X. Wang, J. Li, Y. Nie, G. Liao, Y. Yu, C. Li, Overcoming the reticuloendothelial system barrier to drug delivery with a “don’t-Eat-Us” strategy, *ACS Nano* (2019), <https://doi.org/10.1021/acs.nano.9b05679>.
- [56] A.L. Lainé, J. Gravier, M. Henry, L. Sancey, J. Béjaud, E. Pancani, M. Wiber, I. Texier, J.L. Coll, J.P. Benoit, C. Passirani, Conventional versus stealth lipid nanoparticles: formulation and in vivo fate prediction through FRET monitoring, *J. Control. Release* 188 (2014) 1–8, <https://doi.org/10.1016/j.jconrel.2014.05.042>.
- [57] R. Bouchaala, L. Mercier, B. Andreiuk, Y. Mély, T. Vandamme, N. Anton, J. G. Goetz, A.S. Klymchenko, Integrity of lipid nanocarriers in bloodstream and tumor quantified by near-infrared ratiometric FRET imaging in living mice, *J. Control. Release* 236 (2016) 57–67, <https://doi.org/10.1016/j.jconrel.2016.06.027>.
- [58] C.H.C. Leenaars, C. Kouwenaar, F.R. Stafleu, A. Bleich, M. Ritskes-Hoitinga, R.B. M. de Vries, F.L.B. Meijboom, Animal to human translation: a systematic scoping review of reported concordance rates, *J. Transl. Med.* 17 (2019) 1–22, <https://doi.org/10.1186/s12967-019-1976-2>.
- [59] T. Denayer, T. Stöhrn, M. van Roy, Animal models in translational medicine: validation and prediction, *New Horiz. Transl. Med.* 2 (2014) 5–11, <https://doi.org/10.1016/j.nhtm.2014.08.001>.
- [60] M.S. Valic, M. Halim, P. Schimmer, G. Zheng, Guidelines for the experimental design of pharmacokinetic studies with nanomaterials in preclinical animal models, *J. Control. Release* 323 (2020) 83–101, <https://doi.org/10.1016/j.jconrel.2020.04.002>.

## Chapter 1: *In vitro* oral absorption of intact LNCs

Existing cell culture model for intestinal absorption study only have an epithelium layer and lack the endothelium layer. This might not be problematic for the assay of drug molecule whose absorption mainly rely on chemical process as the endothelium is so thin and provide little barrier effect for chemicals compared to thick epithelium. However, for nanomedicine, the main absorption pathway relies on the biological process, ignoring the presence of another cell layer in the structure could be problematic as it does not give the same biological property. Therefore, in order to evaluate the *in vitro* oral absorption of nanomedicine, a new coculture model that include both epithelium and endothelium is needed. Therefore, a new *in vitro* coculture model between Caco-2 epithelium and HMEC-1 endothelium was developed for evaluating the oral absorption of intact LNCs (**Figure 4**). FRET was utilized as a tool to monitor the amount of intact LNCs transporting across the Transwell®.




This study was published in the journal *Pharmaceutics* in 2021, named “New in vitro coculture model for evaluating intestinal absorption of different lipid nanocapsules”.



**Figure 4.** Illustration of the Caco-2 model and the new coculture model Caco-2/HMEC-1 in Transwell®. The characteristic of the new coculture model is that the HMEC-1 endothelium is contact Caco-2 epithelium imitating the cellular structure of the gut-blood barrier.

## Article

# New In Vitro Coculture Model for Evaluating Intestinal Absorption of Different Lipid Nanocapsules

Norraseth Kaeokhamloed <sup>1</sup>, Emilie Roger <sup>1</sup>, Jérôme Béjaud <sup>1</sup>, Nolwenn Lautram <sup>1</sup>, Florence Manero <sup>2</sup>, Rodolphe Perrot <sup>2</sup>, Marie Briet <sup>3</sup>, Chadi Abbara <sup>3</sup> and Samuel Legeay <sup>1,\*</sup>

<sup>1</sup> MINT, INSERM U1066, CNRS UMR 6021, SFR ICAT, University of Angers, F-49000 Angers, France; norraseth.kaeokhamloed@univ-angers.fr (N.K.); emilie.roger@univ-angers.fr (E.R.); jerome.bejaud@univ-angers.fr (J.B.); nolwenn.lautram@univ-angers.fr (N.L.)

<sup>2</sup> SCIAM, SFR ICAT, University of Angers, F-49000 Angers, France; florence.manero@univ-angers.fr (F.M.); rodolphe.perrot@univ-angers.fr (R.P.)

<sup>3</sup> Laboratoire de Pharmacologie-Toxicologie, CRPV, Angers University Hospital Center, F-49000 Angers, France; chadi.abbara@chu-angers.fr (C.A.); marie.briet@chu-angers.fr (M.B.)

\* Correspondence: samuel.legeay@univ-angers.fr



**Citation:** Kaeokhamloed, N.; Roger, E.; Béjaud, J.; Lautram, N.; Manero, F.; Perrot, R.; Abbara, C.; Briet, M.; Legeay, S. New In Vitro Coculture Model for Evaluating Intestinal Absorption of Different Lipid Nanocapsules. *Pharmaceutics* **2021**, *13*, 595. <https://doi.org/10.3390/pharmaceutics13050595>

Academic Editor: Ana Beloqui Garcia

Received: 6 April 2021

Accepted: 20 April 2021

Published: 21 April 2021

**Publisher's Note:** MDPI stays neutral with regard to jurisdictional claims in published maps and institutional affiliations.



**Copyright:** © 2021 by the authors. Licensee MDPI, Basel, Switzerland. This article is an open access article distributed under the terms and conditions of the Creative Commons Attribution (CC BY) license (<https://creativecommons.org/licenses/by/4.0/>).

**Abstract:** Standard models used for evaluating the absorption of nanoparticles like Caco-2 ignore the presence of vascular endothelium, which is a part of the intestinal multi-layered barrier structure. Therefore, a coculture between the Caco-2 epithelium and HMEC-1 (Human Microvascular Endothelial Cell type 1) on a Transwell® insert has been developed. The model has been validated for (a) membrane morphology by transmission electron microscope (TEM); (b) ZO-1 and  $\beta$ -catenin expression by immunoassay; (c) membrane integrity by trans-epithelial electrical resistance (TEER) measurement; and (d) apparent permeability of drugs from different biopharmaceutical classification system (BCS) classes. Lipid nanocapsules (LNCs) were formulated with different sizes (55 and 85 nm) and surface modifications (DSPE-mPEG (2000) and stearylamine). Nanocapsule integrity and particle concentration were monitored using the Förster resonance energy transfer (FRET) technique. The result showed that surface modification by DSPE-mPEG (2000) increased the absorption of 55-nm LNCs in the coculture model but not in the Caco-2. Summarily, the coculture model was validated as a tool for evaluating the intestinal absorption of drugs and nanoparticles. The new coculture model has a different LNCs absorption mechanism suggesting the importance of intestinal endothelium and reveals that the surface modification of LNCs can modify the in vitro oral absorption.

**Keywords:** intestinal absorption; Caco-2; HMEC-1; apparent permeability; lipid nanocapsule; förster resonance energy transfer

## 1. Introduction

Drug administration by the oral route is considered the most accepted one by patients for drug delivery due to its convenience. However, some drugs present a low oral bioavailability due to low drug solubility or low intestinal permeability. This low permeability can be explained by the intestine's complex multilayer structure, consisting of the mucus barrier, the enterocytic barrier, and the endothelial barrier [1–3]. To improve oral drug delivery, drug encapsulation into nanocarriers, such as lipid nanocapsules (LNCs), is currently one of the most promising technologies. LNCs consist of an oily core enclosed by a shell of pegylated surfactant and phosphatidylcholine and can be prepared by a well-known low-energy emulsification process: The phase-inversion temperature method [4,5]. LNCs have sizes ranging from 20 to 100 nm and can also be prepared with different surface-chemistry. For example, anionic LNCs can be produced by the addition of DSPE-mPEG (2000) [6] and cationic LNCs by adding stearylamine [7] or chitosan [8,9]. Previous studies demonstrated that LNCs enhance the in vivo oral bioavailability of paclitaxel, fondaparinux, albendazole, and praziquantel; and the in vitro intestinal absorption of paclitaxel, Sn38, decitabine,

acyclovir, and efavirenz [7,10–16]. In addition, the use of the *in vitro* Caco-2 model allowed us to describe that LNCs are mainly transported via active endocytosis, or more precisely, through clathrin-dependent and caveolae-dependent transport mechanisms. Recently, the application of the Förster resonance energy transfer (FRET) technique coupled with Nanoparticle Tracking Analysis (NTA) demonstrated that few LNCs (around 0.3% of the initial quantity of LNCs) were able to be transported intact by transcytosis after passage through Caco-2 cell monolayer [17].

FRET is a useful technique to monitor the integrity of nanoparticles. It is based on the interaction between two spatially closed (1–10 nm) fluorophores in which the emission spectrum of the FRET-donor overlaps with the excitation spectrum of the FRET-acceptor. The efficacy of the energy transfer between the two fluorophores is related to their proximity [18–20]. Thus, the loss of FRET-nanoparticles integrity will cause the FRET fluorophores to be released into the external medium and disperse, widening the fluorophores' proximity and resulting in the disappearance of the FRET-acceptor emission spectrum. As such, FRET is currently the only technique that can be used to follow the passage of intact nanoparticles in biological fluids or organisms. By a combination of the FRET technique with the NTA, Roger et al. developed a quantitative method to measure the particle concentration of intact LNCs [21], making this a precise tool for monitoring the membrane transport of nanocarriers.

Nevertheless, to date, the study on the membrane transport of LNCs across the intestinal barrier has been done only in the Caco-2 model, which consists of a monolayer of immortalized enterocyte cells cultivated on a semi-permeable membrane [22–25]. This model is the most commonly used and considered as a reference model for evaluating intestinal drug permeability. The Caco-2 model is used by regulatory agencies such as the USFDA (U.S. Food and Drug Administration) and the ICH (International Council for Harmonization) to establish the biopharmaceutics classification system (BCS) that classifies drugs based on permeability and solubility. The BCS classes can be defined by the apparent permeability ( $P_{app}$ ) of drugs in the Caco-2 model. Drugs with high permeability (class I and II) and low permeability (class III and IV) are defined by the  $P_{app} > 10 \times 10^{-6}$  cm/s and  $P_{app} < 2 \times 10^{-6}$  cm/s, respectively. Drugs with the  $P_{app}$  between  $2-10 \times 10^{-6}$  cm/s are classified on a case-by-case basis because other pharmacokinetics parameters can influence their permeability [26–28]. Over the past few years, the Caco-2 model has been improved with other cell types added as a coculture system (e.g., HT-29, Raji-B coculture model) [22,29,30]. However, all these models for studying intestinal absorption ignore the endothelium layer that LNCs have to cross before reaching blood circulation. A recent study demonstrated that the intestinal endothelium plays a major role as a barrier against antigen and nutrients transport similar to the blood–brain barrier [31]. Another *in vivo* study in rats suggested that the disruption of the endothelium allows pathogens to enter the systemic circulation, strengthening the involvement of the intestinal endothelium in the mechanisms of oral absorption [32,33]. However, the role of intestinal endothelium in regulating drug absorption has never been studied. Besides, endothelium in other barriers such as the pulmonary endothelium (air–blood barrier) has been recently found to have a significant role in regulating the absorption of drugs and macromolecules [34]. Therefore, the role of the intestinal endothelium on drugs and nanoparticle absorption needs to be elucidated. Recently, Kasper et al. [35] developed an *in vitro* intestinal coculture model comprising Caco-2 and human hemangiosarcoma-derived endothelial cells (ISO-HAS-1), but the model was used for studying the pathophysiology of the inflamed intestinal membrane, not for drug absorption. The objective of the present study is to develop and validate a new *in vitro* coculture model in order to systematically evaluate, for the first time, the transport of different LNCs across the intestinal epithelial-endothelial barrier.

In this context, we developed a new coculture model that can better mimic the gut–blood barrier structure for studying the membrane transport of intact lipid nanocapsules. Caco-2 cells and Human Microvascular Endothelial Cell type 1 (HMEC-1) were seeded on the apical and basolateral side of the Transwell® plate, respectively. This model was

characterized by membrane morphology, tight junction expression, and trans-epithelial electric resistance. Five different drugs were selected based on their physicochemical characteristics as a representation of drugs in general with different permeability and solubility according to the BCS [26–28]. Their permeability was evaluated in the coculture model in comparison with the reference Caco-2 model for the conformity with BCS. LNCs with different sizes (55 and 85 nm) and different surface chemistries (DSPE-mPEG (2000) and stearylamine) were formulated and loaded with FRET dyes [35]. The transport of intact FRET-LNCs was investigated across the newly developed coculture compared to the well-established Caco-2 model, using the quantitative FRET fluorimetry technique coupled with the NTA to quantify the particle concentration of intact LNCs.

## 2. Materials and Methods

### 2.1. Materials

Caco-2 and HMEC-1 cells were obtained from American Type Culture Collection (Manassas, VA, USA). Sodium chloride, sodium tetraphenylborate, ethyl acetate, dichloromethane, methanol, triton X-100, Trizma<sup>®</sup> (base), anti- $\beta$ -catenin rabbit mAb, anti-TJP1 (tight junction protein-1; a.k.a. ZO-1, zonula occludens-1) rabbit mAb, collagen type 1 (calf skin), 4',6-diamidino-2-phenylindole (DAPI), Dulbecco's modified Eagle's medium (DMEM D6429, with 4500 mg/L glucose, L-glutamine, sodium pyruvate, and sodium bicarbonate), dimethyl sulfoxide (DMSO), epidermal growth factor, hydrocortisone HCl powder for injection, Osmium tetroxide (OsO<sub>4</sub>), Epon<sup>™</sup> 812 resin, metoprolol tartrate, propranolol HCl, naproxen, atenolol and furosemide, and stearylamine were purchased from Sigma-Aldrich (Saint-Quentin Fallavier, France). Hank's balanced salted solution (HBSS), MCDB 131 medium (Gibco 10372-019), penicillin-streptomycin solution, goat anti-rabbit IgG Alexa Flour<sup>®</sup> 488, DiI (1,10-dioctadecyl-3,3,30,30-tetramethyl-indocarbocyanine perchlorate), and DiD (1,1'-dioctadecyl-3,3,3',3'-tetramethylindocarbocyanine perchlorate) were purchased from Thermofisher (Villebon-sur-Yvette, France). Amphotericin B, Phosphate-buffered saline (PBS), and L-glutamine were purchased from PAA Laboratories (Toronto, ON, Canada). Fetal bovine serum (FBS) was purchased from Biowest (Nuaillé, France). Paraformaldehyde 32% and glutaraldehyde 25% were purchased from Electron Microscopy Science (Hatfield, PA, USA). Nonessential amino acid (NEAA) was purchased from Lonza (Verviers, Belgium). Ultrapure water was obtained from a Milli-Q<sup>®</sup> Advantage A10 System (Merck Millipore, Darmstadt, Germany). Costar<sup>®</sup> Transwell<sup>®</sup> (12-well, polycarbonate membrane filters, 0.4  $\mu$ m pore size, 1.12 cm<sup>2</sup> growth area) and T75 cell culture flasks were purchased from Costar (New York, NY, USA). Captex<sup>®</sup> 8000 (glyceryl tricaprilate) was kindly provided by Abitec Corporation (Columbus, OH, USA). Lipoid<sup>®</sup> S75-3 (phosphatidylcholine and phosphatidylethanolamine mixture) was purchased from Lipoid GmbH (Steinhausen, Switzerland); Kolliphor<sup>®</sup> HS-15 (PEG 660 and polyethylene glycol 660 hydroxystearate mixture) from BASF (Ludwigshafen, Germany); and DSPE-mPEG(2000) (1,2-distearoyl-sn-glycero-3-phosphoethanolamine-N-[methoxy(polyethylene glycol)-2000] (ammonium salt)) from Avanti Polar Lipids (Alabaster, AL, USA).

### 2.2. Caco-2 and HMEC-1 Cells Culture

Caco-2 cells were cultured between passage 18 and 27 in DMEM medium supplemented with 20% *v/v* FBS, 1% *v/v* non-essential amino acids and 100 UI/mL penicillin, 0.5 mg/mL streptomycin. HMEC-1 cells were cultured between passage 4 and 12 in MCDB 131 medium supplemented with 10% *v/v* FBS, 2 mM/mL L-glutamine, 100 UI/mL penicillin, 0.5 mg/mL streptomycin, 2.5  $\mu$ g/mL amphotericin B, 1  $\mu$ g/mL hydrocortisone, and 0.01  $\mu$ g/mL epidermal growth factor. Cells were cultured in a T75 flask (75 cm<sup>2</sup>) and incubated at 37 °C in humidified air with 5% CO<sub>2</sub>.

### 2.3. Caco-2/HMEC-1 Monoculture and Coculture on Transwell<sup>®</sup>

The polycarbonate membrane filters (0.4  $\mu$ m pore size, 1.12 cm<sup>2</sup> growth area) in Transwell<sup>®</sup> inserts were coated with collagen type-1 for 8  $\mu$ g/cm<sup>2</sup> on the apical side and

25  $\mu\text{g}/\text{cm}^2$  on the basolateral side [28]. Caco-2 cells ( $1 \times 10^5$  cells) were seeded onto the apical side of the coated filter and cultured in DMEM medium, which was changed every 2–3 days. On day 18, the Transwell® inserts were taken out, flipped upside down, and submerged under DMEM medium in a sterile basin with no bubbles trapped underneath the filter. Then,  $5 \times 10^4$  HMEC-1 cells were seeded onto the basolateral surface of the filter and were incubated for 2 h at room temperature. The inserts were then placed back into the Transwell® chambers. The Caco-2 media and the HMEC-1 media were filled in the upper chamber and the lower chamber, respectively, and were changed every two days. The coculture membranes were used on day 22 of Caco-2 cells and day 4 of HMEC-1 cells. Moreover,  $1 \times 10^5$  Caco-2 cells and  $5 \times 10^4$  HMEC-1 cells were separately seeded on the Transwell® inserts for the monoculture and then used as control.

#### 2.4. Membrane Morphology

##### 2.4.1. Transmission Electron Microscopy (TEM)

Caco-2/HMEC-1 cell membranes in Transwell® inserts were washed with HBSS and fixed with 2.5% *v/v* glutaraldehyde in phosphate buffer pH 7.4 for 1 h at room temperature, then replaced with phosphate buffer pH 7.4. Afterward, 1% *w/v*  $\text{OsO}_4$  was added to the cell samples and kept for 1 h at room temperature. Then, the samples were washed three times by deionized water and subsequently dehydrated by 50%, 70%, and 95% ethanol twice and four times with 100% ethanol. Next, the samples were embedded in Epon™ 812 resin, which was left to polymerize for 24 h at 60 °C. Thin slices (60 nm) were cut from each sample using Leica UC7 ultramicrotome (Leica microsystems, Wetzlar, Germany) and deposited onto copper grids. The samples were stained with 3% uranyl acetate in 50% ethanol for 5 min and washed with deionized water. The samples were left to dry and then examined using the JEOL JEM-1400 electron microscope (JEOL, Tokyo, Japan).

##### 2.4.2. Confocal Fluorescence Microscopy

Caco-2, HMEC-1, and Caco-2/HMEC-1 cell layers on Transwell® inserts were fixed for 20 min with 4% *v/v* paraformaldehyde at room temperature. The cells were washed three times with TBS and then permeabilized for 10 min with 0.5% *v/v* Triton X-100 in TBS at room temperature. After washing out three times with TBS, 5% *w/v* FBS was added and rinsed out three times by TBS after 1 h. Anti- $\beta$ -catenin rabbit monoclonal antibodies (mAb) (1:300 in 2% *w/v* FBS in TBS) and Anti-ZO-1 rabbit mAb (1:300 in 2% *w/v* FBS in TBS) were separately added to the cells kept overnight at 4 °C. Then cells were rinsed out three times by TBS, and the fluorescence-labeled secondary antibody goat anti-rabbit IgG Alexa Fluor® 488 (1:500 in 2% *w/v* FBS in TBS) was added and kept overnight at 4 °C. Then, the cells were washed three times with TBS before stained with DAPI (3  $\mu\text{g}/\text{mL}$  in TBS) for 10 min at room temperature. Finally, the filter membranes were cut from the Transwell® and mounted between microslides. The immunofluorescent staining images of cell confluency and tight junction structure were characterized by Leica TCS SP8 laser-scanning confocal microscope (Leica Microsystems, Heidelberg, Germany) with the excitation and emission wavelength of 488 and 520 nm, respectively, for tight junction protein ZO-1 and adherens junction protein  $\beta$ -catenin, and 405 nm and 461 nm, respectively, for cell nuclei. The software Leica Application Suite X was used for 3D visualization.

##### 2.4.3. Trans-Epithelial Electrical Resistance (TEER)

TEER ( $\Omega\text{-cm}^2$ ) of the Caco-2 and the coculture cell layers were measured by the Millicell® ESR-2 volt-ohmmeter (Merck Millipore Corporation, Burlington, MA, USA) on days 4, 11, 18, 21, and 22. The values were corrected by the resistance of blank Transwell® insert following the equation:

$$\text{TEER} = (R_{\text{total}} - R_{\text{blank}}) \times A \quad (1)$$

when  $R_{\text{total}}$  is the measured resistance ( $\Omega$ ),  $R_{\text{blank}}$  is the arithmetic mean of the resistance of blank Transwell® insert (110  $\Omega$ ), and  $A$  is the area of Transwell® filter (1.12  $\text{cm}^2$ ).

## 2.5. Transport Assay of the Free Drugs

### 2.5.1. Transport Assay Experiment

Five reference drugs were chosen as a representation of drugs with different solubility and permeability according to the biopharmaceutical classification system (BCS) [36] (see Table 1). The drugs were firstly dissolved in ultrapure water (if necessary, methanol could be used to dissolve the drugs with the final concentration of methanol less than 0.02% *v/v*) and then serially diluted in HBSS to 5  $\mu$ M. 1.5 mL of HBSS and 0.5 mL of diluted drug solutions were added to the basolateral and apical chambers of the Transwell® wells, respectively. Studies were performed on the Caco-2/HMEC-1 coculture model, the Caco-2 model, the HMEC-1 model, and Transwell® without cells (control). The plates were incubated for 2 h at 37 °C with humidified air and 5% CO<sub>2</sub>. Afterward, the apical and the basolateral media were collected and analyzed by HPLC-UV.

**Table 1.** Classification of the studied drugs according to the BCS.

BCS Classes	Solubility	Permeability	Drugs
I	High	High	Metoprolol tartrate, Propranolol HCl
II	Low	High	Naproxen
III	High	Low	Atenolol
IV	Low	Low	Furosemide

### 2.5.2. Drug Analysis by HPLC-UV

HPLC analysis was performed using the Agilent 1200 HPLC system (Agilent Technologies, Les Ulis, France) with a UV detector (deuterium lamp light source) and with the Uptisphere® C18-ODB 100  $\times$  2.1 mm, 5  $\mu$ m column (Agilent Technologies, Les Ulis, France). Sample preparation was explained in Appendix A. The analysis run time was 20 min. The mobile phase consisted of phase A (phosphate buffer pH 7.4) and phase B (acetonitrile). In initial conditions, the mobile-phase composition was 15% B; a linear gradient was applied to reach a composition of 80% B after 16 min, maintained 2 min, and then set to return to initial. The flow rate was 0.4 mL/min. Each drug was analyzed separately, and their retention times were: 1.7 min for atenolol, 4.6 min for metoprolol, 7.4 min for propranolol, 6.2 min naproxen, and 5.6 min for furosemide. Quantification was achieved using calibration curves (area ratio with internal standard vs. nominal analyte concentration) fitted by linear least squares regression. The lower limit of quantification (LLOQ) was validated at 50 ng/mL for all substances, and the limit of detection (LOD) was 10 ng/mL.

### 2.5.3. Apparent Permeability Calculation

The apical-to-basolateral apparent permeability was calculated following the equation:

$$P_{app} = \frac{dQ}{dt} \times \frac{1}{AC_0} \quad (2)$$

where  $dQ/dt$  is the appearance rate of a drug at the basolateral side ( $\mu$ g/s),  $A$  is the surface area of the Transwell® filter (1.12 cm<sup>2</sup>), and  $C_0$  is the initial concentration at the apical side ( $\mu$ g/mL) [21,37].

## 2.6. Formulation of FRET-LNCs

### 2.6.1. Synthesis of DiI- and DiD-TPB

The fluorescence dyes DiI- and DiD-tetraphenylborate (TPB) were synthesized by the method previously described [4,5,10,21]. Dyes were solubilized in Captex® 8000 at the concentration of 2% *w/w*.



## 2.6.2. Formulation of FRET Lipid Nanocapsules (FRET-LNCs)

Six formulations of FRET-LNCs were prepared based on the phase inversion method [6]. The surface modification was adapted from the ‘one-step (OS) stealth LNCs process’ developed by Lainé et al. [38]. The composition of lipid nanocapsules in each batch is described in Table 2. Firstly, Lipoid® S75-3 was dissolved in the Captex® 8000 containing DiI-TPB and DiD-TPB. Then, Kolliphor® HS-15, purified water, and NaCl were added, as well as the surface modification substances, which were DSPE-mPEG (2000) (anionic) or stearylamine (cationic), if applicable. Under agitation, three heat-cool cycles (60–90 °C) were applied to the mixture. In the last cooling cycle, cold ultrapure water (2 °C) was added at the phase inversion temperature, followed by 5 min of a slow stir. Finally, the suspension of FRET-LNCs was filtrated by a 0.22 µm filter (Minisart®) and stored at 2–8 °C.

**Table 2.** Composition of different types of FRET-LNCs.

Compositions	Quantity (% w/w)					
	F1	F1-DSPE-PEG	F1-SA	F2	F2-DSPE-PEG	F2-SA
Captex® 8000 (2% w/w DiI-TPB)	5.5	5.5	5.5	8.5	8.5	8.5
Captex® 8000 (2% w/w DiD-TPB)	5.5	5.5	5.5	8.5	8.5	8.5
Kolliphor® HS-15	11.5	11.5	11.5	9.3	9.3	9.3
Purified water	21.3	21.3	21.3	17.5	17.5	17.5
DSPE-mPEG (2000)	-	0.6	-	-	0.6	-
Stearylamine	-	-	0.1	-	-	0.1
Lipoid® S75-3	0.7	0.7	0.7	0.7	0.7	0.7
NaCl	0.8	0.8	0.8	0.8	0.8	0.8
Purified water (2 °C)	54.7	54.7	54.7	54.7	54.7	54.7

## 2.7. Characterization of FRET-LNCs

The concentration (particles/mL) and the size distribution of the nanoparticles were determined with the nanoparticle tracking analysis (NTA) technique using a NanoSight NS300 (Malvern Instrument, Worcestershire, UK) with a low volume flow cell and a 450 nm laser. FRET-LNCs suspensions were diluted in ultrapure water by factor 300,000 (*v/v*) and then slowly injected into the sample chamber using a 1 mL syringe pump with the rate of 3–4 µL per second. The video sequences of the nanoparticles were captured over 60 s (5 replicates) and then analyzed by NTA analytical software version 3.2.

NTA provides the particle size distribution parameters as D10, D50, and D90; which represents the diameter (nm) at the 10th, 50th (median), and 90th percentiles of the distribution histogram, respectively. Then the span, as a distribution width parameter, is calculated following the equation:

$$\text{Span} = \frac{D90 - D10}{D50} \quad (3)$$

The zeta potential of the FRET-LNCs was determined by laser doppler electrophoresis using Zetasizer® Nano series DTS 1060 (Malvern Instruments SA, Worcestershire, UK).

## 2.8. Transport Assay of Intact LNCs across Membranes

### 2.8.1. Transport Assay of FRET-LNCs

First, 1.5 mL of HBSS and 0.5 mL of diluted FRET-LNCs (1% *v/v* in HBSS) were filled into the basolateral and the apical side of the Transwell® plates, respectively. The plates were incubated for 2 h at 37 °C with humidified air and 5% CO<sub>2</sub>. Then, samples from the basolateral and the apical sides were collected, and fluorescence was analyzed by spectrophotometer. The TEER of all membranes were measured before and after the experiment to ensure their integrity. Membranes with TEER <300 Ω·cm<sup>2</sup> were excluded from the test.

### 2.8.2. Quantitative FRET Fluorimetry of Intact LNCs

Fluorescence emission spectra of collected samples were recorded on a FluoroMax<sup>®</sup> 4 spectrophotometer (Horiba Jobin Yvon Inc., Piscataway, NJ, USA) at room temperature with the 548 nm excitation and 0.5 s integration time. The emission spectra were collected from 555 to 750 nm, with an increment of 1 nm. They were corrected for the lamp source fluctuations and the wavelength-dependent response of the detector. The integrity of nanoparticles was determined by FRET efficiency (proximity ratio) calculated by the following equation:

$$PR = \frac{A}{A + D} \quad (4)$$

where A and D are the maximum fluorescence intensity of the acceptor (678 nm) and donor (569 nm), respectively. The particle concentration of the nanocarriers was calculated from the standard curve of the FRET acceptor signal. An acceptor signal lower than the limit of detection (LOD = 1382 cps/mA) and/or a PR lower than 0.70 was considered as zero particle concentration.

### 2.8.3. Transport Efficiency of FRET-LNCs

The transport efficiency (TE) of FRET-LNCs is the percentage of numbers of nanoparticles presenting at the basolateral medium compared to the initial particle concentration at the apical medium. It was calculated by the equation:

$$TE = \frac{C_f V_B}{C_0 V_A} \times 100\% \quad (5)$$

where  $C_f$  is the particle concentration at the basolateral side after 2 h,  $C_0$  is the initial particle concentration at the apical side (particles/mL),  $V_A$  is the volume of sample at the apical side (1 mL), and  $V_B$  is the volume of sample at the basolateral side (1.5 mL).

### 2.9. Statistical Analysis

The experiments were performed at least in triplicate. For statistical comparison, the Kruskal–Wallis test with uncorrected Dunn's multiple comparison test was the method of statistical analysis. *p*-value of less than or equal to 0.05 was considered statistically significant. All statistical analysis was performed using Prism GraphPad (version 8.4.1, GraphPad Software, San Diego, CA, USA).

## 3. Results and Discussions

### 3.1. Development of the New In Vitro Coculture Model

The new in vitro 2D coculture model between Caco-2 and HMEC-1 cells was developed and intended as a tool to assess the absorption of drugs and nanoparticles. In order to investigate its morphology, cross-sections of cell layers were observed under TEM (Figure 1A). On day 22, Caco-2 cells exhibited a columnar epithelium monolayer structure with ~25 μm thickness with a brush border (microvilli) on the apical surface. When zooming in between the adjacent borders of two Caco-2 cells, junctional complex structures were observed. The morphology of these Caco-2 cells corresponds to mature human enterocytes [23,39,40] and typical Caco-2 cells described elsewhere [41,42]. Furthermore, the HMEC-1 layer was obtained as a very thin squamous epithelium monolayer with 0.2–2 μm thickness covering the basolateral side of the filter (facing downward). The junctional structure was observed along HMEC-1 cell borders. This morphology of HMEC-1 is closely similar to the structure of human vascular endothelium already described by Young et al. and Ru et al. [40,42]. Thus, with this coculture condition, the morphology of both Caco-2 and HMEC-1 cells was maintained.

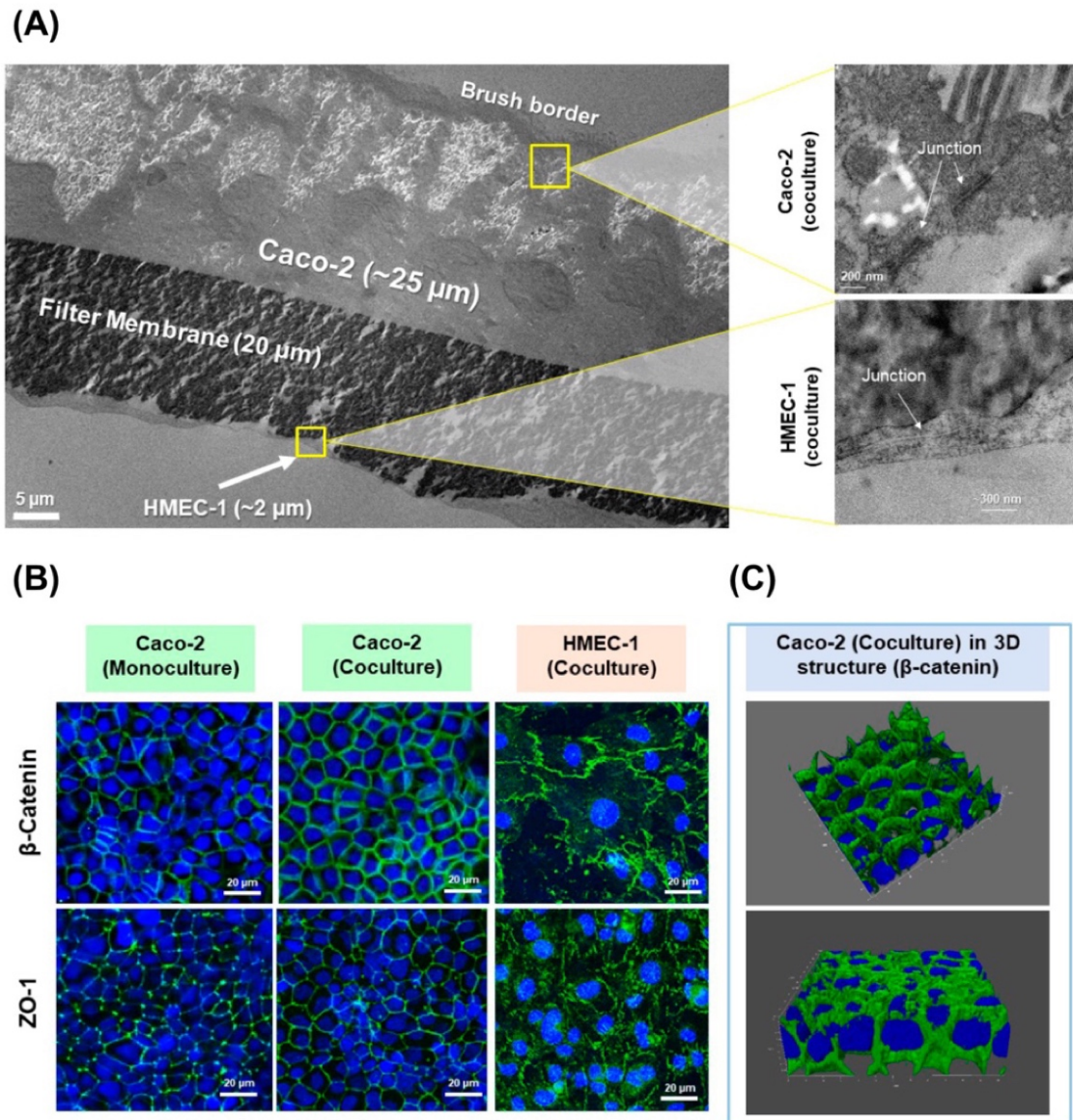


**Figure 1.** (A) Cross-sectioning images of Caco-2 and HMEC-1 coculture layers under TEM (left) and zoomed cross-sectioning images of the junction area between Caco-2 cells (upper right) and HMEC-1 cells (lower right); (B) immunofluorescent staining images of Caco-2 monoculture, cocultured Caco-2 and cocultured HMEC-1 layers, characterized by confocal microscopy for the expression of tight junction protein ZO-1 (Alexa Fluor<sup>®</sup> 488, green) and adherens junction protein  $\beta$ -catenin (Alexa Fluor<sup>®</sup> 488, green). The images are overlaid with cell nuclei (DAPI, blue); (C) the 3D images show only the expression of  $\beta$ -catenin in the cocultured Caco-2 layer and revealed a confluent monolayer with no cell stacking.

In order to investigate the formation of the cell junctional complex, the expression of tight junction protein ZO-1 and adherens junction protein  $\beta$ -catenin were examined by immunofluorescence (Figure 1B). HMEC-1 and Caco-2 cell layers in the coculture model were confluent with the expression of ZO-1 and  $\beta$ -catenin along the cell borders, meaning that tight junctions and adherens junctions were fully developed. A similar structural pattern was observed (Figure 1B) in the Caco-2 monolayer, meaning that the coculture system still maintained the same junctional complex structure as in monoculture. In accordance with our study, Ma et al. described that Caco-2 expressed the ZO-1 as a continuous band along the cell borders after 3 weeks of incubation, while Ruffer et al.

found that HMEC-1 expressed ZO-1 and also  $\beta$ -catenin at the cell borders after 3 days of incubation [39]. In addition, a 3D imagery of  $\beta$ -catenin overlayed with cell nuclei (Figure 1C) revealed that the cocultured Caco-2 had a structure of a confluent monolayer with no cell stacking. As such, a confluent monolayer of Caco-2 and HMEC-1 cocultured on the apical and basolateral side of the Transwell® filter, respectively, was obtained.

The membrane integrity of cell culture membranes was also monitored by TEER measurement from the beginning to the end of the cell culture. As shown in Figure 2, the average TEER of the Caco-2/HMEC-1 coculture model on day 22 had the highest level, with an average of  $1415 \pm 331 \Omega \cdot \text{cm}^2$ . This average is significantly (Kruskal–Wallis) higher than that of the Caco-2 model ( $470 \pm 46 \Omega \cdot \text{cm}^2$ ), which was also significantly (Kruskal–Wallis) higher than HMEC-1 monolayer ( $18 \pm 6 \Omega \cdot \text{cm}^2$ ). Besides, the TEER of the Caco-2 model was in accordance with Briske-Anderson et al., who cultured the Caco-2 cells from passage 22 with similar conditions and obtained a TEER value at around  $500 \Omega \cdot \text{cm}^2$  after 21 days [43–49].

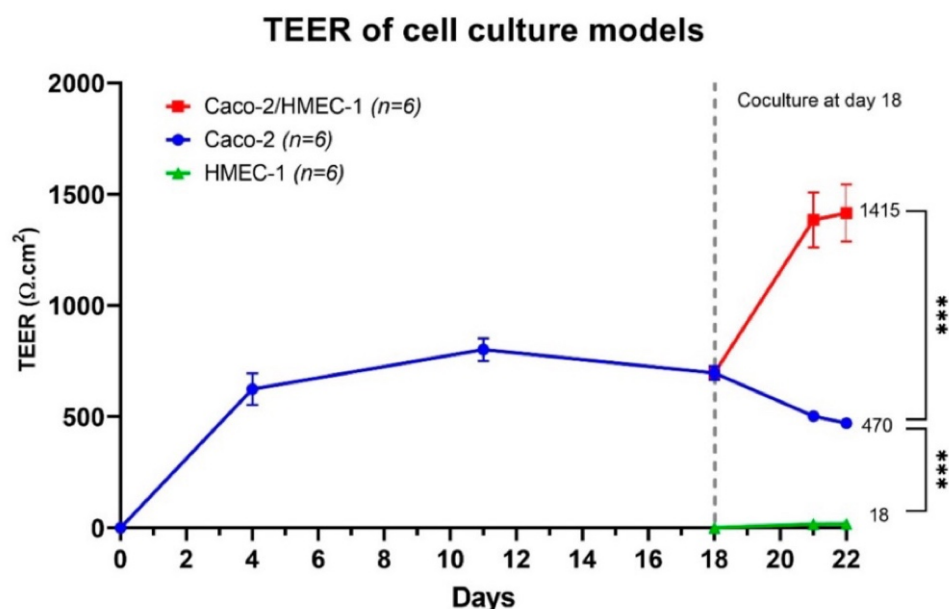


**Figure 2.** Average TEER ( $n = 6$ ) of Caco-2/HMEC-1 coculture (red), Caco-2 monolayer (blue), and HMEC-1 monolayer (green). The whiskers represent a 95% confidence interval (Kruskal–Wallis: \*\*\*  $p \leq 0.001$ ).

Since this new in vitro coculture model was intended as a tool to assess drug absorption, the apical-to-basolateral  $P_{app}$  of five reference drugs from all four BCS classes was evaluated and compared with their  $P_{app}$  from the conventional Caco-2 model (Figure 3). The five drugs in this experiment are chosen because they are commonly used as the reference for evaluating the permeability in the Caco-2 model. Their solubility and permeability are defined by the BCS [45–51]. For atenolol (class III) and furosemide (class IV), the concentration at the basolateral side was lower than the detection limit in both coculture and Caco-2 models. These results were in accordance with the definition of classes III and IV, which have low apparent permeability. For propranolol (class I), metoprolol (class I), and naproxen (class II), their  $P_{app}$  were ranging from  $20.6$  to  $44.2 \times 10^{-6} \text{ cm/s}$  on the coculture model and  $22.4$  to  $44.5 \times 10^{-6} \text{ cm/s}$  on the Caco-2 model, conforming with the BCS classification as well. No significant differences (Kruskal–Wallis) between the  $P_{app}$  of all five drugs across the coculture and the Caco-2 model were obtained. Therefore, the  $P_{app}$  of both Caco-2/HMEC-1 and Caco-2 models were in the same range for the five tested drugs. These values were also similar to those from various literature that high-permeability drugs in BCS class I and II had the  $P_{app}$  in the range from  $9 \times 10^{-6}$  to  $43 \times 10^{-6} \text{ cm/s}$ , while low-

permeability drugs in class III and IV had nearly zero  $P_{app}$  [6,7,10–17]. In addition, the  $P_{app}$  of the drugs across the HMEC-1 monolayer and the blank Transwell® filter (Figure S1) was also examined as a control. The  $P_{app}$  of all drugs were in the same range from  $22 \times 10^{-6}$  to  $34 \times 10^{-6}$  cm/s with no significant difference (Kruskal–Wallis) between drugs of high and low permeability across both HMEC-1 monolayer and blank filter. In conclusion, the addition of the HMEC-1 layer in the coculture model did not change the permeability of these five reference drugs across the membranes, suggesting that the conventional Caco-2 model alone might be adequate for studying the absorption of drug molecules.

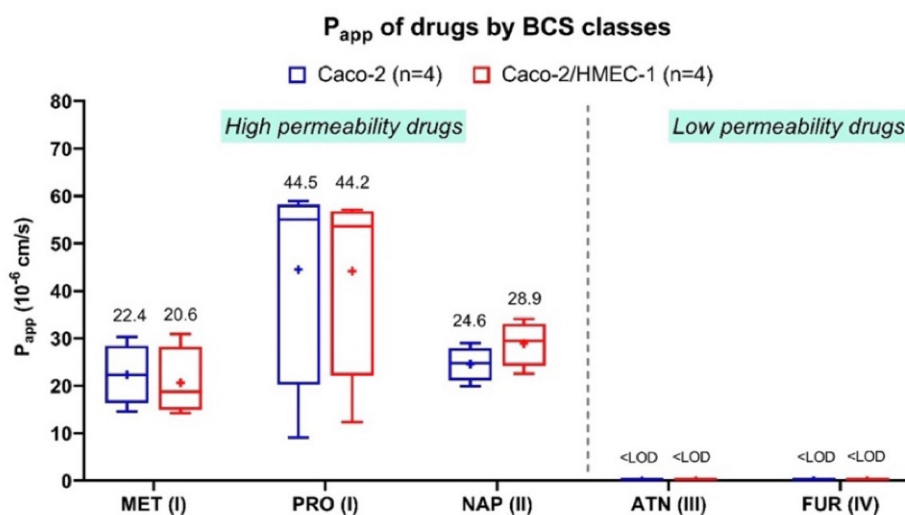


**Figure 3.** Average apparent permeability ( $P_{app}$ ) of five drugs ( $n = 4$ ) classified by four BCS classes across Caco-2 cells (blue) and HMEC-1/Caco-2 coculture cells (red). MET = metoprolol, PRO = propranolol, NAP = naproxen, ATN = atenolol, FUR = furosemide; BCS class numbers are signified in the parentheses. LOD means the limit of detection = 10 ng/mL. The (+) symbol represents the arithmetic mean, and the whiskers represent a 95% confidence interval (Kruskal–Wallis).

### 3.2. Transport Assay of Intact LNCs across Membranes

LNCs demonstrated their ability to improve the oral absorption of several encapsulated drugs [50]. Nanoparticle size can also influence oral drug absorption [7,51]. Furthermore, surface-modified LNCs such as PEG (2000)-amino post-inserted LNCs and stearylamine LNCs can enhance oral drug bioavailability [21]. Hence, in order to study the impact of size and surface chemistry of LNCs on their oral in vitro absorption, the LNCs with two different sizes (F1 and F2) and three different surface chemistry (unmodified LNCs, anionic DSPE-mPEG (2000) added, and cationic stearylamine added) were formulated (Table 2) and tested in both coculture and Caco-2 models. In addition, Roger et al. have recently shown that the FRET technique could be used to detect and quantify the intact LNCs crossing the Caco-2 monolayer [4,5]. Thus, in order to monitor the integrity of LNCs across the membrane, the FRET technique was used.

Table 3 presents the physicochemical characteristics of the FRET-LNCs in terms of hydrodynamic size, particle size distribution, particle concentration, zeta potential, and FRET proximity ratio. The size distribution histogram is shown in Figure S2. The composition F1 and F2 provided the FRET-LNCs with an average diameter of around 55 nm and 85 nm, respectively. The F2 formulation group has a higher amount of Captex® 8000 (oily core) and a slightly lower amount of Kolliphor® HS-15 than the F1 group. In accordance with the ternary diagram of a mixture system established by Heurtault et al. [6,10] and other previous studies [5], increasing the amount of oil composition together with decreasing the amount of the hydrophilic surfactant (Kolliphor® HS-15) could increase the size of LNCs [21]. Moreover, the particle size distribution of all formulations was unimodal and uniform (Figure S2). The D50 value is the median diameter (nm). All the formulations had

a symmetric distribution as their median diameter was almost equal to the mean diameter. Besides, span is the parameter determining the size distribution width normalized by median diameter. The span value closing to zero determines a narrow size distribution. The span of the compositions F1 (0.37–0.38) was lower than the F2 (0.54–0.63), indicating that LNCs with smaller sizes had a narrower distribution width, while the surface modification had no effect on altering the distribution width (Kruskal–Wallis). Furthermore, both F1 and F2 compositions had similar particle concentrations (Kruskal–Wallis) ranging from  $5.5 \times 10^{14}$  to  $8.0 \times 10^{14}$  particles/mL and slightly lower than previously reported in the literature at  $1.2 \times 10^{15}$  particles/mL for 55 nm LNCs [20]. By contrast, the zeta potential of F2 was higher than F1 ( $16.3 \pm 3.7$  mV and  $4.1 \pm 0.8$ , respectively), but such a difference was not observed in the blank F1 and F2 formulations (containing no FRET dyes), of which the zeta potential was around  $-5.0$  mV regardless of sizes. The FRET dyes DiI-TPB and DiD-TPB used in the formulation were positively charged and were previously reported to elevate the zeta potential of 55-nm LNCs [6]. The fact that F2 had a quantity of Captex® 8000, in which FRET dyes were dissolved, higher than F1 could explain the higher zeta potential in F2.

**Table 3.** Characterization of FRET-LNCs (mean  $\pm$  SD): particle size, particle size distribution, particle concentration, zeta potential, and proximity ratio.

Formulas	Particle Size (nm)	Particle Size Distribution				Particle Concentration ( $\times 10^{14}$ Particles/mL)	Zeta Potential (mV)	FRET Proximity Ratio
		D10 (nm)	D50 (nm)	D90 (nm)	Span			
F1 (n = 3)	57.8 $\pm$ 9.7	45.3 $\pm$ 5.0	54.2 $\pm$ 7.7	65.6 $\pm$ 12.5	0.37 $\pm$ 0.08	7.7 $\pm$ 1.2	4.1 $\pm$ 0.8	0.89 $\pm$ 0.04
F1-DSPE-PEG (n = 2)	53.1	42.7	50.9	62.5	0.38	7.9	-4.9	0.89
F1-SA (n = 3)	56.0 $\pm$ 5.6	45.3 $\pm$ 4.5	53.5 $\pm$ 5.1	65.6 $\pm$ 7.2	0.38 $\pm$ 0.04	8.0 $\pm$ 3.1	15.4 $\pm$ 2.1	0.89 $\pm$ 0.04
F2 (n = 3)	92.6 $\pm$ 10.0	67.1 $\pm$ 6.2	88.5 $\pm$ 8.9	120.4 $\pm$ 15.3	0.60 $\pm$ 0.04	5.5 $\pm$ 2.7	16.3 $\pm$ 3.7	0.93 $\pm$ 0.02
F2-DSPE-PEG (n = 2)	83.3	61.3	77.3	109.9	0.63	6.6	3.2	0.92
F2-SA (n = 3)	82.6 $\pm$ 5.8	62.3 $\pm$ 3.7	78.7 $\pm$ 5.2	104.7 $\pm$ 9.9	0.54 $\pm$ 0.07	6.8 $\pm$ 2.3	27.3 $\pm$ 2.8	0.93 $\pm$ 0.02

Adding anionic DSPE-mPEG (2000) and cationic stearylamine at the formulation of FRET-LNCs did not significantly change the size and the particle concentration (Kruskal–Wallis, see Table 3). However, adding DSPE-mPEG (2000) decreased the zeta potential by 9–13 mV, whilst stearylamine increased it by 11 mV, as already described by Lainé et al. [7] and Ramadan et al. [52,53].

Finally, to determine the integrity of LNCs, the FRET proximity ratio (PR) was calculated [21]. Intact LNCs have PR closer to 1 due to the highly efficient energy transfer between FRET dyes in close proximity, while broken LNCs can have PR as low as 0.22 or less [54]. The PR of all formulations (Table 3) ranged from 0.89 to 0.93, meaning that the FRET dyes DiI-TPB/DiD-TPB were well encapsulated, and the formulations were full of intact LNCs. Size or surface modifications had no significant effect on PR. In summary, six FRET-LNCs formulations with different sizes and surface modifications were successfully developed and suitable for the transport assay experiment.

The transport of the six formulations was investigated in the Caco-2 and the Caco-2/HMEC-1 coculture model. The transport efficiency (TE) of each formulation is shown in Figure 4. In the Caco-2 model, when compared by sizes and surface-chemistry, the TEs of all different LNCs did not show statistically significant differences (Kruskal–Wallis). In the coculture model, when compared by sizes, the F2, F2-DSPE-PEG, and F2-SA had higher trends of TEs than their F1 counterparts, but no statistical significance (Kruskal–Wallis) was found. Furthermore, when compared by surface-chemistry, only F1-DSPE-PEG could increase the TEs of F1 with a statistical significance (Kruskal–Wallis). Finally, when compared between models, the TEs of F1-DSPE-PEG, F2-DSPE-PEG, and F2-SA were found to be higher, with a statistical significance (Kruskal–Wallis), in the coculture model than in the Caco-2 model, while in the coculture model, the TEs of F1-DSPE-PEG, F2-DSPE-PEG, and F2-SA were lower than the detection limit (reported as TE = 0). Summarily, results clearly showed a different pattern of TEs between the two models, meaning that the addition of an endothelium layer to the Caco-2 one increases the TE of F1-DSPE-PEG, F2-DSPE-PEG, and F2-SA. LNCs size did not affect TE in both models, while the surface chemistry had an effect on TE but only with F1-DSPE-PEG (55-nm).

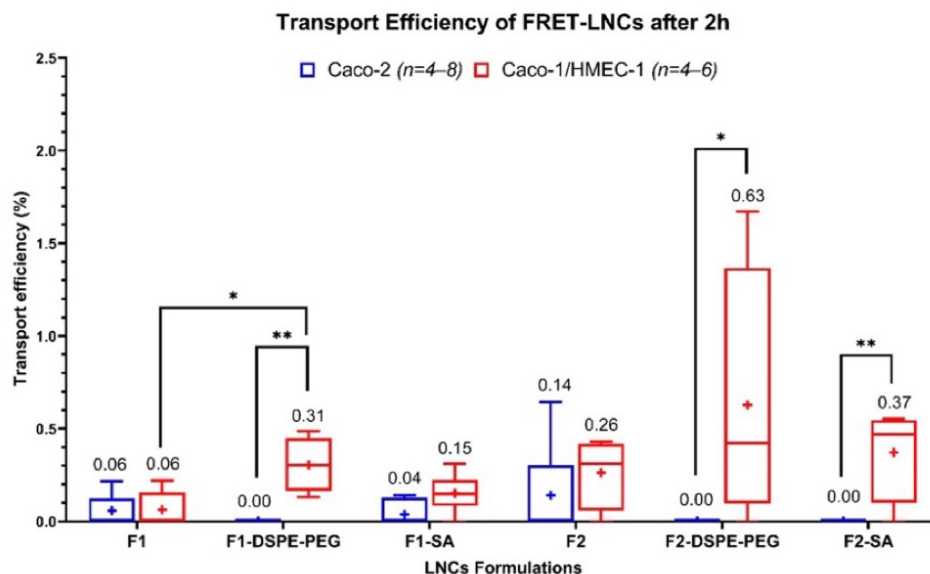


**Figure 4.** Transport efficiency of six FRET-LNCs formulations after 2 h in the Caco-2 model (blue,  $n = 4-8$ ), and the Caco-2/HMEC-1 coculture model (red,  $n = 4-6$ ). The (+) symbols represent the arithmetic mean, and the whiskers represent a 95% confidence interval (Kruskal–Wallis: \*  $p \leq 0.05$ , \*\*  $p \leq 0.01$ ).

Using the new coculture model revealed that F1-DSPE-PEG had a significantly higher transport efficiency than F1, meaning that adding DSPE-mPEG (2000) to the surface of 55-nm LNCs increased their in vitro intestinal absorption. A similar result has been observed by Bannunah et al. [54], who described that anionic polystyrene nanoparticles (PS-NPs) had much higher transportation across the Caco-2 model than cationic PS-NPs. More precisely, transcytosis of anionic PS-NPs mainly occurred via the caveolae-mediated pathway, while it was not the case for cationic PS-NPs whose transcytosis occurred via the clathrin-mediated pathway [55,56]. Moreover, adding more PEG chains, like DSPE-mPEG (2000), to the surface of LNCs would also improve their mucopenetrating property [43–48].

Interestingly, the different absorption patterns between the two models only appeared among the LNCs but not among the reference molecular drugs (Figure 3). Some LNCs, but none of the reference drugs, had significantly higher absorption in the coculture model despite its higher membrane integrity (TEER). Molecular drugs are mainly absorbed via the passive pathway regulated by the membrane's chemical properties rather than the biological ones [10,57–59]. By contrast, the LNCs are absorbed by active transport via the caveolae-mediated or clathrin/caveolae-independent endocytosis in the Caco-2 model [57–59]. The hydrophilic surfactant (Kolliphor® HS-15, previously named Solutol® HS-15) on the outer shell of LNCs could directly interact with the cholesterol-rich microdomain (lipid raft) on the cell surface, inciting the endocytosis [57–59]. The difference in LNCs absorption between the Caco-2 and the coculture models implied that adding the HMEC-1 layer might cause a change in the cell's biological absorption process that affected the LNCs transcytosis, but not the membrane's chemical properties that affected molecular drugs absorption. Therefore, the next step of this work is to determine the LNCs transport mechanism across this coculture model.

#### 4. Conclusions

In conclusion, a new coculture model of Caco-2 intestinal epithelium and human primary vascular endothelium cells (HMEC-1) was successfully developed. The cell morphology, membrane integrity, and drug permeability were validated and proved that the new model was suitable for a tool to evaluate the absorption of drugs and nanoparticles. Improving the conventional Caco-2 model by adding the endothelium layer could change the absorption pattern of LNCs but not drugs in solution. This suggests the necessity of the

new coculture model for studying the absorption of LNCs or other nanocarrier systems. However, for studying the absorption of drug in solutions, the Caco-2 model should be adequate. By using the coculture model, the absorption of DSPE-mPEG (2000) LNCs (55- nm and 85-nm) and stearylamine LNCs (85-nm) was found to be surprisingly higher, despite the coculture model's higher TEER. Furthermore, the new model also revealed the increase in the absorption of 55-nm LNCs when surfaced-modified by DSPE-mPEG (2000). All these distinct absorption patterns between the two models imply the differences in the LNCs transport mechanism and are the proof of concept for the effect and the importance of the intestinal endothelium on the transportation of nanoparticles across gut barriers. The use of the new coculture model combined with the FRET technique could provide a better understanding of the fate of intact LNCs across the intestinal barriers. For future experiments, the details on the transport mechanism of LNCs in the coculture model should be elucidated. The *in vivo*–*in vitro* correlation (IVIVC) of intact LNCs should be further investigated. Besides, the new model should also be used to study the absorption of other types of nanocarriers.

**Supplementary Materials:** The following are available online at <https://www.mdpi.com/article/10.3390/pharmaceutics13050595/s1>, Figure S1: Average apparent permeability ( $P_{app}$ ) of five drugs ( $n = 4$ ) classified by four BCS classes across HMEC-1 monolayer (green) and blank Transwell® filter (gray). MET = metoprolol, PRO = propranolol, NAP = naproxen, ATN = atenolol, FUR = furosemide; BCS class numbers are signified in the parentheses. The (+) symbol represents the arithmetic mean, and the whiskers represent a 95% confidence interval (Kruskal-Wallis). Figure S2: Example of the particle size distribution histogram of the formulations (A–F): F1, F1-DSPE-PEG, F1-SA, F2, F2-DSPE-PEG, and F2-SA, respectively.

**Author Contributions:** Methodology, N.K., E.R., S.L., and C.A.; validation, N.K., E.R., and S.L.; formal analysis, N.K.; investigation, N.K., J.B., N.L., F.M., R.P., C.A., and M.B.; resources, J.B. and N.L.; data curation, N.K.; writing—original draft preparation, N.K.; writing—review and editing, N.K., E.R. and S.L.; visualization, N.K., F.M., and R.P.; supervision, E.R. and S.L.; project administration, E.R. and S.L.; funding acquisition, E.R. and S.L. All authors have read and agreed to the published version of the manuscript.

**Funding:** This work was supported by the Ligue Contre le Cancer, Maine-et-Loire and Charente-Maritime Committees (JPB/FP—223/12.2020), France; and the University of Angers, France.

**Institutional Review Board Statement:** Not applicable.

**Informed Consent Statement:** Not applicable.

**Data Availability Statement:** All data generated or analyzed during this study are included in this published article and its Supplementary information files.

**Conflicts of Interest:** The authors declare no conflict of interest. The funders had no role in the design of the study; in the collection, analyses, or interpretation of data; in the writing of the manuscript, or in the decision to publish the results.

## Appendix A. Sample Preparation for Drug Assay by HPLC-UV

### Appendix A.1. Sample Preparation for Metoprolol and Propranolol

The internal standard was prepared as a solution of 20 mg/L protriptyline (in methanol) for propranolol and 20 mg/L methyl milnacipran (in methanol) for metoprolol. Then, 25  $\mu$ L of the internal standard and 100  $\mu$ L of 4 M NaOH were added to 500  $\mu$ L of the sample. Afterward, liquid-liquid extraction using 4 mL of hexane/isoamyl alcohol (80/20, *v/v*) was performed, and 100  $\mu$ L of 0.02 M HCl was added to the organic phase after mixing. The mixture was centrifuged, and the supernatant was eliminated. 10  $\mu$ L of the preparation was injected into the chromatographic system.



#### Appendix A.2. Sample Preparation for Naproxen

The internal standard was prepared as a solution of 50 mg/L tolbutamide (in acetonitrile). Then, 200  $\mu$ L of the internal standard was added to 50  $\mu$ L of the sample. The preparation was then centrifuged, and 10  $\mu$ L of the supernatant was injected into the chromatographic system.

#### Appendix A.3. Sample Preparation for Atenolol

The internal standard was prepared as a solution of 20 mg/L prazepam (in methanol). Then, 25  $\mu$ L of the internal standard was added to 500  $\mu$ L of the sample. Afterward, liquid-liquid extraction using 5 mL of dichloromethane and 30  $\mu$ L of 1 M NaOH was performed. After mixing, the mixture was centrifuged, and the supernatant (organic phase) was collected and evaporated to dryness at 50 °C under nitrogen gas. The residue was dissolved in 50  $\mu$ L of methanol and 20  $\mu$ L of water. 10  $\mu$ L of the preparation was injected into the chromatographic system.

#### Appendix A.4. Sample Preparation for Furosemide

The internal standard was prepared as a solution of 50 mg/L tolbutamide (in acetonitrile). Then, 25  $\mu$ L of the internal standard and 200  $\mu$ L of ammonium acetate buffer pH 4.0 were added to 200  $\mu$ L of the sample. Afterward, liquid-liquid extraction using 1.5 mL of dichloromethane was performed. After mixing, the mixture was centrifuged, and the supernatant (organic phase) was collected and evaporated to dryness at 50 °C under a nitrogen stream. The residue was dissolved in 50  $\mu$ L of methanol and 20  $\mu$ L of water. 10  $\mu$ L of the preparation was injected into the chromatographic system.

## References

- König, J.; Wells, J.; Cani, P.D.; García-Ródenas, C.L.; MacDonald, T.; Mercenier, A.; Whyte, J.; Troost, F.; Brummer, R.J. Human Intestinal Barrier Function in Health and Disease. *Clin. Trans. Gastroenterol.* **2016**, *7*. [[CrossRef](#)] [[PubMed](#)]
- Groschwitz, K.R.; Hogan, S.P. Intestinal Barrier Function: Molecular Regulation and Disease Pathogenesis. *J. Allergy Clin. Immunol.* **2009**, *124*, 3–20. [[CrossRef](#)]
- Bischoff, S.C.; Barbara, G.; Buurman, W.; Ockhuizen, T.; Schulzke, J.D.; Serino, M.; Tilg, H.; Watson, A.; Wells, J.M. Intestinal Permeability—A New Target for Disease Prevention and Therapy. *BMC Gastroenterol.* **2014**, *14*, 1–25. [[CrossRef](#)] [[PubMed](#)]
- Heurtault, B.; Saulnier, P.; Pech, B.; Proust, J.E.; Benoit, J.P. A Novel Phase Inversion-Based Process for the Preparation of Lipid Nanocarriers. *Pharm. Res.* **2002**, *19*, 875–880. [[CrossRef](#)]
- Heurtault, B.; Saulnier, P.; Pech, B.; Venier-Julienne, M.C.; Proust, J.E.; Phan-Tan-Luu, R.; Benoit, J.P. The Influence of Lipid Nanocapsule Composition on Their Size Distribution. *Eur. J. Pharm. Sci.* **2003**, *18*, 55–61. [[CrossRef](#)]
- Lainé, A.L.; Gravier, J.; Henry, M.; Sancey, L.; Béjaud, J.; Pancani, E.; Wiber, M.; Texier, I.; Coll, J.L.; Benoit, J.P.; et al. Conventional versus Stealth Lipid Nanoparticles: Formulation and in Vivo Fate Prediction through FRET Monitoring. *J. Control. Release* **2014**, *188*, 1–8. [[CrossRef](#)]
- Ramadan, A.; Lagarce, F.; Pierre, L.; Tessier-Martreau, A.; Thomas, O.; Macchi, L.; Saulnier, P.; Benoit, J.-P. Oral Fondaparinux: Use of Lipid Nanocapsules as Nanocarriers and in Vivo Pharmacokinetic Study. *Int. J. Nanomed.* **2011**, *6*, 2941–2951. [[CrossRef](#)]
- Messaoudi, K.; Saulnier, P.; Boesen, K.; Benoit, J.; Lagarce, F. Anti-Epidermal Growth Factor Receptor siRNA Carried by Chitosan-Transacylated Lipid Nanocapsules Increases Sensitivity of Glioblastoma Cells to Temozolomide. *Int. J. Nanomed.* **2014**, *9*, 1479–1490.
- Eissa, M.M.; El-Moslemany, R.M.; Ramadan, A.A.; Amer, E.I.; El-Azzouni, M.Z.; El-Khordagui, L.K. Miltefosine Lipid Nanocapsules for Single Dose Oral Treatment of Schistosomiasis Mansoni: A Preclinical Study. *PLoS ONE* **2015**, *10*, e0141788. [[CrossRef](#)]
- Roger, E.; Lagarce, F.; Garcion, E.; Benoit, J.P. Lipid Nanocarriers Improve Paclitaxel Transport throughout Human Intestinal Epithelial Cells by Using Vesicle-Mediated Transcytosis. *J. Control. Release* **2009**, *140*, 174–181. [[CrossRef](#)]
- Peltier, S.; Oger, J.; Couet, W.; Benoit, J. Enhanced Oral Paclitaxel Bioavailability After Administration of Paclitaxel-Loaded Lipid Nanocapsules. *Pharm. Res.* **2006**, *23*, 1243–1250. [[CrossRef](#)]
- Pensel, P.E.; Ullio, G.; Fabbri, J.; Ceballos, L.; Sanchez, S.; Alvarez, L.I.; Allemandi, D.; Pierre, J.; Palma, S.D.; Elissondo, M.C. Acta Tropica Cystic Echinococcosis Therapy: Albendazole-Loaded Lipid Nanocapsules Enhance the Oral Bioavailability and Efficacy in Experimentally Infected Mice. *Acta Trop.* **2015**, *152*, 185–194. [[CrossRef](#)] [[PubMed](#)]
- Amara, R.O.; Ramadan, A.A.; El-Moslemany, R.M.; Eissa, M.M.; El-Azzouni, M.Z.; El-Khordagui, L.K. Praziquantel—Lipid Nanocapsules: An Oral Nanotherapeutic with Potential Schistosoma Mansoni Tegumental Targeting. *Int. J. Nanomed.* **2018**, *13*, 4493–4505. [[CrossRef](#)]

14. Abozaid, D.; Ramadan, A.; Barakat, H.; Khalafallah, N. Acyclovir Lipid Nanocapsules Gel for Oromucosal Delivery: A Preclinical Evidence of Efficacy in the Chicken Pouch Membrane Model. *Eur. J. Pharm. Sci.* **2018**, *121*, 228–235. [CrossRef] [PubMed]
15. Briot, T.; Roger, E.; Verger, A.; Clavreul, A.; Lagarce, F. Development and in Vitro Evaluations of New Decitabine Nanocarriers for the Treatment of Acute Myeloid Leukemia. *Int. J. Nanomed.* **2017**, *12*, 8427–8442. [CrossRef]
16. Varshosaz, J.; Taymouri, S.; Jahanian-najafabadi, A.; Alizadeh, A. Efavirenz Oral Delivery via Lipid Nanocapsules: Formulation, Optimisation, and Ex-Vivo Gut Permeation Study. *IET Nanobiotechnol.* **2018**, *12*, 795–806. [CrossRef] [PubMed]
17. Roger, E.; Lagarce, F.; Benoit, J. Development and Characterization of a Novel Lipid Nanocapsule Formulation of Sn38 for Oral Administration. *Eur. J. Pharm. Biopharm.* **2011**, *79*, 181–188. [CrossRef]
18. Sahoo, H. Förster resonance energy transfer—A spectroscopic nanoruler: Principle and applications. *J. Photochem. Photobiol. C Photochem. Rev.* **2011**, *12*, 20–30. [CrossRef]
19. Wallace, B.; Atzberger, P.J. Förster resonance energy transfer: Role of diffusion of fluorophore orientation and separation in observed shifts of FRET efficiency. *PLoS ONE* **2017**, *12*, e0177122. [CrossRef]
20. Lagarce, F.; Groo, A.-C.; Saulnier, P.; Gimel, J.-C.; Gravier, J.; Ailhaas, C.; Benoit, J.-P. Fate of paclitaxel lipid nanocapsules in intestinal mucus in view of their oral delivery. *Int. J. Nanomed.* **2013**, *8*, 4291–4302. [CrossRef]
21. Roger, E.; Gimel, J.-C.; Bensley, C.; Klymchenko, A.S.; Benoit, J.-P. Lipid nanocapsules maintain full integrity after crossing a human intestinal epithelium model. *J. Control. Release* **2017**, *253*, 11–18. [CrossRef]
22. Billat, P.-A.; Roger, E.; Faure, S.; Lagarce, F. Models for drug absorption from the small intestine: Where are we and where are we going? *Drug Discov. Today* **2017**, *22*, 761–775. [CrossRef] [PubMed]
23. Hidalgo, I.J.; Raub, T.J.; Borchardt, R.T. Characterization of the Human Colon Carcinoma Cell Line (Caco-2) as a Model System for Intestinal Epithelial Permeability. *Gastroenterology* **1989**, *96*, 736–749. [CrossRef]
24. Han, C.; Wang, B. *Factors That Impact the Developability of Drug Candidates*; Wiley: Hoboken, NJ, USA, 2016; ISBN 9781118833322.
25. Van Breemen, R.B.; Li, Y. Caco-2 cell permeability assays to measure drug absorption. *Expert Opin. Drug Metab. Toxicol.* **2005**, *1*, 175–185. [CrossRef]
26. Rinaki, E.; Valsami, G.; Macheras, P. Classification System: The Central Role of Dose/Solubility Ratio. *Pharm. Res.* **2003**, *20*, 1917–1925. [CrossRef]
27. The International Council for Harmonisation of Technical Requirements for Pharmaceuticals for Human Use ICH Harmonised Guideline. Biopharmaceutics Classification System-Based Biowaivers. M9. Available online: [https://database.ich.org/sites/default/files/M9\\_Guideline\\_Step4\\_2019\\_1116.pdf](https://database.ich.org/sites/default/files/M9_Guideline_Step4_2019_1116.pdf) (accessed on 16 April 2021).
28. Amidon, G.L.; Lennernäs, H.; Shah, V.P.; Crison, J.R. A Theoretical Basis for a Biopharmaceutic Drug Classification: The Correlation of in Vitro Drug Product Dissolution and in Vivo Bioavailability. *Pharm. Res. Off. J. Am. Assoc. Pharm. Sci.* **1995**, *12*, 413–420.
29. Costa, J.; Ahluwalia, A. Advances and Current Challenges in Intestinal in Vitro Model Engineering: A Digest. *Front. Bioeng. Biotechnol.* **2019**, *7*, 1–14. [CrossRef]
30. Belouqui, A.; Brayden, D.J.; Artursson, P.; Prétat, V.; Des Rieux, A. A Human Intestinal M-Cell-like Model for Investigating Particle, Antigen and Microorganism Translocation. *Nat. Protoc.* **2017**, *12*, 1387–1399. [CrossRef]
31. Spadoni, I.; Zagato, E.; Bertocchi, A.; Paolinelli, R.; Hot, E.; Di Sabatino, A.; Caprioli, F.; Bottiglieri, L.; Oldani, A.; Viale, G.; et al. A Gut-Vascular Barrier Controls the Systemic Dissemination of Bacteria. *Science* **2015**, *350*, 830–835. [CrossRef] [PubMed]
32. Sorribas, M.; de Gottardi, A.; Moghadamrad, S.; Hassan, M.; Spadoni, I.; Rescigno, M.; Wiest, R. Isoproterenol Disrupts Intestinal Barriers Activating Gut-Liver-Axis: Effects on Intestinal Mucus and Vascular Barrier as Entry Sites. *Digestion* **2020**, *101*, 717–729. [CrossRef] [PubMed]
33. Ungaro, F.; Tacconi, C.; D’Alessio, S. Beyond Intestinal Barrier: The Blood Endothelium as a Second Wall of Defense Against Bacterial Invasion. *Gastroenterology* **2016**, *150*, 1678–1680. [CrossRef]
34. Deshmukh, R.; Bandyopadhyay, N.; Abed, S.N.; Bandopadhyay, S.; Pal, Y.; Deb, P.K. *Strategies for Pulmonary Delivery of Drugs*; Elsevier: Amsterdam, The Netherlands, 2019; ISBN 9780128145081.
35. Kasper, J.Y.; Hermanns, M.I.; Cavellius, C.; Kraegeloh, A.; Jung, T.; Danzebrink, R.; Unger, R.E.; Kirkpatrick, C.J. The Role of the Intestinal Microvasculature in Inflammatory Bowel Disease: Studies with a Modified Caco-2 Model Including Endothelial Cells Resembling the Intestinal Barrier in Vitro. *Int. J. Nanomed.* **2016**, *11*, 6353–6364. [CrossRef]
36. Hubatsch, I.; Ragnarsson, E.G.E.; Artursson, P. Determination of Drug Permeability and Prediction of Drug Absorption in Caco-2 Monolayers. *Nat. Protoc.* **2007**, *2*, 2111–2119. [CrossRef]
37. Kilin, V.N.; Anton, H.; Anton, N.; Steed, E.; Vermot, J.; Vandamme, T.F.; Mely, Y.; Klymchenko, A.S. Counterion-Enhanced Cyanine Dye Loading into Lipid Nano-Droplets for Single-Particle Tracking in Zebrafish. *Biomaterials* **2014**, *35*, 4950–4957. [CrossRef]
38. Young, B.; O’Dowd, G.; Woodford, P. Membrane Specialisations of Epithelia. In *Wheater’s Functional Histology: A Text and Colour Atlas*; Churchill Livingstone: London, UK, 2013; pp. 88–91. ISBN 9780702047473.
39. Briske-Anderson, M.J.; Finley, J.W.; Newman, S.M. The Influence of Culture Time and Passage Number on the Morphological and Physiological Development of Caco-2 Cells. *Proc. Soc. Exp. Biol. Med.* **1997**, *214*, 248–257. [CrossRef] [PubMed]
40. Ma, T.Y.; Hollander, D.; Tran, L.T.; Nguyen, D.; Hoa, N.; Bhalla, D. Cytoskeletal Regulation of Caco-2 Intestinal Monolayer Paracellular Permeability. *J. Cell. Physiol.* **1995**, *164*, 533–545. [CrossRef] [PubMed]
41. Young, B.; O’Dowd, G.; Woodford, P. The microcirculation. In *Wheater’s Functional Histology: A Text and Colour Atlas*; Churchill Livingstone: London, UK, 2013; pp. 150–153. ISBN 9780702047473.

42. Ruffer, C.; Strey, A.; Janning, A.; Kim, K.S.; Gerke, V. Cell–Cell Junctions of Dermal Microvascular Endothelial Cells Contain Tight and Adherens Junction Proteins in Spatial Proximity. *Biochemistry* **2004**, *43*, 5360–5369. [[CrossRef](#)] [[PubMed](#)]
43. Hilgendorf, C.; Spahn-Langguth, H.; Regårdh, C.G.; Lipka, E.; Amidon, G.L.; Langguth, P. Caco-2 versus Caco-2/HT29-MTX Co-Cultured Cell Lines: Permeabilities via Diffusion, inside- and Outside-Directed Carrier-Mediated Transport. *J. Pharm. Sci.* **2000**, *89*, 63–75. [[CrossRef](#)]
44. Artursson, P.; Karlsson, J. Correlation between Oral Drug Absorption in Humans and Apparent Drug Permeability Coefficients in Human Intestinal Epithelial (Caco-2) Cells. *Biochem. Biophys. Res. Commun.* **1991**, *175*, 880–885. [[CrossRef](#)]
45. Aungst, B.J.; Nguyen, N.H.; Bulgarelli, J.P.; Oates-lenz, K. The Influence of Donor and Reservoir Additives on Caco-2 Permeability and Secretory Transport of HIV Protease Inhibitors and Other Lipophilic Compounds. *Pharm. Res.* **2000**, *17*, 1–5. [[CrossRef](#)]
46. Jung, S.J.; Choi, S.O.; Um, S.Y.; Kim, J.I.; Choo, H.Y.P.; Choi, S.Y.; Chung, S.Y.; Youn, S. Prediction of the Permeability of Drugs through Study on Quantitative Structure—Permeability Relationship. *J. Pharm. Biomed. Anal.* **2006**, *41*, 469–475. [[CrossRef](#)] [[PubMed](#)]
47. Artursson, P.; Magnusson, C. Epithelial Transport of Drugs in Cell Culture. II: Effect of Extracellular Calcium Concentration on the Paracellular Transport of Drugs of Different Lipophilicities across Monolayers of Intestinal Epithelial (Caco-2) Cells. *J. Pharm. Sci.* **1990**, *79*, 595–600. [[CrossRef](#)] [[PubMed](#)]
48. Artursson, P. Epithelial Transport of Drugs in Cell Culture. I: A Model for Studying the Passive Diffusion of Drugs over Intestinal. *J. Pharm. Sci.* **1990**, *79*, 476–482. [[CrossRef](#)] [[PubMed](#)]
49. Volpe, D.A.; Faustino, P.J.; Ciavarella, A.B.; Asafu-Adjaye, E.B.; Ellison, C.D.; Yu, L.X.; Hussain, A.S. Classification of Drug Permeability with a Caco-2 Cell Monolayer Assay. *Clin. Res. Regul. Aff.* **2007**, *24*, 39–47. [[CrossRef](#)]
50. Roger, E.; Lagarce, F.; Garcion, E.; Benoit, J.P. Biopharmaceutical Parameters to Consider in Order to Alter the Fate of Nanocarriers after Oral Delivery. *Nanomedicine* **2010**, *5*, 287–306. [[CrossRef](#)]
51. Groo, A.C.; Bossiere, M.; Trichard, L.; Legras, P.; Benoit, J.P.; Lagarce, F. In Vivo Evaluation of Paclitaxel-Loaded Lipid Nanocapsules after Intravenous and Oral Administration on Resistant Tumor. *Nanomedicine* **2015**, *10*, 589–601. [[CrossRef](#)]
52. Mccann, J.J.; Choi, U.B.; Zheng, L.; Weninger, K.; Bowen, M.E. Optimizing Methods to Recover Absolute FRET Efficiency from Immobilized Single Molecules. *Biophys. J.* **2010**, *99*, 961–970. [[CrossRef](#)]
53. Nir, E.; Michalet, X.; Hamadani, K.M.; Laurence, T.A.; Neuhauser, D. Shot-Noise Limited Single-Molecule FRET Histograms: Comparison between Theory and Experiments. *J. Phys. Chem.* **2006**, *110*, 22103–22124. [[CrossRef](#)]
54. Bannunah, A.M.; Vllasaliu, D.; Lord, J.; Stolnik, S. Mechanisms of Nanoparticle Internalization and Transport Across an Intestinal Epithelial Cell Model: Effect of Size and Surface Charge. *Mol. Pharm.* **2014**, *11*, 4363–4373. [[CrossRef](#)]
55. Hua, S.; Marks, E.; Schneider, J.J.; Keely, S. Advances in Oral Nano-Delivery Systems for Colon Targeted Drug Delivery in Inflammatory Bowel Disease: Selective Targeting to Diseased versus Healthy Tissue. *Nanomed. Nanotechnol. Biol. Med.* **2015**, *11*, 1117–1132. [[CrossRef](#)]
56. Furst, T.; Dakwar, G.R.; Zagato, E.; Lechanteur, A.; Remaut, K.; Evrard, B.; Braeckmans, K.; Piel, G. Freeze-Dried Mucoadhesive Polymeric System Containing Pegylated Lipoplexes: Towards a Vaginal Sustained Released System for siRNA. *J. Control. Rel.* **2016**, *236*, 68–78. [[CrossRef](#)] [[PubMed](#)]
57. Paillard, A.; Hindré, F.; Vignes-colombeix, C.; Benoit, J.; Garcion, E. The Importance of Endo-Lysosomal Escape with Lipid Nanocapsules for Drug Subcellular Bioavailability. *Biomaterials* **2010**, *31*, 7542–7554. [[CrossRef](#)] [[PubMed](#)]
58. Garcion, E.; Lamprecht, A.; Paillard, A.; Aubert-Pouessel, A.; Menei, P.; Benoit, J. A New Generation of Anticancer, Drug-Loaded, Colloidal Vectors Reverses Multidrug Resistance in Glioma and Reduces Tumor Progression in Rats. *Mol. Cancer Ther.* **2006**, *5*, 1710–1723. [[CrossRef](#)] [[PubMed](#)]
59. Hamelers, I.H.L.; Staffhorst, R.W.H.M.; Voortman, J.; De Kruijff, B.; Reedijk, J.; Van Bergen, P.M.P.; Kroon, A.I.P.M. De Cancer Therapy: Preclinical High Cytotoxicity of Cisplatin Nanocapsules in Ovarian Carcinoma Cells Depends on Uptake by Caveolae-Mediated Endocytosis. *Clin. Cancer Res.* **2009**, *15*, 1259–1269. [[CrossRef](#)] [[PubMed](#)]

## Supplementary data

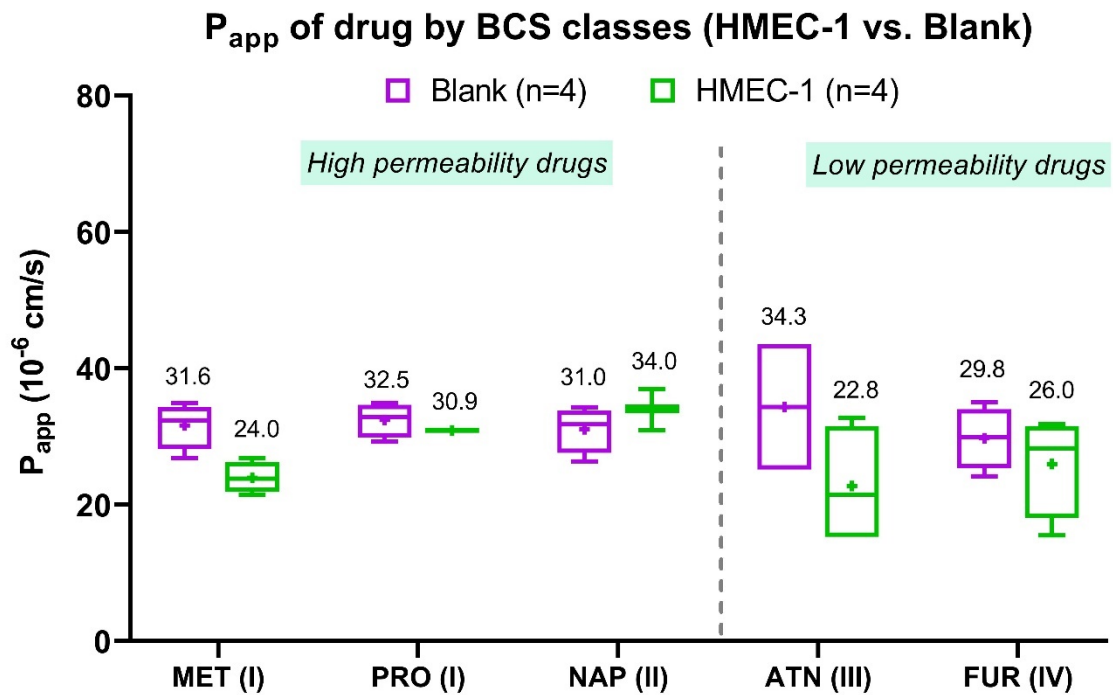


**Figure S1.** Average apparent permeability ( $P_{app}$ ) of five drugs ( $n = 4$ ) classified by four BCS classes across HMEC-1 monolayer (green) and blank Transwell® filter (gray). MET = metoprolol, PRO = propranolol, NAP = naproxen, ATN = atenolol, FUR = furosemide; BCS class numbers are signified in the parentheses. The (+) symbol represents the arithmetic mean, and the whiskers represent a 95% confidence interval (Kruskal-Wallis).

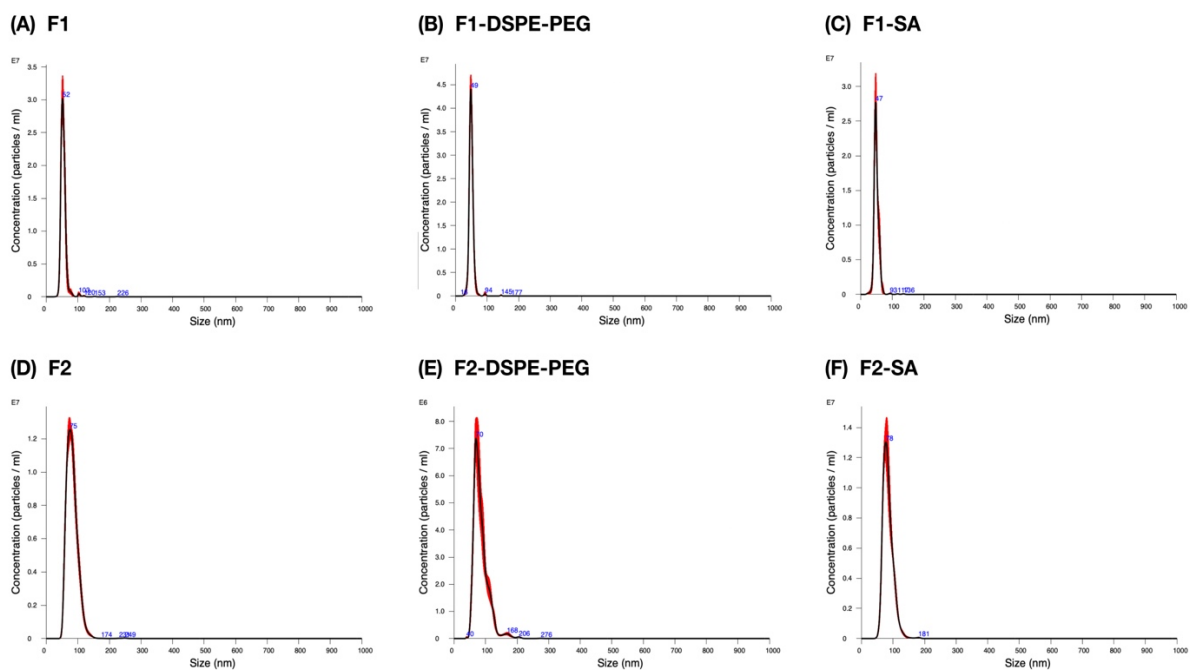


**Figure S2.** Example of the particle size distribution histogram of the formulations (A-F): F1, F1-DSPE-PEG, F1-SA, F2, F2-DSPE-PEG, and F2-SA, respectively.

## Chapter 2: Quantitative FRET for determining intact LNCs in blood

In order to evaluate the oral bioavailability information of intact LNCs, the method to quantify the plasma particle concentration of intact LNCs is required. FRET was chosen because it is the method that can directly monitor the particle integrity. The method has been already adapted to use for *in vivo* nanoparticle tracking of intact LNCs [128,130–132], which could be considered as the proof of concept for the practicality of this technique on LNCs [129]. However, there exists only the qualitative imagery FRET and semi-quantitative FRET techniques for *in vivo* nanoparticle tracking, which is inadequate to obtain plasma particle concentration information. Thus, the new quantitative FRET for blood sample was developed to solve this problem. The new method gives the quantitative information of intact FRET-LNCs in the systemic circulation that can be used for advanced pharmacokinetics analysis i.e., non-compartmental analysis, and population-based pharmacokinetics, as a proof of concept and practicality of the quantitative method.

In this chapter, the new quantitative FRET technique was developed for quantifying particle concentration in biological media such as blood. The article demonstrates that the new FRET technique can be successfully employed to quantify plasma particle concentration and AUC of six LNCs formulations i.e., classical LNCs, anionic DSPE-mPEG-2000-LNCs, and cationic stearylamine-LNCs with the size of 50 nm and 85 nm. The information obtained from this new FRET technique was used after intravenous administration to determine the non-compartmental and population pharmacokinetics of intact LNCs.

The article has been published in the *Journal of Controlled Release* in 2022, entitled “Pharmacokinetics of intact lipid nanocapsules using new quantitative FRET technique”.



Contents lists available at ScienceDirect

Journal of Controlled Release

journal homepage: [www.elsevier.com/locate/jconrel](http://www.elsevier.com/locate/jconrel)

## Pharmacokinetics of intact lipid nanocapsules using new quantitative FRET technique

Vincent Lebreton<sup>a,b,1</sup>, Norraseth Kaeokhamloed<sup>a,1</sup>, Anastasiia Vasylaki<sup>a</sup>, Grégory Hilairat<sup>c</sup>, Adélie Mellinger<sup>a</sup>, Jérôme Béjaud<sup>a</sup>, Patrick Saulnier<sup>a,b</sup>, Frédéric Lagarce<sup>a,b</sup>, Florence Gattacceca<sup>d</sup>, Samuel Legeay<sup>a</sup>, Emilie Roger<sup>a,\*</sup>

<sup>a</sup> MINT, INSERM U1066, CNRS 6021, UNIV Angers, SFR-ICAT 4208, Angers, France

<sup>b</sup> CHU Angers, 49033 Angers, France

<sup>c</sup> UNIV Angers, SFR ICAT4208, Angers, France

<sup>d</sup> Computational Pharmacology and Clinical Oncology (COMPO) Unit, Inria Sophia Antipolis-Méditerranée, Cancer Research Center of Marseille, Inserm UMR1068, CNRS UMR7258, Aix Marseille University UM105, 13385 Marseille, France

### ARTICLE INFO

#### Keywords:

FRET  
Lipid nanocapsules  
Pharmacokinetics  
Population pharmacokinetics  
Drug delivery

### ABSTRACT

The present study investigated the pharmacokinetics of intact lipid nanocapsules (LNCs) after intravenous administration in rats. Six different Förster resonance energy transfer LNCs (FRET-LNCs) have been studied with 2 sizes (50 and 85 nm) and 3 coating types (none, DSPE-mPEG 2000 or stearylamine). A FRET-LNCs blood extraction method was developed to retain an accurate FRET signal. Intact FRET-LNCs were specifically quantified through combination of FRET signal and Nano Tracker Analysis. Pharmacokinetic data were first described by non-compartmental analysis, then used to develop a population pharmacokinetic model.

The pharmacokinetic elimination of FRET-LNCs was non-linear and dependent on size and surface modification, while the distribution was dependent on size. The LNCs 85 nm volume of distribution was lower than LNCs 50 nm. As expected, LNCs 85 nm with PEG coating displayed a lower clearance than other formulations. Surprisingly, this study highlighted a faster elimination of LNCs 50 nm with PEG compared to other formulations which could be explained by instability in blood. This first pharmacokinetic model of intact LNCs allowed a thorough understanding of the influence of size and coating on pharmacokinetic properties and paves the way for future mechanistic modeling approaches to predict the fate of LNCs *in vivo*.

### 1. Introduction

Drug encapsulation into nanocarriers is currently one of the most promising technologies to improve drug delivery. Lipid nanocapsules (LNCs) are organic nanocarriers, consisting of a triglyceride core and surfactant shell, and have already been well characterized [1–3]. It is firstly developed by our group [1,4], allows the delivery of several drugs *via* intravenous (IV) or oral administration routes (paclitaxel [2,5], fondaparinux [6], albendazole [7], praziquantel [8], etc.). However, the limited understanding of the pharmacokinetics (PKs) of this nanocarrier itself is a major issue that can lead to poor translation to the clinical level's application. The limited knowledge about PK of organic

nanocarrier itself is probably one reason, notably due to the lack of technique to specifically quantify the intact organic nanoparticles concentration in the blood. Most of PK organic nanoparticles studies were performed on drugs without evaluating integrity of the nanocarrier. For example, Singh et al., Carreño et al., and Menzel et al. describe the pharmacokinetics of drug encapsulated into NPs (exemestane, quetiapine and exenatide, respectively) which is relevant for total drug but not for encapsulated drug [9–11]. In some other works, the radiolabeling technique was utilized to evaluate the PK parameters of NPs. Unfortunately, with this method, which follows the radioelement, the signal indistinctly quantifies intact and degraded LNCs, not taking into account their structural integrity which might have been compromised after

**Abbreviations:** FRET, Förster resonance energy transfer; LNCs, Lipid nanocapsules; PKs, pharmacokinetics; NTA, Nanoparticle Tracking Analysis system; IV, intravenous; PR, proximity ratio; PEG, polyethylene glycol.

\* Corresponding author.

E-mail address: [emilie.roger@univ-angers.fr](mailto:emilie.roger@univ-angers.fr) (E. Roger).

<sup>1</sup> Both authors contributed equally.

<https://doi.org/10.1016/j.jconrel.2022.09.057>

Received 17 June 2022; Received in revised form 7 September 2022; Accepted 27 September 2022

Available online 7 October 2022

0168-3659/© 2022 Elsevier B.V. All rights reserved.

interaction with biological media [12]. In this context, Förster resonance energy transfer (FRET) method presents a great potential to describe the *in vivo* fate of LNCs [13].

FRET is the interaction between one fluorescent dye (called FRET donor) which transfers its energy to the second dye (FRET acceptor) by the energy resonance (distance inferior at 10 nm). The FRET donor and acceptor dyes can be coloaded in the nanocarriers, and the short-distance FRET phenomenon will occur only if the nanocarrier is intact [13]. Roger et al. have previously developed a combination of FRET method with the Nanoparticle Tracking Analysis system (NTA) to measure particle concentration, which allows to quantify the concentration of intact LNCs. This technique combination was used *in vitro* to measure intact LNCs particle concentration after intestinal epithelium barrier crossing [4,14]. Therefore, this method seems well suited for quantifying the intact LNCs particles in biological media. Nevertheless, to use this technique, another challenge of quantifying intact LNCs in biological fluids and tissues is to develop an extraction method from the blood that conserves particles integrity [13,15].

Moreover, it has been known that the PEGylation can provide a stealth effect to increase the circulation time of nanoparticles because of lower opsonization phenomenon and so, lower elimination after macrophage uptake [16–18]. In contrast, PEGylation can increase elimination of nanoparticles after PEG antibodies synthesis as a result of the first injection, it is called accelerated blood clearance (ABC) phenomenon and this phenomenon has never been studied for LNCs [16–18]. Because this topic seems interesting and widely studied, and the only way to study this phenomenon is the repeated injection.

The aim of this study was to investigate the PK analysis of intact LNCs after IV administration in rats and reinjection after 7 days using the FRET method of quantitation. In this context, different FRET-LNCs formulations, already developed in our lab, have been studied. Firstly, an extraction method in blood by ultracentrifugation has been developed to achieve an efficient FRET signal. PK data were first described using non-compartmental analysis (NCA). A population compartmental (PopPK) model was then developed to provide a deeper understanding of PK properties of LNCs and their variability depending on size and coating. Finally, particles stability was assessed in rat blood to explain some *in vivo* results.

## 2. Materials and methods

### 2.1. Materials

DiI (1,10-dioctadecyl-3,3,30,30-tetramethyl-indocarbocyanine perchlorate), DiD (1,1'-dioctadecyl-3,3,3',3'-tetramethylindocarbocyanine perchlorate), and Histopaque®-1083 were purchased from ThermoFisher (Villebon-sur-Yvette, France). Ultrapure water was obtained from a Milli-Q® Advantage A10 System (Merck Millipore, Darmstadt, Germany). Captex® 8000 (glyceryl tricaprilate) was kindly provided by Abitec Corporation (Columbus, OH, USA). Lipoid® S75-3 (phosphatidylcholine and phosphatidylethanolamine mixture) were purchased from Lipoid GmbH (Steinhausen, Switzerland). Kolliphor® HS-15 (PEG 660 and polyethylene glycol 660 hydroxystearate mixture) was purchased from BASF (Ludwigshafen, Germany). DSPE-mPEG-2000 (1,2-distearoyl-sn-glycero-3-phosphoethanolamine-N-[methoxy(polyethylene glycol)-2000] (ammonium salt)) was purchased Avanti Polar Lipids (Alabaster, AL, USA). Phosphate-buffered saline (PBS) was purchased from PAA Laboratories (Toronto, ON, Canada). Polycarbonate centrifuge tube size 7 × 20 mm (reference 343,775) was purchased from Beckman Coulter (Villepinte, France). Heparin sodium 5000 UI/mL was purchased from Panpharma (Luitré, France).

### 2.2. Formulation of LNCs coloaded with DiI- and DiD-TPB (FRET-LNCs)

DiI- and DiD-tetraphenylborate (TPB) were synthesized using the method described previously [14,19]. Six formulations of LNCs

coloaded with DiI-TPB and DiD-TPB (called FRET-LNCs) with different sizes: 50 nm (LNC-50) and 85 nm (LNC-85), surface modifications: DSPE-mPEG-2000 (PEG) (LNC-50-PEG; LNC-85-PEG) and stearylamine (SA) (LNC-50-SA; LNC-85-SA) were prepared using the phase inversion method (composition shown Table 1) [4].

### 2.3. FRET-LNCs characterization

The mean size (nm), particle concentration (particle/mL), and particle size distribution were measured with the NTA technique using a NanoSight NS300 (Malvern Instrument, Worcestershire, UK) with a low volume flow cell and a 450 nm laser. FRET-LNCs suspensions were diluted in ultrapure water by the factor from  $5 \times 10^5$  to  $1 \times 10^6$  and then slowly injected into the sample chamber using a 1 mL syringe pump with the rate of 3–4 µL per second. The video sequences of the nanoparticles were captured over 60 s (5 replicates) and then analyzed by NTA analytical software version 3.2.

NTA provides the particle distribution width parameters, which are calculated following the equation:  $\text{Span} = (D90 - D10)/D50$  where D10, D50, and D90 represent the diameter (nm) at the 10th, 50th (median), and 90th percentiles of the distribution histogram, respectively.

The zeta potential of the FRET-LNCs was determined by laser doppler electrophoresis using Zetasizer® Nano series DTS 1060 (Malvern Instruments SA, Worcestershire, the UK) diluted by factor  $1 \times 10^2$ .

The fluorescence emission spectra of FRET-LNCs were recorded on a FluoroMax® 4 spectrophotometer (Horiba Jobin Yvon Inc., Piscataway, NJ, USA) at room temperature with the 548 nm excitation and 0.5 s integration time. FRET-LNCs suspension was diluted by factor  $3 \times 10^3$ . The emission spectra were collected from 530 to 720 nm, with an increment of 1 nm. They were corrected for the lamp source fluctuations and the wavelength-dependent response of the detector. The maximum intensity of the FRET donor and acceptor were recorded at  $569 \pm 5$  nm and  $675 \pm 5$  nm, respectively.

The integrity of nanoparticles was determined by the FRET proximity ratio (PR) calculated by the following equation:  $PR = A/(A + D)$ , where A and D are the maximum fluorescence intensity of the aforementioned FRET acceptor and donor signals, respectively.

### 2.4. Animal studies

Male Sprague-Dawley rats ( $n = 28$ ) aged  $11 \pm 2$  weeks and weighing  $480 \pm 73$  g were purchased from Janvier Labs (Le Genest-Saint-Isle, France). All rats received a standard laboratory diet and water *ad*

**Table 1**  
Compositions of different FRET-LNCs formulations.

Compositions	Quantity (% w/w)					
	LNC-50	LNC-50-PEG	LNC-50-SA	LNC-85	LNC-85-PEG	LNC-85-SA
Captex® 8000 (2% w/w DiI-TPB)	5.5	5.5	5.5	8.5	8.5	8.5
Captex® 8000 (2% w/w DiD-TPB)	5.5	5.5	5.5	8.5	8.5	8.5
Kolliphor® HS-15	11.5	11.5	11.5	9.3	9.3	9.3
Purified water	21.3	21.3	21.3	17.5	17.5	17.5
DSPE-mPEG-2000	–	0.6	–	–	0.6	–
Stearylamine	–	–	0.1	–	–	0.1
Lipoid® S75-3	0.7	0.7	0.7	0.7	0.7	0.7
NaCl	0.8	0.8	0.8	0.8	0.8	0.8
Purified water (2°C)	54.7	54.7	54.7	54.7	54.7	54.7

LNC-50: LNC with an expected size of 50 nm; LNC-50-PEG: LNC with DSPE-mPEG and expected size of 50 nm; LNC-50-SA: LNC with stearylamine and expected size of 50 nm. LNC-85: LNC with an expected size of 85 nm; LNC-85-PEG: LNC with DSPE-mPEG and expected size of 85 nm; LNC-85-SA: LNC with stearylamine and expected size of 85 nm.



*libitum*. The experimental protocol on animals was carried out to the EU Directive 2010/63/EU and was approved by the Committee on the Ethics of Animal Experiment of the Pays de la Loire, France (APAFIS #2020092411444021).

## 2.5. IV administration of FRET-LNCs

### 2.5.1. First injection

Six FRET-LNCs formulations were intravenously injected into Sprague-Dawley rats via dorsal penile vein with the dose of  $2 \times 10^{14}$  particles/100 g rat. Ten samples of 150  $\mu$ L of blood were collected in tail vein at 5, 30, 60, 90, 120, 180, 240, 360, 600 and 1440 min post-dosing. No >1500  $\mu$ L were collected over the 24-h study period (< 5% total blood volume). Samples were analyzed as described previously.

### 2.5.2. Repeated injection

After 7 days, the same dose of the same type of FRET-LNCs was injected into the same rat. Blood was collected and analyzed with the same method as mentioned above.

## 2.6. Quantification FRET-LNCs in plasma

### 2.6.1. FRET-LNCs extraction from blood

A 100  $\mu$ L blood sample was taken and immediately mixed with 100  $\mu$ L of Histopaque®-1083 in the polycarbonate centrifuge tube kept in ice. Then, the samples were centrifuged using Optima MAX-UP Ultracentrifuge (Beckman Coulter, Villepinte, France) and the fixed-angle rotor TLA-100 (Beckmann Coulter, Villepinte, France) with a relative centrifugal force of  $4 \times 10^5$  G at 25 °C for 2 h. Finally, 75  $\mu$ L of the supernatant was immediately collected and mixed with 225  $\mu$ L of ultrapure water. FRET donor and acceptor spectra of the samples were measured, and the PR was calculated. Then, the particle concentrations were calculated from the equation derived from the quantitative calibration curve.

### 2.6.2. Particle integrity analysis

Sample's mean PR at any time point was calculated. The time duration that FRET-LNCs having full integrity was coined as the *full-integrity phase*. A time point was included in the *full-integrity phase* if the mean PR at a time point was  $\geq 0.80$  and was statistically equivalent to the mean PR of the pooled reference formulations ( $n = 38$ ) using the equivalence test (see supplementary S1). Only the FRET acceptor intensity in the *full-integrity phase* was quantified as the *in vivo* plasma particle concentration by the calibration curve, otherwise, the data was reported as below the limit of quantification (BLOQ). Algorithm for FRET-LNCs particle concentration quantification procedure is detailed in supplementary Scheme S1.

### 2.6.3. Quantitative calibration curve

For the standard solutions, seven dilutions of FRET-LNCs were prepared with the dilution factors ranging from  $1 \times 10^3$  to  $5 \times 10^4$  and then spiked into blood or PBS. The initial particle concentration of the formulation had been measured in the characterization step by NTA (section 2.3). Maximum FRET acceptor emission intensities of the spiked standard were measured ( $675 \pm 5$  nm) and plotted as a function of particle concentration with the curve fitted by a double logarithmic regression function in the linear form:  $F_A = 10^k \times C^m$  where  $F_A$  is FRET acceptor maximum emission intensity ( $675 \pm 5$  nm) of a sample;  $k$  is the intercept;  $C$  is FRET-LNCs particle concentration of a sample;  $m$  is the slope of the fitting curve. The linearity of the fitting curve was estimated by the coefficient of determination ( $R^2$ ) with the acceptance of  $R^2 \geq 0.980$ . Due to the interference from background fluorescent noise at low concentration, the standard concentration with PR < 0.80 was excluded from the calibration curve.

### 2.6.4. Lower limit of quantification (LLOQ)

The LLOQ of each FRET-LNCs formulation was defined as the mean of the lowest *in vivo* particle concentration in the *full-integrity phase*.

## 2.7. Pharmacokinetics analysis and modeling

NCA and PopPK analyses were performed on blood concentrations of intact FRET-LNCs concentrations vs time data using PKanalix and Monolix softwares, respectively (MonolixSuite 2021R1, Lixoft, Antony, France). Actual sampling times and doses were used in the analysis. Default software settings were used unless otherwise stated.

For NCA, BLOQ was considered as missing values. The linear trapezoidal linear integral method was used to compute the area under the curve from time zero to the time of the last measured concentration ( $AUC_{last}$ ). All available observations were included for calculation of the slope of the terminal log-linear phase  $\lambda_Z$  and the corresponding half-life (HL), which was performed with a uniform weighting. Kinetic profiles with fewer than 5 observations were excluded from the analysis. Rats having received two administrations were analyzed independently for each administration. Area under the curve from time zero to infinity ( $AUC_{0 \rightarrow \infty}$ ), mean residence time (MRT), plasma clearance (CL) and volume of distribution ( $V_D$ ) were determined from the observed concentrations.

For PopPK, BLOQ concentrations were interval-censored, between 0 and the LLOQ for each type of FRET-LNCs. PK parameters from rats having received two administrations were estimated from the two obtained PK profiles, each administration being considered as an occasion. PK parameters were assumed to follow a log-normal distribution. Structural models with 1 or 2 compartments and linear or non-linear elimination were tested. Combined, constant and proportional residual error models were tested on the best structural model. LNCs were categorized by type of surface modification (classical, PEGylated or coated with SA), size (50 or 85 nm), or the combination of both (type of LNC). Impact of the categorical covariates coating, size and type on PK parameters was assessed by the stepwise covariate modeling procedure, using exponential relationships. Inter-occasion variability was also assessed. Among alternate models, the model displaying the lowest corrected Bayesian Information Criterion (cBIC) was retained. Model evaluation was performed based on the relative standard error (RSE) of the estimates, which was considered acceptable under 30% for fixed effects and under 50% for random effects. Graphical evaluation of models included goodness of fit (GOF) plots (observations versus predictions and distribution of weighted residuals) and visual predictive checks (VPC). For the final model, stability was additionally assessed by evaluating the sensitivity of fixed effect parameters to changes of their initial values.

## 2.8. In vitro stability of FRET-LNCs in rat blood

Rat blood was obtained by cardiac puncture and kept in a lithium heparin tube (Vacutainer®, Becton-Dickinson, Franklin Lakes, NJ, USA). FRET-LNCs were added to 1 mL of the blood to obtain a final concentration of 28.5 Teraparticles/mL (Teraparticles or  $T_p = 10^{12}$  particles). The mixture was incubated at 37 °C with stirring. 100  $\mu$ L of blood was collected at 5, 30, 60, 90, 120, 180, 240, 360 and 600 min. FRET-LNCs particle concentration was quantified with the same method in section 2.6. A control group in PBS was analyzed with the same experimental condition. The concentration results were normalized with the results from the first time point (5 min) and reported as:  $\%C_N = (C_t/C_5) \times 100\%$  where  $\%C_N$  is the percentage normalized particle concentration,  $C_t$  is the particle concentration at each time point, and  $C_5$  is the initial particle concentration at the time 5 min. To ensure the integrity of the extracted FRET-LNCs, the FRET signal has been monitored for each sample. The mean PR of the sample from each time point ( $n = 3$ ) has been statistically compared.

## 2.9. Statistical analyses

All statistical analyses were performed using the software Prism GraphPad (version 9.3.1, GraphPad Software, San Diego, CA, USA). The statistical significance was assessed for a *p*-value under 0.05.

### 2.9.1. Formulation and characterization

The statistical analyses were conducted by two-way ANOVA (Tukey's multiple comparisons) to investigate the effect of size and surface modification.

### 2.9.2. Noncompartmental pharmacokinetics

The difference of NCA of the 1st injection (day-0) between each formulation was analyzed by two-way ANOVA with size and surface modification factors. The difference of NCA of the 2nd injection (day-7) was statistically compared to the 1st injection (day-0) by paired *t*-test.

### 2.9.3. In vitro particle stability

Particle integrity equivalence test was assessed by two one-sided tests (TOST) as the method mentioned earlier. The particle concentration as %C<sub>N</sub> from each time point was statistically compared to the initial %C<sub>N</sub> at 5 min (time factor) and between blood vs PBS (media factor) by repeated-measures two-way ANOVA.

## 3. Results and discussions

### 3.1. FRET-LNCs formulations and characterization

To follow the behavior of intact LNCs [1], the FRET method has been chosen. FRET relies on the interaction between two encapsulated dyes which is more precisely for monitoring intact LNCs than the single encapsulated dye system. Indeed, the fluorescence signal of the single dye system can originate from the dye already released outside the LNCs, while the FRET signal can only be detected from the two dyes in close proximity inside the intact LNCs. Moreover, to avoid any modification of the nanocarrier's physicochemical properties and dyes dissociations, dyes have been encapsulated and not conjugated to one of the LNCs components. Six FRET-LNCs formulations with different sizes (50 and 85 nm) and surface modifications (none, DSPE-mPEG-2000 or stearylamine) were prepared following the compositions described in our previous work [4]. Two sizes were formulated in the range of 47.5–52.7 nm and 78.6–84.8 nm with a span in the range of 0.40–0.67, suggesting a narrow and uniform size distribution (Table 2). Because NTA determines the Brownian motion by video image analysis, particles in the samples are visualized, and a photo of particles can be extracted (Supplementary Fig. S2). The zeta potential varied by both size and surface modification. The proximity ratio (PR) of all the formulations were in a range from 0.86 to 0.93, as obtained in our previous work for optimal FRET signal, and demonstrating their full integrity [20]. Finally, the particle concentration, except for LNC-50-PEG, ranged from  $2.5 \times 10^2$  to  $3.8 \times 10^2$  Tp/mL. Surprisingly, LNC-50-PEG had a particle concentration of  $10.1 \times 10^2$  Tp/mL, which is significantly (*p* < 0.05) higher than all the others as already obtained in our previous work (Table 2) [4]. This difference in particles concentration was considered in the following *in vitro* and *in vivo* experiments.

### 3.2. FRET-LNCs extraction and quantification method

For the noncompartmental pharmacokinetic and the population pharmacokinetic analyses, quantitative information (and not qualitative or semi-quantitative information) regarding the plasma particle concentration is required. For the PK studies, a new extraction method was developed for quantifying intact FRET-LNCs in biological media. Blood itself has the autofluorescent emission spectrum at 548 nm which overlaps the FRET spectrum of FRET-LNCs [21,22]. Various methods of extraction are available e.g., solid-phase extraction (SPE), liquid-liquid

**Table 2**  
FRET-LNCs Characterization (mean ± SD).

Formulations	Particle Size (nm)	Span	Zeta Potential (mV)	FRET Proximity Ratio (PR)	Particle Concentration (10 <sup>2</sup> Tp/mL)
LNC-50 (a) (n = 5)	49.3 ± 4.8 <sup>d</sup>	0.51 ± 0.20	4.2 ± 2.1 <sup>bcd</sup>	0.90 ± 0.02	3.2 ± 0.8 <sup>b</sup>
LNC-50-PEG (b) (n = 5)	47.5 ± 2.3 <sup>e</sup>	0.40 ± 0.04 <sup>e</sup>	-7.1 ± 2.8 <sup>ae</sup>	0.87 ± 0.04	10.1 ± 1.1 <sup>ae</sup>
LNC-50-SA (c) (n = 7)	52.7 ± 4.9 <sup>f</sup>	0.56 ± 0.09	18.0 ± 1.0 <sup>af</sup>	0.86 ± 0.03 <sup>f</sup>	3.8 ± 0.5
LNC-85 (d) (n = 5)	84.8 ± 3.1 <sup>a</sup>	0.61 ± 0.04	16.9 ± 1.1 <sup>aef</sup>	0.90 ± 0.03	2.5 ± 0.8
LNC-85-PEG (e) (n = 3)	78.6 ± 2.1 <sup>b</sup>	0.67 ± 0.09 <sup>b</sup>	-1.3 ± 1.8 <sup>bd</sup>	0.93 ± 0.01	3.3 ± 0.5 <sup>b</sup>
LNC-85-SA (f) (n = 3)	83.1 ± 5.4 <sup>c</sup>	0.62 ± 0.03	30.0 ± 1.1 <sup>cd</sup>	0.93 ± 0.01 <sup>c</sup>	2.8 ± 0.8

*T<sub>p</sub>* = 10<sup>12</sup> particles (Teraparticle). Statistical significance was conducted by two-way ANOVA (Tukey) and expressed as a comparison: (a) vs. LNC-50, (b) vs LNC-50-PEG, (c) vs LNC-50-SA, (d) vs LNC-85, (e) vs LNC-85-PEG, (f) vs LNC-85-SA; if the level of significance with *p* < 0.05.

extraction (LLE), protein precipitation (PP) [15]. Preliminary unpublished work demonstrated that these methods were not appropriate to our study because they use organic solvents that destroy LNCs. The dissociated FRET-LNCs do not give FRET signal because the dyes will dissipate out, causing their distance to widen beyond the FRET distance. In order to avoid using organic solvents and to get rid of solid blood components from the sample, the sucrose density gradient centrifugation technique was employed using Histopaque®-1083, which is the polysucrose solution with the density 1.083 g/mL [23]. FRET-LNCs have a lower density than Histopaque®-1083 and the aqueous phase of blood. So that, after the centrifugation, LNCs will be at the top of the supernatant. At last, the FRET spectrum of FRET-LNCs was measured by the fluorimeter.

In a previous work [14], no apparent variation was observed between the particle concentration of LNCs calculated by the fluorescence calibration curve at the FRET acceptor wavelength and the one determined by the NTA. However, the plasma extract could still contain natural lipid or protein particles. As a result, a microscopic analysis (TEM, SEM) or a direct NTA measurement would overmeasure the presence of the particles because these methods did not distinguish natural lipid or protein particles from LNCs. Meanwhile, the *in vivo* experiment with a routine analytical method testing numerous samples must be developed. Accordingly, the particle concentration in blood was determined by using the fluorimeter. To ensure that only the FRET acceptor intensity of fully intact FRET-LNCs was quantified as particle concentration, FRET-LNCs particle integrity at any time point was determined by PR with equivalence test. Only FRET acceptor intensity during the *full-integrity phase* was quantifiable by the calibration curve. To quantify the FRET-LNCs particle concentration in the extract, a calibration curve was constructed between the FRET acceptor intensities at 675 ± 5 nm and FRET-LNCs particle concentration. The different standard concentrations were spiked in blood and, after the extraction, FRET acceptor intensities were measured and plotted as a function of the known FRET-LNCs particle concentrations. The linearity of every calibration curve was >0.980. A new calibration curve was constructed for every freshly prepared batch of FRET-LNCs to reduce the variability caused by the varying particle concentration of each formulation. Matrix effect was observed (see supplementary S4). In accordance with the ICH and USFDA guidelines, to analyze *in vivo* sample, the calibration curve was prepared in the same biological matrix as of the sample, which is

blood (or PBS in the *in vitro* experiment) [24,25].

The LLOQ of the *in vivo* plasma particle concentration was determined by both plasma particle concentration and particle integrity (the PR). The LLOQ of each formulation is shown in Table 3.

Moreover, to detect free dyes released from FRET-LNCs, the extraction by ultracentrifugation was performed on DiI-TPB/blood and DiD-TPB/blood mixtures. Nevertheless, this extraction method could not efficiently extract the free DiI-TPB and DiD-TPB dyes from blood, as only around 0.0002% of the free dyes were retrieved. The dyes were observed to adsorb to the glass vial, plastic tube, and plastic pipette tips. Thus, only the FRET signals from the dyes inside FRET-LNCs could be determined by this extraction method.

### 3.3. Particle concentration-time profile and NCA

Forty-three PK profiles were obtained in 28 rats, 15 rats being dosed twice (Fig. 1). Of note, 2 out of 3 rats suddenly died after reinjection of LNC-85-SA. As a consequence, reinjection of LNC-85-SA was discontinued for ethical reasons, in agreement with the protocol, and reinjection data were obtained in 1 animal only. An interaction with erythrocyte or platelet and toxicity of stearylamine was already demonstrated with liposomes by Nishiya et al., which would explain the death of these 2 rats [26].

In order to carry out the quantitative particle analysis in rat plasma, the FRET spectra was measured with  $\lambda_{\text{ex}} = 548$  nm. Firstly, the PR was checked qualitatively for the overall integrity of FRET-LNCs. Then, the concentration of intact nanoparticles was estimated with the equation obtained from every freshly prepared batch of FRET-LNCs. The following experiments take into account 430 samples collected, 55 values were missing, while 80 values were BLOQ. As an example of the obtained spectra, the emission spectra of LNC-50 in rat plasma (FRET donor and FRET acceptor) were given in Supplementary S3, as well as a photo of particles extracted from video images obtained by NTA.

The PKs of the intact FRET-LNCs has never been elucidated due to the lack of technique to directly quantify their particle concentration in biological media. The BLOQ values were considered as missing. Nine PK profiles with fewer than 5 observations (2 to 4) were considered too poor for NCA and excluded. Finally, the 34 analyzed PK profiles contained 6 to 9 observations, and a total of 268 observations. The FRET LNCs were considered intact, and the concentration has been calculated with the appropriate standard curve. The PR was monitored and plotted as a function of time (see supplementary Fig. S5). After concentration analysis, PK data showed that, while the decreased  $V_D$  for bigger LNCs was observed for all coatings without a significant difference (18.6 vs 24.8, 15.4 vs 16.8, 16.4 vs 22.1 mL for LNCs 85 nm vs 50 nm classical, PEG and SA respectively), the decreased CL for bigger LNCs was only observed for PEG LNCs (3.0 mL/min). Interestingly, LNC-50-PEG displayed a significantly higher CL than 50 nm classical and SA LNCs (12.1 vs 5.5 and 6.3  $10^{-3}$  mL/min respectively), while LNC-85-PEG displayed a significantly lower CL than 85 nm classical and SA LNCs (3.0  $10^{-3}$  mL/min vs 5.6 and 5.8  $10^{-3}$  mL/min respectively). Accordingly, HL and MRT were significantly shorter for LNC-50-PEG and higher for LNC-85-PEG than for other LNC types (Table 4). LNCs 85-PEG displayed significantly higher  $AUC_{0 \rightarrow \infty}$  (27,672 vs 9432 Tp.min/mL) and significantly lower CL (3.0 vs 12.1  $10^{-3}$  mL/min) when compared to LNC-50-PEG (Table 4). Groo et al, have performed a study with paclitaxel-loaded LNCs-50 with and without PEG length of 2000 to compare their PK profiles. After IV

administration in rats, circulation time of PEGylated paclitaxel-loaded LNCs is longer than classical paclitaxel-loaded LNCs. Indeed, the MRT of paclitaxel after IV administration was 80 min and 54 min for paclitaxel-loaded PEG LNCs and paclitaxel-loaded LNCs, respectively [27]. Similarly, in another study using qualitative fluorescence detection technique, Morille et al., concluded to a longer time circulation of PEG<sub>2000</sub> LNCs 50 nm than LNCs 50 nm without PEG<sub>2000</sub> after measuring the fluorescence signal of encapsulated DiD [28]. All these studies seem to demonstrate the longer circulation time of PEG LNCs. However, it is important to not forget that, in these studies, the total paclitaxel or dye (free and encapsulated) was quantified or followed and not only the encapsulated one.

To conclude, by employing the quantitative FRET technique detection of LNCs, these results highlight a size-dependent clearance of PEGylated LNCs in blood, which is associated with modifications of their PK profiles. This study allows describing for the first-time quantitative results about *in vivo* fate of LNCs.

To study the effect of the ABC phenomenon and its pharmacokinetics consequences, the FRET-LNCs formulations with the same dose were reinjected to the same rat ( $n = 3$ ) after 7 days. The PR-time profile had the same pattern as in the first injection (see supplementary Fig. S5). The particle concentration-time profile of the reinjection was shown in Fig. 1B and compared with each first injection datum in Fig. 1A. These results demonstrated that the 1-week reinjection plasma particle concentration-time profile was similar to the first injection for the 6 formulations. Moreover, NCA was performed on the reinjection data (shown in Table 4) and no significant difference (paired *t*-test) was obtained compared to the parameters from the initial injection. Thus, NCA results showed that PK parameters were similar after the first and the second administration for all formulations. Note that all formulations contain small PEG chains (PEG<sub>660</sub>) because Kolliphor® HS-15, which acts as a surfactant, is composed of a mixture of free PEG<sub>660</sub> and the PEG<sub>660</sub> with mono- and the di-esters of 12-hydroxystearic acid. Nevertheless, as demonstrated by Basile et al. with similar formulations, LNCs with only Kolliphor® HS-15 had low *in vitro* activation of complement proteins in the *in vitro* study [29]. With our *in vivo* study, we can hypothesize that no immune reaction against PEG would occur in rats after a 7-day reinjection. In comparison, Ichihara et al., have previously demonstrated that after administration of PEGylated liposomes (DSPE-PEG<sub>2000</sub>) with mean size around 100 nm, in mice and rats, anti-PEG IgM production appeared after 3 days with a peak at 5 days [30]. Even if the interval between the two injections was very important to observe this phenomenon, these authors confirmed that the maximum level of anti-PEG is around 5 to 7 days [31]. Other parameters are known to influence the ABC phenomenon like size of nanoparticles, density and dose of PEG [31]. For the dose, it is possible that, with our LNCs formulations, induction of the ABC phenomenon was abrogated because the amount of PEG was higher than 0.5  $\mu\text{mol/kg}$ , as suggested by Hashimoto et al. [32]. Indeed, by calculation, the total amount of injected PEG<sub>660</sub> and PEG<sub>2000</sub> (for LNC-50-PGE, and LNC-85-PEG) were between 90 and 1900  $\mu\text{mol/kg}$  and 5–25  $\mu\text{mol/kg}$ , respectively. In addition, Li et al, have performed a study about animal species effect on ABC phenomenon with PEGylated liposomes. They observed that the antibodies PEG production could be inhibited by cytotoxic drug loaded in liposomes. Then, in dogs, the ABC phenomenon was more pronounced than in rats or mice [33]. Therefore, it is possible to suppose that the production of antibodies after the first injection of PEGylated nanoparticles does not modify the PK profile, especially the clearance. In the previous cited studies, they were only interested in increasing plasma antibody levels and not in the potential PK parameter modifications.

Conclusively, all the results pointed out that 1-week reinjection did not significantly change any pharmacokinetics in the 6 tested FRET-LNCs formulations. Therefore, for the popPK, the results from the first injection and the reinjection could be combined to increase the sample size for popPK and thus to improve the accuracy of the model.

Table 3

LLOQ for each formulation.

	LNC-50	LNC-50-PEG	LNC-50-SA	LNC-85	LNC-85-PEG	LNC-85-SA
LLOQ (Tp/ mL) (m + sd)	16.7± 6.3	15.6± 6.8	13.1± 2.7	7.6± 2.3	16.6± 2.3	6.0± 2.4

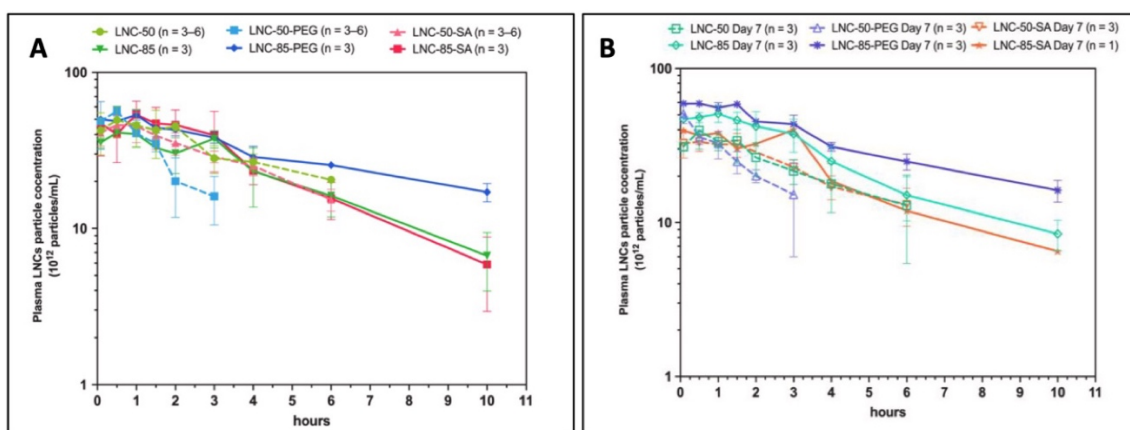


**Fig. 1.** Plasma particle concentration-time profile of 50-nm & 85-nm FRET-LNCs following the IV bolus. (A) with day-0 injection. (B) with day-7 injection. Data is reported as the arithmetic mean and standard deviation (whisker). Particle concentration is in the unit of  $10^{12}$  particles/mL (Teraparticles).

**Table 4**

NCA of the pharmacokinetic parameters (mean and 95 %CI) of six different FRET-LNCs by IV bolus injection route in the rat model (D0) and after a second injection separate by one week (D7).

PK parameters (NCA) 1st injection (D0)/2nd injection (D7)		LNCs 50 nm			LNCs 85 nm		
		LNC-50 (a) (n = 3)/ (n = 3)	LNC-50-PEG (b) (n = 3)/(n = 3)	LNC-50-SA (c) (n = 3)/(n = 3)	LNC-85 (d) (n = 3)/ (n = 3)	LNC-85-PEG (e) (n = 3)/(n = 3)	LNC-85-SA (f) (n = 3)/(n = 1)
$AUC_{0 \rightarrow \infty}$ ( $T_p \bullet$ min/mL)	D0	22016 <sup>b</sup> [18,172, 25,860]	9432 <sup>ac</sup> [4524, 14,340]	17,733 [10,282, 25,184]	15984 <sup>e</sup> [8767, 23,200]	27672 <sup>bd</sup> [21,890, 33,454]	17,091 [9369, 24,813]
	D7	14,376 [0, 30,261]	7906 [0, 16,814]	13,569 [4125, 23,012]	18,318 [9688, 26,948]	26,858 [18,578, 35,138]	14,217 [8996, 21,400]
$AUC_{0 \rightarrow last}$ ( $T_p \bullet$ min/mL)	D0	12768 <sup>b</sup> [7622, 17,914]	6871 <sup>ac</sup> [6034, 7708]	11,441 [9182, 13,699]	13505 <sup>e</sup> [9664, 17,346]	18744 <sup>bd</sup> [17,982, 19,506]	15,198 [8996, 21,400]
	D7	8623 [4220, 13,027]	5010 [3493, 6528]	7968 [4357, 11,580]	15,563 [9565, 21,560]	19,927 [16,419, 23,425]	12,201 [16,419, 23,425]
Half-life (min)	D0	312 <sup>b</sup> [25, 599]	102 <sup>ac</sup> [5, 199]	252 [53, 451]	240 [86, 394]	358 <sup>b</sup> [243, 474]	202 [41, 362]
	D7	257 [0, 610]	111 [0, 239]	268 [21, 514]	221 [129, 313]	294 [212, 375]	215 [212, 375]
$MRT_{obs}$ (min)	D0	441 <sup>b</sup> [28, 854]	143 <sup>ac</sup> [3, 283]	353 [84, 623]	323 [128, 519]	522 <sup>b</sup> [347, 697]	272 [72, 471]
	D7	365 [0, 871]	164 [0, 378]	369 [51, 686]	312 [196, 428]	429 [308, 551]	300.0 [308, 551]
$Cl_{obs}$ ( $10^{-3}$ mL/min)	D0	5.5 <sup>b</sup> [4.5, 6.2]	12.1 <sup>ac</sup> [5.5, 18.7]	6.3 [3.1, 9.4]	5.6 [2.8, 8.3]	3.0 <sup>b</sup> [2.2, 3.8]	5.8 [3.6, 7.9]
	D7	7.4 [0, 16.8]	14.0 [1.4, 26.6]	7.3 [2.4, 12.3]	5.5 [2.5, 8.5]	3.3 [1.9, 4.7]	7.1 [1.9, 4.7]
$V_D$ (mL)	D0	24.8 [0.7, 48.8]	16.8 [9.6, 23.9]	22.1 [11.8, 32.3]	18.6 [14.8, 22.5]	15.4 [11.7, 19.2]	16.4 [5.1, 27.7]
	D7	22.5 [18.4, 26.5]	20.1 [18.8, 21.4]	26.6 [16.4, 36.8]	17.2 [12.4, 21.9]	13.9 [11.6, 16.1]	22.2 [11.6, 16.1]

$T_p = 10^{12}$  particles (Teraparticle). Statistical analysis was conducted by two-way ANOVA and is expressed if the level of significance  $\leq p 0.05$  as: (a) vs LNC-50, (b) vs LNC-50-PEG, (c) vs LNC-50-SA, (d) vs LNC-85, (e) vs LNC-85-PEG, (f) vs LNC-85-SA. A statistical analysis was conducted by paired t-test to compare the first injection and second injection.

### 3.4. Population pharmacokinetics analysis (popPK) of intact FRET-LNCs

All 375 measured concentrations from 43 kinetics and 28 rats were included in the analysis. BLOQ concentrations were interval-censored, between 0 and the LLOQ for each subtype of LNC (Table 3). The data were best described by a 1 compartment model with a Michaelis-Menten elimination and a proportional residual error. A strong correlation between  $V_m$  (maximum elimination rate) and  $K_m$  (Michaelis-Menten constant) was observed, suggesting an over-parameterization of the model, which was corrected by fixing  $K_m$ . After a parameter sensitivity analysis between 25 and 35  $T_p/mL$ , the value of 27  $T_p/mL$ , resulting in the lowest BICc, was retained for  $K_m$ . Importantly, other estimated parameters were stable for the various tested values of  $K_m$ . Base model parameters were estimated with a good precision, with relative standard

errors (RSE) below 20% (Table 5). Inter-occasion variability did not improve the model.

Effect of size, coating and type of LNCs on  $V_D$  and  $V_m$  were assessed. Inclusion of the type of LNC as a covariate on  $V_m$  resulted in the highest decrease of the BICc value (Table 6). Addition of a second covariate on this new reference model with type of LNC on  $V_m$  allowed to include effect of size on  $V_D$  as the most significant covariate. Addition of any other covariate did not further reduce the BICc value. Since the estimated value of the effect of LNC-SA-50 on  $V_m$  was low ( $-0.08$ ) and poorly estimated (RSE = 107%), it was fixed to zero, resulting in a lower BICc value. In the final model, reference  $V_m$  value consequently corresponded to the value of  $V_m$  for LNC-50 and LNC-50-SA. Other types of LNCs significantly influenced  $V_m$  when compared to the reference value (Table 6). The type of LNCs explained 35% of the variability of  $V_m$ ,

**Table 5**

Population PK model parameters: one compartment model with non-linear elimination and proportional error model. Typical value (TV) was obtained from reference value (RV = 21.49 mL for  $V_D$ , 3.89 Tp/min for  $V_m$ ) and  $\beta$  using the formula:  $\log TV = \log RV + \beta$ .

Parameters	BASE MODEL		FINAL MODEL		Typical value
	Estimate	RSE (%)	Estimate	RSE (%)	
<i>Fixed Effects</i>					
$V_D$ (mL)	20.29	3.30	21.49	3.68	21.49
$\beta_{85\_V_D}$	NA	NA	-0.16	36.00	18.31
$V_m$ (Tp/min)	3.93	8.89	3.89	4.19	3.89
$\beta_{LNC-85\_V_m}$	NA	NA	-0.30	25.60	2.88
$\beta_{LNC-50-PEG\_V_m}$	NA	NA	0.75	9.21	8.24
$\beta_{LNC-85-PEG\_V_m}$	NA	NA	-0.74	12.10	1.86
$\beta_{LNC-85-SA\_V_m}$	NA	NA	-0.20	41.00	3.18
$K_m$ (Tp/mL)	27.00	NA	27.00	NA	27.00
<i>Standard Deviation of the Random Effects</i>					
$\omega_{V_D}$	0.15	19.80	0.13	17.50	NA
$\omega_{V_m}$	0.46	18.00	0.11	13.70	NA
<i>Error Model Parameters</i>					
b	0.20	4.73	0.20	4.68	NA

RSE: relative standard error.  $V_D$ : volume of distribution.  $V_m$ : maximum elimination rate.  $K_m$ : Michaelis-Menten constant. Tp: teraparticles ( $10^{12}$  particles).  $\beta_{A,B}$ : effect of covariate A on parameter B.  $\omega_{A,B}$ : unexplained inter-individual variability (standard deviation) of parameter B. b: proportional residual error (standard deviation).

**Table 6**

Population PK model: impact of covariates on BICc and random effect parameters.

	BICc	$\omega_{V_D}$	$\omega_{V_m}$	b
Base	2094.45	0.15	0.46	0.20
Size on V	2090.98	0.13	0.46	0.20
LNC type on $V_m$ (6 types)	2041.43	0.15	0.11	0.20
LNC type on $V_m$ (5 types)	2039.11	0.15	0.11	0.20
Final	2035.86	0.13	0.11	0.20

while size of LNCs explained only 2% of the variability of  $V_D$ .

All the parameters of the final model were estimated with a good precision, with RSE below 20% (Table 5). Shrinkage of  $V_D$  and  $V_m$  distribution were below 20% (Table 6). The residual error of 20% was acceptable. The final model was stable, as assessed by estimating parameters starting from 5 random combinations of initial estimates for  $V_D$  and  $V_m$ , varying between 11.89 and 32.33 mL and 1.21 and 3.30 Tp/min respectively (supplementary Fig. S6).

Diagnostic plots showed that the final model was able to accurately predict observations, all over the observed concentrations range and all along the kinetics (Fig. 2). Indeed, observations versus population and individual predictions splines were close to the identity line (Fig. 2A), while individual weighted residuals (IWRES) versus time and individual predictions showed that percentiles were close to the theoretical percentiles from the normal centered reduced law (Fig. 2B). Corrected visual predictive checks confirmed that the final model accurately captured the mean PK profile and its associated variability (Fig. 2C).

The PopPK analysis confirmed the results obtained with the NCA. Parameter values were similar, and the same impact of size and coating properties of LNCs was identified.  $V_D$  was 21.49 mL for pooled 50 nm LNCs and 18.31 mL for pooled 85 nm LNCs from PopPK (Table 5), these values are comparable to the mean values obtained from NCA (22.2 mL and 17.2 mL respectively, from Table 4). Comparison of elimination parameters is less straightforward, since a constant CL is estimated using NCA, while a non-linear CL dependent on plasma concentration could be characterized with PopPK modeling. However, the value of CL at a plasma concentration ( $C_p$ ) of 35 Tp/mL which is roughly half the

maximum  $C_p$  measured in the current study, was of  $6.3 \times 10^{-3}$  mL/min for LNC-50 and LNC-50-SA (with  $V_m$  and  $K_m$  from Table 6), as calculated from the following equation:

$$CL = \frac{V_m}{K_m + C_p}$$

This value is similar to the values of 5.5 and  $6.3 \times 10^{-3}$  mL/min obtained from NCA for both types of LNCs, LNC-50 and LNC-50-SA respectively (Table 4). On the same principle, CL from PopPK when  $C_p$  is 35 Tp/mL was 4.6, 13.3, 3.0 and  $5.1 \times 10^{-3}$  mL/min respectively for LNC-85, LNC-50-PEG, LNC-85-PEG and LNC-85-SA, in line with CL calculated from NCA, of 5.6, 12.1, 3.0 and  $5.8 \times 10^{-3}$  mL/min respectively (Table 4).

No inter-occasion variability was observed when the LNCs were administered twice. The absence of PK parameters modification in our study might be explained by a limited production of antibodies, or a lack of effect of antibody production on the clearance of the LNC.

Altogether, PK analysis showed that, independently from the coating features, LNCs with smaller size (50 nm versus 85 nm) displayed a slightly larger  $V_D$  (+14% from PopPK, +23% from NCA respectively). A wider distribution of smaller particles has been described [34,35] and ascribed to a vascular permeability and a capability to circulate in capillaries of blood circulation system.

The effect of LNC characteristics on CL was more complex. For all coating types, elimination was decreased for LNC-85 compared to their LNC-50 nm counterparts, with  $V_m$  reduced by 26% and 18% for LNC-85 and LNC-85-SA respectively, and by 77% for LNC-85 and LNC-50 with PEG coating (Table 5). A faster elimination of smaller particles has been previously described [35,36] and ascribed to a more easily destabilized nanostructure by hepatobiliary excretion because of liver fenestration size. Interestingly, PopPK allowed to evidence a significantly decreased  $V_m$  for LNC-85 versus LNC-50, which could not be captured by NCA. This might be due to the less complete information usable in NCA, with only 34 PK profiles and 268 observations compared to 43 PK profiles and 375 observations for PopPK, and the lowest concentrations and higher clearance profiles being excluded from the analysis for methodological reasons.

Consistently, for LNCs 85 nm, PEGylation reduced CL by 46% and 48% compared to classical and LNCs with SA respectively as shown by NCA (Table 4). PEGylation also reduced  $V_m$  by 35% and 42% compared to classical and LNCs with SA respectively as shown by PopPK (Table 5). However, surprisingly, LNC-50-PEG was faster eliminated than LNC-50 and LNC-50-SA, with CL and  $V_m$  approximately doubled. PEGylation appears to have a counterproductive effect on LNC-50: another elimination route might be activated. Interestingly, a recent review from Adhipandito et al. [37] reported that several authors had observed that nanoparticles theoretically too large to be filtrated by the kidney were found intact in the urine after administration in mice. Among various possible mechanisms, cell-membrane wrapping has been shown to be possible for 30 to 60 nm diameter spherical nanoparticles [38]. Moreover, caveolae-mediated endocytosis, which is more likely for 60 nm diameter nanoparticles than clathrin-mediated endocytosis [39], might also be involved. We could then hypothesize that only LNC-50-PEG, which are both small enough and certainly less opsonized, could be eliminated by this renal route, explaining their surprisingly faster elimination. However, the precise identification of the clearance routes for LNCs needs to be further studied. In addition to providing a deeper understanding of PK variability depending on LNCs characteristics, PopPK analysis of intact LNCs concentrations allowed to characterize a non-linear elimination of LNCs. Few studies have reported non-linear elimination of nanomedicines so far. Non-linearity was identified based on administration of various doses and it was observed that the clearance was dose-dependent [40,41]. Further studies will be needed to explore the mechanisms involved in the distribution and clearance of these LNCs in the body [42]. In the future, the FRET method should be valuable to compare the PK of intact nanocarrier to the PK of

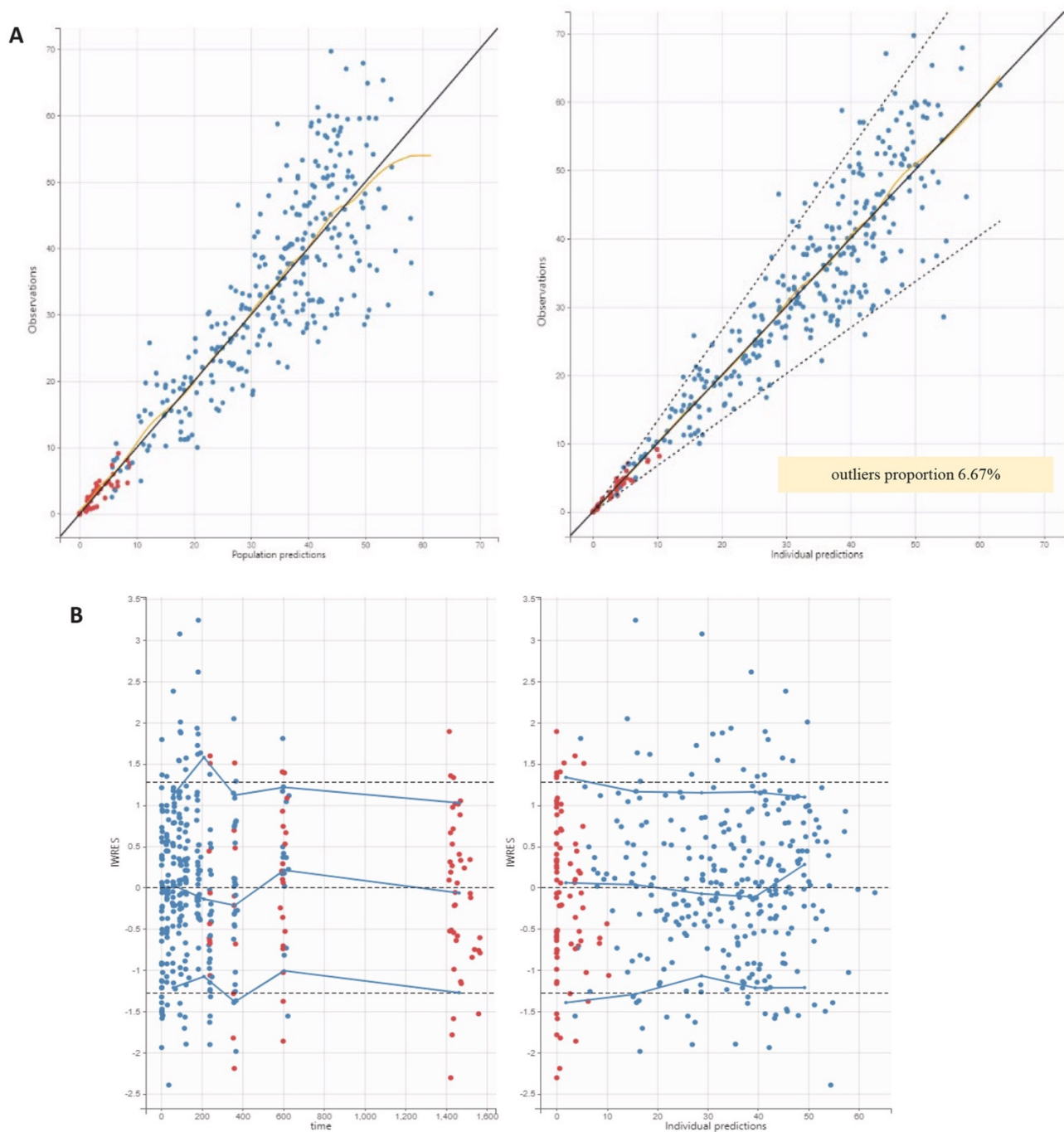


**Fig. 2.** Diagnostic plots of the final model with covariates. Blue and red dots respectively represent uncensored and censored observations. Concentrations expressed in  $\text{Tp/mL}$ , time in hours. A) Observations vs population predictions (left) and vs individual predictions (right). Black solid line: identity line. Dotted line: 90% prediction interval. Orange line: spline. B) Individual weighted residuals vs time (left) and vs individual predictions (right). Solid lines: empirical mean and percentiles. Dotted lines: predicted mean, 10th and 90th percentiles. C) Prediction corrected visual predictive check obtained from 500 simulations. Solid lines: empirical mean, 10th and 90th percentiles. Shaded areas: 90% prediction intervals of empirical mean (red) and 10th and 90th percentiles (blue). (For interpretation of the references to colour in this figure legend, the reader is referred to the web version of this article.)

encapsulated and free drug, providing lacking information on the release kinetics. Such data will be able to feed more advanced predictive PBPK models for nanomedicines [43,44].

The combination of an innovative FRET-based quantification

method specific of intact LNCs and of advanced PK modeling allowed to characterize for the first time a non-linear elimination of intact LNCs, and to evidence that PEGylation unexpectedly increased clearance of LNCs 50 nm, while decreasing the clearance of LNCs 85 nm.

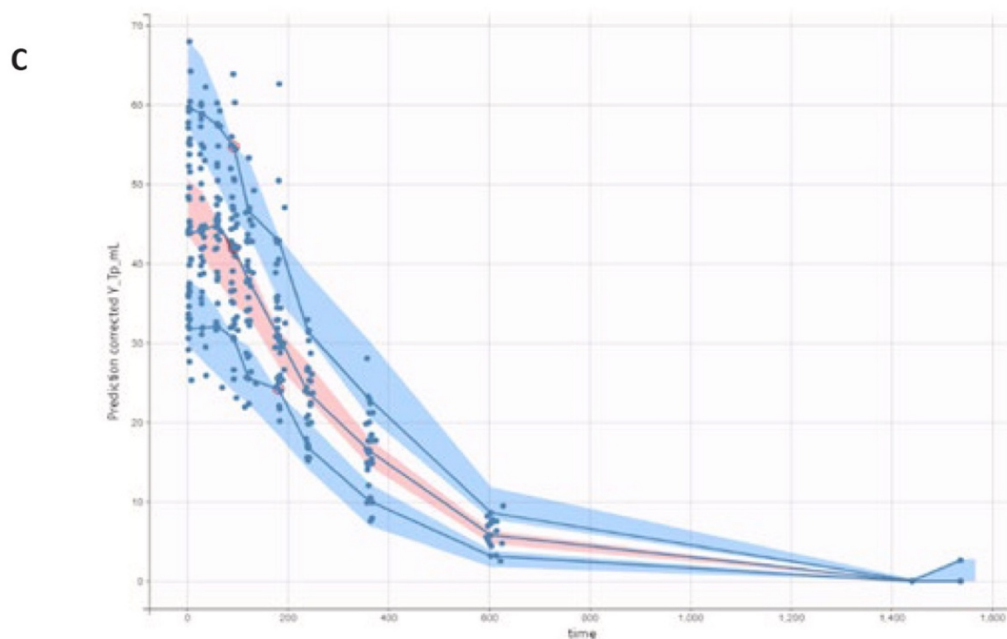


Fig. 2. (continued).

### 3.5. FRET-LNCs *in vitro* stability in blood

In regards of number studies among literature [18,41,46], the results of our *in vivo* fate nanoparticle after administration to rats were not as expected for LNC-50-PEG. To deeper understand this phenomenon, the *in vitro* stability of FRET-LNCs in the blood of rat was performed. A final concentration of 28.5 Tp/mL has been chosen in accordance with *in vivo* results. This particle concentration was equivalent to the peak time zero concentration of the *in vivo* study when it is considered that a rat has a theoretical total blood volume of 7.0 mL/100 g rat [47]. Fig. 3B shows a stable PR for all formulations for 10 h. Nevertheless, a significant decrease of normalized particle concentration was observed after 3 h of incubation in blood for LNC-50-PEG when no significant decline after 10 h was observed for all other formulations. (Fig. 3A). This result was correlated to the *in vivo* experiment showing a decrease in the blood concentration of LNC-50-PEG formulation after 4 h. This phenomenon was not observed in PBS, meaning that a degradation process only occurs in the blood for this type of LNCs. Consequently, the observed *in vivo* results could be, at least, partly explained by a faster degradation of LNC-50-PEG particles in blood. However, future in depth studies will be needed to confirm whether this phenomenon is the only one which can explain the faster clearance of the LNC-50-PEG.

In comparison to the literature, this result could be explained by the detection technique. The frequently used technique for quantifying the integrity of nanocarriers in the biological medium is the semi-quantitative FRET techniques [48–50]. In these studies, the PR has been interpreted like a percentage of degradation and converted to a quantity of intact nanoparticles. Thus, this method seems not adapted to measure the concentration of intact nanoparticles, but only to approximately evaluate the value of FRET ratio ( $DiI/DiD$ ). This would probably explain the differences of the results from the present study using a quantitative method and the results described in the literature.

This instability of LNC-50-PEG during *in vivo* and *in vitro* experiments was surprising because the PEGylated LNCs had been reported to be more stable in human plasma (*in vitro*) than conventional LNCs due to the so-called stealth effect [20]. The PEGylation concept, which was born with Professor Davis in 1970s, gives the main advantages to enhance the residence time in the bloodstream [51]. This prolonged

circulation time has been associated with both a reduced uptake and a reduced immune response, and can induce an enhanced therapeutic efficacy [52]. However, the particles stability should be considered as another particle characteristic. The physicochemical instability can probably be explained by the PEG surface density on the LNCs. Adding PEG on the LNC-50 which already contains PEG could induce this chemical frailty [53]. Recently, Professor Kinam Park gave some issues about PEGylated nanomedicines because if many studies confirmed the advantages of circulation time, this mechanism always seems totally unknown [54]. However, adding PEG could also enhance the instability of nanostructures. As it is exposed by Battler et al., a high surface density of PEG coating induces an entropic penalty of confining and stretching PEG chains which can be compensated by electrostatic binding gain. It has been shown that this equilibrium may occur in high ionic strength solutions [55]. Consequently, plasma, which is a high salt medium, would increase the instability of PEGylated LNCs. In addition, bio-distribution and accumulation in certain organs could also be another factor contributing to the blood elimination of LNCs [34]. Future experiments should investigate these hypotheses to elaborate on the true cause behind the decreased particle stability of LNC-50-PEG in blood.

### 4. Conclusion

To conclude, a new quantitative FRET method was developed to describe for the first time the specific pharmacokinetic properties of intact LNCs after IV injection in rats. As shown both by NCA and PopPK results, 85 nm LNCs were less intensively distributed than their 50 nm counterparts. As expected, PEGylation reduced elimination of 85 nm LNCs, compared to other types of coating. Surprisingly, PEGylation had an opposite effect on 50 nm LNCs, with an increased elimination compared to all other LNCs. This effect can be explained by a decreased *in vitro* stability of LNC-50-PEG in blood compared to the other formulations. Finally, population analysis of the PK profiles showed that PK of intact LNCs was non-linear, which has been seldom reported so far. The present *in vitro* and *in vivo* study of six different types of LNCs with various coatings and sizes, combining an innovative FRET-based quantification method of intact LNCs with an advanced population modeling approach, allowed a major breakthrough in the understanding of the PK

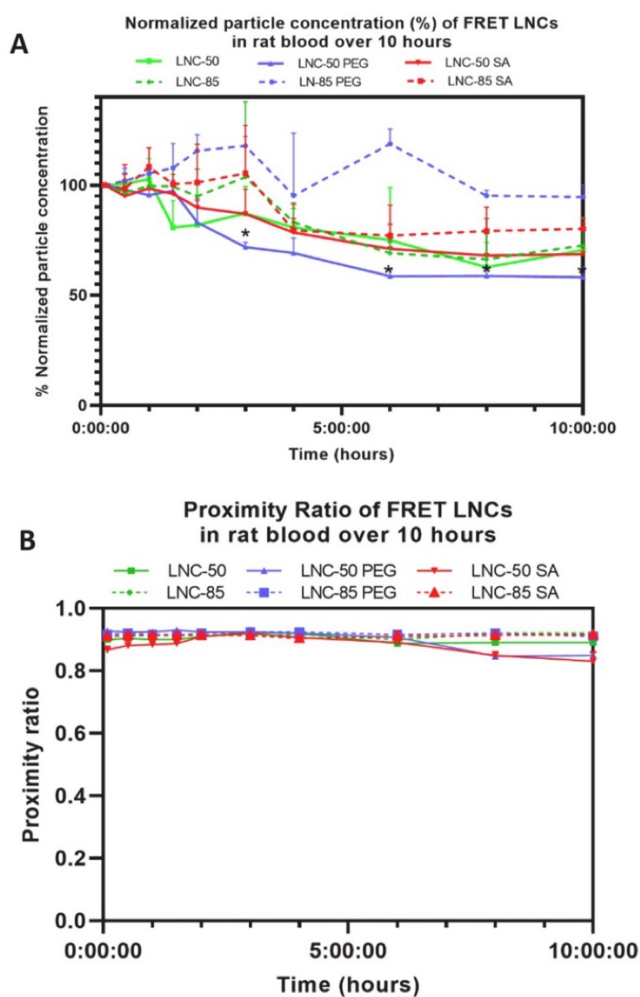


**Fig. 3.** Stability of FRET-LNCs in rat blood over 10 h. (A) The graph represents % normalized particle concentration (%C<sub>N</sub>) (B) The graph represents the proximity ratio. The experiment was conducted in triplicate and reported as the arithmetic mean and 95% CI (whisker) with the significance level indicated as \* $p < 0.05$  compared to the initial %C<sub>N</sub> at 5 min.

behavior of LNCs. This work will be helpful to predict the fate of various types of LNCs *in vivo* and will consequently facilitate their clinical translation. The specificity of the FRET-based quantification technique for intact nanoparticles is the corner stone of an accurate understanding of the PK of nanoparticles and will create new opportunities in the field of nanomedicines.

#### Funding

This work was supported by Ligue Contre le Cancer, Maine et Loire et Loiret Committee (JPB/FP -441/12.2019 and JPB/FP-223/12.2020). Anastasiia Vasyliki was funded by NANOMED EMJMD supported by the European Union and the Erasmus+ Program by the European Union in the Framework Agreement Number 2016–2057/001–001 EMJMD, No. 574439-EPP-1-FR-EPPKA1-JMD-MOB.

#### CRediT authorship contribution statement

**Vincent Lebreton:** Methodology, Formal analysis, Investigation, Writing – original draft. **Norraseth Kaeokhamloed:** Methodology, Investigation, Writing – original draft. **Anastasiia Vasyliki:** Investigation. **Grégory Hilairet:** Investigation. **Adélie Mellinger:** Investigation.

**Jérôme Béjaud:** Investigation. **Patrick Saulnier:** Supervision, Funding acquisition. **Frédéric Lagarce:** Supervision, Funding acquisition. **Florence Gattacceca:** Formal analysis, Validation, Writing – review & editing. **Samuel Legeay:** Conceptualization, Supervision, Visualization, Writing – review & editing. **Emilie Roger:** Conceptualization, Supervision, Visualization, Writing – review & editing.

#### Declaration of Competing Interest

The authors declare that they have no known competing financial interests or personal relationships that could have appeared to influence the work reported in this paper.

#### Data availability

Data will be made available on request.

#### Appendix A. Supplementary data

Supplementary data to this article can be found online at <https://doi.org/10.1016/j.jconrel.2022.09.057>.

#### References

- [1] B. Heurtault, P. Saulnier, B. Pech, J.-E. Proust, J.-P. Benoit, A novel phase inversion-based process for the preparation of lipid Nanocarriers, *Pharm. Res.* 19 (2002) 875–880, <https://doi.org/10.1023/A:1016121319668>.
- [2] E. Roger, F. Lagarce, E. Garcion, J.P. Benoit, Lipid nanocarriers improve paclitaxel transport throughout human intestinal epithelial cells by using vesicle-mediated transcytosis, *J. Control. Release* 140 (2009) 174–181, <https://doi.org/10.1016/j.jconrel.2009.08.010>.
- [3] D. Urimi, M. Hellsing, N. Mahmoudi, C. Söderberg, R. Widenbring, L. Gedda, K. Edwards, T. Loftsson, N. Schipper, Structural characterization study of a lipid Nanocapsule formulation intended for drug delivery applications using small-angle scattering techniques, *Mol. Pharm.* 19 (2022) 1068–1077, <https://doi.org/10.1021/acs.molpharmaceut.1c00648>.
- [4] N. Kaeokhamloed, E. Roger, J. Béjaud, N. Lautram, F. Manero, R. Perrot, C. Abbara, M. Briet, S. Legeay, New *in vitro* coculture model for evaluating intestinal absorption of different lipid nanocapsules, *Pharmaceutics*. 13 (2021), <https://doi.org/10.3390/pharmaceutics13050595>.
- [5] S. Peltier, J.M. Oger, F. Lagarce, W. Couet, J.P. Benoit, Enhanced oral paclitaxel bioavailability after administration of paclitaxel-loaded lipid nanocapsules, *Pharm. Res.* 23 (2006) 1243–1250, <https://doi.org/10.1007/s11095-006-0022-2>.
- [6] A. Ramadan, F. Lagarce, A. Tessier-Marteanu, O. Thomas, P. Legras, L. Macchi, P. Saulnier, J.P. Benoit, Oral fondaparinux: use of lipid nanocapsules as nanocarriers and *in vivo* pharmacokinetic study, *Int. J. Nanomedicine* (2011), <https://doi.org/10.2147/IJN.S25791>.
- [7] P.E. Pensel, G. Ullio Gamboa, J. Fabbri, L. Ceballos, S. Sanchez Bruni, L.I. Alvarez, D. Allemandi, J.P. Benoit, S.D. Palma, M.C. Elisondo, Cystic echinococcosis therapy: Albendazole-loaded lipid nanocapsules enhance the oral bioavailability and efficacy in experimentally infected mice, *Acta Trop.* (2015), <https://doi.org/10.1016/j.actatropica.2015.09.016>.
- [8] R.O. Amara, A.A. Ramadan, R.M. El-Moslemany, M.M. Eissa, M.Z. El-Azzouni, L. K. El-Khordagui, Praziquantel–lipid nanocapsules: an oral nanotherapeutic with potential *Schistosoma mansoni* tegumental targeting, *Int. J. Nanomedicine* 13 (2018) 4493–4505, <https://doi.org/10.2147/IJN.S167285>.
- [9] A. Singh, Y.R. Neupane, S. Shafi, B. Mangla, K. Kohli, PEGylated liposomes as an emerging therapeutic platform for oral nanomedicine in cancer therapy: *in vitro* and *in vivo* assessment, *J. Mol. Liq.* 303 (2020), <https://doi.org/10.1016/j.molliq.2020.112649>.
- [10] C. Menzel, T. Holzeisen, F. Laffleur, S. Zaichik, M. Abdulkarim, M. Gumblerton, A. Bernkop-Schnürch, *In vivo* evaluation of an oral self-emulsifying drug delivery system (SEDDS) for exenatide, *J. Control. Release* 277 (2018) 165–172, <https://doi.org/10.1016/j.jconrel.2018.03.018>.
- [11] F. Carreño, V.E. Helfer, K.J. Staudt, L.B. Olivo, K. Paese, F.S. Meyer, A. P. Herrmann, S.S. Guterres, S.M.K. Rates, I. Trocóniz, T.D. Costa, Semi-mechanistic pharmacokinetic modeling of lipid core nanocapsules: understanding quetiapine plasma and brain disposition in a neurodevelopmental animal model of schizophrenia, *J. Pharmacol. Exp. Ther.* 375 (2020) 49–58, <https://doi.org/10.1124/JPET.120.000109>.
- [12] H. Guo, J.A. MacKay, A pharmacokinetics primer for preclinical nanomedicine research, in: *Nanoparticles for Biomedical Applications*, Elsevier, 2020, pp. 109–128, <https://doi.org/10.1016/b978-0-12-816662-8.00008-4>.
- [13] G. Yang, Y. Liu, J. Teng, C.-X. Zhao, FRET Ratiometric Nanoprobes for nanoparticle monitoring, *Biosensors*. 11 (2021) 505, <https://doi.org/10.3390/bios11120505>.
- [14] E. Roger, J.C. Gimel, C. Bensley, A.S. Klymchenko, J.P. Benoit, Lipid nanocapsules maintain full integrity after crossing a human intestinal epithelium model, *J. Control. Release* 253 (2017) 11–18, <https://doi.org/10.1016/j.jconrel.2017.03.005>.



- [15] S. Bonnet, R. Elfatairi, F. Franconi, E. Roger, S. Legeay, Organic nanoparticle tracking during pharmacokinetic studies, *Nanomedicine*. 16 (2021), <https://doi.org/10.2217/nmm-2021-0155>, 2539–2536.
- [16] K. Partikel, R. Korte, N.C. Stein, D. Mulac, F.C. Herrmann, H.U. Humpf, K. Langer, Effect of nanoparticle size and PEGylation on the protein corona of PLGA nanoparticles, *Eur. J. Pharm. Biopharm.* 141 (2019) 70–80, <https://doi.org/10.1016/j.ejpb.2019.05.006>.
- [17] J.S. Suk, Q. Xu, N. Kim, J. Hanes, L.M. Ensign, PEGylation as a strategy for improving nanoparticle-based drug and gene delivery, *Adv. Drug Deliv. Rev.* (2016), <https://doi.org/10.1016/j.addr.2015.09.012>.
- [18] A. Vonarbourg, C. Passirani, P. Saulnier, J.P. Benoit, Parameters influencing the stealthiness of colloidal drug delivery systems, *Biomaterials*. 27 (2006) 4356–4373, <https://doi.org/10.1016/j.biomaterials.2006.03.039>.
- [19] V.N. Killin, H. Anton, N. Anton, E. Steed, J. Vermot, T.F. Vandamme, Y. Mely, A. S. Klymchenko, Counterion-enhanced cyanine dye loading into lipid nano-droplets for single-particle tracking in zebrafish, *Biomaterials*. 35 (2014) 4950–4957, <https://doi.org/10.1016/j.biomaterials.2014.02.053>.
- [20] A.L. Lainé, J. Gravier, M. Henry, L. Sancey, J. Béjaud, E. Pancani, M. Wiber, I. Texier, J.L. Coll, J.P. Benoit, C. Passirani, Conventional versus stealth lipid nanoparticles: formulation and in vivo fate prediction through FRET monitoring, *J. Control. Release* (2014), <https://doi.org/10.1016/j.jconrel.2014.05.042>.
- [21] M. Toprak, Fluorescence study on the interaction of human serum albumin with Butein in liposomes, *Spectrochimica Acta - part a: molecular and biomolecular, Spectroscopy*. 154 (2016) 108–113, <https://doi.org/10.1016/j.saa.2015.10.023>.
- [22] S. Seyedi, P. Parvin, A. Jafarholi, A. Abbasian, M. Mehdinejad, A. Khorrami, M. Mehrabi, A. Moafi, Fluorescence emission quenching of RdB fluorophores in attendance of various blood type RBCs based on stern-Volmer formalism, *Spectrochim. Acta A Mol. Biomol. Spectrosc.* 248 (2021), <https://doi.org/10.1016/j.saa.2020.119237>.
- [23] L. Vergori, E. Lauret, R. Soleti, M.C. Martinez, R. Andriantsitohaina, Low concentration of ethanol favors progenitor cell differentiation and neovascularization in high-fat diet-fed mice model, *Int. J. Biochem. Cell Biol.* 78 (2016) 43–51, <https://doi.org/10.1016/j.biocel.2016.07.004>.
- [24] U.S. Food and Drug Administration, Bioanalytical Method Validation Guidance for Industry, U.S. Food and Drug Administration, 2020. <https://www.fda.gov/regulatory-information/search-fda-guidance-documents/bioanalytical-method-validation-guidance-industry> (accessed September 6, 2022).
- [25] EMA, ICH M10 on bioanalytical method validation, European Medicines Agency. <https://www.ema.europa.eu/en/ich-m10-bioanalytical-method-validation>, 2019 (accessed September 6, 2022).
- [26] T. Nishiya, R.T.T. Lam, F. Eng, M. Zerey, S. Lau, Mechanistic study on toxicity of positively charged liposomes containing Stearylamine to blood, *Artif. Cells Blood Substit. Biotechnol.* 23 (1995) 505–512, <https://doi.org/10.3109/10731199509117966>.
- [27] A.C. Groo, M. Bossiere, L. Trichard, P. Legras, J.P. Benoit, F. Lagarce, In vivo evaluation of paclitaxel-loaded lipid nanocapsules after intravenous and oral administration on resistant tumor, *Nanomedicine*. 10 (2015) 589–601, <https://doi.org/10.2217/nmm.14.124>.
- [28] M. Morille, T. Montier, P. Legras, N. Carmoy, P. Brodin, B. Pitard, J.P. Benoit, C. Passirani, Long-circulating DNA lipid nanocapsules as new vector for passive tumor targeting, *Biomaterials*. (2010), <https://doi.org/10.1016/j.biomaterials.2009.09.044>.
- [29] L. Basile, C. Passirani, N.-T. Huynh, J. Béjaud, J.-P. Benoit, G. Puglisi, R. Pignatello, Serum-stable, long-circulating paclitaxel-loaded colloidal carriers decorated with a new amphiphilic PEG derivative, *Int. J. Pharm.* 426 (2012) 231–238, <https://doi.org/10.1016/j.ijpharm.2012.01.038>.
- [30] M. Ichihara, T. Shimizu, A. Imoto, Y. Hashiguchi, Y. Uehara, T. Ishida, H. Kiwada, Anti-PEG IgM response against PEGylated liposomes in mice and rats, *Pharmaceutics*. 3 (2011) 1–11, <https://doi.org/10.3390/pharmaceutics3010001>.
- [31] T. Ishida, H. Kiwada, Accelerated blood clearance (ABC) phenomenon upon repeated injection of PEGylated liposomes, *Int. J. Pharm.* 354 (2008) 56–62, <https://doi.org/10.1016/j.ijpharm.2007.11.005>.
- [32] Y. Hashimoto, T. Shimizu, A.S.A. Lila, T. Ishida, H. Kiwada, Relationship between the concentration of anti-polyethylene glycol (PEG) immunoglobulin M (IgM) and the intensity of the accelerated blood clearance (ABC) phenomenon against PEGylated liposomes in mice, *Biol. Pharm. Bull.* 38 (2015) 417–424, <https://doi.org/10.1248/bpb.b14-00653>.
- [33] C. Li, J. Cao, Y. Wang, X. Zhao, C. Deng, N. Wei, J. Yang, J. Cui, Accelerated blood clearance of pegylated liposomal topotecan: influence of polyethylene glycol grafting density and animal species, *J. Pharm. Sci.* 101 (2012) 3864–3876, <https://doi.org/10.1002/jps.23254>.
- [34] S. Hirsjärvi, L. Sancey, S. Dufort, C. Belloche, C. Vanpouille-Box, E. Garcion, J.-L. Coll, F. Hindré, J.-P. Benoit, Effect of particle size on the biodistribution of lipid nanocapsules: comparison between nuclear and fluorescence imaging and counting, *Int. J. Pharm.* 453 (2013) 594–600, <https://doi.org/10.1016/j.ijpharm.2013.05.057>.
- [35] H. Lee, H. Fonge, B. Hoang, R.M. Reilly, C. Allen, The effects of particle size and molecular targeting on the intratumoral and subcellular distribution of polymeric nanoparticles, *Mol. Pharm.* 7 (2010) 1195–1208, <https://doi.org/10.1021/mp100038h>.
- [36] S. Hirsjärvi, S. Dufort, J. Gravier, I. Texier, Q. Yan, J. Bibette, L. Sancey, V. Josserand, C. Passirani, J.P. Benoit, J.L. Coll, Influence of size, surface coating and fine chemical composition on the in vitro reactivity and in vivo biodistribution of lipid nanocapsules versus lipid nanoemulsions in cancer models, *Nanomedicine* (2013), <https://doi.org/10.1016/j.nano.2012.08.005>.
- [37] C.F. Adhipandito, S.H. Cheung, Y.H. Lin, S.H. Wu, Atypical renal clearance of nanoparticles larger than the kidney filtration threshold, *Int. J. Mol. Sci.* 22 (2021), <https://doi.org/10.3390/ijms222011182>.
- [38] N. Hoshiyar, S. Gray, H. Han, G. Bao, The effect of nanoparticle size on in vivo pharmacokinetics and cellular interaction, *Nanomedicine*. 11 (2016) 673–692, <https://doi.org/10.2217/nmm.16.5>.
- [39] R.M. Pearson, H.J. Hsu, J. Bugno, S. Hong, Understanding nano-bio interactions to improve nanocarriers for drug delivery, *MRS Bull.* 39 (2014) 227–237, <https://doi.org/10.1557/mrs.2014.9>.
- [40] A. Gabizon, D. Tzemach, L. Mak, M. Bronstein, A.T. Horowitz, Dose dependency of pharmacokinetics and therapeutic efficacy of Pegylated liposomal doxorubicin (DOXIL) in murine models, *J. Drug Target.* 10 (2002) 539–548, <https://doi.org/10.1080/1061186021000072447>.
- [41] H. Wu, J.R. Infante, V.L. Keedy, S.F. Jones, E. Chan, J.C. Bendell, W. Lee, B. A. Zamboni, S. Ikeda, H. Kodaira, M.L. Rothenberg, H.A. Burris, W.C. Zamboni, Population pharmacokinetics of PEGylated liposomal CPT-11 (IHL-305) in patients with advanced solid tumors, *Eur. J. Clin. Pharmacol.* 69 (2013) 2073–2081, <https://doi.org/10.1007/s00228-013-1580-y>.
- [42] M. Danaei, M. Dehghankhold, S. Ataei, F. Hasanzadeh Davarani, R. Javanmard, A. Dokhani, S. Khorasani, M.R. Mozafari, Impact of particle size and polydispersity index on the clinical applications of lipidic nanocarrier systems, *Pharmaceutics*. 10 (2018), <https://doi.org/10.3390/pharmaceutics10020057>.
- [43] D. Yuan, H. He, Y. Wu, J. Fan, Y. Cao, Physiologically based pharmacokinetic modeling of nanoparticles, *J. Pharm. Sci.* 108 (2019) 58–72, <https://doi.org/10.1016/j.xphs.2018.10.037>.
- [44] J.H. Byun, D.G. Han, H.J. Cho, I.S. Yoon, I.H. Jung, Recent advances in physiologically based pharmacokinetic and pharmacodynamic models for anticancer nanomedicines, *Arch. Pharm. Res.* 43 (2020) 80–99, <https://doi.org/10.1007/s12272-020-01209-2>.
- [45] A. Gabizon, H. Shmueda, Y. Barenholz, Pharmacokinetics of Pegylated liposomal doxorubicin, *Clin. Pharmacokinet.* 42 (2003) 419–436, <https://doi.org/10.2165/00003088-200342050-00002>.
- [46] R.J. Probst, J.M. Lim, D.N. Bird, G.L. Pole, A.K. Sato, J.R. Claybaugh, Gender differences in the blood volume of conscious Sprague-Dawley rats, *J. Am. Assoc. Lab. Anim. Sci.* 45 (2006) 49–52.
- [47] J. Gravier, L. Sancey, S. Hirsjärvi, E. Rustique, C. Passirani, J.P. Benoit, J.L. Coll, I. Texier, FRET imaging approaches for in vitro and in vivo characterization of synthetic lipid nanoparticles, *Mol. Pharm.* 11 (2014) 3133–3144, <https://doi.org/10.1021/mp500329z>.
- [48] R. Bouchaala, L. Mercier, B. Andreiuk, Y. Mély, T. Vandamme, N. Anton, J. G. Goetz, A.S. Klymchenko, Integrity of lipid nanocarriers in bloodstream and tumor quantified by near-infrared ratiometric FRET imaging in living mice, *J. Control. Release* 236 (2016) 57–67, <https://doi.org/10.1016/j.jconrel.2016.06.027>.
- [49] F. Cayre, S. Mura, B. Andreiuk, D. Sobot, S. Gouazou, D. Desmaële, A. S. Klymchenko, P. Couvreur, In vivo FRET imaging to predict the risk associated with hepatic accumulation of squalene-based prodrug nanoparticles, *Adv. Healthc. Mater.* 7 (2018), <https://doi.org/10.1002/adhm.201700830>.
- [50] F.F. Davis, The origin of pegnology, *Adv. Drug Deliv. Rev.* 54 (2002) 457–458, [https://doi.org/10.1016/S0169-409X\(02\)00021-2](https://doi.org/10.1016/S0169-409X(02)00021-2).
- [51] K. Park, Impact of anti-PEG antibodies on PEGylated nanoparticles fate in vivo, *J. Control. Release* 287 (2018) 257, <https://doi.org/10.1016/j.jconrel.2018.09.014>.
- [52] L.A.S. Bahari, H. Hamishehkar, The impact of variables on particle size of solid lipid nanoparticles and nanostructured lipid carriers: A comparative literature review, *Adv. Pharm. Bull.* 6 (2016) 143–151, <https://doi.org/10.1517/apb.2016.021>.
- [53] H. Park, A. Otte, K. Park, Evolution of drug delivery systems: from 1950 to 2020 and beyond, *J. Control. Release* (2021), <https://doi.org/10.1016/j.jconrel.2021.12.030>.
- [54] T.M. Blättler, S. Pasche, M. Textor, H.J. Griesser, High salt stability and protein resistance of poly(L-lysine)-g-poly(ethylene glycol) copolymers covalently immobilized via aldehyde plasma polymer interlayers on inorganic and polymeric substrates, *Langmuir*. 22 (2006) 5760–5769, <https://doi.org/10.1021/la0602766>.

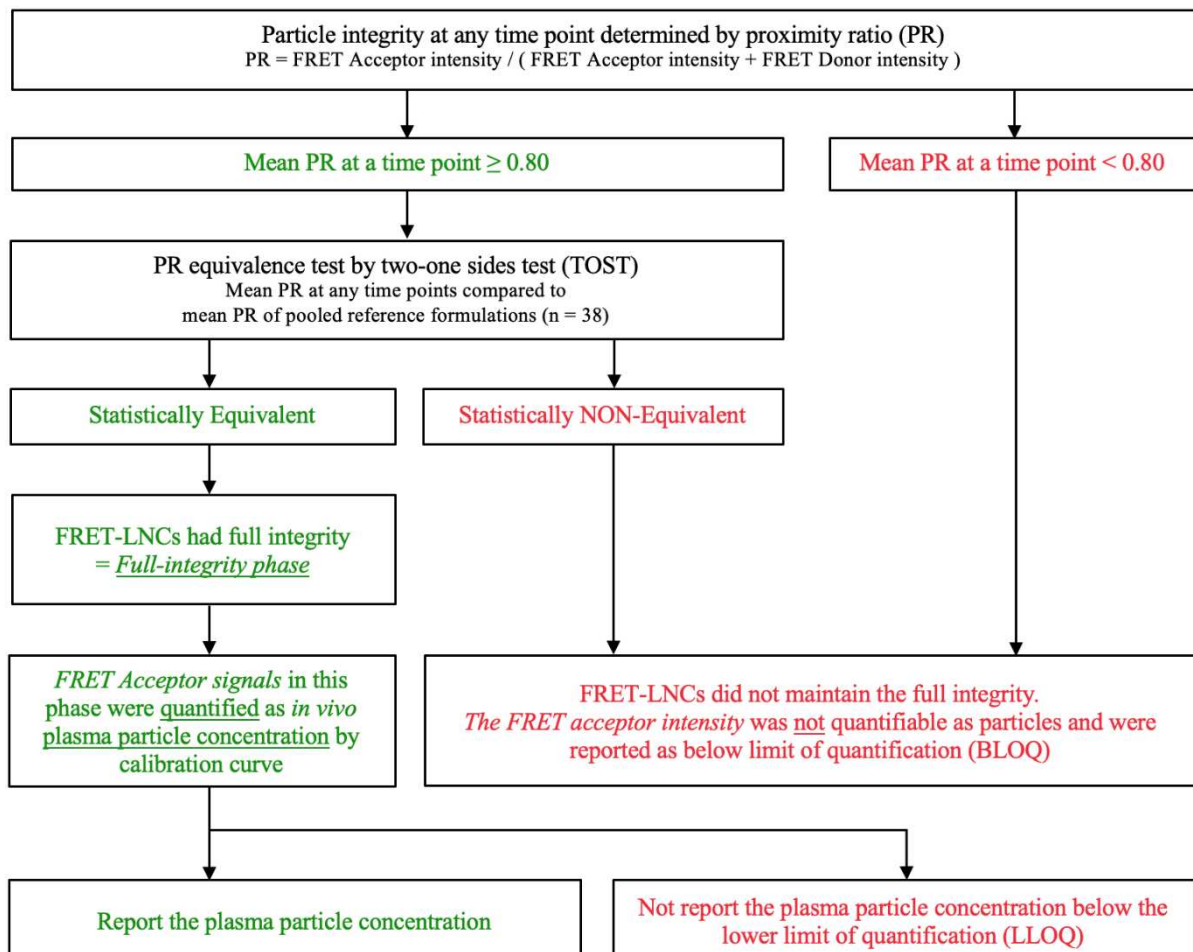
## Supplementary data

### Supplementary S1. Particle integrity criteria

It is rationalized that only the FRET-LNCs whose integrity is equivalent to that of the original formulations are quantified for the particle concentration to ensure that the FRET-LNCs plasma particle concentration-time profile represents only the FRET-LNCs that retained their physicochemical properties. Therefore, to ensure that only the FRET acceptor intensity of fully-intact FRET-LNCs was quantified as particle concentration, FRET-LNCs particle integrity at any time point was determined by PR with the equivalence test.

The PR equivalence test was performed by the two one-sided tests (TOST). The mean PR at any time point ( $\mu_{sample}$ ) was statistically compared to the mean PR of the pooled reference formulations ( $\mu_{ref}$ ) in terms of the difference between group means with a 90% confidence interval (90% CI). It was found that  $\mu_{ref} = 0.894$  with the standard deviation  $\sigma_{ref} = 0.032$ . The equivalence range ( $\Delta$ ) was set to be  $\Delta = \pm 5\sigma_{ref}$  which equals  $\Delta = \pm 0.16$ . In conclusion, the equivalence limit can be concluded and restated as: the time point whose 90% CI of the difference between groups means  $\leq 0.16$  being considered statistically equivalent and thus be included in the *full-integrity phase*.

The plasma particle concentration was reported according to the following approach.



Scheme S1. Algorithm for FRET-LNCs particle concentration quantification procedure.

**Supplementary S2. Photo of LNC particles captured by NTA**

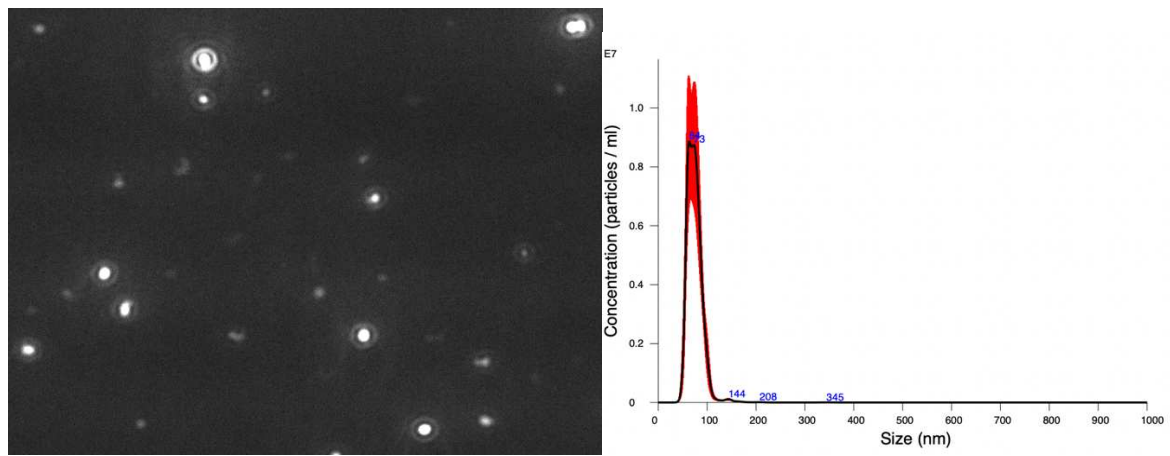


**Figure S2.** Photo of LNC-85 extracted from a 60-second video image provided by the Nanoparticle Tracking Analysis System (NTA) (left); Size analysis generated from the video clip by NTA (right); given as an example.

### Supplementary S3. FRET donor and FRET acceptor spectra

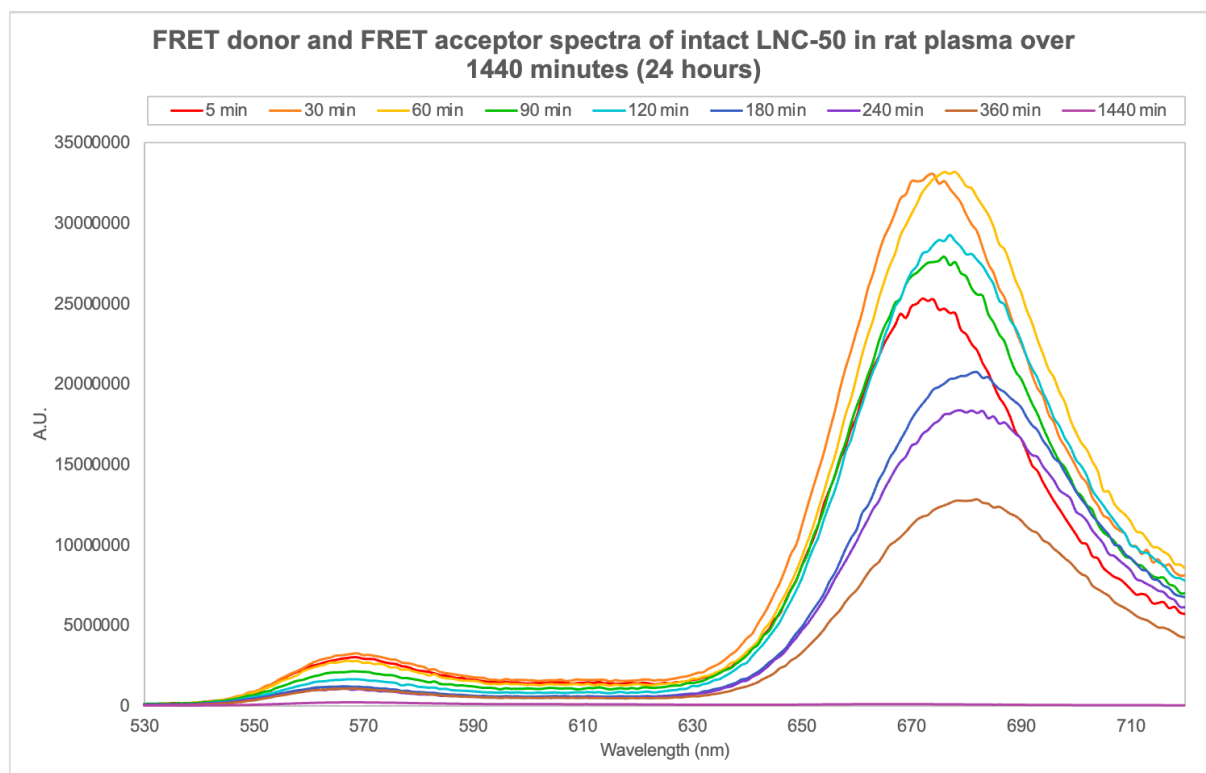


**Figure S3.** Example of emission spectra of FRET-LNCs-50 of rat plasma at time points 5, 30, 60, 90, 120, 180, 240, 360, and 1440 min (a reference to color in the figure legend). Emission spectra were recorded using  $\lambda_{\text{ex}} = 548 \text{ nm}$ , the same fluorimeter setting, and the same 4-fold dilution of extracted samples in water. Consequently, absolute intensity could be compared.

FRET donor (~570 nm) and FRET acceptor (~670 nm) spectra of intact LNC-50

## Supplementary S4. Calibration curves analysis

Calibration curves for each FRET-LNCs formulation were prepared in blood and water. Curve fitting equations were determined, and the matrix effect on the FRET acceptor intensity was studied (n = 1). % Matrix effect (%ME) was determined by the % relative error of the slope of the matrix-matched calibration curve (in blood) vs. the slope of the calibration curve in water.

$$\%ME = 100 \times \left( \frac{\text{Slope}_{\text{blood}} - \text{Slope}_{\text{water}}}{\text{Slope}_{\text{water}}} \right)$$

The preliminary result (Figure S4, Table S4) found that blood obviously had a matrix effect on the calibration curve, with %ME ranging between -10% to 20%.

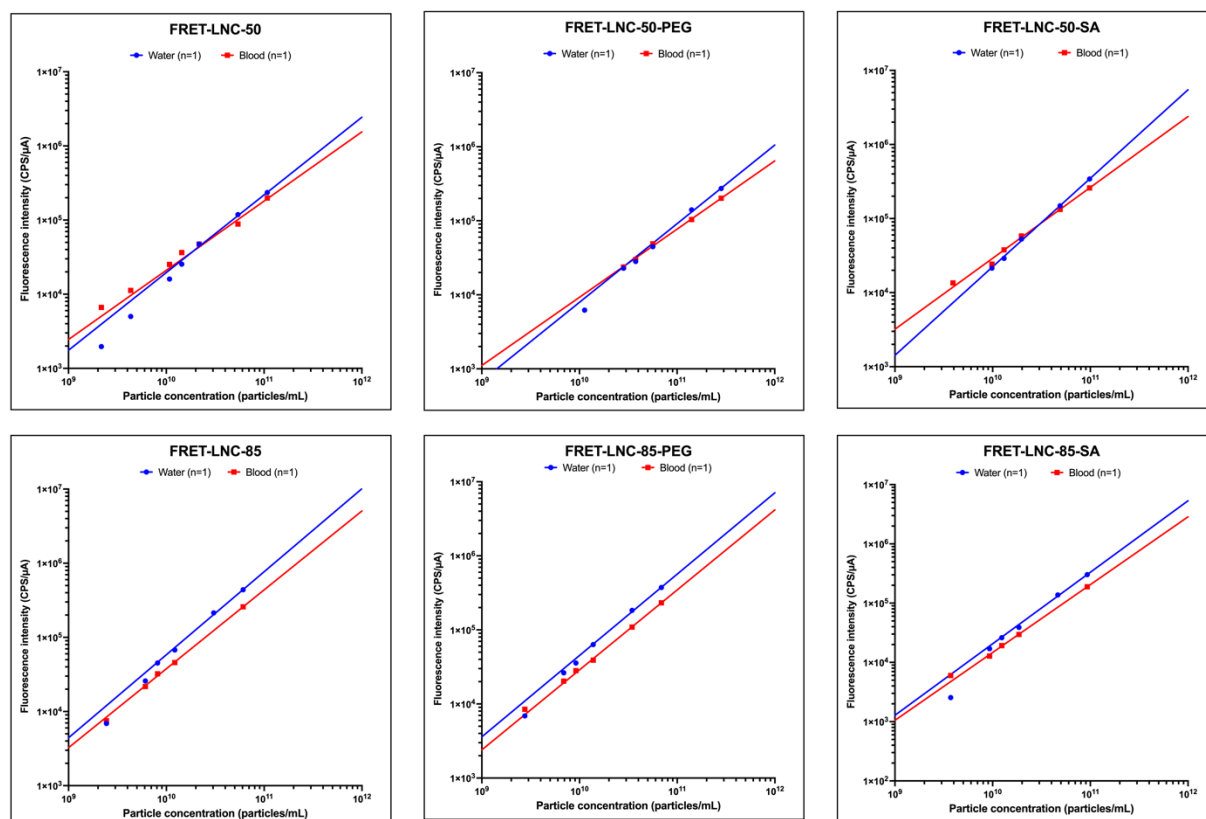


**Figure S4.** Calibration curve of particle concentration of FRET-LNCs in water (blue line) and in blood (red line) for preliminary study (n = 1) on matrix effect of blood.

**Table S4.** Calibration curve fitting and linearity of FRET-LNCs formulations in water and in blood.

FRET Formulation	Medium	Calibration curve fitting equation				%ME
		Intercept (k)	Slope (m)	Equation	R <sup>2</sup>	
LNC-50	Water	-6.81	1.047	$F_A = 10^{-7.19} \times C^{1.079}$	0.998	-10.9
	Blood	-5.57	0.933	$F_A = 10^{-5.57} \times C^{0.933}$	0.990	
LNC-50-PEG	Water	-5.83	0.924	$F_A = 10^{-7.19} \times C^{1.079}$	0.924	14.7
	Blood	-7.34	1.060	$F_A = 10^{-7.34} \times C^{1.060}$	0.997	
LNC-50-SA	Water	-8.34	1.197	$F_A = 10^{-7.19} \times C^{1.079}$	1.000	20.0
	Blood	-5.70	0.958	$F_A = 10^{-5.70} \times C^{0.958}$	0.999	
LNC-85	Water	-7.11	1.120	$F_A = 10^{-7.19} \times C^{1.079}$	0.998	4.1
	Blood	-7.87	1.166	$F_A = 10^{-7.87} \times C^{1.166}$	0.993	
LNC-85-PEG	Water	-6.97	1.097	$F_A = 10^{-7.19} \times C^{1.079}$	0.999	-1.6
	Blood	-6.98	1.079	$F_A = 10^{-6.98} \times C^{1.079}$	1.000	
LNC-85-SA	Water	-8.43	1.207	$F_A = 10^{-7.19} \times C^{1.079}$	0.999	-5.1
	Blood	-7.92	1.145	$F_A = 10^{-7.92} \times C^{1.145}$	1.000	

### Supplementary S5: Proximity ratio-time profile of 50 and 85-nm FRET-LNCs

PR-time profile (the first criterion) is shown in Figure S5A, S5B, and the equivalence test (TOST) result (the second criterion) is shown in Figure S5C, S5D. Judging from these two criteria, the *full-integrity phase* of LNC-50 and LNC-50-SA lasted until 6 hours, whilst LNC-50-PEG only lasted until 3 hours. On the other hand, the *full-integrity phase* of 85-nm FRET-LNCs, regardless of the surface modification, lasted until 10 hours. Besides, the re-injection on day 7 did not substantially change the PR-time profile nor the duration of the *full-integrity phase*, suggesting that re-injection on day 7 did not affect the *in vivo* particle integrity of FRET-LNCs.

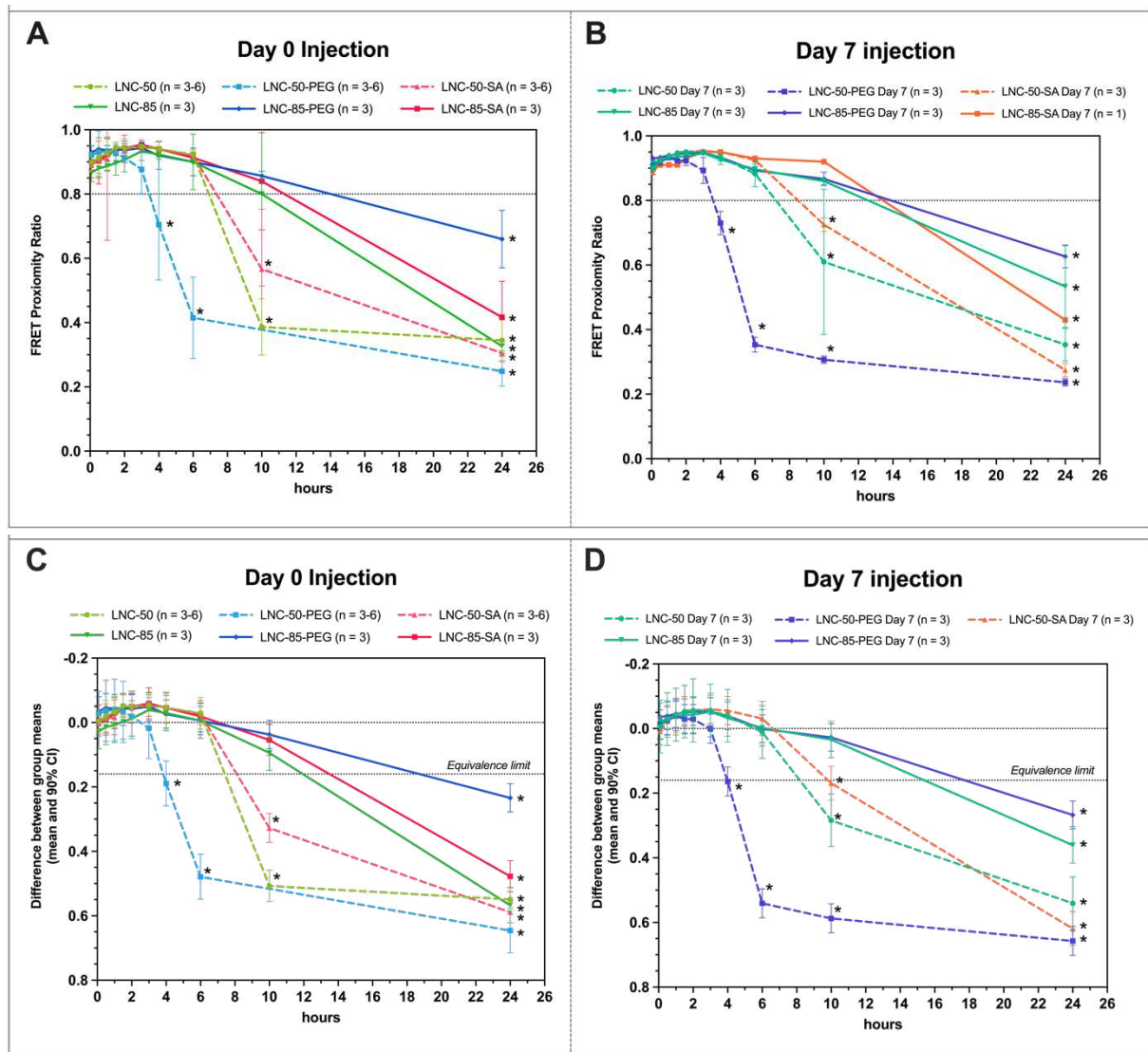


**Figure S5.** (A) and (B) The first criterion for quantification: Proximity ratio-time profile of 50-nm and 85-nm FRET-LNCs following the IV bolus at day-0 injection and day-7 injection. Data is reported as the arithmetic means with standard deviation (whisker). The line at PR = 0.80 determines the first criterion for quantification, that the mean PR  $\geq$  0.80. The asterisks signify the time point not passing the criterion; (C) and (D) the second criterion for quantification: Equivalence test result by TOST of 50-nm and 85-nm FRET-LNCs following the IV bolus at day-0 injection and day-7 injection. Data is reported as the difference between group means with 90% CI (whisker). The line at 0.16 signifies the lower equivalence limit. The asterisks signify the time point deemed statistically non-equivalent. Data from LNC-85-SA on day-7 was not included in TOST because it has n = 1, and was judged by the first criterion only.

## Supplementary S6: Population pharmacokinetic modeling (PKpop)

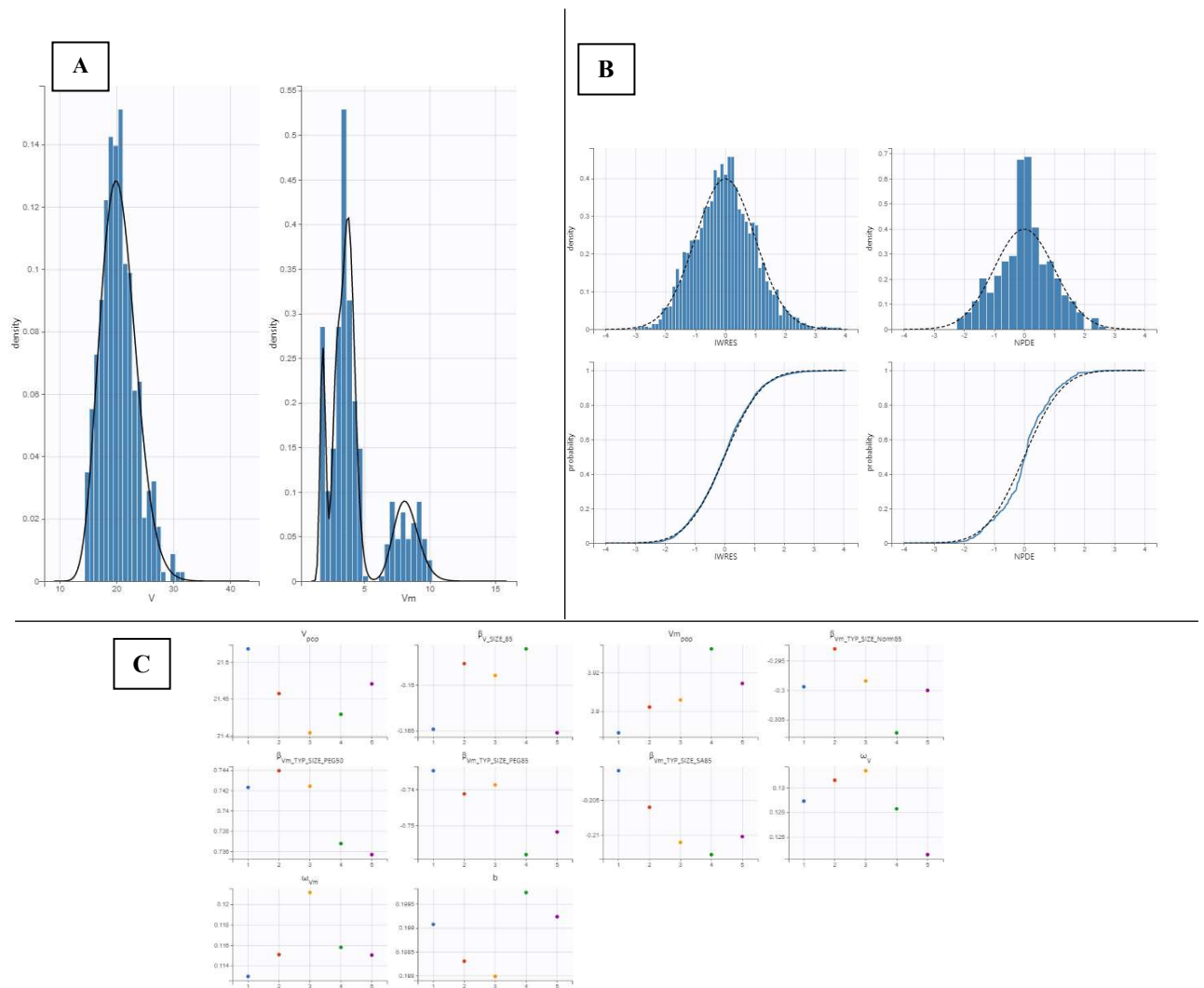


**Figure S6.** Supplementary diagnostic plots of the final model with covariates.  $V$  volume of distribution (mL).  $V_m$  maximal rate of the kinetics (Tp/min).  $\beta$  covariate effect. IWRES individual weighted residuals. NPDE normalized prediction distribution errors.  $b$  proportional residual error. A) Distribution of individual parameters  $V$  (left) and  $V_m$  (right). Solid line: theoretical distribution. Histograms: empirical distribution. B) Distribution density (up) and cumulative probability (down) of IWRES (left) and NPDE (right). Dotted lines: theoretical distribution. Histograms or solid blue line: empirical distribution. C) Stability assessment: parameters estimates from 5 runs with initial values of  $V$  between 11.89 and 32.33 mL and initial values of  $V_m$  between 1.21 and 3.30 Tp/min.

## Unpublished Supplementary data

### Supplementary S7. Calibration curve fitting equation of each formulation

Calibration curves fitting equation and linearity of all FRET-LNCs formulation in blood (*in vitro* and *in vivo* experiment) are listed in Table S3; in PBS (*in vitro* experiment) are listed in Table S4. All the calibration curves had linearity >0.980.

**Table S7-1.** Calibration curve fitting equation and linearity of FRET-LNCs in blood

FRET Formulation	Calibration curve fitting equation in blood			
	Intercept (k)	Slope (m)	Equation	R <sup>2</sup>
LNC-50	-7.19	1.079	$F_A = 10^{-7.19} \times C^{1.079}$	0.996
	-4.82	0.876	$F_A = 10^{-4.82} \times C^{0.876}$	0.997
	-5.57	0.933	$F_A = 10^{-5.57} \times C^{0.933}$	0.990
	-5.06	0.892	$F_A = 10^{-5.06} \times C^{0.892}$	0.989
	-5.77	0.965	$F_A = 10^{-5.77} \times C^{0.965}$	1.000
	-5.91	0.974	$F_A = 10^{-5.91} \times C^{0.974}$	0.998
	-6.22	0.974	$F_A = 10^{-6.22} \times C^{0.974}$	1.000
LNC-50-PEG	-6.18	0.971	$F_A = 10^{-6.18} \times C^{0.971}$	1.000
	-4.80	0.832	$F_A = 10^{-4.80} \times C^{0.832}$	0.984
	-7.34	1.060	$F_A = 10^{-7.34} \times C^{1.060}$	0.997
	-5.21	0.873	$F_A = 10^{-5.21} \times C^{0.873}$	0.997
	-6.81	1.026	$F_A = 10^{-6.81} \times C^{1.026}$	1.000
LNC-50-SA	-5.86	0.983	$F_A = 10^{-5.86} \times C^{0.983}$	0.991
	-5.89	0.972	$F_A = 10^{-5.89} \times C^{0.972}$	0.999
	-5.88	0.966	$F_A = 10^{-5.88} \times C^{0.966}$	1.000
	-5.70	0.958	$F_A = 10^{-5.70} \times C^{0.958}$	0.999
	-5.12	0.888	$F_A = 10^{-5.12} \times C^{0.888}$	0.998
LNC-85	-6.47	1.039	$F_A = 10^{-6.47} \times C^{1.039}$	1.000
	-8.38	1.209	$F_A = 10^{-8.38} \times C^{1.209}$	0.997
	-7.87	1.166	$F_A = 10^{-7.87} \times C^{1.166}$	0.993
	-5.56	0.978	$F_A = 10^{-5.56} \times C^{0.978}$	0.999
LNC-85-PEG	-6.98	1.079	$F_A = 10^{-6.98} \times C^{1.079}$	1.000
	-8.67	1.229	$F_A = 10^{-8.67} \times C^{1.229}$	0.991
	-5.63	0.992	$F_A = 10^{-5.63} \times C^{0.992}$	1.000
LNC-85-SA	-7.92	1.145	$F_A = 10^{-7.92} \times C^{1.145}$	1.000
	-7.79	1.165	$F_A = 10^{-7.79} \times C^{1.165}$	0.997
	-6.50	1.066	$F_A = 10^{-6.50} \times C^{1.066}$	1.000

**Table S7-2.** Calibration curve fitting equation and linearity of FRET-LNCs in PBS.

FRET Formulation	Calibration curve fitting equation in PBS			
	Intercept (k)	Slope (m)	Equation	R <sup>2</sup>
LNC-50	-9.71	1.303	$F_A = 10^{-9.71} \times C^{1.303}$	0.999
LNC-50-PEG	-7.82	1.122	$F_A = 10^{-7.82} \times C^{1.122}$	0.996
LNC-50-SA	-8.54	1.190	$F_A = 10^{-8.54} \times C^{1.190}$	0.998
LNC-85	-7.64	1.179	$F_A = 10^{-7.64} \times C^{1.179}$	0.998
LNC-85-PEG	-7.68	1.196	$F_A = 10^{-7.68} \times C^{1.196}$	1.000
LNC-85-SA	-9.14	1.316	$F_A = 10^{-9.14} \times C^{1.316}$	0.994



## Supplementary S8. Determination of LOD

EMA and USFDA guidelines were adapted for the determination of the limit of detection (LOD) of each FRET-LNCs formulation. The LOD was determined by two parameters: the particle integrity and the % accuracy. The particle integrity was determined by the mean proximity ratio (PR), and % accuracy was determined by % relative error as in the equation S6:

$$\%RE = 100 \times \left( \frac{C_{\text{back-calculation}} - C_{\text{nominal}}}{C_{\text{nominal}}} \right) \quad (\text{equation S6})$$

Where  $C_{\text{nominal}}$  is the mean nominal (true) particle concentration;  $C_{\text{back-calculation}}$  is the mean particle concentration back-calculated from the calibration curve fitting equation. The calculation was done at least in triplicate. The nominal particle concentration was calculated as the mean due to the variation of the particle concentration in each FRET-LNCs formulation.

Each calibration standard was calculated for the PR and %RE. The LOD is defined as having PR  $\geq 0.80$  [3,4] and %RE within  $\pm 20\%$  range. The PR  $\geq 0.80$  ensures FRET-LNCs having full integrity as only the fully intact FRET-LNCs are quantified by our method.

The mean PR and %RE of each calibration standard of each FRET-LNCs formulations are detailed in Table S5–S10, with the LOD particle concentration signified in the table. The LOD of each formulation is summarized in Table S11. Particle concentration is expressed as a unit of Tp/mL =  $10^{12}$  particles/mL. The LOD was found to range from  $1.68 \times 10^{-2}$  to  $4.10 \times 10^{-2}$  Tp/mL, which is around  $2 \times 10^3$  times lower than the plasma concentration of the injected dose.

**Table S8-1.** Determination of LOD for FRET-LNC-50 (n=7).

Dilution factor ( $10^3$ )	Mean Nominal particle concentration (Tp/mL)	Mean Back-calculation particle concentration (Tp/mL)	Mean proximity ratio	%RE	Note
50.0	$8.42 \times 10^{-3}$	$1.12 \times 10^{-2}$	0.75	32.9	Excluded (PR < 0.80)
20.0	$1.68 \times 10^{-2}$	$1.84 \times 10^{-2}$	0.81	9.0	LOD
10.0	$4.55 \times 10^{-2}$	$4.68 \times 10^{-2}$	0.90	2.9	
7.5	$5.83 \times 10^{-2}$	$5.91 \times 10^{-2}$	0.89	1.3	
5.0	$8.42 \times 10^{-2}$	$8.51 \times 10^{-2}$	0.92	1.0	
2.0	$2.11 \times 10^{-1}$	$2.09 \times 10^{-1}$	0.93	-0.6	
1.0	$4.21 \times 10^{-1}$	$4.22 \times 10^{-1}$	0.94	0.1	

Tp =  $10^{12}$  particles/mL

**Table S8-2.** Determination of LOD for FRET-LNC-50-PEG (n=5).

Dilution factor ( $10^3$ )	Mean Nominal particle concentration (Tp/mL)	Mean Back-calculation particle concentration (Tp/mL)	Mean proximity ratio	%RE	Note
50.0	$2.05 \times 10^{-2}$	$1.84 \times 10^{-2}$	0.74	-9.93	Excluded (PR < 0.80)
20.0	$4.10 \times 10^{-2}$	$3.45 \times 10^{-2}$	0.80	-15.74	LOD
10.0	$1.02 \times 10^{-2}$	$9.54 \times 10^{-2}$	0.88	-6.82	
7.5	$1.37 \times 10^{-1}$	$1.25 \times 10^{-1}$	0.90	-8.75	
5.0	$2.05 \times 10^{-1}$	$1.96 \times 10^{-1}$	0.92	-4.42	
2.0	$5.12 \times 10^{-1}$	$5.45 \times 10^{-1}$	0.93	6.47	
1.0	1.02	1.01	0.93	-1.23	

Tp =  $10^{12}$  particles/mL

**Table S8-3.** Determination of LOD for FRET-LNC-50-SA (n=5).

Dilution factor (10 <sup>3</sup> )	Mean Nominal particle concentration (Tp/mL)	Mean Back-calculation particle concentration (Tp/mL)	Mean proximity ratio	%RE	Note
50.0	$8.69 \times 10^{-3}$	$8.18 \times 10^{-3}$	0.74	-5.89	Excluded (PR < 0.80)
20.0	$1.74 \times 10^{-2}$	$1.74 \times 10^{-2}$	0.81	0.08	LOD
10.0	$4.35 \times 10^{-2}$	$4.48 \times 10^{-2}$	0.88	3.00	
7.5	$5.80 \times 10^{-2}$	$5.68 \times 10^{-2}$	0.89	-2.09	
5.0	$8.69 \times 10^{-2}$	$8.67 \times 10^{-2}$	0.91	-0.21	
2.0	$2.17 \times 10^{-1}$	$2.18 \times 10^{-1}$	0.92	0.41	
1.0	$4.35 \times 10^{-1}$	$4.34 \times 10^{-1}$	0.93	-0.07	

Tp = 10<sup>12</sup> particles/mL**Table S8-4.** Determination of LOD for FRET-LNC-85 (n=4).

Dilution factor (10 <sup>3</sup> )	Mean Nominal particle concentration (Tp/mL)	Mean Back-calculation particle concentration (Tp/mL)	Mean proximity ratio	%RE	Note
50.0	$5.48 \times 10^{-3}$	$8.65 \times 10^{-3}$	0.71	57.96	Excluded (PR < 0.80)
20.0	$1.10 \times 10^{-2}$	$1.38 \times 10^{-2}$	0.79	25.80	Excluded (PR < 0.80)
10.0	$2.74 \times 10^{-2}$	$2.89 \times 10^{-2}$	0.87	5.53	LOD
7.5	$3.65 \times 10^{-2}$	$4.03 \times 10^{-2}$	0.88	10.38	
5.0	$5.48 \times 10^{-2}$	$5.68 \times 10^{-2}$	0.90	3.83	
2.0	$1.37 \times 10^{-1}$	$1.34 \times 10^{-1}$	0.92	-2.44	
1.0	$2.74 \times 10^{-1}$	$2.75 \times 10^{-1}$	0.93	0.30	

Tp = 10<sup>12</sup> particles/mL**Table S8-5.** Determination of LOD for FRET-LNC-85-PEG (n=3).

Dilution factor (10 <sup>3</sup> )	Mean Nominal particle concentration (Tp/mL)	Mean Back-calculation particle concentration (Tp/mL)	Mean proximity ratio	%RE	Note
50.0	$4.66 \times 10^{-3}$	$7.65 \times 10^{-3}$	0.73	64.13	Excluded (PR < 0.80)
20.0	$9.32 \times 10^{-3}$	$1.26 \times 10^{-2}$	0.83	35.49	Excluded (%RE > 20%)
10.0	$2.33 \times 10^{-2}$	$2.78 \times 10^{-2}$	0.88	19.50	LOD
7.5	$3.11 \times 10^{-2}$	$3.50 \times 10^{-2}$	0.90	12.57	
5.0	$4.66 \times 10^{-2}$	$4.84 \times 10^{-2}$	0.91	3.84	
2.0	$1.16 \times 10^{-1}$	$1.12 \times 10^{-1}$	0.93	-4.15	
1.0	$2.33 \times 10^{-1}$	$2.34 \times 10^{-1}$	0.94	0.59	

Tp = 10<sup>12</sup> particles/mL

**Table S8-6.** Determination of LOD for FRET-LNC-85-SA (n=3).

Dilution factor (10 <sup>3</sup> )	Mean Nominal particle concentration (Tp/mL)	Mean Back-calculation particle concentration (Tp/mL)	Mean proximity ratio	%RE	Note
50.0	$4.70 \times 10^{-3}$	$7.72 \times 10^{-3}$	0.68	64.31	Excluded (PR < 0.80)
20.0	$9.40 \times 10^{-3}$	$1.23 \times 10^{-2}$	0.79	31.20	Excluded (PR < 0.80)
10.0	$2.35 \times 10^{-2}$	$2.32 \times 10^{-2}$	0.85	-1.24	LOD
7.5	$3.13 \times 10^{-2}$	$3.34 \times 10^{-2}$	0.88	6.64	
5.0	$4.70 \times 10^{-2}$	$4.90 \times 10^{-2}$	0.89	4.31	
2.0	$9.13 \times 10^{-2}$	$8.76 \times 10^{-2}$	0.92	-4.00	
1.0	$2.35 \times 10^{-1}$	$2.36 \times 10^{-1}$	0.94	0.28	

Tp = 10<sup>12</sup> particles/mL**Table S8-7.** Summary of LOD in blood.

FRET Formulation	LOD (Tp/mL)
LNC-50	$1.68 \times 10^{-2}$
LNC-50-PEG	$4.10 \times 10^{-2}$
LNC-50-SA	$1.74 \times 10^{-2}$
LNC-85	$2.74 \times 10^{-2}$
LNC-85-PEG	$2.33 \times 10^{-2}$
LNC-85-SA	$2.35 \times 10^{-2}$

Tp = 10<sup>12</sup> particles/mL

## Chapter 3: *In vivo* oral absorption of intact LNCs

In **Chapter 1**, the *in vitro* absorption study of intact LNCs found that less than 0.3% of intact LNCs crossed the Caco-2 and Caco-2/HMEC-1 cell membranes [128,133]. It is necessary to investigate the mechanisms of *in vivo* absorption of intact LNCs across GI barriers.

In **Chapter 2**, the quantitative FRET technique was successfully developed for quantifying intact FRET-LNCs in blood samples allowing for the plasma particle concentration of intact FRET-LNCs to be measured and paving the way for the bioavailability study. Recently, in an unpublished work by Elfatairi *et al.* [134], quantitative FRET was successfully adapted for liver, lungs, and spleen tissue samples, providing the method for a biodistribution study of intact LNCs.

In this chapter, oral bioavailability and biodistribution of intact FRET-LNCs after oral administration are evaluated by quantitative FRET for the following aspects:

- 1) the nanoparticle concentration of intact FRET-LNCs in the systemic circulation as oral bioavailability.
- 2) the nanoparticle concentration of intact FRET-LNCs in the hepatic portal system (small intestinal tissue, liver, portal vein's blood)
- 3) the remaining intact FRET-LNCs after digestion in feces and the behavior of FRET-LNCs in the GI.

These experiments are rationalized also based on the pathway of drug oral absorption: xenobiotics absorbs through the intestinal barriers to the mesenteric vein and then altogether in the portal vein and finally enter the liver before entering the systemic circulation, also known as the hepatic portal system [20,135,136] (**figure 5**). It could be hypothesized that during the absorption process, the intact LNCs (if absorbed) accumulate over time with higher concentration in the hepatic portal system than in the systemic circulation and thus intact LNCs will be more easily detectable here. On the other hand, the remaining intact LNCs in feces was investigated, because in the bioavailability assay, we observed that the feces of the rat after orally given by FRET-LNCs were lightly purple, which is the color of the FRET dyes used for the LNC's quantitative FRET assay. It was hypothesized that the purple color in the rat feces could be a result of either intact FRET-LNCs that were not absorbed and survived the digestion, or the trace of destroyed FRET-LNCs. The information about the remaining FRET-LNCs in the feces could also be compared to the information of the absorbed LNCs. Moreover, in order to quantify the intact FRET-LNCs in the hepatic portal system and feces, the quantitative FRET technique is needed to be adapted for liver, intestinal tissue, and feces. For liver, the quantitative FRET technique has already been developed by Elfatairi *et al.* [134] in an unpublished

Master's dissertation. For intestinal tissue and feces sample, the new quantitative FRET technique was developed in this thesis.

The study in this chapter is presented as a manuscript for future publication.

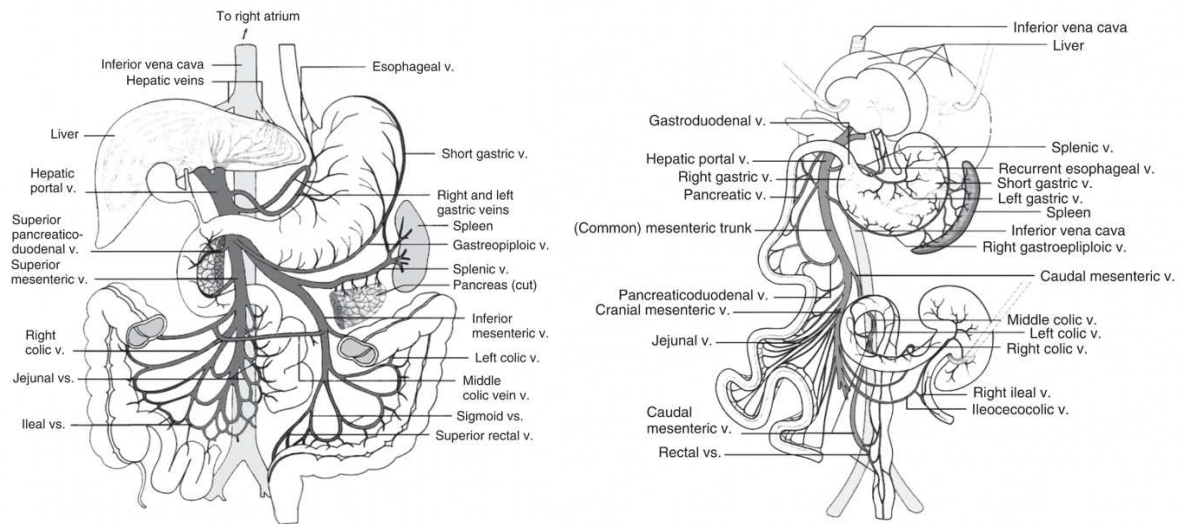


**Figure 5.** The Illustrations show the similarity between the hepatic portal system of (left) human and (right) rat (the animal model used in this thesis). Drugs and xenobiotics are absorbed through the intestinal tissue entering the mesenteric vein, portal vein, and liver before the systemic circulation [135,136]. Reprinted form DeSesso et al. [20].

# Evidence from quantitative FRET suggests intact lipid nanocapsules not absorbing via rat's GI

Norraseth Kaeokhamloed<sup>1</sup>, Vincent Lebreton<sup>1, 2</sup>, Thomas James Bennett<sup>3</sup>, Rana Elfatairi<sup>1</sup>  
Adélie Mellinger<sup>1</sup>, Jérôme Béjaud<sup>1</sup>, Samuel Legeay<sup>1</sup>, Emilie Roger<sup>1</sup>

<sup>1</sup> MINT, INSERM U1066, CNRS 6021, UNIV Angers, SFR-ICAT 4208, Angers, France.

<sup>2</sup> CHU Angers, 49033 Angers, France

<sup>3</sup> School of Pharmacy, The University of Nottingham, Nottingham, United Kingdom.

## Abstract

Lipid nanocapsules (LNCs) were one of the promising nanomedicines for oral delivery as they could enhance the oral bioavailability of various drugs. However, *in vitro* absorption experiment found very low intact LNCs transport across epithelium and endothelium membranes. Hence, this phenomenon needs to be investigated *in vivo*. This study aimed to investigate the *in vivo* oral absorption of the intact LNCs. In this study, intact LNCs were investigated for their oral bioavailability, biodistribution into the hepatic portal system (portal vein and liver), and remaining in the feces in a rat model, using the quantitative FRET technique developed in our previous work. The result found that intact LNCs did not absorb *via* the GI route, and no intact LNCs were found in the feces. This study provides the evidence that the increased drug bioavailability in LNCs encapsulated formulation previously reported in the literature was not a result of intact LNCs absorption.

## Keywords

Lipid nanocapsules; Oral absorption; Oral bioavailability; FRET; Biodistribution; Hepatic portal system; Nanomedicine; Fluorescence; *in vivo* study

## 1. Introduction

Oral route is one of the most preferential routes of drug administration among patients and medical professionals. However, the hurdle is that several drugs have poor oral bioavailability preventing them from the benefit of oral delivery [2]. In recent years, nanomedicines have been employed as one venue to overcome the oral bioavailability issue [137]. Lipid nanocapsules (LNCs), which were developed in our laboratory [96], were one of the promising nanomedicines for oral delivery as they were reported to enhance the oral bioavailability of paclitaxel [29,91,92], Sn38 [124], praziquantel [95], and fondaparinux [111]. One of the hypothetical explanations for this advantage was that intact LNCs might be able to cross the intestinal barrier into the systemic circulation [91,94,102,133,138]. Our previous *in vitro* absorption study of intact LNCs found that less than 0.3% of intact LNCs crossed the Caco-2 and Caco-2/HMEC-1 cell membranes [128,133]. It is necessary to investigate the mechanisms of *in vivo* absorption of intact LNCs across GI barriers.

*Förster resonance energy transfer* (FRET) is a technique that allows the integrity of nanoparticles to be monitored. FRET is the process of the resonance energy transfer between two fluorophores, which occurs only in the vicinity of less than 10 nm, making it suitable as a probe for monitoring the structural integrity of the nanomedicines [139]. In our previous work [140], quantitative FRET was successfully developed for quantifying intact FRET-LNCs in blood samples allowing for the plasma particle concentration of intact FRET-LNCs to be measured and paving the way for the bioavailability study. Recently, in an unpublished work by Elfatairi *et al.* [134], quantitative FRET was successfully adapted for liver, lungs, and spleen tissue samples, providing the method for a biodistribution study of intact LNCs.

This study aimed to investigate the oral absorption of FRET-LNCs to the systemic circulation after oral administration (oral bioavailability); to the hepatic portal system (biodistribution to the intestine, the portal vein, and the liver); and the remaining intact FRET-LNCs in the feces in a rat model. At first, LNCs with different sizes and surface modifications were formulated into FRET-LNCs following our previous study [133,140]. FRET was employed as a technique for monitoring the integrity of the LNCs *in vivo* and *ex vivo*. The oral bioavailability of different FRET-LNCs formulations was evaluated using quantitative FRET developed in our previous work [140]. The FRET-LNCs extraction was studied in the intestinal tissue, and the quantitative FRET was developed for feces samples. Hence, the biodistribution of intact FRET-LNCs into portal vein and liver was evaluated to give a broader view of oral absorption of the intact LNCs.

## 2. Materials and methods

### 2.1 Materials

DiI (1,10-dioctadecyl-3,3,30,30-tetramethyl-indocarbocyanine perchlorate), DiD (1,1'-dioctadecyl-3,3,3',3'-tetramethylindo-dicarbocyanine perchlorate), and Histopaque®-1083 were purchased from Thermofisher (Villebon-sur-Yvette, France). MilliQ water was obtained from a Milli-Q® Advantage A10 System (Merck Millipore, Darmstadt, Germany). Captex® 8000 (glyceryl tricaprilate) was kindly provided by Abitec Corporation (Columbus, OH, USA). Lipoid® S75-3 (phosphatidylcholine and phosphatidylethanolamine mixture) was purchased from Lipoid GmbH (Steinhausen, Switzerland). Kolliphor® HS-15 (PEG 660 and polyethylene glycol 660 hydroxystearate mixture) was purchased from BASF (Ludwigshafen, Germany). DSPE-PEG-2000 (1,2-distearoyl-sn-glycero-3-phosphoethanolamine-N- [methoxy(polyethylene glycol)-2000] (ammonium salt)) was purchased from Avanti Polar Lipids (Alabaster, AL, USA). Phosphate-buffered saline (PBS) was purchased from PAA Laboratories (Toronto, ON, Canada). Polycarbonate centrifuge tube size 7 × 20 mm (reference 343775) was purchased from Beckman Coulter (Villepinte, France). Heparin sodium 5000 UI/mL was purchased from Panpharma (Luitré, France).

### 2.2 FRET-LNCs formulation and characterization

DiI- and DiD-tetraphenylborate (TPB) were synthesized and solubilized in Captex® 8000 by the method previously published [138,141]. Six FRET-LNCs formulations were formulated by the phase inversion method, and the compositions were similar to our previous works [133,140]. LNCs were co-loaded with DiI-TPB and DiD-TPB into different sizes (50-nm and 85-nm) and surface modifications (none, DSPE-mPEG-200, and stearylamine). **Table 5** details the composition of each FRET-LNCs formulation where LNC-50 is 50-nm LNCs, LNC-50-PEG is 50-nm LNCs with DSPE-PEG-2000 surface added, LNC-50-SA is 50-nm LNCs with stearylamine surface added, LNC-85 is 85-nm LNCs, LNC-85-PEG is 85-nm LNCs with DSPE-PEG-2000 surface added, and LNC-85-SA is 85-nm LNCs with stearylamine surface added.



**Table 5.** Compositions of different FRET-LNCs formulations

Compositions	Quantity (% w/w)					
	LNC-50	LNC-50-PEG	LNC-50-SA	LNC-85	LNC-85-PEG	LNC-85-SA
Captex® 8000 (2%w/w DiI-TPB)	5.5	5.5	5.5	8.5	8.5	8.5
Captex® 8000 (2%w/w DiD-TPB)	5.5	5.5	5.5	8.5	8.5	8.5
Kolliphor® HS-15	11.5	11.5	11.5	9.3	9.3	9.3
Purified water	21.3	21.3	21.3	17.5	17.5	17.5
DSPE-mPEG-2000	-	0.6	-	-	0.6	-
Stearylamine	-	-	0.1	-	-	0.1
Lipoid® S75-3	0.7	0.7	0.7	0.7	0.7	0.7
NaCl	0.8	0.8	0.8	0.8	0.8	0.8
Purified water (2° C)	54.7	54.7	54.7	54.7	54.7	54.7

*LNC-50: 50-nm LNCs; LNC-50-PEG: 50-nm LNCs with DSPE-PEG-2000 surface added; LNC-50-SA: 50-nm LNCs with stearylamine surface added. LNC-85: 85-nm LNCs; LNC-85-PEG: 85-nm LNCs with DSPE-PEG-2000 surface added; LNC-85-SA: 85-nm LNCs with stearylamine surface added.*

The nanoparticle tracking analysis system (NTA) was employed to measure mean size (nm), particle concentration (particle/mL), and particle size distribution using NanoSight NS300 (Malvern Instrument, Worcestershire, UK) with a low volume flow cell and a 450 nm laser. FRET-LNCs suspensions were diluted in MilliQ water by the factor ranging from  $1/5 \times 10^5$  to  $1/1 \times 10^6$  and then slowly injected into the sample chamber using a 1 mL syringe pump with the rate of 3-4  $\mu$ L per second. The video sequences of the nanoparticles were captured over 60 seconds (5 replicates) and then analyzed by NTA analytical software version 3.2.

NTA provides the particle distribution width parameters, which can be calculated into the span following the equation:

$$\text{Span} = \frac{(D90 - D10)}{D50}$$

Where D10, D50, and D90 represent the diameter (nm) at the 10<sup>th</sup>, 50<sup>th</sup> (median), and 90<sup>th</sup> percentiles of the distribution histogram, respectively.

The zeta potential of the FRET-LNCs was determined by laser doppler electrophoresis using Zetasizer® Nano series DTS 1060 (Malvern Instruments SA, Worcestershire, the UK) diluted by factor 1/100.

### 2.3. FRET measurements

The fluorescence emission spectra of FRET-LNCs were recorded on a FluoroMax® 4 spectrophotometer (Horiba Jobin Yvon Inc., Piscataway, NJ, USA) at room temperature with the 548 nm excitation and 0.5 s integration time. FRET-LNCs suspension was diluted by a factor of 1/3000. The emission spectra were collected from 550 to 720 nm, with an

increment of 1 nm. They were corrected for the lamp source fluctuations and the wavelength-dependent response of the detector. The maximum intensity of the FRET donor and acceptor were recorded at  $569 \pm 5$  nm and  $675 \pm 5$  nm, respectively.

The integrity of nanoparticles was determined by the FRET proximity ratio (PR) calculated by the following equation:

$$PR = \frac{A}{(A+D)}$$

Where  $A$  and  $D$  are the maximum fluorescence intensity of the aforementioned FRET acceptor and donor signals, respectively.

## 2.4 Animals

Male Sprague-Dawley rats ( $n=30$ ) aged 10-14 weeks and weight 350-500 g were purchased from Javier Labs (Saint Bertevein, France). All rats received a standard laboratory diet and water *ad libitum*. The experimental protocol on animals was carried out to the EU Directive 2010/63/EU and was approved by the Committee on the Ethics of Animal Experiment of the Pays de la Loire, France (APAFIS #2020092411444021).

## 2.5 Absolute oral bioavailability of FRET-LNCs

### 2.5.1 Oral administration

The six FRET-LNCs formulations were orally given to the rats by the gavage tube with the dose ranging from  $1.5 \times 10^{14}$  for LNC-50 ( $n=3$ ), LNC-50-PEG ( $n=3$ ), and LNC-50-SA ( $n=2$ ); and to  $2 \times 10^{14}$  particles/100 g rat for LNC-85 ( $n=2$ ), LNC-85-PEG ( $n=2$ ), and LNC-85-SA ( $n=1$ ). Not more than 150  $\mu$ L of blood was collected from the rat's tail vein during the period from 5, 30, 60, 90, 120, 360, 480, and 1440 minutes.

### 2.5.2 Blood sample preparation

FRET-LNCs particle concentration and PR of blood samples were quantified using the method largely adapted from our previous work [140]. A 100  $\mu$ L blood sample was taken and immediately mixed with 100  $\mu$ L of Histopaque®-1083 in the polycarbonate centrifuge tube kept in ice. Then, the samples were centrifuged in the Optima MAX-UP Ultracentrifuge (Beckman Coulter, Villepinte, France) using the fixed-angle rotor TLA-100 (Beckmann Coulter, Villepinte, France) with a relative centrifugal force of  $4 \times 10^5$  G at 25 °C for 2 hours. Finally, 75  $\mu$ L of the supernatant was immediately collected and mixed with 225  $\mu$ L of ultrapure water. FRET donor and acceptor spectra of the samples were measured, and the PR was calculated.

### 2.5.3 Quantitative calibration curve for blood

Only the FRET acceptor intensity at the time point with the  $PR \geq 0.80$  was quantified as the *in vivo* plasma particle concentration by the quantitative calibration curve. A

quantitative FRET calibration curve for blood was constructed by the method described in our previous work [140]. For the standard solutions, seven dilutions of FRET-LNCs were prepared with the dilution factors ranging from 1/1000 to 1/50000 and then spiked into the blood. The initial particle concentration of the formulation was measured in the characterization step by NTA (section 2.2). Maximum FRET acceptor emission intensities of the spiked standard were measured ( $675 \pm 5$  nm) and plotted as a function of particle concentration with the curve fitted by a double logarithmic regression function in the linear form:

$$F_A = 10^k \times C^m$$

Where  $F_A$  is the FRET acceptor maximum emission intensity ( $675 \pm 5$  nm) of a sample;  $k$  is the intercept;  $C$  is the FRET-LNCs particle concentration of a sample;  $m$  is the slope of the fitting curve. The linearity of the fitting curve was estimated by the coefficient of determination ( $R^2$ ) with the acceptance of  $R^2 \geq 0.980$ . Due to the interference from the background fluorescent noise at a low concentration, the standard concentration with  $PR < 0.80$  was excluded from the calibration curve.

#### **2.5.4 Absolute oral bioavailability**

The absolute oral bioavailability was calculated by the equation:

$$F = \frac{AUC_{PO} \times D_{IV}}{AUC_{IV} \times D_{PO}}$$

Where  $F$  is the absolute oral bioavailability;  $AUC_{PO}$  is the AUC of FRET-LNCs administered orally;  $AUC_{IV}$  is the AUC of FRET-LNCs administered intravenously;  $D_{PO}$  is the dose of FRET-LNCs administered orally;  $D_{IV}$  is the dose of FRET-LNCs administered intravenously. The  $AUC_{IV}$  of all six FRET-LNCs formulations were obtained from our previous work [140].

## **2.6. Study on FRET-LNCs extraction from intestinal tissue**

### **2.6.1 FRET-LNCs particle stability under homogenization**

LNC-50 was prepared with the dilution of 1/500 and the volume of 6 mL in flacon and then put under the homogenization with the speed of 13500, 17500, 24000 rpm for 1, 2, 5, and 10 min. FRET signals of the sample were measured with PR calculated.

### **2.6.2 Extraction and effect of mucolytic agents**

A Sprague-Dawley rat was euthanized with the intestine harvested. The intestine was rinsed to remove the feces matter inside, dried, and then cut into small pieces. One gram of the intestinal piece was taken into a culture tube with 1 mL of FRET-LNCs (dilution 1/80) added thereafter. In the first culture tube, 5 mL of MilliQ water was added, the second culture tube with 5%w/v L-cysteine to dissolve the mucus, and the third culture tube with 5 mL of phosphate buffer pH 4.0 to denature the mucus. The samples were homogenized with Ultra-Turrax® at the speed of 24,000 rpm for 8 min.

### **2.6.3 Ultracentrifugation and % FRET recovery**

At first, 100  $\mu\text{L}$  of the sample was taken and immediately mixed with 100  $\mu\text{L}$  of Histopaque®-1083 in the polycarbonate centrifuge tube kept in ice. After, the samples were centrifuged using Optima MAX-UP Ultracentrifuge (Beckman Coulter, Villepinte, France) and the fixed-angle rotor TLA-100 (Beckmann Coulter, Villepinte, France) with a relative centrifugal force of 400,000 G at 25 °C for 2 hours. Finally, 75  $\mu\text{L}$  of the supernatant was immediately collected and mixed with 225  $\mu\text{L}$  of ultrapure water. FRET donor and acceptor spectra of the samples were measured, and the PR was calculated. Finally, the percentage of the FRET acceptor recovery was calculated as:

$$\% \text{ FRET recovery} = \left( \frac{I_{\text{SAMPLE}}}{I_{\text{REF}}} \right) \times 100\%$$

Where  $I_{\text{SAMPLE}}$  is the intensity of the FRET acceptor signal from the studied sample; and  $I_{\text{REF}}$  is the intensity of the FRET acceptor signal from a reference sample which contains FRET-LNCs and MilliQ water with the same concentration as the studied samples but without any extraction procedure applied.

## **2.7 Development of quantitative FRET for feces**

Feces were collected from Male Sprague-Dawley rats aged 10-14 weeks and weight 350-500 g fed by laboratory standard food and water *ad libitum*.

### **2.7.1 Study on method for feces fiber removal**

Feces sample in a culture test tube was prepared following the conditions in **Table 6**. Conditions A were the test sample with feces, while conditions B were a control prepared without feces. For conditions A, 1 mL of LNC-50 (dilution 1/80) was spiked into 0.5 g of rat feces and then mixed with 2 mL of MilliQ water. The feces were cut under a liquid mixture using a spatula until all the feces became broken and suspended in the mixture. Then, the samples were homogenized by Ultra-Turrax® T25 with a speed of 24,000 rpm for 10 min. For conditions A2 and B2, the sample tube was centrifuged using Centrifuge 5810R (Eppendorf) with rotor A-4-81 with 3100 G force for 15 min. For conditions A3 and B3, the sample was filtrated with the Büchner with glass sinter, and then the filtrate was collected. For condition B4, the sample was filtrated with the porcelain Büchner with a paper filter, and then the filtrate was collected. Finally, 100  $\mu\text{L}$  of each sample (supernatant for A2, B2 and filtrate for A3, B3, A4, and B4) was collected for ultracentrifugation, FRET measurement, proximity ratio, and %FRET recovery calculation following the method in section 2.6.3

**Table 6.** Experimental condition for the selection of the fiber removal method

Condition	Feces weight (g)	LNC-50 stock (mL)	MilliQ water (mL)	Homogenization method	Fiber removal method
A1	0.5	1	2	Ultra-Turrax®	n/a
A2	0.5	1	2	Ultra-Turrax®	Centrifugation 3100 G, 15 min
A3	0.5	1	2	Ultra-Turrax®	Filtration by Büchner with glass sinter
B1	-	1	2	Ultra-Turrax®	n/a
B2	-	1	2	Ultra-Turrax®	Centrifugation 3100 G, 15 min
B3	-	1	2	Ultra-Turrax®	Filtration by Büchner with glass sinter
B4	-	1	2	Ultra-Turrax®	Filtration by porcelain Büchner + paper filter

The volumetric yield of the filtration method was studied as the feces sample being prepared in a culture test tube following the conditions in **Table 7**. Then, 0.5 mL of LNC-50 (dilution 1/80) was spiked into 0.25 g of rat feces and then mixed with different volumes of MilliQ water (see table). Then, the samples were homogenized by Ultra-Turrax® T25 with a speed of 24,000 rpm for 10 min. Then, the samples were filtrated with the Büchner with filter paper, and then the filtrate was collected. The %volumetric yield of each sample was calculated as:

$$\% \text{volumetric yield} = \left( \frac{\text{volume after filtration}}{\text{volume before filtration}} \right) \times 100\%.$$

**Table 7.** Experimental condition for the volumetric yield of Büchner filtration

Condition	Feces weight (g)	LNC-50 stock (mL)	MilliQ water (mL)	Total volume (mL)	Homogenization method	Fiber removal method
Vol-1	0.25	0.5	4	4.5	Ultra-Turrax®	Filtration by porcelain Büchner + paper filter
Vol-2	0.25	0.5	4.5	5	Ultra-Turrax®	Filtration by porcelain Büchner + paper filter
Vol-3	0.25	0.5	5.5	6	Ultra-Turrax®	Filtration by porcelain Büchner + paper filter
Vol-4	0.25	0.5	6.5	7	Ultra-Turrax®	Filtration by porcelain Büchner + paper filter

### 2.7.2 Study on method for homogenization

Feces were ground up using mortar and pestle until a fine powder was obtained. Then, 0.25 g of the feces power was taken into a culture tube and then spiked with 0.5 mL of LNC-50 (dilution 1/80) and mixed with 5.5 mL of MilliQ water. Different methods of extraction were tested as described in **Table 8**. Finally, 100 µL of filtrate or supernatant was collected for ultracentrifugation, FRET measurement, proximity ratio, and %FRET recovery calculation following the method in section 2.6.3

**Table 8.** Experimental condition for the mortar and pestle method

Condition	Feces weight (g)	LNC-50 stock (mL)	MilliQ water (mL)	Homogenization method	Fiber removal method
D1	0.25	0.5	5.5	Mortar-Pestle & Ultra-Turrax® 24,000 rpm for 10 min	Büchner + paper filter
D2	0.25	0.5	5.5	Mortar-Pestle (wet)	Büchner + paper filter
D3	0.25	0.5	5.5	Mortar-Pestle (dry)	Büchner + paper filter
D4	0.25	0.5	5.5	Mortar-Pestle (dry)	Centrifugation 3100 G, 15 min

### 2.7.3 Calibration curve construction

For the standard solutions, seven dilutions of LNC-50 were prepared with dilution factors ranging from 1/300 to 1/30,000. Feces were ground up using mortar and pestle until a fine powder was obtained. Then, 0.25 g of the feces power was taken into a culture tube and then spiked with 0.5 mL of different LNC-50 standard stock and mixed with 5.5 mL of MilliQ water. The standard tubes were centrifuged using Centrifuge 5810R (Eppendorf) with rotor A-4-81 with 3100 G force for 15 min. Then, 100  $\mu$ L of the supernatant was taken and immediately mixed with 100  $\mu$ L of Histopaque®-1083 in the polycarbonate centrifuge tube kept in ice. After, the samples were centrifuged using Optima MAX-UP Ultracentrifuge (Beckman Coulter, Villepinte, France) and the fixed-angle rotor TLA-100 (Beckmann Coulter, Villepinte, France) with a relative centrifugal force of 400,000 G at 25 °C for 2 hours. Finally, 75  $\mu$ L of the supernatant was immediately collected and mixed with 225  $\mu$ L of ultrapure water. FRET donor and acceptor spectra of the samples were measured, and the PR was calculated.

The initial particle concentration of the formulation had been measured in the characterization step by the NTA. Maximum FRET acceptor emission intensities of the spiked standard were measured ( $675 \pm 5$  nm) and plotted as a function of particle concentration with the curve fitted by a double logarithmic regression function in the linear form:

$$F_A = 10^k \times C^m$$

Where  $F_A$  is the FRET acceptor maximum emission intensity ( $675 \pm 5$  nm) of a sample;  $k$  is the intercept;  $C$  is the FRET-LNCs particle concentration of a sample;  $m$  is the slope of the fitting curve. The linearity of the fitting curve was estimated by the coefficient of determination ( $R^2$ ) with the acceptance of  $R^2 \geq 0.980$ . Due to the interference from background fluorescent noise at low concentration, the standard concentration with  $PR < 0.70$  was excluded from the calibration curve

## 2.8 Biodistribution of intact LNCs in the hepatic portal system

### 2.8.1 Oral administration

Rats were orally given FRET-LNCs via the gavage tube with the FRET-LNCs formulations, doses, and sacrifice time as specified in **Table 9**. After being euthanized, the autopsy was performed on the rat with not more than 150  $\mu\text{L}$  of blood from the portal vein collected, 1 g of liver harvested, and whole feces collected.

**Table 9.** Experimental conditions for biodistribution studies after oral gavage

Formulations	Condition	n	Gavage dose (particles/100 g rat)	Sacrifice after (hours)
LNC-50-PEG	A	3	$2 \times 10^{14}$	24
LNC-50	B	2	$2 \times 10^{14}$	4
	C	1	$5 \times 10^{13}$	4
LNC-85-PEG	C	1	$5 \times 10^{13}$	4
LNC-85	C	1	$5 \times 10^{13}$	4

### 2.8.2 Blood sample preparation

Blood samples were prepared and quantified for intact FRET-LNCs using a similar method from section 2.5.2.

### 2.8.3 Liver sample preparation

Liver samples were mixed with 3.5 mL MilliQ water and then homogenized by T25 Ultra-Turrax® at the speed of 13,500 rpm for 45 seconds. 100  $\mu\text{L}$  of the liver sample were taken, prepared, and then quantified for FRET-LNCs particle concentration using the method adapted from section 2.5.2.

### 2.8.4 Feces sample preparation

The weight of the whole feces was recorded. Then, the whole feces were ground up using mortar and pestle until a fine powder was obtained. Next, 0.25 g of the feces powder was taken into a culture tube, and then 6 mL of MilliQ Water was added. The sample was vortexed gently for 2 minutes. The sample was centrifuged using Centrifuge 5810R (Eppendorf) with rotor A-4-81 with 3100 G force for 15 min. Finally, 100  $\mu\text{L}$  of the supernatant was taken, prepared, and then quantified for FRET-LNCs particle concentration using the method adapted from section 2.5.2.

### 3. Results and discussion

#### 3.1. FRET-LNCs formulations and characterization

FRET-LNCs were used for monitoring the nanoparticle's integrity. Hence, six FRET-LNCs formulations were formulated following the compositions in our prior works [133,140] with the size of 50 and 85 nm, and the surface modifications of DSPE-PEG-2000 and stearylamine. **Table 10** shows the characterization results of the six FRET-LNCs formulations. LNC-50, LNC-50-PEG, and LNC-50-SA had the size ranging from 47.0 – 53.1 nm, while LNC-85, LNC-85-PEG, and LNC-85-SA from 78.5 – 80.9 nm. The span of all formulations was in the range of 0.38 – 0.63, meaning that the particle size distribution was uniform and narrow. The proximity ratio (PR) of all six formulations was 0.83 – 0.92, indicating full integrity. The particle concentration was ranging from  $2.4 \times 10^{14}$  to  $3.4 \times 10^{14}$  particles/mL except for LNC-50-PEG with  $7.0 \times 10^{14}$  particles/mL. All the characterization parameters were as expected and conformed with the results obtained in our previous studies [133,140].

**Table 10.** FRET-LNCs Characterization (mean  $\pm$  SD)

Formulations	Particle Size (nm)	Span	Zeta Potential (mV)	FRET Proximity Ratio (PR)	Particle Concentration ( $10^{14}$ particle/mL)
LNC-50 (n=3)	47.0 $\pm$ 0.5	0.40 $\pm$ 0.07	3.0 $\pm$ 0.5	0.90 $\pm$ 0.01	3.2 $\pm$ 2.4
LNC-50-PEG (n=3)	47.8 $\pm$ 2.4	0.38 $\pm$ 0.05	-9.2 $\pm$ 1.7	0.89 $\pm$ 0.01	7.0 $\pm$ 4.9
LNC-50-SA (n = 1)	53.1	0.54	19.1	0.83	3.1
LNC-85 (n = 2)	78.8	0.52	18.1	0.88	3.3
LNC-85-PEG (n = 2)	78.5	0.57	0.6	0.91	3.4
LNC-85-SA (n = 1)	80.9	0.63	30.8	0.92	2.4

#### 3.2 Absolute oral bioavailability

In parallel to our previous work to quantify the plasma particle concentration of intact FRET-LNCs in a rat model [140], the absolute oral bioavailability of the six formulations of intact FRET-LNCs was evaluated by the quantitative FRET method described in our previous study [140]. It was found that no FRET donor and FRET acceptor signals were retrieved from rat's systemic blood at any time point from 5–1440 min for all six FRET-LNCs formulations and dose, meaning that no intact FRET LNCs or the trace of the FRET dyes were found in rat plasma at this dose. Therefore, the absolute bioavailability (F) of intact LNCs was  $F = 0$ . This result suggested that intact FRET-LNCs did not absorb *via* the oral route, or that the amount of intact LNCs was relatively too low to be detectable in the systemic circulation by the current method with the detection limit of  $10^{10}$  particles/mL.



Consequently, the new strategy to evaluate the *in vivo* oral absorption of intact FRET-LNCs was adopted by quantifying the intact FRET-LNCs biodistribution to the hepatic portal system (small intestine, portal vein, liver) after orally administered. Because the concentration of FRET-LNCs could be higher and detectable in this area than in the systemic circulation.

Besides, the feces of the rat, after being orally given by FRET-LNCs, were observed to be purple, which was the color of the FRET dyes. It was hypothesized that this could be a result of either the remaining intact FRET-LNCs or the trace of destroyed FRET-LNCs in the feces. Hence, it was necessary to quantify the intact FRET-LNCs in the feces.

Summarily, with these new approaches, a new quantitative FRET technique suitable for intact FRET-LNCs in the intestinal tissue, liver, and feces was required. The quantitative FRET for liver tissue had been developed by Elfatairi *et al.* in an unpublished work [134] while the new technique for intestinal tissue and feces needed to be developed.

### 3.3 Study on FRET-LNCs extraction from intestinal tissue

New quantitative FRET technique was developed for the intestinal sample based on the prior technique successfully employed for the liver sample [134]. The technique was based on two steps: homogenization of the tissue and intact FRET-LNCs extraction using ultracentrifugation. At first, the particle stability of FRET-LNCs under homogenization was tested. FRET-LNCs were found to maintain their integrity ( $PR > 0.80$ ) under homogenization up to the speed of  $2.4 \times 10^4$  rpm with a duration of 10 minutes. For the intestinal sample, the homogenization with the speed of  $2.4 \times 10^4$  rpm with a duration of 8 minutes was optimal. However, due to the nature of the intestinal tissue that contains a large amount of mucus that could hinder the release of intact FRET-LNCs, the study on the mucolytic agent was carried on. The homogenized samples spiked with FRET-LNCs were treated with 3%w/v L-cysteine, phosphate buffer pH 4.0, and MilliQ water as a control. The result found that all three samples had  $PR < 0.30$  and %FRET recovery  $< 8\%$ , indicating that no intact FRET-LNCs were retrieved from the three intestinal samples and the extraction was unsuccessful (**Table 11**).

**Table 11.** LNCs intestinal extraction results.

Conditions	%FRET recovery	PR
Intestine + water	8	0.21
Intestine + L-cysteine	3	0.25
Intestine + phosphate buffer pH 4.0	6	0.27

The use of mucolytic L-cysteine with a relatively high concentration of 3%w/v and phosphate buffer pH 4.0 to help denature the mucus did not show to be effective in improving the extraction. The mucus still strongly retained the FRET-LNCs and overcame the effect of the mucolytic agent, making it inseparable (**Supplementary Figures S3-1, S3-2, S3-3**). The sample prepared by L-cysteine was also found to be crystalized after ultracentrifugation deeming this method not practical (**Supplementary Figure S3-2**). Besides, other methods might be more appropriate. That said, it could be interesting for future research to test this with the method from Liu *et al.* by using FRET confocal microscopy imaging the cryosection of the intestinal lumen or the live *in vivo* imaging system (IVIS) taking the image of the FRET signal directly from the intestinal tract as a whole [142].

In summary, the intestinal tissue contains a high amount of mucus that can highly retain the FRET-LNCs making it unable to be extracted by this technique. The development of intact FRET-LNCs extraction method from the intestinal tissue was not successful using this approach.

### **3.4 Development of quantitative FRET for feces**

New quantitative FRET technique was developed for feces samples based on the technique previously described [134]. At first, the method was developed to extract intact FRET-LNCs from feces samples. Then, the calibration curve between intact FRET-LNCs in feces and the FRET acceptor maximum intensity signal was developed.

#### **3.4.1 Study on method for feces fiber removal**

From the experiment, it was observed that rat's fecal matter contained a large amount of large undigested fiber [143] that, after being mixed with water and homogenized, could still obstruct the pipette or was too large for the ultracentrifugation. Therefore, the priority for developing the extraction technique for feces was to remove the fiber. The first experiment compared the % FRET recovery from two fiber removal methods: centrifugation and filtration by Büchner with glass sinter. **Table 12** shows the result of % FRET recovery and PR of the FRET-LNCs spiked feces samples and their references (no feces added) using the two fiber removal methods. Firstly, the PR > 0.80 confirmed the presence of intact FRET-LNCs in condition A2 (filtration method) and all control samples (B1, B2, B3, B4). Secondly, it was found that, without fiber removal (condition A1), % FRET recovery was zero, meaning that fiber in feces itself could retain 100% of intact FRET-LNCs, and the fiber removal method was crucial. Thirdly, it was evident that the filtration method (condition A2) by glass Büchner gave 52% FRET recovery better than the centrifugation method (condition A3) with 0% yield. It means that FRET-LNCs could be extracted out using the filtration method while they were still

retained in the feces if using the centrifugation method. However, the result from the reference of the filtration method with the glass Büchner (condition B2) showed only 46% FRET recovery. Since there were no feces in the control sample, the loss could be the result of FRET-LNCs being retained by the glass Büchner's sinter filter, suggesting other types of filters should be used to optimize this fiber removal. Therefore, the porcelain Büchner with filter paper was tested with the control sample (condition B4). The result found 84% FRET recovery, meaning that the paper filter caused less particle loss than the glass Büchner. Hence, the porcelain Büchner and paper filter was chosen as the main method for fiber removal.

**Table 12.** Result of the test on the selection of fiber removal method

Condition	Feces	Fiber removal method	%FRET recovery	PR
A1	0.5 g	n/a	0	0.36
A2	0.5 g	Filtration by Büchner with glass sinter	52	0.87
A3	0.5 g	Centrifugation 3100 G, 15 min	0	0.34
B1	-	n/a	82	0.89
B2	-	Filtration by Büchner with glass sinter	46	0.91
B3	-	Centrifugation 3100 G, 15 min	101	0.89
B4	-	Filtration by porcelain Büchner + paper filter	84	0.87

Nevertheless, it was observed that there was a loss in the sample volume after the filtration by porcelain Büchner with a paper filter. It was also observed that the sample prepared with 0.5 g feces and in a total of 3 mL of the liquid part was very viscous and difficult to be filtrated, probably being the culprit for volume loss. Therefore, the optimal volume for the filtration was reconsidered. The weight of feces was reduced by 2-fold from 0.5 to 0.25 g, while the water volume was double starting at 4, 4.5, 5.5, and 6.5 mL giving a total volume of 4.5, 5, 6, and 7 mL. After being filtrated by the porcelain Büchner and filter paper, the % volumetric yield of these samples was reported (**Table 13**). The optimal volume was found to be the condition Vol-3 with a volumetric yield of 79%. This condition was chosen as a standard volume for sample preparation. It had 0.5 mL of stock FRET-LNCs and 5.5 mL of MilliQ water, making a total volume of 6 mL.

**Table 13.** Result of the test on volumetric yield after filtration via porcelain Büchner + paper filter

Condition	Feces weight (g)	FRET-LNCs stock solution (mL)	MilliQ water (mL)	Total volume (mL)	%Volumetric yield
Vol-1	0.25	0.5	4	4.5	55
Vol-2	0.25	0.5	4.5	5	75
Vol-3	0.25	0.5	5.5	6	79
Vol-4	0.25	0.5	6.5	7	68

### 3.4.2 Study on method for homogenization

From the experiment, one rat was observed to produce a large number of feces, around 10 g over 24 hours. Therefore, the use of mortar and pestle was introduced to help to homogenize a big bulk of feces before sampling. Different combinations between the use of mortar and pestle, homogenizer (Ultra-Turrax®), and filtration were evaluated, and the results are shown in **Table 14**. The condition D1 was the mix between mortar and pestle with Ultra-Turrax®. It turned out that this condition gave a low %signal recovery at 12% and also caused damage to the integrity of the FRET-LNCs as the PR dropped to 0.68. Compared to condition D3, in which mortar and pestle were used for the homogenization, the % signal recovery was higher at 59%, while the LNCs sample still maintain the full integrity. This means the Ultra-Turrax® should not be used further as their force might be excessive to the LNCs. Interestingly, the worst condition is D2, in which mortar and pestle were rinsed with water. It turned out that the rinse caused the feces powder to be adhesive to the mortar and pestle's porcelain surface. The poor %signal recovery of this condition was a result of this loss. Hence, the mortar and pestle should not be rinsed with water. Finally, the best condition was D4 (Mortar-Pestle with centrifugation of 3100 G for 15 min), with the %signal recovery as high as 84% with LNCs maintaining full integrity. This result means that centrifugation worked better as a fiber removal method while preserving the LNCs integrity and has no adsorption problem. This also means that the reason that the previous experiment with centrifugation (**Table 12**) had zero %signal recovery was a result of the use of Ultra-Turrax® rather than the problem from the centrifugation method itself. In conclusion, condition D4 was chosen as a standard method for the next step to construct the FRET calibration curve.

**Table 14.** Result of the test on the mortar and pestle method

Condition	Homogenization method	Fiber removal method	%signal recovery	PR
D1	Mortar-Pestle & Ultra-Turrax®	Filtration by porcelain Büchner + paper filter	12	0.68
D2	Mortar-Pestle (wet)	Filtration by porcelain Büchner + paper filter	8	0.59
D3	Mortar-Pestle (dry)	Filtration by porcelain Büchner + paper filter	59	0.81
D4	Mortar-Pestle (dry)	Centrifugation 3100 G, 15 min	84	0.82

### 3.4.3 Calibration curve construction

Using condition D4 (mortar-pestle with centrifugation at 3100 G force for 15 min), the calibration curve between FRET acceptor intensity and LNC-50-PEG particle concentration (particle/g feces) was successfully constructed with the limit of detection at  $8 \times 10^{11}$  particles/g feces, the linearity  $R^2 = 0.998$ , and the PR in the range of 0.71-0.78. The quantitative FRET technique for feces extraction was successfully developed with a calibration curve validated (**Supplementary Figure S3-4**).

### 3.5. Biodistribution of intact LNCs in hepatic portal system and feces

**Table 15** shows the result of the experiment in each condition and in each rat. At first, rats were treated with LNC-50-PEG with the dose of  $2 \times 10^{14}$  particle/100 g rat and the sacrifice time at 24 hours (condition A). After 24 hours, no FRET acceptor signal was found in the portal vein's blood, liver, and feces. Rat autopsy also showed that no FRET-LNCs remained in the GI system. It is possible that the 24-hour time period was too long that FRET-LNCs had been completely eliminated from the rat body. Hence, the sacrifice time was reduced to 4 hours in the next experiment.

For condition B, three rats were treated, each with LNC-50, LNC-85, and LNC-85-PEG with the lower gavage dose of  $5 \times 10^{13}$  particles/100 g rat and a sacrifice time at 4 hours. All rats were still sacrificed after 4 hours, and the autopsy results found that, even with lower dose and gavage volume, FRET-LNCs were still present throughout the GI tract. However, no FRET acceptor signal was found in the portal vein's blood, liver, and feces.

In conclusion, intact FRET-LNCs were not found in the hepatic portal system and feces after oral gavage either by the high dose of  $2 \times 10^{14}$  particles/100 g rat or the low dose of  $5 \times 10^{13}$  particles/100 g. FRET-LNCs may enter the intestine after 2.5 hours after the administration and reach all parts of the GI tract after 4 hours, meaning that the absorption process of FRET-LNCs (regardless of dose) starts at around 2.5-4 hours after the oral administration (**Figure S3-5 to Figure S3-6** **Figure S3-8**). Moreover, for feces,

despite the fact that the pellet of the fecal matter after centrifugation still had a taint of purple (color of FRET dyes), intact FRET-LNCs were not found in the feces sample either at 4 hours or after 24 hours, suggesting that FRET-LNCs might be fully destroyed in the rat's GI. However, food content might also be another factor affecting the absorption. Therefore, a renew experiment with fasted rats should be conducted in the future.

**Table 15.** Experiment results of intact LNCs in the hepatic portal system and feces.

Formulations	Condition	Gavage dose (particles/100 g rat)	Sacrifice after (hours)	Rat No.	Portal vein's blood	Liver	Feces
LNC-50-PEG	A	$2 \times 10^{14}$	24	1	No FRET	No FRET	No FRET
	A	$2 \times 10^{14}$	24	2	No FRET	No FRET	No FRET
	A	$2 \times 10^{14}$	24	3	No FRET	No FRET	No FRET
LNC-50	B	$5 \times 10^{13}$	4	1	No FRET	No FRET	No FRET
LNC-85-PEG	B	$5 \times 10^{13}$	4	1	No FRET	No FRET	No FRET
LNC-85	B	$5 \times 10^{13}$	4	1	No FRET	No FRET	No FRET

No FRET = no FRET acceptor signal found i.e., %FRET recovery = 0%.

Combining all the obtained results (**Figure 6**), it is evident that FRET-LNCs did not absorb *via* the intestinal barrier and were completely destroyed in the GI tract. This means the evidence did not support the hypothesis that intact LNCs absorption across the intestinal barrier contributed to the increased oral bioavailability of many drugs. Similar results were obtained in the literature that the solid lipid nanoparticles (SLN) with the size of 50, 75, and 90 nm [144], which are closely related to the LNCs used in the study. SLN is made of lipid and shelled with surfactant but different from LNCs that its core is in a solid state while the core of LNCs is in liquid state. An *in vivo* SLN oral bioavailability study using water-quenching fluorescent probes found that SLN quickly degraded in the small intestine of mouse and no intact SLN found being absorbed into the systemic circulation [144]. Another oral absorption study on 100, 200, and 500-nm liposome also found no intact liposome entering the systemic circulation [142]. It seems that this is a common trait of lipid-type nanoparticle. Future projects should investigate the particle stability of LNCs in the intestinal fluid and elucidate the mechanisms which LNCs was destroyed in the GI tract.

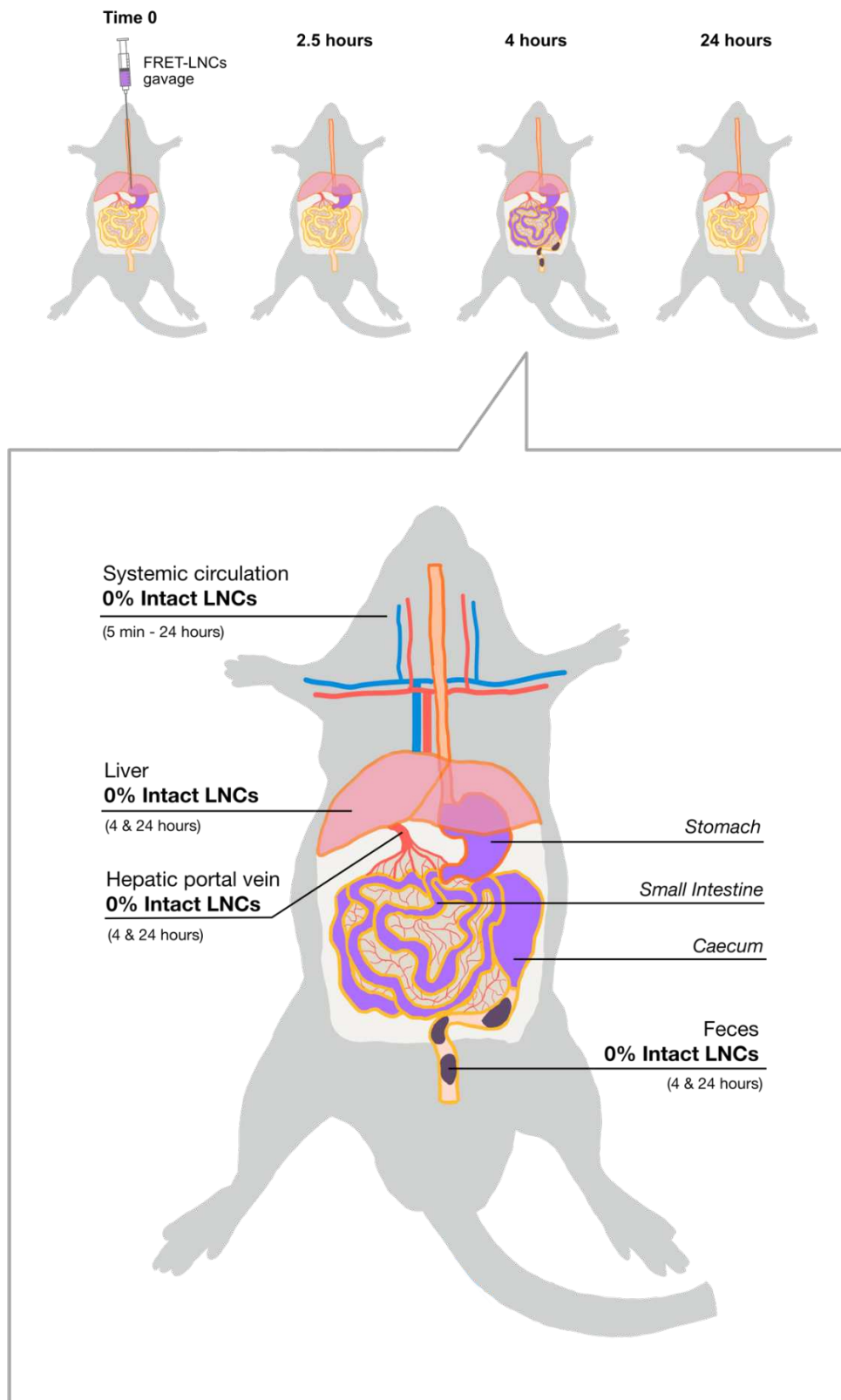


**Figure 6.** Schematic illustration showing the location of FRET-LNCs in the rat's GI system at 0, 2.5, 4, and 24 hours after oral gavage (above). Quantity of intact LNCs in rat's GI system, hepatic portal vein, liver, feces, and systemic circulation, quantified by quantitative FRET (below).

## 4. Conclusion

Summarily, first, FRET encapsulated LNC-50, LNC-50-PEG, LNC-50-SA, LNC-85, LNC-85-PEG, and LNC-85-SA were not found in the systemic circulation during the time period of 24 h after oral gavage with the dose of  $1.5 \times 10^{14}$  and  $2 \times 10^{14}$  particles/100 g rat. The oral bioavailability of intact LNCs is  $F = 0 \%$ . Second, the development of quantitative FRET for feces samples was successful but not for the intestinal tissue sample. Third, FRET-LNCs and pegylated FRET-LNCs were not found in the hepatic portal system (liver and portal vein's blood) and feces at 4 or 24 hours after the oral administration either by the high dose  $2 \times 10^{14}$  particle/100 g rat or low dose  $5 \times 10^{13}$  particle/100 g rat. In conclusion, it is evident that, in a rat model, intact FRET-LNCs did not absorb through the GI route and were completely destroyed in the GI. This discovery should be taken into consideration for the future design of LNCs formulation as the oral drug delivery system.

### Funding

This work was supported by Ligue Contre le Cancer, Maine et Loire et Loiret Committee (JPB/FP -441/12.2019 and JBP/FP-223/12.2020). Rana Elfatairi was funded by NANOMED EMJMD supported by the European Union and the Erasmus+ Program by the European Union in the Framework Agreement Number 2016-2057/001- 001 EMJMD, No. 574439-EPP-1-FR-EPPKA1-JMD-MOB.



## Supplementary data



**Figure S3-1.** Intestinal sample prepared in 5-mL water (control) after the ultracentrifugation with  $4 \times 10^5$  G force for 2 hours. Thick mucus layer was observed on the top of the supernatant, blocking the separation of LNC-50.



**Figure S3-2.** Intestinal sample prepared in 5-mL of 3% L-cysteine after the ultracentrifugation with  $4 \times 10^5$  G force for 2 hours. Thick mucus layer was observed on the top of the supernatant with a crystallized L-cysteine at the bottom and the wall of the tube, blocking the separation of LNC-50.



**Figure S3-3.** Intestinal sample prepared in 5-mL of acetate buffer pH 5.0 after the ultracentrifugation with  $4 \times 10^5$  G force for 2 hours. No separation was clearly observed, indicating a failure to separate LNC-50.

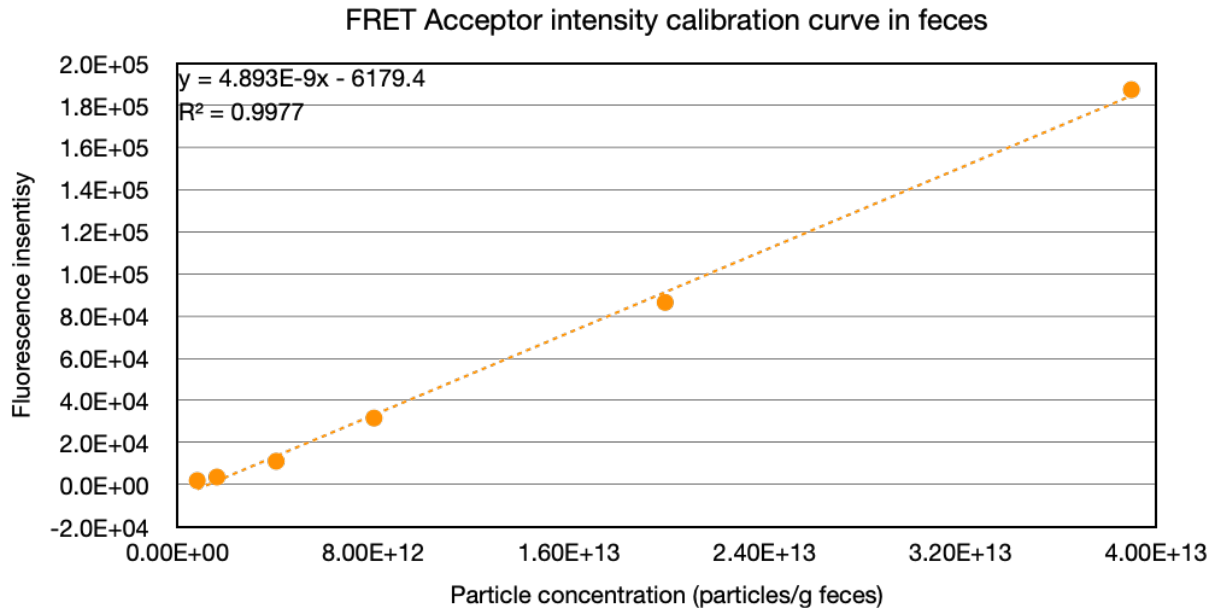


**Figure S3-4.** Example of feces quantitative FRET calibration curve of LNC-50-PEG between FRET acceptor intensity and particle concentration per gram of feces.

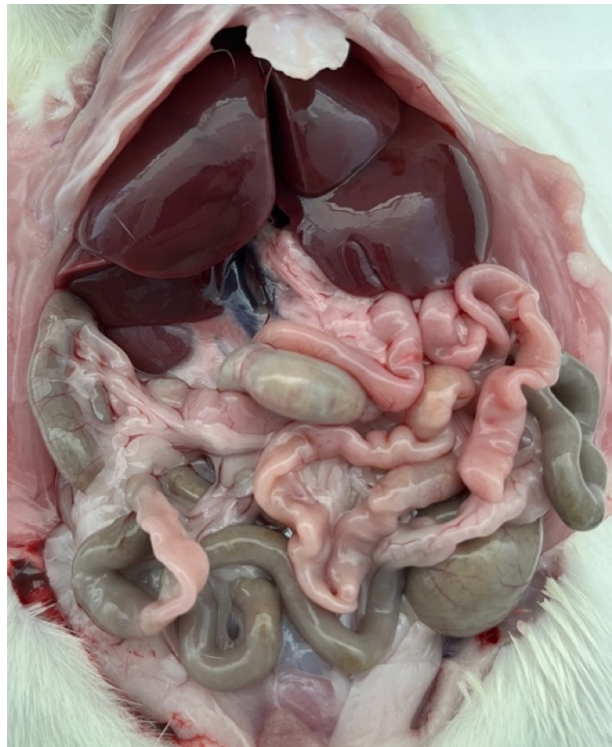


**Figure S3-5.** Rat autopsy at 24 hours after the gavage of LNC-50-PEG with the dose  $2 \times 10^{14}$  particle/100 g rat. FRET-LNCs were not observed in any part of the GI tract.

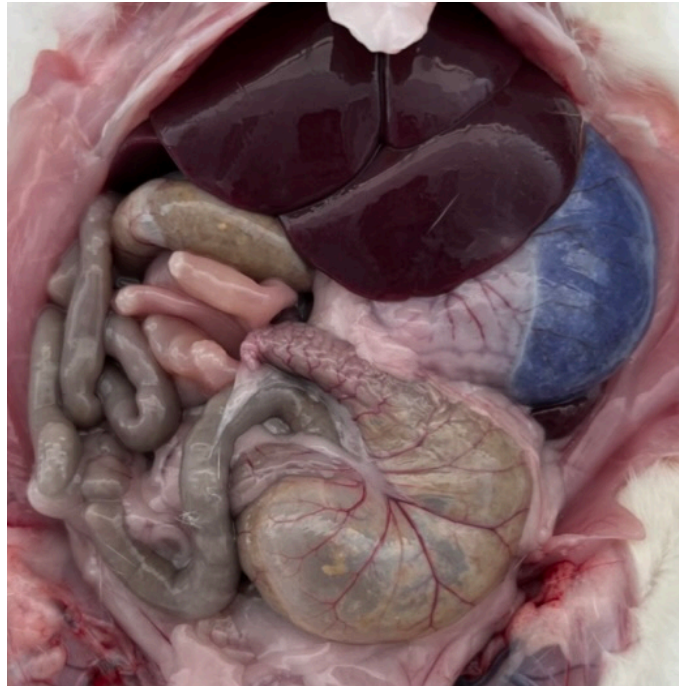


**Figure S3-6.** Rat autopsy at 2.5 hours after the gavage of LNC-50 with the dose  $2 \times 10^{14}$  particle/100 g rat. FRET-LNCs were not observed in the intestine yet.

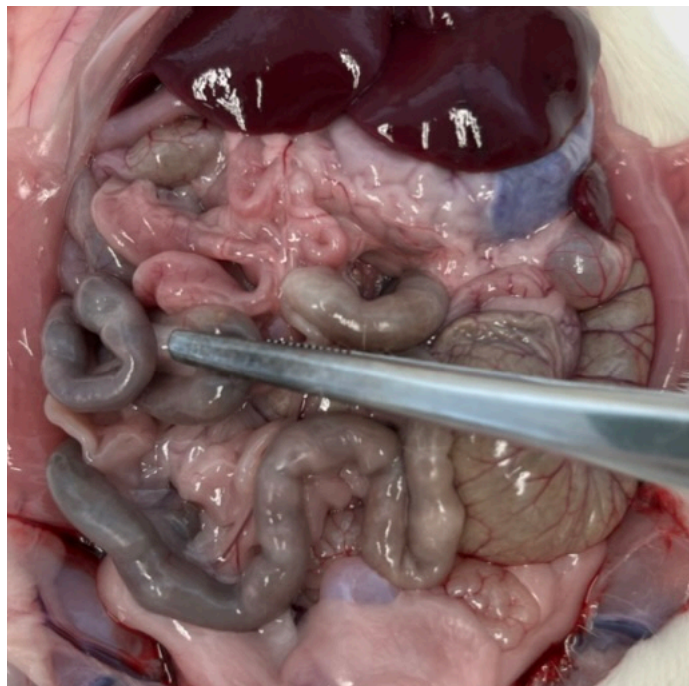


**Figure S3-7.** Rat autopsy at 4 hours after the gavage of LNC-50 with the dose  $2 \times 10^{14}$  particle/100 g rat. FRET-LNCs were observed in all parts of the GI tract.

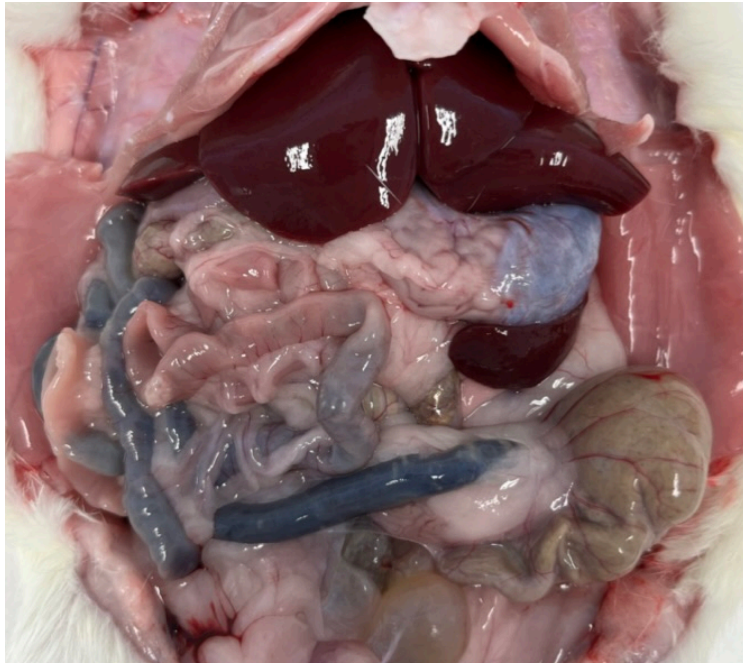


**Figure S3-8.** Rat autopsy at 4 hours after the gavage of LNC-85 with the dose  $5 \times 10^{13}$  particle/100 g rat. FRET-LNCs were observed in all parts of the GI tract.

## Chapter 4: General discussion

LNCs provide great benefits for its ability to increase oral bioavailability of many encapsulated drugs, making it one of the promising oral nanomedicines. However, the oral absorption of the intact LNCs itself has not yet been well studied because of a lack of an appropriate tool. The conventional approach studying only the absorption of the encapsulated drugs alone is also incapable to give the full picture of the behavior of nanomedicine formulations.

Hence to fill in the gap and to advance the knowledge of nanomedicine oral absorption, this thesis had the objectives to develop the appropriate tool for absorption study of intact LNCs and then characterize their oral bioavailability. The *in vivo* pharmacokinetics and the *in vivo* bioavailability of intact LNCs were more precisely characterized with the implementation of the new tools, namely, 1) the *in vitro* Caco-2/HMEC-1 coculture model and 2) the quantitative FRET techniques for *in vivo* samples, the *in vitro* absorption.

### 1. *In vitro* oral absorption of intact LNCs

#### 1.1 Development of the new *in vitro* Caco-2/HMEC-1 coculture model

The development of this Caco-2/HMEC-1 is the resolution to the lack of endothelium cell lines in the conventional *in vitro* model. The new coculture model between Caco-2 and HMEC-1 was observed to have a 3-times increase in the transepithelial electrical resistant (TEER) compared to the Caco-2 model alone (**Chapter 1, Figure 2**), meaning that the coculture model had the elevated in tight junction integrity possibly caused by the addition of the HMEC-1 endothelium [145]. Interestingly, a monolayer of HMEC-1 in Transwell® has almost the same TEER as the Transwell® filter. Hence, it is less likely that the huge increase in the tight junction integrity is caused solely by the integrity of the HMEC-1, but rather the result of change in the Caco-2's tight junction integrity. An increase in tight junction integrity of Caco-2 cells is generally associated with the balance between the upregulation of thigh junction-sealing protein claudin-4 and the downregulation of tight junction pore-forming protein claudin-2 [146,147]. The cytokine Interleukin-6 (IL-6) was observed to promote claudin-2 in Caco-2 [148,149]. Transforming Growth Factor- $\beta$

isoform 1 (TGF $\beta$ -1) was found to be responsible for the upregulation of claudin-4 in a monolayer of HT-29/B6 cells, which is a subtype of Caco-2 cell [150]. It could be hypothesized that the presence of HMEC-1 in the coculture model may alter many cytokines levels in the Transwell® system influencing Caco-2 and resulting in, at least, the reduction of IL-6 and the increase of TGF $\beta$ -1. However, the elevation in the integrity of tight junction could also associate with other protein, for example, claudin-1, -3, -5, -6, -8, -12, -18, and -19 which also involve many other cytokines [146]. Further studies on the expression of claudin proteins and TGF $\beta$ -1 may be needed to elucidate this phenomenon [151].

Summarily, the addition of HMEC-1 to the Caco-2 causes the change in the biological function of the membranes by greatly increase the tight junction's integrity. Thus, the new Caco-2/HMEC-1 model has different biological property from the conventional Caco-2 model.

#### **1.1.1 Caco-2/HMEC-1 coculture model for drug molecule permeability assay**

Despite increase in the membrane integrity (TEER), the Caco-2/HMEC-1 coculture model has the same permeability to drug molecule as the Caco-2 model (**Chapter 1, Figure 3**). A monolayer of HMEC-1 endothelium also has the permeability to drug molecules similar to that of the blank Transwell® filter. However, this is unsurprising because the pathway of drug molecule absorption relies mainly on the chemical process of passive diffusion that tight junction has little effect on it [152,153]. Therefore, for the study on the permeability of drug molecule in terms of the chemical assay, the new Caco-2/HMEC-1 coculture model may be considered as an optional to the conventional Caco-2. However, since the new coculture model has different biological property to that of Caco-2, the permeability of drugs that rely on the biological process may be different from the conventional Caco-2 model.

#### **1.1.2 Future improvements for Caco-2/HMEC-1 coculture model**

The development of this Caco-2/HMEC-1 is just the first step and a proof of concept for the epithelium-endothelium coculture model. In order to better imitate the intestinal barrier structure, different cell types can replace the Caco-2 and HMEC-1. One interesting cell line is HT-29 which is a subtype of Caco-2 but can differentiate to a goblet cell that can produce mucus layer. If the coculture between HT-29/HMEC-1 is successful, it would be a model that contain all three barriers: the mucus, the epithelium, and the endothelium.

Recently, it has been discovered that the intestinal crypts isolated from the human intestine can form a 3D structure called "enteroids" in culture and present the same histological and functional properties as the intestine. The conformation of enteroids can

also be transformed from 3D to 2D and seeded onto the Transwell membrane [154–157]. Therefore, these enteroids technology could be beneficial for the optimization and amelioration of the current *in vitro* model for future project. The future generation of the *in vitro* coculture model should include both the enteroids epithelium and vascular endothelium, to mimic the actual gut-blood barrier as much as possible.

For the endothelium, the use of HIMEC (human intestinal microvascular endothelium cells) would also better reflex real intestinal cell structure than HMEC- 1 [158].

## 1.2 *In vitro* oral absorption of intact LNCs

The transport of the six LNCs formulations were evaluated in the Caco-2 model and Caco-2/HMEC-1 coculture model with the control in HMEC-1 monolayer, blank Transwell® filter. FRET was employed for the technique to quantify intact FRET-LNCs particles.

In the control blank Transwell® filter (**Figure 6**), the transport efficiency of the all six intact FRET-LNCs formulations was around 8%. HMEC-1 monolayer alone was found to act as the barrier that can decrease the transport efficiency of all formulation for around 5 times (from around 8% down to 2%), while this was not the case for drug molecules. As mentioned previously, HMEC-1 has the same permeability to drug molecule as blank Transwell® filter. This is one evidence that the *in vitro* absorption of drug molecule and nanomedicine across the endothelium membrane are distinct and strengthen the need of the endothelial barrier for the evaluation of the intestinal absorption of LNCs.

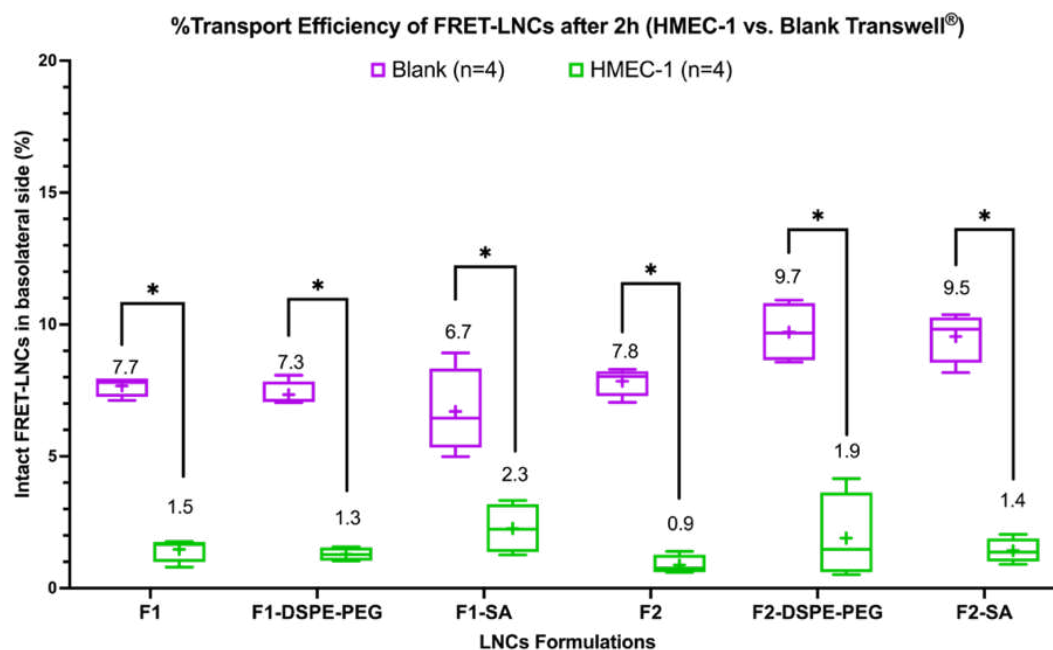


**Figure 7.** Transport efficiency of six FRET-LNCs formulations after 2 hours in the blank Transwell® (purple, n = 4), and HMEC-1 monolayer (green, n = 4). F1 = 50-nm FRET-LNCs, F2 = 85-nm FRET-LNCs. The (+) symbols represent the arithmetic mean, and the whiskers represent a 95% confidence interval (Kruskal-Wallis: \* p ≤ 0.05).

For the Caco-2 model (**Chapter 1, Figure 4**), the transport efficiency of the FRET-LNCs was very low <1%, some FRET-LNCs namely LNC-50-PEG, LNC-85-PEG, LNC-85-SA even had 0% transport. It seems that pegylated LNCs could not cross the Caco-2 membrane at all regardless of size. And only 0.06% of LNC-50 crossed the Caco-2, which was even lower than what observed previously in the literature [128], possibly because the more experimental repetition (n=4–8) has been done in this study so that the average decreased due to the fact that some repetition LNC-50 had 0% transport, while only 1 repetition was done in the literature. Hence, the result in our study was more accurate. Besides, 92-100% of FRET-LNCs was still on the apical side after 2 hours of incubation in Caco-2 and Caco-2/HMEC-1 models (**Figure 7**).



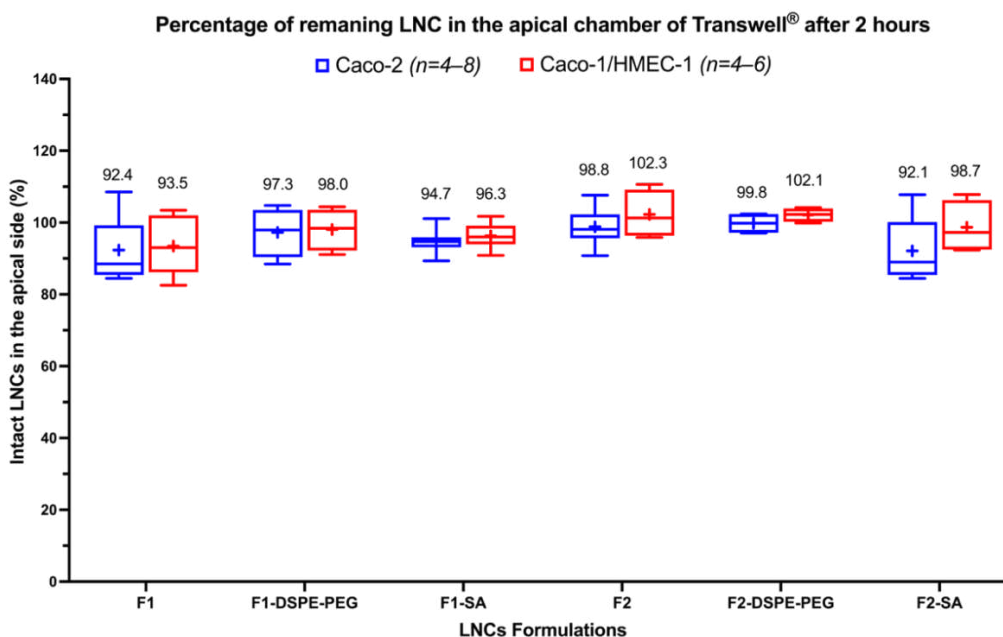


**Figure 8.** % Remaining of six FRET-LNCs formulations after 2 hours in the Caco-2 model (blue, n = 4-8), and the Caco-2/HMEC-1 coculture model (red, n = 4-6). F1 = 50-nm FRET-LNCs, F2 = 85-nm FRET-LNCs. The (+) symbols represent the arithmetic mean, and the whiskers represent a 95% confidence interval

As such, one would hypothesize that, if intact LNCs had to transport through both Caco-2 and HMEC-1 as in the coculture model, the transport would be less or even impossible. Surprisingly, the result was the opposite as LNC-50-PEG, LNC-85-PEG, LNC-85-SA, which had 0% transport in Caco-2, now had >0% transport in Caco-2/HMEC-1 model (**Chapter 1, Figure 4**). That means the coculture model reacts to LNCs differently from Caco-2 model. This result is in accordance with the discussion in **section 1.1** that the biological properties of Caco-2/HMEC-1 is distinct to that of the Caco-2 and as a result of the addition of the HMEC-1 endothelium.

The main pathway of nanomedicine transport across GI epithelium occurs *via* biological process such as active transports (also called transcytosis) [78,153,159-161]. Active transport consists of several pathways namely macropinocytosis, clathrin-mediated endocytosis, caveolin-mediated endocytosis, clathrin- and caveolin-independent endocytosis (a.k.a. lipid raft) *via* enterocytes as well as the phagocytosis *via* M-cell [78,159].

For LNCs, it was found that the main absorption process across Caco-2 model occurs *via* clathrin-dependent and caveolin-dependent transcytosis and is size-independent [61,124]. The fact that LNC-50-PEG, LNC-85-PEG, and LNC-85-SA having an increase in the transport in the new coculture model suggests an increase in transcytosis that is more selective to pegylated LNCs and 85-nm size. As discussed before, it could be hypothesized that the change in protein expression of cells or in cytokine level in the

coculture system may also have an effect on the transcytosis mechanisms. There is a report that TGF $\beta$ -1 can change the activity of receptor-mediated endocytosis [162,163]. Future studies should evaluate the transcytosis mechanism of LNCs in the Caco-2/HMEC-1 model to find how the transcytosis, in this new coculture model, differs from the conventional Caco-2.

Finally, it could be concluded that the transport efficiency of intact LNCs across the Caco-2 and Caco-2/HMEC-1 models is very low as <1% of the intact LNCs found in the basolateral chamber. The transport less than 1% might look small, but considering that GI transit can take several hours (the *in vitro* test only took 2 hours of incubation) and the surface area of the intestine is extremely large around 1 m<sup>2</sup> for rat model [164], compared to around 1 cm<sup>2</sup> for the Transwell® filter [165]. Therefore, it can be hypothesized that intact LNCs would be detectable in the systemic circulation at some degree. It is also important to have a final prove on *in vivo* oral absorption of intact LNCs, in order to define their oral bioavailability. The successful use of FRET in this experiment to quantify the % transport efficiency (amount of intact LNCs across Transwell®) is also the proof of concept of the further use of FRET in the next *in vivo* study.

## 2. *In vivo* oral absorption of intact LNCs

### 2.1 Quantitative FRET for blood sample

The problem of the existing other *in vivo* FRET technique is that the method to extract LNCs from the blood sample has not been adapted to conserve nanoparticles integrity. Since LNCs is lipid particles, it could be rationalized that they can be extracted from the blood sample using the widely-used technique to separate plasma called the “density gradient centrifugation” technique [166–168]. It is the technique to separate blood composition based on the density of each substance after applying the centrifugation force. Polysucrose solution with certain density is added to the blood sample to act as a separator between red blood cells and plasma. In this project, Histopaque® 1083, the polysucrose with the density of 1.083 g/mL was utilized. **Figure 9** shows the illustration of the density gradient separation of rat blood sample containing intact FRET-LNCs after the ultracentrifugation with 400,000 G force for 120 min. FRET-LNCs, which is lipid, go to the top of the supernatant because it has the density less than water (1 g/mL) and plasma (1.025 g/mL) [169].

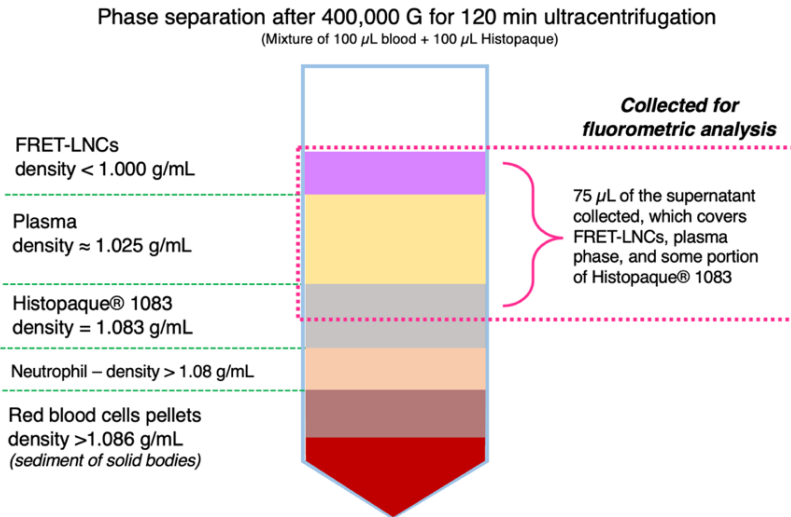


**Figure 9.** Illustration shows the density gradient separation of rat blood sample containing FRET-LNCs (in a 200- $\mu$ L polycarbonate tube) after ultracentrifugation with 400,000 G force for 120 min. Density information of plasma and neutrophil obtained from Zipursky et al. [169].

**Figure 10** shows the real example distribution of the density gradient that blood sample after the ultracentrifugation.

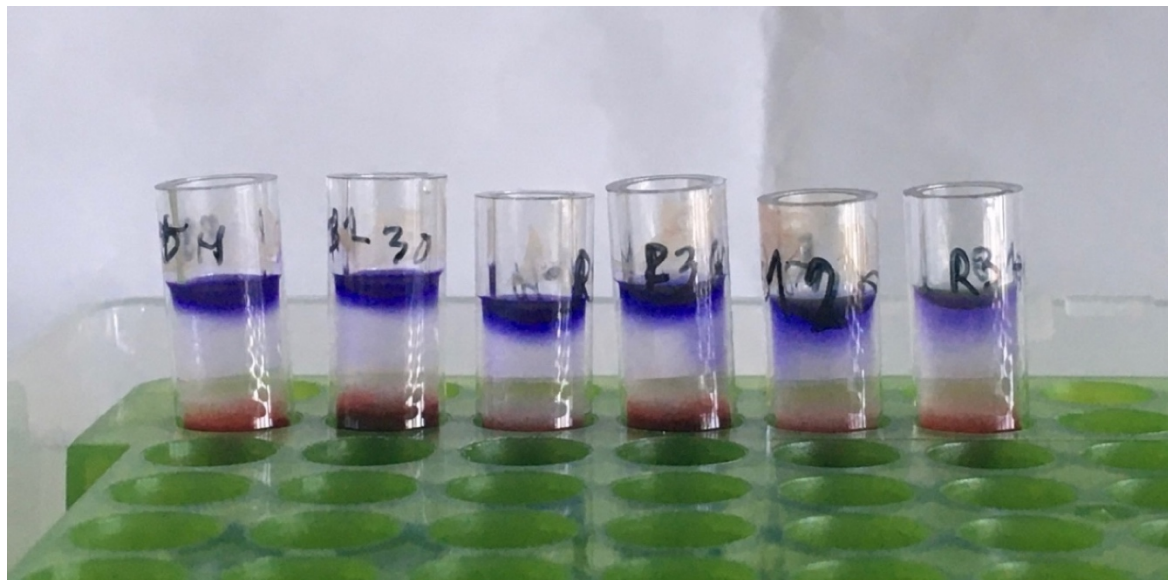


**Figure 10.** Real example of FRET-LNCs separated from blood of the rat injected with FRET-LNCs after ultracentrifugation. The purple layer of FRET-LNCs on the top is clearly visible due to high injected dose ( $2 \times 10^{14}$  particles/100 g rat). The clear layer in the middle indicates blood plasma and polysucrose solution. Red layer at the bottom (partially observable over the rack) indicates the red blood cell pellet. A thin white layer of neutrophile can also be observed as a boundary between the red layer and clear layer (not clearly visible in the photo).

Besides, the extraction of LNCs from blood is just one step of the quantitative FRET technique. The important step is to construct the calibration curves that link between the FRET acceptor intensity signal to the FRET-LNCs particle concentration. The calibration curves of the six LNCs formulations were successfully constructed (**Chapter 2, Supplementary 5**) with the limit of detection (LOD) as low as  $10^{10}$  particle/mL (**Chapter 2, Table S8-7**), which corresponds to the 0.001% of the plasma concentration of the injected dose (around  $10^{13}$  particle/mL plasma).

The reliability of the extraction method was also evaluated by the study on the matrix effect between the calibration curves of the FRET-LNCs spiked blood sample compared to the spiked water. The result showed a similar trend between the two. A slight matrix effect of blood was observed, which can be fixed by preparing a new calibration curve in each experimental session (**Chapter 2, Figure S4**).

A new quantitative FRET technique was successfully utilized to determine the plasma particle concentration-time profile and AUC of the intact FRET-LNCs (all six formulations). The full algorithm for FRET-LNCs particle concentration quantification procedure is detailed in **Chapter 2, Scheme S1**. This is the first true quantitative FRET technique allowing for the advanced pharmacokinetic analyses such as the non-compartmental analysis (NCA) and population pharmacokinetics.

## 2.2 Quantitative FRET for hepatic portal system's organs

### 2.2.1 Development of quantitative FRET for liver, intestinal tissue, and feces samples

LNCs extraction from liver, intestinal tissue, and feces is different from blood because these are solid mass that needs an extra step for homogenization. The aim is to reduce the size of the solid sample into a micron level to make it more resembling to blood so that the same density gradient centrifugation technique can be applied.

Liver tissue is soft and requires only 45 seconds of homogenization with the speed of 13,500 rpm. However, that is not the case for intestinal tissue and feces matter. Intestinal tissue has a strong connective tissue and sticky mucus that is very difficult to get homogenized. The feces matter, despite being soft, it is very greasy and contains large amount of undigested fiber filaments with the size as long as 1 cm, which is also very difficult to be homogenized. Longer homogenization time with faster speed was required for these two samples. The integrity of LNCs was proved to be well resistant to the homogenization up to 24,000 rpm for 10 minutes (**Chapter 3**) meaning that the use of homogenizer seems practical. Heat produced by the homogenization (around 40 °C) was observed but did not have a significant effect on the integrity of FRET-LNCs.

The intestinal tissue was found to require the homogenization for 8 min with the speed of 24,000 rpm. However, the intact LNCs extraction from the FRET-LNCs spiked intestinal tissue sample failed. The cause of the failure was possible to be the high content of mucus in the tissue that has high affinity to entrap FRET-LNCs [125]. The addition of mucolytic agents (L-cysteine) could not improve the extraction of FRET-LNCs. Therefore, the quantitative FRET for the intestinal tissue was not achievable. The extraction technique is not appropriate for quantitatively assay of intact LNCs in the intestinal tissue. Besides, it might be more appropriate to use qualitative imagery FRET for investigating cross-section of intestinal tissue slides as in Liu et al. [142]. This technique does not allow for quantification or semi-quantification of intact LNCs but allows for the penetration of FRET-nanoparticle to be observed.

For the feces sample, the feces matter requires the homogenization for 10 min with the speed of 24,000 rpm. However, very poor (almost none) recovery of intact LNCs was obtained. It is possible that the spiked FRET-LNCs was destructed in the process by being emulsified with the greasy feces matter under the fast homogenization condition. Thus, the homogenization method was abandoned. The new technique used mortar and pestle to grind up the feces matter into fine powder. Then, the fibers were removed by either paper filtration with Büchner or centrifugation at 3000 G force for 15 min. This new procedure was proved to be successful with the centrifugation method having higher FRET-LNCs recovery than the filtration method, possibly because FRET-LNCs can be adsorbed to the filter paper causing higher loss in the filtration method. Finally, the calibration curve of FRET-LNCs in feces was achievable.

Summarily, the quantitative FRET technique for solid sample was achieved in liver and feces.

### **2.2.2 Future improvements for the quantitative FRET**

It seems that this technique is now proved to be capable only for the blood, liver, spleen, and feces but not for the intestinal tissue. By the way, the quantitative FRET technique has not yet been developed for other major organs such as brain, skin, ovary, etc. If the quantitative method is developed for these organs, it is possible to study whole biodistribution of intact nanoparticle in each organ in the true quantitative level. Indeed, this quantitative FRET technique has a potentiality to be adapted to use with absorption of intact LNCs *via* other routes of administration. Therefore, this new quantitative FRET technique could also be a model for other FRET-system to adapt and follow. That would be a great benefit for advanced pharmacokinetics study as a whole and not just study on oral absorption.

### 2.2.3 Intact LNCs in hepatic portal system and feces

The study on the amount of intact FRET-LNCs in the hepatic portal system (liver and portal vein's blood) and feces after oral administration of FRET-LNCs (LNC-50, LNC-50-PEG, LNC-85, LNC-85-PEG) were conducted in rat model and reported in **Chapter 3**. No intact FRET-LNCs (all 4 formulations) was found in liver and portal vein's blood after 4, and 24 hours, similar to the result from the systemic circulation that has virtually 0% oral bioavailability. This result also correlates with the *in vitro* model in **Chapter 1**, the intact LNCs have only 0.06% transport *via* Caco-2/HEMEC-1 membrane. That is hypothetically corresponded to  $2.4 \times 10^{10}$  particles/mL rat plasma (considering that the initial concentration of the intact FRET-LNCs in rat plasma was  $4 \times 10^{13}$  particles/mL rat plasma, **Chapter 2**), which is very close to the detection limit of the quantitative FRET in blood sample at around  $10^{10}$  particle/mL. Therefore, it is reasonable that intact FRET-LNCs were not less likely to be detected in blood after absorption. By the way, it is still possible that little amount of intact FRET-LNCs with the concentration lower than the detection limit could enter the hepatic portal system and the systemic circulation system. However, the concentration of  $10^{10}$  particle/mL is only around 0.001% of the plasma concentration of the injected dose, this amount of intact FRET-LNCs would not yield any significance to the therapeutic effect. Therefore, it could be finally concluded that the absorb of intact FRET-LNCs through the intestinal route is unlikely.

For feces, the whole feces were collected after 24 hours after FRET-LNCs was orally administrated. The traces of the DiI and DiD (FRET dyes) were visibly observed in the feces pellet after the centrifugation as the matter still had a tint of purple. However, neither intact LNCs nor FRET dyes were found in the extracts, meaning that no intact LNCs survived the digestion. The apparent purple color could just be a remnant of the FRET dyes that was released from the dissociated FRET-LNCs and attached to the greasy fecal matter. From rat autopsy, at 4 hours after the oral administration, FRET-LNCs were present in the stomach, small intestine, and the caecum of the rat. Fermentation of the feces matter in the caecum of the rat may be the cause that FRET-LNCs were completely destroyed in the digestive tract. The particle stability in the rat caecum can be investigated by incubating FRET-LNCs in the slurry of the caecum content obtained from rat [170]. In addition, the effect of food on the absorption should also be considered. Hence, a renew experiment in fasted rat should also be conducted in the future.

## 2.3 Lack of intact LNCs oral absorption

**Figure 11** provides a schematic illustration summarizing the thesis project. The evidence from both the *in vitro* and *in vivo* results are in accordance that it does not supports the hypothesis that intact LNCs can absorb *via* the intestinal membrane. The evidence also suggests that LNCs may be completely destroyed in the GI.

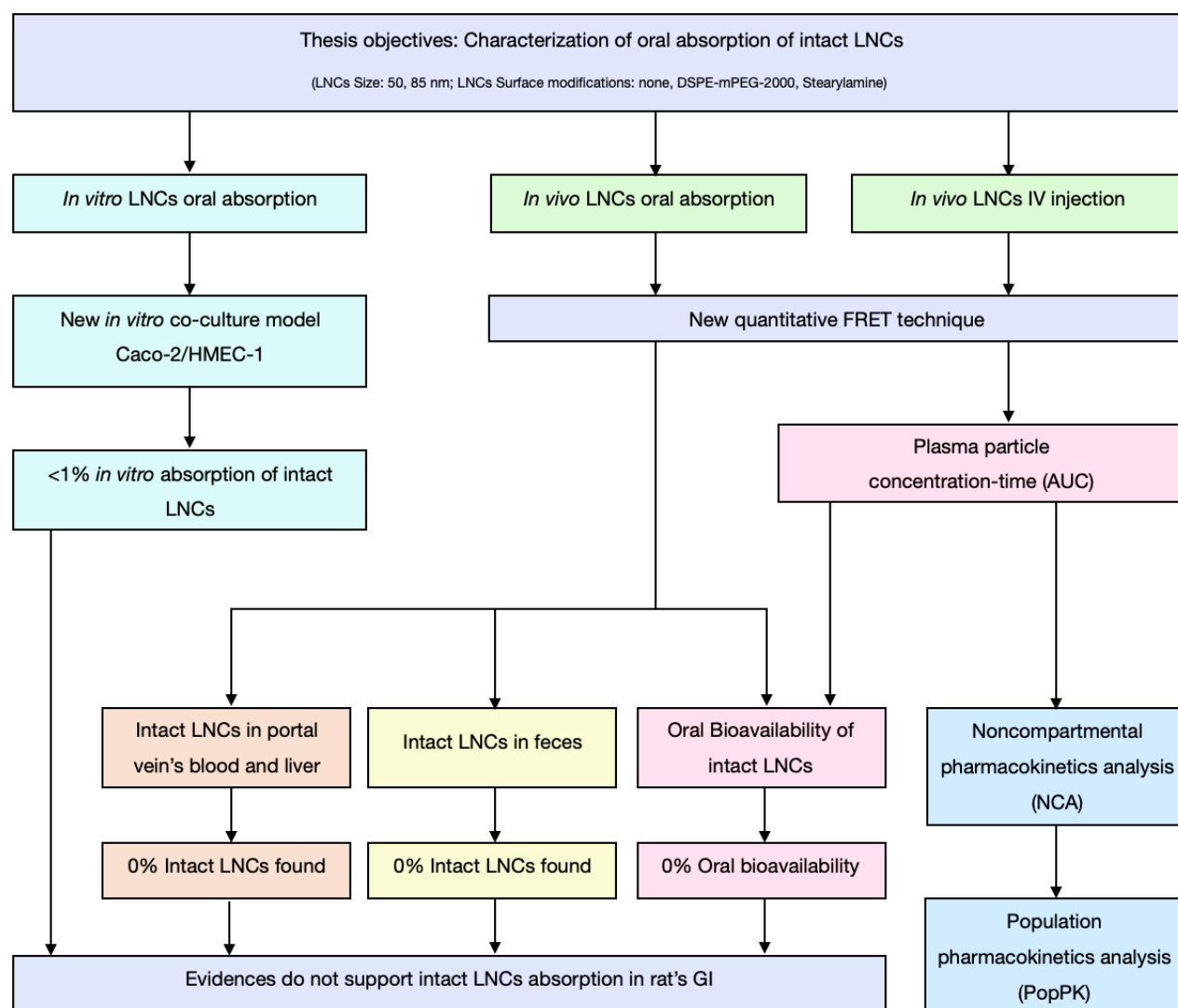


**Figure 11.** Schematic illustration summarizing the thesis project.

There are two scenarios of the effect of LNCs formulation on the oral bioavailability and therapeutic efficacy. First, the scenario that LNCs formulation help to increase the therapeutic efficacy in correlation with an elevated oral bioavailability. It could be hypothesized that while the LNCs is destroyed by GI enzyme, their remnants including triglyceride and surfactant can also facilitate the absorption of the encapsulated drugs [171]. The surfactant macrogol 15 hydroxystearates (Solutol® HS-15 a.k.a.

Kolliphor® HS-15) that making up the shell of LNCs can also inhibit the Pgp reducing efflux pump of drug such as paclitaxel resulting in the increase in the oral bioavailability [29,172].

Second, the scenario that oral bioavailability and therapeutic efficacy do not correlate causing the inexplicable discrepancy to the classical pharmacokinetic model [91,102]. It could be hypothesized that the remnants of LNCs in the lumen also absorb by the pathway similar to that of the digested lipid nutrients. That is to say, if the LNCs remnant is long-chain triglyceride (carbon atom > 12), it can mainly absorb by incorporating to the chylomicron and biodistribute in the body *via* the lymphatic system. And if the remnant is medium- or short-chain triglyceride (carbon atom < 12), it will mainly absorb by entering the hepatic portal system [173]. **Figure 12** illustrates the absorption pathway of the digested lipid-type nanoparticles.

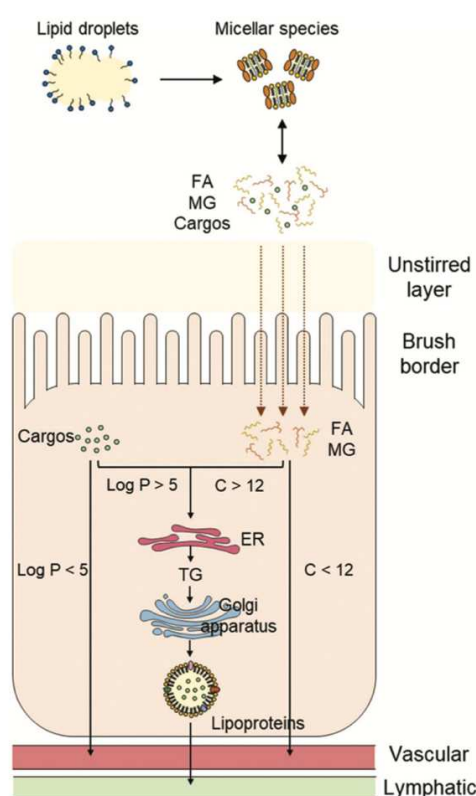


**Figure 12.** Absorption pathway of digested lipid-type nanoparticles. FA = fatty acid. MG = medium chain triglycerides. C = carbon atom. TG = triglycerides. ER = endoplasmic reticuli. Lipoproteins = chylomicrons. Reprinted from Wang et al. [173].

As the lipid core of LNCs makes up by the medium-chain triglycerides, its remnant could theoretically have the main absorption through the hepatic portal system. However, one evidence may suggest otherwise. A study by Tran et al. [92] found that paclitaxel encapsulated in LNCs having a 2-fold increase in the absorption *via* lymphatic system (rat auxiliary lymph node at 4 hours) compared to paclitaxel solution. That means the



absorption of LNCs remnant *via* lymphatic system may be higher than what described in the literature [173].

The lymph absorption hypothesis can also explain the discrepancy in the study by Eissa et al. [102] and Groo et al. [91]. In case of Eissa et al., LNCs formulations and drug solution had the same oral bioavailability, but LNCs formulations gave higher anthelmintic efficacy to the parasite-infected liver. It could be hypothesized that triglycerides of LNCs facilitate the extra amount of miltefosine absorption *via* lymphatic system to reach the infected liver more than oral solution. Triglycerides (LNCs remnants with miltefosine) will be collected by chylomicron in the lymphatic system and enters the systemic circulation at subclavian vein. Chylomicron will be metabolized by lipoprotein lipase to be the chylomicron remnant. Then, this chylomicron remnant will be taken up by liver via Lipoprotein receptor-related protein (LRP). In this case, the chylomicron, as an endogenous lipid particles, can act as if it is a miltefosine encapsulated nanoparticle targeting liver [45,173]. Besides, miltefosine has 98% plasma protein binding, which can greatly reduce drug efficacy [174]. Chylomicrons transport may also help to protect miltefosine from protein binding and to prolong the miltefosine stability *in vivo*, resulting in higher therapeutic efficacy. Meanwhile, miltefosine solution may only have one absorption pathway *via* hepatic portal vein as free miltefosine which almost all of it will bind to blood protein. That is why miltefosine oral solution has poor efficacy, despite the fact that it is absorbed *via* hepatic portal vein which goes directly to liver. **Figure 13** shows the lymphatic pathway of lipid absorption *via* intestinal lumen. **Figure 14** shows chylomicron transport from lymphatic system to liver.

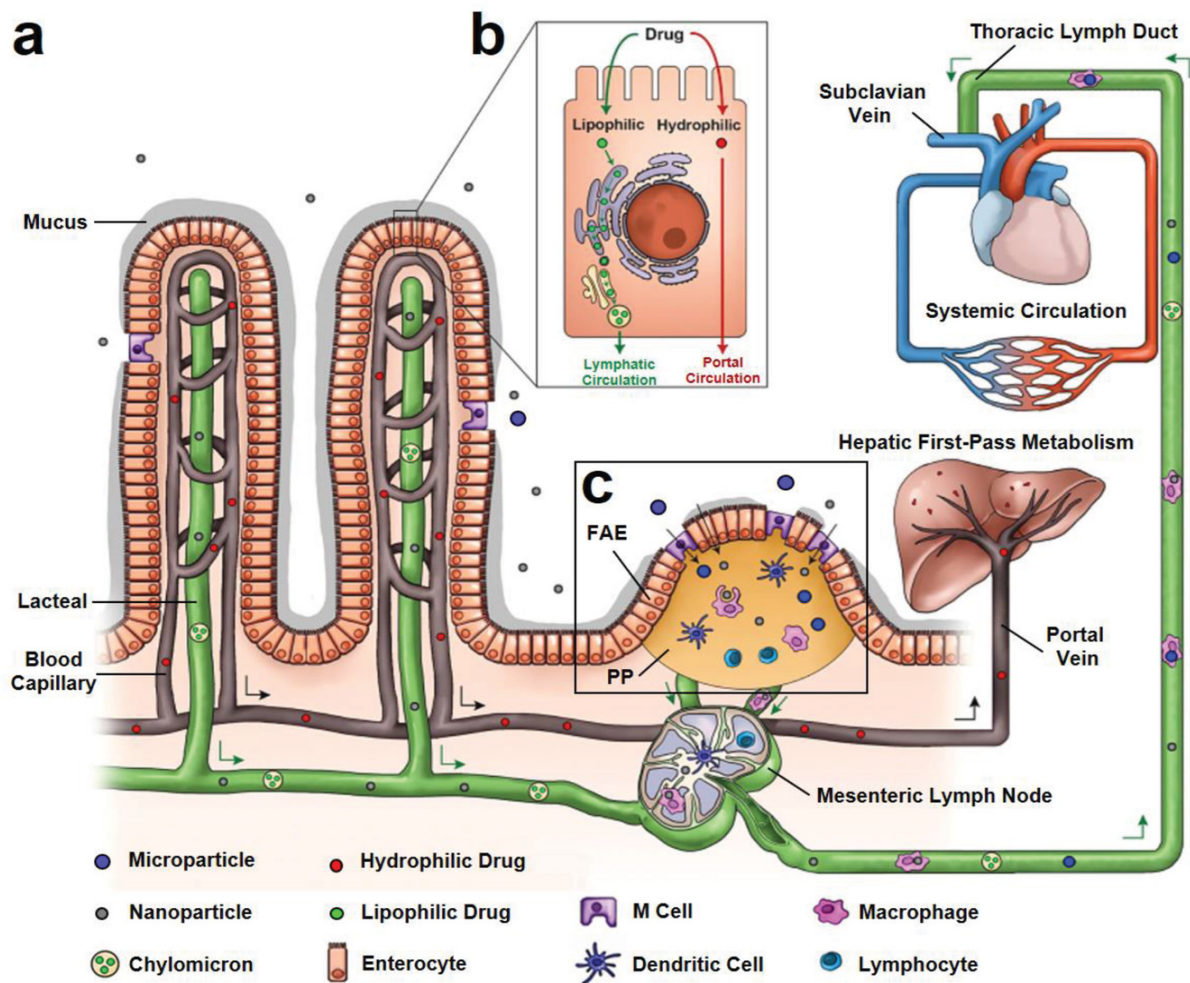


**Figure 13.** Lymphatic pathway of lipid absorption *via* intestinal lumen. Lipid molecules (hydrophobic) are absorbed through the lymphatic system *via* chylomicron transport. Reprinted from Miao et al. [175].

### Chylomicron Formation and Metabolism

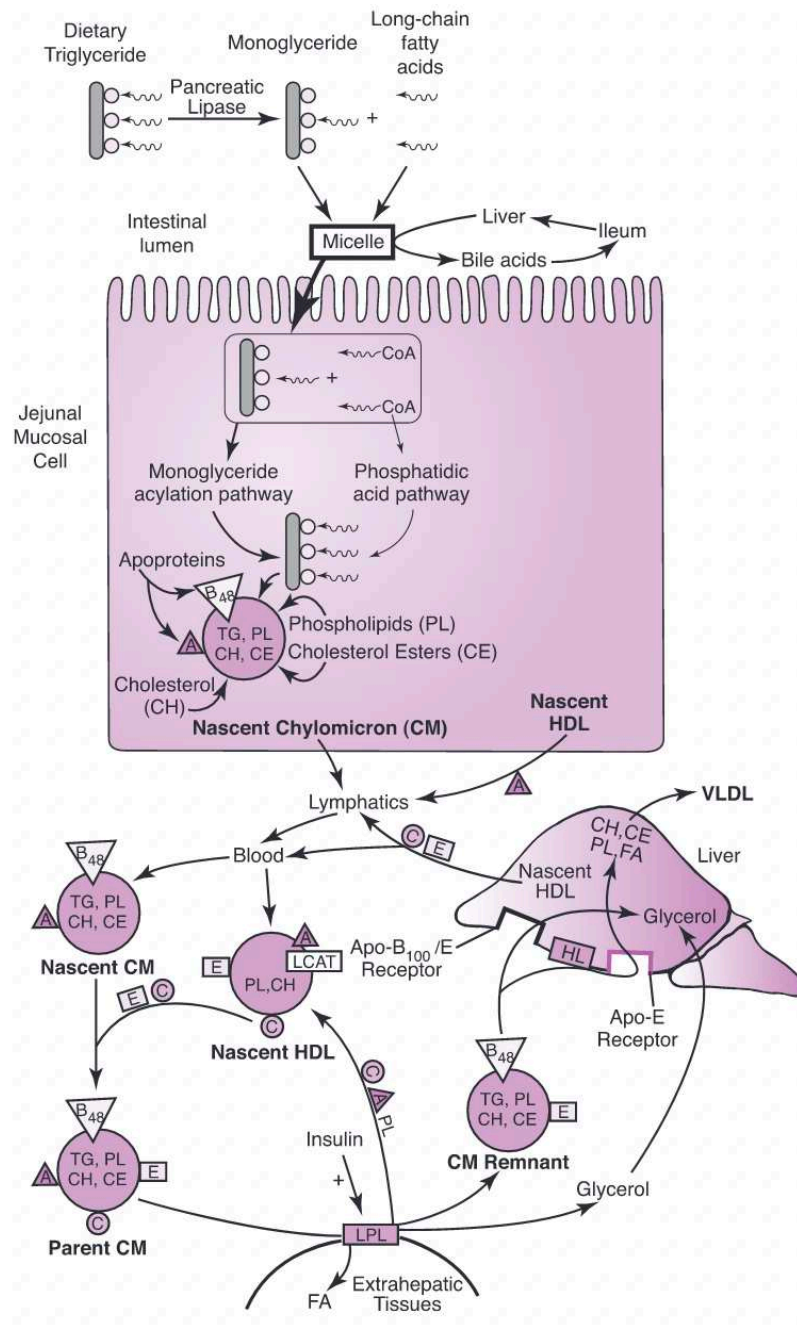


**Figure 14.** Chylomicron transport from lymphatic system to liver. Reprinted from Engelking L. R. [176].

In case of Groo et al., paclitaxel encapsulated in pegylated LNCs (by DSPE-mPEG-2000) had the highest increase in oral bioavailability with 11-fold (compared to paclitaxel oral solution) but failed to give anti-tumor efficacy (tumor size reduction), despite the fact that classical LNCs with only 4-fold increase in oral bioavailability provided the highest anti-tumor efficacy. It seems obvious that surface modification can have the effect to alter both oral bioavailability and drug efficacy. According to the lymphatic absorption

hypothesis, it could be hypothesized that the remnant of this pegylated formulation (DSPE-mPEG-2000 coating LNCs) better absorbs through the hepatic portal system rather than the lymphatic system like other LNCs formulations (classical LNCs, or chitosan-LNCs) so that the plasma concentration of paclitaxel by this pegylated formulation appears the highest. Pegylated nanoparticles were reported to have mucopenetrating effect [177] and liposome coated with DSPE-PEG-2000 was found to increase mucus penetration [178]. *In vitro* study in Caco-2/HT-29 model found that the cellular uptake of liposome coated with DSPE-PEG-2000 was not perturbed by the mucus [179]. Hence, it is possible that, due to this highly mucopenetrating effect, pegylated paclitaxel-LNCs may be able to reach the enterocyte cell surface, internalize, get destroyed in the cell, and then release to the mesenteric vein (and hepatic portal vein) as free paclitaxel. Meanwhile, classical paclitaxel-LNCs will get stuck to the mucus and turn into a lipid droplet, which will finally absorb via lymphatic system (**Figure 12**). Paclitaxel also has high plasma protein binding at 89-98% [180]. Therefore, the absorption via chylomicron will help prevent paclitaxel from protein binding resulting in better drug efficacy. Meanwhile, DSPE-PEG-2000 coated LNCs with higher absorption via hepatic portal vein as free drug does not have this benefit. Moreover, the tumor may be more accessible *via* lymphatic system so that high absorption *via* blood system rather causes the drug to reach the tumor less and resulting in the discrepancy between elevating oral bioavailability and fail anti-tumor efficacy.

In order to prove this lymph absorption hypothesis, a study on drug level in the lymphatic system after oral administration of drug encapsulating LNCs formulation should be conducted. Another study that can be performed is to use chylomicron blocker such as cycloheximide to block the absorption *via* lymphatic system. Cycloheximide will be given to rats before the oral administration of drug encapsulating LNCs formulations, then the decreasing in oral bioavailability or therapeutic efficacy will be determined to find magnitude of lymphatic absorption [173].

This discovery and explanation may help future project to take better decision on the design of LNCs formulation. LNCs formulations is still useful to improve the oral bioavailability and therapeutic efficacy of many drugs. However, since the intact LNCs do not orally absorb, this nano-delivery system may not be suitable *via* oral route for targeting therapy of inner organs such as brain, heart, kidney, etc. Instead, following its absorption pathway, LNCs may still be beneficial for drugs that target liver or lymphatic system.

## Conclusion

In conclusion, we successfully achieved the new *in vitro* coculture model of Caco-2 epithelium and HMEC-1 endothelium and developed the new quantitative FRET technique for *in vivo* tracking intact LNCs, and finally proved that intact LNCs do not cross the intestinal membrane.

The new *in vitro* Caco-2/HMEC-1 coculture model is a useful tool that can be utilized to study with other type of nanoparticles, drugs, or even food products which, more and more, nanotechnology has been involved. The new model is also relatively cheaper and easier to produce. It could be useful for high-thruput screening or daily use in the laboratory. The interesting thing about the model is that it has a specific interaction with nanoparticles. The new *in vitro* model gave surprising results that LNCs had an increase in permeability despite an increase in the integrity of the membrane due to the addition of the endothelium layer. This result seems counterintuitive and could imply that unknown transport mechanisms may be involved to increase the transport of the intact nanoparticles. To elucidate this, more studies on the endocytosis mechanisms should be performed in future projects.

The new quantitative FRET technique is the first true quantitative technique for *in vivo* nanoparticle tracking using FRET. However, it seems that this technique is now proved to be capable only for the blood, liver tissue, and feces but not for intestinal tissue. By the way, the quantitative FRET technique has not yet been developed for other major organs such as brain, lungs, spleen, ovary. If the quantitative method is developed for these organs, it is possible to study whole biodistribution of intact nanoparticle in each organ in the true quantitative level. Indeed, this quantitative FRET technique has a potentiality to be adapted to use with absorption of intact LNCs *via* other route of administration. Besides, in the **Bibliographic study**, there are many other semiquantitative FRET techniques that are capable to be upgraded to be a true quantitative FRET. Therefore, this new quantitative FRET could also be a model for other FRET-system to adapt and follow. That would be a great benefit for advanced pharmacokinetics study as a whole and not just study on oral absorption.

Finally, evidence form the *in vitro* and *in vivo* studies do not support that intact LNCs can absorb *via* the GI. It also suggests that LNCs may be completely destroyed in the GI. Therefore, it is hypothesized that the increase in oral bioavailability could be a result of the elevated absorption of LNCs remnants through lymphatic system as LNCs is lipid, which generally would absorb mainly through this path. This discovery is beneficial for future nanomedicine design to better suit the absorption *via* this pathway. And if future research could prove that LNCs prefer the absorption *via* lymphatics route, this would be beneficial for LNCs drug delivery *via* the lymph node.

## Reference

- [1] A.F. Borges, C. Silva, J.F.J. Coelho, S. Simões, Oral films: Current status and future perspectives II — Intellectual property, technologies and market needs, *J. Controlled Release*. 206 (2015) 108–121. <https://doi.org/10.1016/j.jconrel.2015.03.012>.
- [2] H. Rosen, T. Abribat, The rise and rise of drug delivery, *Nat. Rev. Drug Discov.* 4 (2005) 381–385. <https://doi.org/10.1038/nrd1721>.
- [3] A. Shahiwala, Formulation approaches in enhancement of patient compliance to oral drug therapy, *Expert Opin. Drug Deliv.* 8 (2011) 1521–1529. <https://doi.org/10.1517/17425247.2011.628311>.
- [4] A.Z. Fu, Y. Qiu, L. Radican, Impact of fear of insulin or fear of injection on treatment outcomes of patients with diabetes, *Curr. Med. Res. Opin.* 25 (2009) 1413–1420. <https://doi.org/10.1185/03007990902905724>.
- [5] S. Farsaei, M. Radfar, Z. Heydari, F. Abbasi, M. Qorbani, Insulin adherence in patients with diabetes: Risk factors for injection omission, *Prim. Care Diabetes*. 8 (2014) 338–345. <https://doi.org/10.1016/j.pcd.2014.03.001>.
- [6] D.S.U. Lee, H. Lee, Adherence and persistence rates of major antidiabetic medications: a review, *Diabetol. Metab. Syndr.* 14 (2022) 12. <https://doi.org/10.1186/s13098-022-00785-1>.
- [7] A. Wessell, M.J. Kole, N. Badjatia, G. Parikh, J.S. Albrecht, D.L. Schreiber, J.M. Simard, High Compliance with Scheduled Nimodipine Is Associated with Better Outcome in Aneurysmal Subarachnoid Hemorrhage Patients Cotreated with Heparin Infusion, *Front. Neurol.* 8 (2017) 268. <https://doi.org/10.3389/fneur.2017.00268>.
- [8] E. Menditto, V. Orlando, G. De Rosa, P. Minghetti, U.M. Musazzi, C. Cahir, M. Kurczewska-Michalak, P. Kardas, E. Costa, J.M. Sousa Lobo, I.F. Almeida, Patient Centric Pharmaceutical Drug Product Design—The Impact on Medication Adherence, *Pharmaceutics*. 12 (2020) 44. <https://doi.org/10.3390/pharmaceutics12010044>.
- [9] A. Golay, Pharmaco-economic aspects of poor adherence: can better adherence reduce healthcare costs?, *J. Med. Econ.* 14 (2011) 594–608. <https://doi.org/10.3111/13696998.2011.597808>.
- [10] S. Perreault, Global Clinical Consequences of Poor Adherence, in: M. Burnier (Ed.), *Drug Adherence Hypertens. Cardiovasc. Prot.*, Springer International Publishing, Cham, 2018: pp. 297–314. [https://doi.org/10.1007/978-3-319-76593-8\\_22](https://doi.org/10.1007/978-3-319-76593-8_22).
- [11] K. Kvarnström, A. Westerholm, M. Airaksinen, H. Liira, Factors Contributing to Medication Adherence in Patients with a Chronic Condition: A Scoping Review of Qualitative Research, *Pharmaceutics*. 13 (2021) 1100. <https://doi.org/10.3390/pharmaceutics13071100>.

- [12] F.E. Stuurman, B. Nuijen, J.H. Beijnen, J.H.M. Schellens, Oral Anticancer Drugs: Mechanisms of Low Bioavailability and Strategies for Improvement, *Clin. Pharmacokinet.* 52 (2013) 399–414. <https://doi.org/10.1007/s40262-013-0040-2>.
- [13] K. Boye, M. Ross, R. Mody, M. Konig, H. Gelhorn, Patients' preferences for once-daily oral versus once-weekly injectable diabetes medications: The REVISE study, *Diabetes Obes. Metab.* 23 (2021) 508–519. <https://doi.org/10.1111/dom.14244>.
- [14] T.B. Niewold, One Size Doesn't Fit All, *Sci. Transl. Med.* 3 (2011) 103ec162–103ec162. <https://doi.org/10.1126/scitranslmed.3003257>.
- [15] J.F.P. Bridges, A.F. Mohamed, H.W. Finnern, A. Woehl, A.B. Hauber, Patients' preferences for treatment outcomes for advanced non-small cell lung cancer: A conjoint analysis, *Lung Cancer.* 77 (2012) 224–231. <https://doi.org/10.1016/j.lungcan.2012.01.016>.
- [16] J.M. Cyriac, E. James, Switch over from intravenous to oral therapy: A concise overview, *J. Pharmacol. Pharmacother.* 5 (2014) 83–87. <https://doi.org/10.4103/0976-500X.130042>.
- [17] M.N. Al-Hasan, H. Rac, Transition from intravenous to oral antimicrobial therapy in patients with uncomplicated and complicated bloodstream infections, *Clin. Microbiol. Infect.* 26 (2020) 299–306. <https://doi.org/10.1016/j.cmi.2019.05.012>.
- [18] B. Spellberg, H.F. Chambers, D.M. Musher, T.L. Walsh, A.S. Bayer, Evaluation of a Paradigm Shift From Intravenous Antibiotics to Oral Step-Down Therapy for the Treatment of Infective Endocarditis: A Narrative Review, *JAMA Intern. Med.* 180 (2020) 769–777. <https://doi.org/10.1001/jamainternmed.2020.0555>.
- [19] V.R. Devadasu, P.K. Deb, R. Maheshwari, P. Sharma, R.K. Tekade, Chapter 5 - Physicochemical, Pharmaceutical, and Biological Considerations in GIT Absorption of Drugs, in: R.K. Tekade (Ed.), *Dos. Form Des. Consid.*, Academic Press, 2018: pp. 149–178. <https://doi.org/10.1016/B978-0-12-814423-7.00005-8>.
- [20] J.M. DeSesso, C.F. Jacobson, A.L. Williams, Anatomical and Physiological Parameters that Influence Gastrointestinal Absorption, in: *Encycl. Drug Metab. Interact.*, John Wiley & Sons, Ltd, 2012: pp. 1–35. <https://doi.org/10.1002/9780470921920.edm022>.
- [21] E. Salah, M.M. Abouelfetouh, Y. Pan, D. Chen, S. Xie, Solid lipid nanoparticles for enhanced oral absorption: A review, *Colloids Surf. B Biointerfaces.* 196 (2020) 111305. <https://doi.org/10.1016/j.colsurfb.2020.111305>.
- [22] M.R. Rekha, C.P. Sharma, Chapter 8 - Nanoparticle Mediated Oral Delivery of Peptides and Proteins: Challenges and Perspectives, in: C. Van Der Walle (Ed.), *Pept. Protein Deliv.*, Academic Press, Boston, 2011: pp. 165–194. <https://doi.org/10.1016/B978-0-12-384935-9.10008-2>.

- [23] G.L. Amidon, H. Lennernäs, V.P. Shah, J.R. Crison, A Theoretical Basis for a Biopharmaceutic Drug Classification: The Correlation of in Vitro Drug Product Dissolution and in Vivo Bioavailability, *Pharm. Res.* 12 (1995) 413–420. <https://doi.org/10.1023/A:1016212804288>.
- [24] T. Takagi, C. Ramachandran, M. Bermejo, S. Yamashita, L.X. Yu, G.L. Amidon, A Provisional Biopharmaceutical Classification of the Top 200 Oral Drug Products in the United States, Great Britain, Spain, and Japan, *Mol. Pharm.* 3 (2006) 631–643. <https://doi.org/10.1021/mp0600182>.
- [25] U.S. food and drug administration, M9 Biopharmaceutics Classification System-Based Biowaivers, US Food Drug Adm. (2021). <https://www.fda.gov/regulatory-information/search-fda-guidance-documents/m9-biopharmaceutics-classification-system-based-biowaivers> (accessed August 13, 2022).
- [26] H. Lennernäs, B. Abrahamsson, E.M. Persson, L. Knutson, Oral drug absorption and the Biopharmaceutics Classification System, *J. Drug Deliv. Sci. Technol.* 17 (2007) 237–244. [https://doi.org/10.1016/S1773-2247\(07\)50090-0](https://doi.org/10.1016/S1773-2247(07)50090-0).
- [27] R. Ghadi, N. Dand, BCS class IV drugs: Highly notorious candidates for formulation development, *J. Controlled Release.* 248 (2017) 71–95. <https://doi.org/10.1016/j.jconrel.2017.01.014>.
- [28] M. Rodriguez-Aller, D. Guillarme, J.-L. Veuthey, R. Gurny, Strategies for formulating and delivering poorly water-soluble drugs, *J. Drug Deliv. Sci. Technol.* 30 (2015) 342–351. <https://doi.org/10.1016/j.jddst.2015.05.009>.
- [29] S. Peltier, J.-M. Oger, F. Lagarce, W. Couet, J.-P. Benoît, Enhanced Oral Paclitaxel Bioavailability After Administration of Paclitaxel-Loaded Lipid Nanocapsules, *Pharm. Res.* 23 (2006) 1243–1250. <https://doi.org/10.1007/s11095-006-0022-2>.
- [30] D. Pham, Dilemmas in the Dosing of Heart Failure Drugs: Titrating Diuretics in Chronic Heart Failure, (2017). <https://www.cfrjournal.com/articles/dilemmas-dosing-heart-failure-drugs-titrating-diuretics-chronic-heart-failure> (accessed August 21, 2022).
- [31] M.D. Murray, K.M. Haag, P.K. Black, S.D. Hall, D.C. Brater, Variable Furosemide Absorption and Poor Predictability of Response in Elderly Patients, *Pharmacother. J. Hum. Pharmacol. Drug Ther.* 17 (1997) 98–106. <https://doi.org/10.1002/j.1875-9114.1997.tb03681.x>.
- [32] D.C. Brater, Diuretic Therapy, *N. Engl. J. Med.* 339 (1998) 387–395. <https://doi.org/10.1056/NEJM199808063390607>.
- [33] W. Niu, T. Sun, L. Liu, X. Liu, R. Zhang, L. Yin, J. Wang, X. Jia, H.-Z. Lu, M. Zhong, Z. Jiao, L. Zhang, Population pharmacokinetics and dosing regimen optimisation of lopinavir in Chinese adults infected with HIV, *Basic Clin. Pharmacol. Toxicol.* 124 (2019) 456–465. <https://doi.org/10.1111/bcpt.13154>.



- [34] H.L. Sham, D.J. Kempf, A. Molla, K.C. Marsh, G.N. Kumar, C.-M. Chen, W. Kati, K. Stewart, R. Lal, A. Hsu, D. Betebenner, M. Korneyeva, S. Vasavanonda, E. McDonald, A. Saldivar, N. Wideburg, X. Chen, P. Niu, C. Park, V. Jayanti, B. Grabowski, G.R. Granneman, E. Sun, A.J. Japour, J.M. Leonard, J.J. Plattner, D.W. Norbeck, ABT-378, a Highly Potent Inhibitor of the Human Immunodeficiency Virus Protease, *Antimicrob. Agents Chemother.* 42 (1998) 3218–3224. <https://doi.org/10.1128/AAC.42.12.3218>.
- [35] P. Cawthorne, N. Ford, D. Wilson, K. Kijtiwatchakul, V. Purahong, N. Tianudom, S. Nacapew, Access to drugs: the case of Abbott in Thailand, *Lancet Infect. Dis.* 7 (2007) 373–374. [https://doi.org/10.1016/S1473-3099\(07\)70118-4](https://doi.org/10.1016/S1473-3099(07)70118-4).
- [36] A. Singh, Z.A. Worku, G. Van den Mooter, Oral formulation strategies to improve solubility of poorly water-soluble drugs, *Expert Opin. Drug Deliv.* 8 (2011) 1361–1378. <https://doi.org/10.1517/17425247.2011.606808>.
- [37] M.S. Alqahtani, M. Kazi, M.A. Alsenaidy, M.Z. Ahmad, Advances in Oral Drug Delivery, *Front. Pharmacol.* 12 (2021). <https://www.frontiersin.org/articles/10.3389/fphar.2021.618411> (accessed August 21, 2022).
- [38] T. Flanagan, Potential for pharmaceutical excipients to impact absorption: A mechanistic review for BCS Class 1 and 3 drugs, *Eur. J. Pharm. Biopharm.* 141 (2019) 130–138. <https://doi.org/10.1016/j.ejpb.2019.05.020>.
- [39] A. Duschl, Chapter 12 - Nanomedicine, in: D. Boraschi, G. Penton-Rol (Eds.), *Immune Rebalancing*, Academic Press, 2016: pp. 251–274. <https://doi.org/10.1016/B978-0-12-803302-9.00012-9>.
- [40] M. Li, K.T. Al-Jamal, K. Kostarelos, J. Reineke, Physiologically Based Pharmacokinetic Modeling of Nanoparticles, *ACS Nano.* 4 (2010) 6303–6317. <https://doi.org/10.1021/nn1018818>.
- [41] M. Li, P. Zou, K. Tyner, S. Lee, Physiologically Based Pharmacokinetic (PBPK) Modeling of Pharmaceutical Nanoparticles, *AAPS J.* 19 (2017) 26–42. <https://doi.org/10.1208/s12248-016-0010-3>.
- [42] V. Lebreton, S. Legeay, P. Saulnier, F. Lagarce, Specificity of pharmacokinetic modeling of nanomedicines, *Drug Discov. Today.* 26 (2021) 2259–2268. <https://doi.org/10.1016/j.drudis.2021.04.017>.
- [43] D. Sahoo, R. Bandaru, S.K. Samal, R. Naik, P. Kumar, P. Kesharwani, R. Dandela, Chapter 9 - Oral drug delivery of nanomedicine, in: P. Kesharwani, S. Taurin, K. Greish (Eds.), *Theory Appl. Nonparenteral Nanomedicines*, Academic Press, 2021: pp. 181–207. <https://doi.org/10.1016/B978-0-12-820466-5.00009-0>.
- [44] E.-Y. Chuang, K.-J. Lin, F.-Y. Su, F.-L. Mi, B. Maiti, C.-T. Chen, S.-P. Wey, T.-C. Yen, J.-H. Juang, H.-W. Sung, Noninvasive imaging oral absorption of insulin delivered by nanoparticles and its stimulated glucose utilization in controlling postprandial

- hyperglycemia during OGTT in diabetic rats, *J. Controlled Release*. 172 (2013) 513–522. <https://doi.org/10.1016/j.jconrel.2013.05.006>.
- [45] G. Poovi, N. Damodharan, Lipid nanoparticles: A challenging approach for oral delivery of BCS Class-II drugs, *Future J. Pharm. Sci.* 4 (2018) 191–205. <https://doi.org/10.1016/j.fjps.2018.04.001>.
- [46] N.T. Huynh, C. Passirani, P. Saulnier, J.P. Benoit, Lipid nanocapsules: A new platform for nanomedicine, *Int. J. Pharm.* 379 (2009) 201–209. <https://doi.org/10.1016/j.ijpharm.2009.04.026>.
- [47] P. Fonte, F. Araújo, S. Reis, B. Sarmento, Oral Insulin Delivery: How Far are We?, *J. Diabetes Sci. Technol.* 7 (2013) 520–531. <https://doi.org/10.1177/193229681300700228>.
- [48] O. of the Commissioner, Fact Sheet: FDA at a Glance, FDA. (2022). <https://www.fda.gov/about-fda/fda-basics/fact-sheet-fda-glance> (accessed August 21, 2022).
- [49] M.S. Kinch, A. Haynesworth, S.L. Kinch, D. Hoyer, An overview of FDA-approved new molecular entities: 1827–2013, *Drug Discov. Today*. 19 (2014) 1033–1039. <https://doi.org/10.1016/j.drudis.2014.03.018>.
- [50] A.A. Halwani, Development of Pharmaceutical Nanomedicines: From the Bench to the Market, *Pharmaceutics*. 14 (2022) 106. <https://doi.org/10.3390/pharmaceutics14010106>.
- [51] J.K. Patra, G. Das, L.F. Fraceto, E.V.R. Campos, M. del P. Rodriguez-Torres, L.S. Acosta-Torres, L.A. Diaz-Torres, R. Grillo, M.K. Swamy, S. Sharma, S. Habtemariam, H.-S. Shin, Nano based drug delivery systems: recent developments and future prospects, *J. Nanobiotechnology*. 16 (2018) 71. <https://doi.org/10.1186/s12951-018-0392-8>.
- [52] D. Singh, N. Bedi, A.K. Tiwary, Enhancing solubility of poorly aqueous soluble drugs: critical appraisal of techniques, *J. Pharm. Investig.* 48 (2018) 509–526. <https://doi.org/10.1007/s40005-017-0357-1>.
- [53] S.Z. Alshawwa, A.A. Kassem, R.M. Farid, S.K. Mostafa, G.S. Labib, Nanocarrier Drug Delivery Systems: Characterization, Limitations, Future Perspectives and Implementation of Artificial Intelligence, *Pharmaceutics*. 14 (2022) 883. <https://doi.org/10.3390/pharmaceutics14040883>.
- [54] W. Lu, J. Yao, X. Zhu, Y. Qi, Nanomedicines: Redefining traditional medicine, *Biomed. Pharmacother.* 134 (2021) 111103. <https://doi.org/10.1016/j.biopha.2020.111103>.
- [55] C.L. Ventola, Progress in Nanomedicine: Approved and Investigational Nanodrugs, *Pharm. Ther.* 42 (2017) 742–755.

- [56] A. Beloqui, A. des Rieux, V. Pr eat, Mechanisms of transport of polymeric and lipidic nanoparticles across the intestinal barrier, *Adv. Drug Deliv. Rev.* 106 (2016) 242–255. <https://doi.org/10.1016/j.addr.2016.04.014>.
- [57] A. Fedi, C. Vitale, G. Ponschin, S. Ayehunie, M. Fato, S. Scaglione, In vitro models replicating the human intestinal epithelium for absorption and metabolism studies: A systematic review, *J. Controlled Release.* 335 (2021) 247–268. <https://doi.org/10.1016/j.jconrel.2021.05.028>.
- [58] P.A. Billat, E. Roger, S. Faure, F. Lagarce, Models for drug absorption from the small intestine: where are we and where are we going?, *Drug Discov. Today.* 22 (2017) 761–775. <https://doi.org/10.1016/j.drudis.2017.01.007>.
- [59] C. Righeschi, M.C. Bergonzi, B. Isacchi, C. Bazzicalupi, P. Gratteri, A.R. Bilia, Enhanced curcumin permeability by SLN formulation: The PAMPA approach, *LWT - Food Sci. Technol.* 66 (2016) 475–483. <https://doi.org/10.1016/j.lwt.2015.11.008>.
- [60] G. Graverini, V. Piazzini, E. Landucci, D. Pantano, P. Nardiello, F. Casamenti, D.E. Pellegrini-Giampietro, A.R. Bilia, M.C. Bergonzi, Solid lipid nanoparticles for delivery of andrographolide across the blood-brain barrier: in vitro and in vivo evaluation, *Colloids Surf. B Biointerfaces.* 161 (2018) 302–313. <https://doi.org/10.1016/j.colsurfb.2017.10.062>.
- [61] E. Roger, F. Lagarce, E. Garcion, J.P. Benoit, Lipid nanocarriers improve paclitaxel transport throughout human intestinal epithelial cells by using vesicle-mediated transcytosis, *J. Controlled Release.* 140 (2009) 174–181. <https://doi.org/10.1016/j.jconrel.2009.08.010>.
- [62] P. Artursson, K. Palm, K. Luthman, Caco-2 monolayers in experimental and theoretical predictions of drug transport, *Adv. Drug Deliv. Rev.* 46 (2001) 27–43. [https://doi.org/10.1016/S0169-409X\(00\)00128-9](https://doi.org/10.1016/S0169-409X(00)00128-9).
- [63] A. Wikman-Larhed, P. Artursson, Co-cultures of human intestinal goblet (HT29-H) and absorptive (Caco-2) cells for studies of drug and peptide absorption, *Eur. J. Pharm. Sci.* 3 (1995) 171–183. [https://doi.org/10.1016/0928-0987\(95\)00007-Z](https://doi.org/10.1016/0928-0987(95)00007-Z).
- [64] L. Baricault, G. Denari az, J.-J. Houri, C. Bouley, C. Sapin, G. Trugnan, Use of HT-29, a cultured human colon cancer cell line, to study the effect of fermented milks on colon cancer cell growth and differentiation, *Carcinogenesis.* 16 (1995) 245–252. <https://doi.org/10.1093/carcin/16.2.245>.
- [65] C. Hilgendorf, H. Spahn-Langguth, C.G. Reg ardh, E. Lipka, G.L. Amidon, P. Langguth, Caco-2 versus Caco-2/HT29-MTX Co-cultured Cell Lines: Permeabilities Via Diffusion, Inside- and Outside-Directed Carrier-Mediated Transport, *J. Pharm. Sci.* 89

- (2000) 63–75. [https://doi.org/10.1002/\(SICI\)1520-6017\(200001\)89:1<63::AID-JPS7>3.0.CO;2-6](https://doi.org/10.1002/(SICI)1520-6017(200001)89:1<63::AID-JPS7>3.0.CO;2-6).
- [66] I. Caro, X. Boulenc, M. Rousset, V. Meunier, M. Bourri , B. Julian, H. Joyeux, C. Roques, Y. Berger, A. Zweibaum, G. Fabre, Characterisation of a newly isolated Caco-2 clone (TC-7), as a model of transport processes and biotransformation of drugs, *Int. J. Pharm.* 116 (1995) 147–158. [https://doi.org/10.1016/0378-5173\(94\)00280-I](https://doi.org/10.1016/0378-5173(94)00280-I).
- [67] L.W. Peterson, D. Artis, Intestinal epithelial cells: regulators of barrier function and immune homeostasis, *Nat. Rev. Immunol.* 14 (2014) 141–153. <https://doi.org/10.1038/nri3608>.
- [68] S.C. Corr, C.C.G.M. Gahan, C. Hill, M-cells: origin, morphology and role in mucosal immunity and microbial pathogenesis, *FEMS Immunol. Med. Microbiol.* 52 (2008) 2–12. <https://doi.org/10.1111/j.1574-695X.2007.00359.x>.
- [69] I. Lozoya-Agullo, F. Ara jo, I. Gonz lez- lvarez, M. Merino-Sanju n, M. Gonz lez- lvarez, M. Bermejo, B. Sarmiento, Usefulness of Caco-2/HT29-MTX and Caco-2/HT29-MTX/Raji B Coculture Models To Predict Intestinal and Colonic Permeability Compared to Caco-2 Monoculture, *Mol. Pharm.* 14 (2017) 1264–1270. <https://doi.org/10.1021/acs.molpharmaceut.6b01165>.
- [70] E. Le Ferrec, C. Chesne, P. Artusson, D. Brayden, G. Fabre, P. Gires, F. Guillou, M. Rousset, W. Rubas, M.-L. Scarino, In Vitro Models of the Intestinal Barrier: The Report and Recommendations of ECVAM Workshop 461,2, *Altern. Lab. Anim.* 29 (2001) 649–668. <https://doi.org/10.1177/026119290102900604>.
- [71] R. Nielsen, H. Birn, S.K. Moestrup, M. Nielsen, P. Verroust, E.I. Christensen, Characterization of a kidney proximal tubule cell line, LLC-PK1, expressing endocytotic active megalin., *J. Am. Soc. Nephrol.* 9 (1998) 1767–1776. <https://doi.org/10.1681/ASN.V9101767>.
- [72] S. Tavelin, J. Taipalensuu, F. Hallb ok, K.-S. Vellonen, V. Moore, P. Artursson, An improved cell culture model based on 2/4/A1 cell monolayers for studies of intestinal drug transport: characterization of transport routes, *Pharm. Res.* 20 (2003) 373–381. <https://doi.org/10.1023/a:1022643802296>.
- [73] C. Moon, K.L. VanDussen, H. Miyoshi, T.S. Stappenbeck, Development of a primary mouse intestinal epithelial cell monolayer culture system to evaluate factors that modulate IgA transcytosis, *Mucosal Immunol.* 7 (2014) 818–828. <https://doi.org/10.1038/mi.2013.98>.
- [74] I. Hubatsch, E.G.E. Ragnarsson, P. Artursson, Determination of drug permeability and prediction of drug absorption in Caco-2 monolayers, *Nat. Protoc.* 2 (2007) 2111–2119. <https://doi.org/10.1038/nprot.2007.303>.
- [75] T. Briot, E. Roger, N. Lautram, A. Verger, A. Clavreul, F. Lagarce, Development and in vitro evaluations of new decitabine nanocarriers for the treatment of acute myeloid

- leukemia, *Int. J. Nanomedicine*. Volume 12 (2017) 8427–8442. <https://doi.org/10.2147/IJN.S147659>.
- [76] R.C.R. Beck, A.R. Pohlmann, C. Hoffmeister, M.R. Gallas, E. Collnot, U.F. Schaefer, S.S. Guterres, C.M. Lehr, Dexamethasone-loaded nanoparticle-coated microparticles: Correlation between in vitro drug release and drug transport across Caco-2 cell monolayers, *Eur. J. Pharm. Biopharm.* 67 (2007) 18–30. <https://doi.org/10.1016/j.ejpb.2007.01.007>.
- [77] M.C. Tadini, G. Ballester, I.S. Perovani, N.C. Perez de Albuquerque, A.L.A. Forte, F. Marquele-Oliveira, A.R.M. de Oliveira, Predicting absorption of amphotericin B encapsulated in a new delivery system by an in vitro Caco-2 cell model, *J. Drug Deliv. Sci. Technol.* 71 (2022) 103345. <https://doi.org/10.1016/j.jddst.2022.103345>.
- [78] E. Roger, F. Lagarce, E. Garcion, J.-P. Benoit, Biopharmaceutical parameters to consider in order to alter the fate of nanocarriers after oral delivery, *Nanomed.* 5 (2010) 287–306. <https://doi.org/10.2217/nnm.09.110>.
- [79] J.M. Gamboa, K.W. Leong, In vitro and in vivo models for the study of oral delivery of nanoparticles, *Adv. Drug Deliv. Rev.* 65 (2013) 800–810. <https://doi.org/10.1016/j.addr.2013.01.003>.
- [80] K. Gillois, C. Stoffels, M. Leveque, I. Fourquaux, J. Blesson, V. Mils, S. Cambier, J. Vignard, H. Terrisse, G. Mirey, J.-N. Audinot, V. Theodorou, M.-H. Ropers, H. Robert, M. Mercier-Bonin, Repeated exposure of Caco-2 versus Caco-2/HT29-MTX intestinal cell models to (nano)silver in vitro: Comparison of two commercially available colloidal silver products, *Sci. Total Environ.* 754 (2021) 142324. <https://doi.org/10.1016/j.scitotenv.2020.142324>.
- [81] E. Walter, S. Janich, B.J. Roessler, J.M. Hilfinger, G.L. Amidon, HT29-MTX/Caco-2 Cocultures as an in Vitro Model for the Intestinal Epithelium: In Vitro–in Vivo Correlation with Permeability Data from Rats and Humans, *J. Pharm. Sci.* 85 (1996) 1070–1076. <https://doi.org/10.1021/js960110x>.
- [82] C. Prego, M. Fabre, D. Torres, M.J. Alonso, Efficacy and Mechanism of Action of Chitosan Nanocapsules for Oral Peptide Delivery, *Pharm. Res.* 23 (2006) 549–556. <https://doi.org/10.1007/s11095-006-9570-8>.
- [83] F. Antunes, F. Andrade, F. Araújo, D. Ferreira, B. Sarmiento, Establishment of a triple co-culture in vitro cell models to study intestinal absorption of peptide drugs, *Eur. J. Pharm. Biopharm.* 83 (2013) 427–435. <https://doi.org/10.1016/j.ejpb.2012.10.003>.
- [84] A. des Rieux, V. Fievez, I. Théate, J. Mast, V. Pr at, Y.J. Schneider, An improved in vitro model of human intestinal follicle-associated epithelium to study nanoparticle transport by M cells, *Eur. J. Pharm. Sci.* 30 (2007) 380–391. <https://doi.org/10.1016/j.ejps.2006.12.006>.

- [85] C. Schimpel, B. Teubl, M. Absenger, C. Meindl, E. Fröhlich, G. Leitinger, A. Zimmer, E. Roblegg, Development of an Advanced Intestinal in Vitro Triple Culture Permeability Model To Study Transport of Nanoparticles, *Mol. Pharm.* 11 (2014) 808–818. <https://doi.org/10.1021/mp400507g>.
- [86] F.J.O. Varum, F. Veiga, J.S. Sousa, A.W. Basit, Mucus thickness in the gastrointestinal tract of laboratory animals, *J. Pharm. Pharmacol.* 64 (2012) 218–227. <https://doi.org/10.1111/j.2042-7158.2011.01399.x>.
- [87] K. Boussey, F.M. Belpaire, J. Van de Voorde, Chapter 23 - Physiological Aspects Determining the Pharmacokinetic Properties of Drugs, in: C.G. Wermuth, D. Aldous, P. Raboisson, D. Rognan (Eds.), *Pract. Med. Chem. Fourth Ed.*, Academic Press, San Diego, 2008: pp. 539–559. <https://doi.org/10.1016/B978-0-12-417205-0.00023-7>.
- [88] U.S. food and drug administration, Bioavailability Studies Submitted in NDAs or INDs – General Considerations, US Food Drug Adm. (2022). <https://www.fda.gov/regulatory-information/search-fda-guidance-documents/bioavailability-studies-submitted-ndas-or-inds-general-considerations> (accessed July 15, 2022).
- [89] S.-C. Chow, Bioavailability and bioequivalence in drug development, *WIREs Comput. Stat.* 6 (2014) 304–312. <https://doi.org/10.1002/wics.1310>.
- [90] P.L. Toutain, A. Bousquet-Mélou, Bioavailability and its assessment, *J. Vet. Pharmacol. Ther.* 27 (2004) 455–466. <https://doi.org/10.1111/j.1365-2885.2004.00604.x>.
- [91] A.C. Groo, M. Bossiere, L. Trichard, P. Legras, J.P. Benoit, F. Lagarce, In vivo evaluation of paclitaxel-loaded lipid nanocapsules after intravenous and oral administration on resistant tumor, *Nanomed.* 10 (2015) 589–601. <https://doi.org/10.2217/nnm.14.124>.
- [92] P. Tran, J.-H. Jang, S.-H. Jeong, Y.-B. Lee, Oral and Lymphatic Delivery of Paclitaxel via Lipid Nanocapsules, *Yakhak Hoeji.* 65 (2021) 375–385. <https://doi.org/10.17480/psk.2021.65.5.375>.
- [93] P.E. Pensel, G. Ullio Gamboa, J. Fabbri, L. Ceballos, S. Sanchez Bruni, L.I. Alvarez, D. Allemandi, J.P. Benoit, S.D. Palma, M.C. Elissondo, Cystic echinococcosis therapy: Albendazole-loaded lipid nanocapsules enhance the oral bioavailability and efficacy in experimentally infected mice, *Acta Trop.* 152 (2015) 185–194. <https://doi.org/10.1016/j.actatropica.2015.09.016>.
- [94] J. Fabbri, J.P. Espinosa, P.E. Pensel, S.K. Medici, G.U. Gamboa, J.P. Benoit, M.C. Elissondo, Do albendazole-loaded lipid nanocapsules enhance the bioavailability of albendazole in the brain of healthy mice?, *Acta Trop.* 201 (2020) 105215. <https://doi.org/10.1016/j.actatropica.2019.105215>.

- [95] R. Amara, A. Ramadan, R. El-Moslemany, M. Eissa, M. El-Azzouni, L. El-Khordagui, Praziquantel–lipid nanocapsules: an oral nanotherapeutic with potential *Schistosoma mansoni* tegumental targeting, *Int. J. Nanomedicine*. Volume 13 (2018) 4493–4505. <https://doi.org/10.2147/IJN.S167285>.
- [96] B. Heurtault, P. Saulnier, B. Pech, J.-E. Proust, J.-P. Benoit, A Novel Phase Inversion-Based Process for the Preparation of Lipid Nanocarriers, *Pharm. Res.* 19 (2002) 875–880. <https://doi.org/10.1023/A:1016121319668>.
- [97] D. Urimi, M. Hellsing, N. Mahmoudi, C. Söderberg, R. Widenbring, L. Gedda, K. Edwards, T. Loftsson, N. Schipper, Structural Characterization Study of a Lipid Nanocapsule Formulation Intended for Drug Delivery Applications Using Small-Angle Scattering Techniques, *Mol. Pharm.* 19 (2022) 1068–1077. <https://doi.org/10.1021/acs.molpharmaceut.1c00648>.
- [98] K. Shinoda, H. Saito, The Stability of O/W type emulsions as functions of temperature and the HLB of emulsifiers: The emulsification by PIT-method, *J. Colloid Interface Sci.* 30 (1969) 258–263. [https://doi.org/10.1016/S0021-9797\(69\)80012-3](https://doi.org/10.1016/S0021-9797(69)80012-3).
- [99] N. Dabholkar, T. Waghule, V. Krishna Rapalli, S. Gorantla, A. Alexander, R. Narayan Saha, G. Singhvi, Lipid shell lipid nanocapsules as smart generation lipid nanocarriers, *J. Mol. Liq.* 339 (2021) 117145. <https://doi.org/10.1016/j.molliq.2021.117145>.
- [100] A. Clavreul, E. Roger, M. Pourbaghi-Masouleh, L. Lemaire, C. Tétaud, P. Menei, Development and characterization of sorafenib-loaded lipid nanocapsules for the treatment of glioblastoma, *Drug Deliv.* 25 (2018) 1756–1765. <https://doi.org/10.1080/10717544.2018.1507061>.
- [101] Y. Zhai, X. Yang, L. Zhao, Z. Wang, G. Zhai, Lipid nanocapsules for transdermal delivery of ropivacaine: in vitro and in vivo evaluation, *Int. J. Pharm.* 471 (2014) 103–111. <https://doi.org/10.1016/j.ijpharm.2014.05.035>.
- [102] M.M. Eissa, R.M. El-Moslemany, A.A. Ramadan, E.I. Amer, M.Z. El-Azzouni, L.K. El-Khordagui, Miltefosine Lipid Nanocapsules for Single Dose Oral Treatment of Schistosomiasis *Mansoni*: A Preclinical Study, *PLOS ONE*. 10 (2015) e0141788–e0141788. <https://doi.org/10.1371/journal.pone.0141788>.
- [103] R.M. El-Moslemany, M.M. Eissa, A.A. Ramadan, L.K. El-Khordagui, M.Z. El-Azzouni, Miltefosine lipid nanocapsules: Intersection of drug repurposing and nanotechnology for single dose oral treatment of pre-patent schistosomiasis *Mansoni*, *Acta Trop.* 159 (2016) 142–148. <https://doi.org/10.1016/j.actatropica.2016.03.038>.
- [104] N.A. El-Sheridy, R.M. El-Moslemany, A.A. Ramadan, M.W. Helmy, L.K. El-Khordagui, Enhancing the in vitro and in vivo activity of itraconazole against breast cancer using miltefosine-modified lipid nanocapsules, *Drug Deliv.* 28 (2021) 906–919. <https://doi.org/10.1080/10717544.2021.1917728>.

- [105] G.V. Ullio Gamboa, P.E. Pensel, M.C. Elissondo, S.F. Sanchez Bruni, J.-P. Benoit, S.D. Palma, D.A. Allemandi, Albendazole-lipid nanocapsules: Optimization, characterization and chemoprophylactic efficacy in mice infected with *Echinococcus granulosus*, *Exp. Parasitol.* 198 (2019) 79–86. <https://doi.org/10.1016/j.exppara.2019.02.002>.
- [106] A. Lamprecht, J.-L. Saumet, J. Roux, J.-P. Benoit, Lipid nanocarriers as drug delivery system for ibuprofen in pain treatment, *Int. J. Pharm.* 278 (2004) 407–414. <https://doi.org/10.1016/j.ijpharm.2004.03.018>.
- [107] M.F. Kabil, M.Y. Mahmoud, A.F. Bakr, D. Zaafar, I.M. El-Sherbiny, Switching indication of PEGylated lipid nanocapsules-loaded with rolapitant and deferasirox against breast cancer: Enhanced in-vitro and in-vivo cytotoxicity, *Life Sci.* (2022) 120731. <https://doi.org/10.1016/j.lfs.2022.120731>.
- [108] D. Séhédic, L. Roncali, A. Djoudi, N. Buchtova, S. Avril, M. Chérel, F. Boury, F. Lacoëuille, F. Hindré, E. Garcion, Rapamycin-Loaded Lipid Nanocapsules Induce Selective Inhibition of the mTORC1-Signaling Pathway in Glioblastoma Cells, *Front. Bioeng. Biotechnol.* 8 (2021). <https://www.frontiersin.org/articles/10.3389/fbioe.2020.602998> (accessed July 14, 2022).
- [109] Q. Zhai, H. Li, Y. Song, R. Wu, C. Tang, X. Ma, Z. Liu, J. Peng, J. Zhang, Z. Tang, Preparation and Optimization Lipid Nanocapsules to Enhance the Antitumor Efficacy of Cisplatin in Hepatocellular Carcinoma HepG2 Cells, *AAPS PharmSciTech.* 19 (2018) 2048–2057. <https://doi.org/10.1208/s12249-018-1011-6>.
- [110] L.M. Eldesouky, R.M. El-Moslemany, A.A. Ramadan, M.H. Morsi, N.M. Khalafallah, Cyclosporine Lipid Nanocapsules as Thermoresponsive Gel for Dry Eye Management: Promising Corneal Mucoadhesion, Biodistribution and Preclinical Efficacy in Rabbits, *Pharmaceutics.* 13 (2021) 360. <https://doi.org/10.3390/pharmaceutics13030360>.
- [111] A. Ramadan, F. Lagarce, P. Legras, A. Tessier-Marteau, O. Thomas, L. Macchi, P. Saulnier, J.-P. Benoit, Oral fondaparinux: use of lipid nanocapsules as nanocarriers and in vivo pharmacokinetic study, *Int. J. Nanomedicine.* (2011) 2941–2941. <https://doi.org/10.2147/IJN.S25791>.
- [112] A. Umerska, N. Matougui, A.-C. Groo, P. Saulnier, Understanding the adsorption of salmon calcitonin, antimicrobial peptide AP114 and polymyxin B onto lipid nanocapsules, *Int. J. Pharm.* 506 (2016) 191–200. <https://doi.org/10.1016/j.ijpharm.2016.04.028>.
- [113] N. Matougui, A.-C. Groo, A. Umerska, V. Cassisa, P. Saulnier, A comparison of different strategies for antimicrobial peptides incorporation onto/into lipid nanocapsules, *Nanomed.* 14 (2019) 1647–1662. <https://doi.org/10.2217/nnm-2018-0337>.



- [114] M.L. Formica, S. Legeay, J. Bejaud, G.G. Montich, G.V. Ullio Gamboa, J.-P. Benoit, S.D. Palma, Novel hybrid lipid nanocapsules loaded with a therapeutic monoclonal antibody – Bevacizumab – and Triamcinolone acetonide for combined therapy in neovascular ocular pathologies, *Mater. Sci. Eng. C.* 119 (2021) 111398. <https://doi.org/10.1016/j.msec.2020.111398>.
- [115] M. Morille, C. Passirani, E. Letrou-Bonneval, J.-P. Benoit, B. Pitard, Galactosylated DNA lipid nanocapsules for efficient hepatocyte targeting, *Int. J. Pharm.* 379 (2009) 293–300. <https://doi.org/10.1016/j.ijpharm.2009.05.065>.
- [116] A. Vonarbourg, C. Passirani, L. Desigaux, E. Allard, P. Saulnier, O. Lambert, J.-P. Benoit, B. Pitard, The encapsulation of DNA molecules within biomimetic lipid nanocapsules, *Biomaterials.* 30 (2009) 3197–3204. <https://doi.org/10.1016/j.biomaterials.2009.03.009>.
- [117] N. Skandrani, A. Barras, D. Legrand, T. Gharbi, H. Boulahdour, R. Boukherroub, Lipid nanocapsules functionalized with polyethyleneimine for plasmid DNA and drug co-delivery and cell imaging, *Nanoscale.* 6 (2014) 7379–7390. <https://doi.org/10.1039/C4NR01110D>.
- [118] P. Resnier, E. Lepeltier, A.L. Emina, N. Galopin, J. Bejaud, S. David, C. Ballet, T. Benvegna, F. Pecorari, I. Chourpa, J.-P. Benoit, C. Passirani, Model Affitin and PEG modifications onto siRNA lipid nanocapsules: cell uptake and in vivo biodistribution improvements, *RSC Adv.* 9 (2019) 27264–27278. <https://doi.org/10.1039/C9RA03668G>.
- [119] P. Resnier, P. LeQuinio, N. Lautram, E. André, C. Gaillard, G. Bastiat, J.-P. Benoit, C. Passirani, Efficient in vitro gene therapy with PEG siRNA lipid nanocapsules for passive targeting strategy in melanoma, *Biotechnol. J.* 9 (2014) 1389–1401. <https://doi.org/10.1002/biot.201400162>.
- [120] B. Le Moal, E. Lepeltier, V. Geoffroy, A. Galvani, C. Le Visage, C. Passirani, J. Guicheux, J. Clouet, Lipid nanocapsules for the sustained release of therapeutic miRNA: new perspective in regenerative medicine of intervertebral disc, *Osteoarthritis Cartilage.* 27 (2019) S462. <https://doi.org/10.1016/j.joca.2019.02.502>.
- [121] B. Le Moal, É. Lepeltier, D. Rouleau, C. Le Visage, J.-P. Benoit, C. Passirani, J. Guicheux, M. Fusellier, J. Clouet, Lipid nanocapsules for intracellular delivery of microRNA: A first step towards intervertebral disc degeneration therapy, *Int. J. Pharm.* 624 (2022) 121941. <https://doi.org/10.1016/j.ijpharm.2022.121941>.
- [122] Y. Zhao, L. Wang, C. Ma, K. Zhao, Y. Liu, N. Feng, Preparation and characterization of tetrandrine-phospholipid complex loaded lipid nanocapsules as potential oral carriers, *Int. J. Nanomedicine.* 8 (2013) 4169–4181. <https://doi.org/10.2147/IJN.S50557>.

- [123] A.A. Ashour, A.A. Ramadan, D.A. Abdelmonsif, A.H. El-Kamel, Enhanced oral bioavailability of Tanshinone IIA using lipid nanocapsules: Formulation, in-vitro appraisal and pharmacokinetics, *Int. J. Pharm.* 586 (2020) 119598. <https://doi.org/10.1016/j.ijpharm.2020.119598>.
- [124] E. Roger, F. Lagarce, J.-P. Benoit, Development and characterization of a novel lipid nanocapsule formulation of Sn38 for oral administration, *Eur. J. Pharm. Biopharm.* 79 (2011) 181–188. <https://doi.org/10.1016/j.ejpb.2011.01.021>.
- [125] A.-C. Groo, P. Saulnier, J.-C. Gimel, J. Gravier, C. Ailhas, J.-P. Benoit, F. Lagarce, Fate of paclitaxel lipid nanocapsules in intestinal mucus in view of their oral delivery, *Int. J. Nanomedicine.* 8 (2013) 4291–4291. <https://doi.org/10.2147/ijn.s51837>.
- [126] B. Toussaint, H. Hillaireau, C. Cailleau, Y. Ambroise, E. Fattal, Stability, pharmacokinetics, and biodistribution in mice of the EPAC1 inhibitor (R)-CE3F4 entrapped in liposomes and lipid nanocapsules, *Int. J. Pharm.* 610 (2021) 121213. <https://doi.org/10.1016/j.ijpharm.2021.121213>.
- [127] J. Varshosaz, S. Taymouri, A. Jahanian-Najafabadi, A. Alizadeh, Efavirenz oral delivery via lipid nanocapsules: formulation, optimisation, and ex-vivo gut permeation study, *IET Nanobiotechnol.* 12 (2018) 795–806. <https://doi.org/10.1049/iet-nbt.2018.0006>.
- [128] E. Roger, J.C. Gimel, C. Bensley, A.S. Klymchenko, J.P. Benoit, Lipid nanocapsules maintain full integrity after crossing a human intestinal epithelium model, *J. Controlled Release.* 253 (2017) 11–18. <https://doi.org/10.1016/j.jconrel.2017.03.005>.
- [129] S. Bonnet, R. Elfatairi, F. Franconi, E. Roger, S. Legeay, Organic nanoparticle tracking during pharmacokinetic studies, *Nanomed.* 16 (2021) 2539–2536. <https://doi.org/10.2217/nnm-2021-0155>.
- [130] A.-L. Lainé, J. Gravier, M. Henry, L. Sancey, J. Béjaud, E. Pancani, M. Wiber, I. Texier, J.-L. Coll, J.-P. Benoit, C. Passirani, Conventional versus stealth lipid nanoparticles: Formulation and in vivo fate prediction through FRET monitoring, *J. Controlled Release.* 188 (2014) 1–8. <https://doi.org/10.1016/j.jconrel.2014.05.042>.
- [131] R. Bouchaala, L. Mercier, B. Andreiuk, Y. Mély, T. Vandamme, N. Anton, J.G. Goetz, A.S. Klymchenko, Integrity of lipid nanocarriers in bloodstream and tumor quantified by near-infrared ratiometric FRET imaging in living mice, *J. Controlled Release.* 236 (2016) 57–67. <https://doi.org/10.1016/j.jconrel.2016.06.027>.
- [132] J. Gravier, L. Sancey, S. Hirsjärvi, E. Rustique, C. Passirani, J.-P. Benoît, J.-L. Coll, I. Texier, FRET Imaging Approaches for in Vitro and in Vivo Characterization of Synthetic Lipid Nanoparticles, *Mol. Pharm.* 11 (2014) 3133–3144. <https://doi.org/10.1021/mp500329z>.
- [133] N. Kaeokhamloed, E. Roger, J. Béjaud, N. Lautram, F. Manero, R. Perrot, C. Abbara, M. Briet, S. Legeay, New in vitro coculture model for evaluating intestinal absorption

- of different lipid nanocapsules, *Pharmaceutics*. 13 (2021). <https://doi.org/10.3390/pharmaceutics13050595>.
- [134] R. Elfatairi, S. Legeay, Evaluation of biodistribution of lipid nanocapsules in rat with a new quantitative method using FRET, University of Angers, MINT laboratory (UMR 1066, CRS 6021), France, France, 2021.
- [135] B.M. Carlson, Chapter 10 - The Circulatory System, in: B.M. Carlson (Ed.), *Hum. Body*, Academic Press, 2019: pp. 271–301. <https://doi.org/10.1016/B978-0-12-804254-0.00010-7>.
- [136] B.M. Carlson, Chapter 12 - The Digestive System, in: B.M. Carlson (Ed.), *Hum. Body*, Academic Press, 2019: pp. 321–355. <https://doi.org/10.1016/B978-0-12-804254-0.00012-0>.
- [137] P.P. Desai, A.A. Date, V.B. Patravale, Overcoming poor oral bioavailability using nanoparticle formulations – opportunities and limitations, *Drug Discov. Today Technol.* 9 (2012) e87–e95. <https://doi.org/10.1016/j.ddtec.2011.12.001>.
- [138] E. Roger, J.C. Gimel, C. Bensley, A.S. Klymchenko, J.P. Benoit, Lipid nanocapsules maintain full integrity after crossing a human intestinal epithelium model, *J. Controlled Release*. 253 (2017) 11–18. <https://doi.org/10.1016/j.jconrel.2017.03.005>.
- [139] N. Kaeokhamloed, S. Legeay, E. Roger, FRET as the tool for in vivo nanomedicine tracking, *J. Controlled Release*. 349 (2022) 156–173. <https://doi.org/10.1016/j.jconrel.2022.06.048>.
- [140] N. Kaeokhamloed, V. Lebreton, A. Vasylaki, G. Hilairat, A. Mellinger, J. Béjaud, P. Saulnier, F. Lagarce, F. Gattacceca, S. Legeay, E. Roger, Pharmacokinetics of intact lipid nanocapsules using new quantitative FRET technique, (2022).
- [141] V.N. Kilin, H. Anton, N. Anton, E. Steed, J. Vermot, T.F. Vandamme, Y. Mely, A.S. Klymchenko, Counterion-enhanced cyanine dye loading into lipid nano-droplets for single-particle tracking in zebrafish, *Biomaterials*. 35 (2014) 4950–4957. <https://doi.org/10.1016/j.biomaterials.2014.02.053>.
- [142] W. Liu, D. Li, Z. Dong, K. Liu, H. He, Y. Lu, W. Wu, Q. Li, L. Gan, J. Qi, Insight into the in vivo translocation of oral liposomes by fluorescence resonance energy transfer effect, *Int. J. Pharm.* 587 (2020) 119682. <https://doi.org/10.1016/j.ijpharm.2020.119682>.
- [143] J.B.J. Kamphuis, M. Mercier-Bonin, H. Eutamène, V. Theodorou, Mucus organisation is shaped by colonic content; a new view, *Sci. Rep.* 7 (2017) 8527. <https://doi.org/10.1038/s41598-017-08938-3>.
- [144] X. Hu, W. Fan, Z. Yu, Y. Lu, J. Qi, J. Zhang, X. Dong, W. Zhao, W. Wu, Evidence does not support absorption of intact solid lipid nanoparticles via oral delivery, *Nanoscale*. 8 (2016) 7024–7035. <https://doi.org/10.1039/C5NR07474F>.

- [145] M. Buchert, K. Turksen, F. Hollande, Methods to Examine Tight Junction Physiology in Cancer Stem Cells: TEER, Paracellular Permeability, and Dilution Potential Measurements, *Stem Cell Rev. Rep.* 8 (2012) 1030–1034. <https://doi.org/10.1007/s12015-011-9334-7>.
- [146] V. Garcia-Hernandez, M. Quiros, A. Nusrat, Intestinal epithelial claudins: expression and regulation in homeostasis and inflammation, *Ann. N. Y. Acad. Sci.* 1397 (2017) 66–79. <https://doi.org/10.1111/nyas.13360>.
- [147] A. Fischer, M. Gluth, F. Weege, U.-F. Pape, B. Wiedenmann, D.C. Baumgart, F. Theuring, Glucocorticoids regulate barrier function and claudin expression in intestinal epithelial cells via MKP-1, *Am. J. Physiol.-Gastrointest. Liver Physiol.* 306 (2014) G218–G228. <https://doi.org/10.1152/ajpgi.00095.2013>.
- [148] T. Suzuki, N. Yoshinaga, S. Tanabe, Interleukin-6 (IL-6) Regulates Claudin-2 Expression and Tight Junction Permeability in Intestinal Epithelium \*, *J. Biol. Chem.* 286 (2011) 31263–31271. <https://doi.org/10.1074/jbc.M111.238147>.
- [149] R. Al-Sadi, D. Ye, M. Boivin, S. Guo, M. Hashimi, L. Ereifej, T.Y. Ma, Interleukin-6 Modulation of Intestinal Epithelial Tight Junction Permeability Is Mediated by JNK Pathway Activation of Claudin-2 Gene, *PLOS ONE.* 9 (2014) e85345. <https://doi.org/10.1371/journal.pone.0085345>.
- [150] N.A. Hering, S. Andres, A. Fromm, E.A. van Tol, M. Amasheh, J. Mankertz, M. Fromm, J.D. Schulzke, Transforming Growth Factor- $\beta$ , a Whey Protein Component, Strengthens the Intestinal Barrier by Upregulating Claudin-4 in HT-29/B6 Cells, *J. Nutr.* 141 (2011) 783–789. <https://doi.org/10.3945/jn.110.137588>.
- [151] K.R. Groschwitz, D. Wu, H. Osterfeld, R. Ahrens, S.P. Hogan, Chymase-mediated intestinal epithelial permeability is regulated by a protease-activating receptor/matrix metalloproteinase-2-dependent mechanism, *Am. J. Physiol.-Gastrointest. Liver Physiol.* 304 (2013) G479–G489. <https://doi.org/10.1152/ajpgi.00186.2012>.
- [152] P.-A. Billat, E. Roger, S. Faure, F. Lagarce, Models for drug absorption from the small intestine: where are we and where are we going?, *Drug Discov. Today.* 22 (2017) 761–775. <https://doi.org/10.1016/j.drudis.2017.01.007>.
- [153] M. Goldberg, I. Gomez-Orellana, Challenges for the oral delivery of macromolecules, *Nat. Rev. Drug Discov.* 2 (2003) 289–295. <https://doi.org/10.1038/nrd1067>.
- [154] M.M. Mahe, N. Sundaram, C.L. Watson, N.F. Shroyer, M.A. Helmrich, Establishment of human epithelial enteroids and colonoids from whole tissue and biopsy, *J. Vis. Exp.* 2015 (2015) 1–13. <https://doi.org/10.3791/52483>.
- [155] C.A. Thorne, I.W. Chen, L.E. Sanman, M.H. Cobb, L.F. Wu, S.J. Altschuler, Enteroid Monolayers Reveal an Autonomous WNT and BMP Circuit Controlling Intestinal

- Epithelial Growth and Organization, *Dev. Cell.* 44 (2018) 624-633.e4. <https://doi.org/10.1016/j.devcel.2018.01.024>.
- [156] J. Braverman, Ö.H. Yilmaz, From 3D Organoids back to 2D Enteroids, *Dev. Cell.* 44 (2018) 533–534. <https://doi.org/10.1016/j.devcel.2018.02.016>.
- [157] F. Radtke, H. Clevers, Self-renewal and cancer of the gut: Two sides of a coin, *Science.* 307 (2005) 1904–1909. <https://doi.org/10.1126/science.1104815>.
- [158] G. Haraldsen, J. Rugtveit, D. Kvale, T. Scholz, W.A. Muller, T. Hovig, P. Brandtzaeg, Isolation and longterm culture of human intestinal microvascular endothelial cells, *Gut.* 37 (1995) 225–234. <https://doi.org/10.1136/gut.37.2.225>.
- [159] M. Desjardins, ER-mediated phagocytosis: a new membrane for new functions, *Nat. Rev. Immunol.* 3 (2003) 280–291. <https://doi.org/10.1038/nri1053>.
- [160] S.D. Conner, S.L. Schmid, Regulated portals of entry into the cell, *Nature.* 422 (2003) 37–44. <https://doi.org/10.1038/nature01451>.
- [161] H. Meng, W. Leong, K.W. Leong, C. Chen, Y. Zhao, Walking the line: The fate of nanomaterials at biological barriers, *Biomaterials.* 174 (2018) 41–53. <https://doi.org/10.1016/j.biomaterials.2018.04.056>.
- [162] M. Gekle, P. Knaus, R. Nielsen, S. Mildenerger, R. Freudinger, V. Wohlfarth, C. Sauvant, E.I. Christensen, Transforming growth factor- $\beta$ 1 reduces megalin- and cubilin-mediated endocytosis of albumin in proximal-tubule-derived opossum kidney cells, *J. Physiol.* 552 (2003) 471–481. <https://doi.org/10.1113/jphysiol.2003.048074>.
- [163] S. Nazir, A. Kumar, I. Chatterjee, A.N. Anbazhagan, T. Gujral, S. Priyamvada, S. Saksena, W.A. Alrefai, P.K. Dudeja, R.K. Gill, Mechanisms of Intestinal Serotonin Transporter (SERT) Upregulation by TGF- $\beta$ 1 Induced Non-Smad Pathways, *PLOS ONE.* 10 (2015) e0120447. <https://doi.org/10.1371/journal.pone.0120447>.
- [164] T.M. Mayhew, C. Middleton, Crypts, villi and microvilli in the small intestine of the rat. A stereological study of their variability within and between animals., *J. Anat.* 141 (1985) 1–17.
- [165] Transwell® Permeable Supports | Guidelines for Use | Corning, (n.d.). <https://www.corning.com/worldwide/en/products/life-sciences/products/permeable-supports/transwell-guidelines.html> (accessed July 15, 2022).
- [166] T.S. Work, E. Work, eds., Chapter 7 - Applications of density gradient centrifugation, in: *Lab. Tech. Biochem. Mol. Biol.*, Elsevier, 1978: pp. 205–242. [https://doi.org/10.1016/S0075-7535\(08\)70161-X](https://doi.org/10.1016/S0075-7535(08)70161-X).
- [167] F.G. Rodriguez-Gonzalez, D.A.M. Mustafa, B. Mostert, A.M. Sieuwerts, The challenge of gene expression profiling in heterogeneous clinical samples, *Methods.* 59 (2013) 47–58. <https://doi.org/10.1016/j.ymeth.2012.05.005>.

- [168] K. Kizaki, A. Shichijo-Kizaki, T. Furusawa, T. Takahashi, M. Hosoe, K. Hashizume, Differential neutrophil gene expression in early bovine pregnancy, *Reprod. Biol. Endocrinol.* 11 (2013) 6. <https://doi.org/10.1186/1477-7827-11-6>.
- [169] A. Zipursky, E. Bow, R. Seshadri, E. Brown, Leukocyte density and volume in normal subjects and in patients with acute lymphoblastic leukemia, *Blood.* 48 (1976) 361–371. <https://doi.org/10.1182/blood.V48.3.361.361>.
- [170] M. Wahlgren, M. Axenstrand, Å. Håkansson, A. Marefati, B. Lomstein Pedersen, In Vitro Methods to Study Colon Release: State of the Art and An Outlook on New Strategies for Better In-Vitro Biorelevant Release Media, *Pharmaceutics.* 11 (2019) 95. <https://doi.org/10.3390/pharmaceutics11020095>.
- [171] C.J.H. Porter, N.L. Trevaskis, W.N. Charman, Lipids and lipid-based formulations: optimizing the oral delivery of lipophilic drugs, *Nat. Rev. Drug Discov.* 6 (2007) 231–248. <https://doi.org/10.1038/nrd2197>.
- [172] J.S. Coon, W. Knudson, K. Clodfelter, B. Lu, R.S. Weinstein, Solutol HS 15, nontoxic polyoxyethylene esters of 12-hydroxystearic acid, reverses multidrug resistance, *Cancer Res.* 51 (1991) 897–902.
- [173] T. Wang, Y. Luo, Biological fate of ingested lipid-based nanoparticles: current understanding and future directions, *Nanoscale.* 11 (2019) 11048–11063. <https://doi.org/10.1039/C9NR03025E>.
- [174] T.P.C. Dorlo, M. Balasegaram, J.H. Beijnen, P.J. de Vries, Miltefosine: a review of its pharmacology and therapeutic efficacy in the treatment of leishmaniasis, *J. Antimicrob. Chemother.* 67 (2012) 2576–2597. <https://doi.org/10.1093/jac/dks275>.
- [175] Y.-B. Miao, Y.-J. Lin, K.-H. Chen, P.-K. Luo, S.-H. Chuang, Y.-T. Yu, H.-M. Tai, C.-T. Chen, K.-J. Lin, H.-W. Sung, Engineering Nano- and Microparticles as Oral Delivery Vehicles to Promote Intestinal Lymphatic Drug Transport, *Adv. Mater.* 33 (2021) 2104139. <https://doi.org/10.1002/adma.202104139>.
- [176] L.R. Engelking, Chapter 64 - Chylomicrons, in: L.R. Engelking (Ed.), *Textb. Vet. Physiol. Chem. Third Ed.*, Academic Press, Boston, 2015: pp. 411–415. <https://doi.org/10.1016/B978-0-12-391909-0.50064-5>.
- [177] K. Netsomboon, A. Bernkop-Schnürch, Mucoadhesive vs. mucopenetrating particulate drug delivery, *Eur. J. Pharm. Biopharm.* 98 (2016) 76–89. <https://doi.org/10.1016/j.ejpb.2015.11.003>.
- [178] V. Bourganis, T. Karamanidou, E. Samaridou, K. Karidi, O. Kammona, C. Kiparissides, On the synthesis of mucus permeating nanocarriers, *Eur. J. Pharm. Biopharm.* 97 (2015) 239–249. <https://doi.org/10.1016/j.ejpb.2015.01.021>.
- [179] E. Yamazoe, J.-Y. Fang, K. Tahara, Oral mucus-penetrating PEGylated liposomes to improve drug absorption: Differences in the interaction mechanisms of a

mucoadhesive liposome, *Int. J. Pharm.* 593 (2021) 120148.  
<https://doi.org/10.1016/j.ijpharm.2020.120148>.

[180] Paclitaxel, Drugbank. (n.d.). <https://go.drugbank.com/drugs/DB01229> (accessed September 9, 2022).

**Titre :** Évaluation des nanocapsules lipidiques pour l'absorption orale à l'aide de la nouvelle technique quantitative FRET

**Mots clés :** Nanocapsules lipidiques ; nanomédicaments ; FRET ; absorption orale ; culture cellulaire ; Caco-2

**Résumé :** Les nanocapsules lipidiques (LNC) bénéficient de leur capacité à augmenter la biodisponibilité orale des nombreux médicaments encapsulés, ce qui en fait des nanomédecines orales très prometteuses. Cependant, l'absorption orale des LNC intactes n'a pas encore été bien étudiée en raison de l'absence d'un outil approprié pour les quantifier. Par conséquent, cette thèse vise à caractériser l'absorption orale des LNC intactes *in vitro* et *in vivo*. Des LNC de différentes tailles (50 et 85 nm) et des modifications de surface (aucune, DSPE-mPEG2000 et stéarylamine) ont été développées pour les tests tout au long de la thèse. Pour la première partie, un nouveau modèle de coculture *in vitro* de l'épithélium Caco-2 et de l'endothélium HMEC-1 (modèle Caco-2/HMEC-1) a été développé pour étudier le transport *in vitro* des particules des LNC à travers les membranes de type épithélium intestinal-endothélium.

Pour la deuxième partie, la nouvelle technique quantitative FRET (transfert d'énergie par résonance de Förster) a été développée pour l'analyse quantitative des LNC intactes dans le sang, le foie et les fèces. Ensuite, la pharmacocinétique des LNC intactes a été étudiée après l'administration IV à l'aide de FRET. Enfin, l'absorption orale *in vivo* des LNC intactes a été étudiée chez le rats à travers 1) la biodisponibilité orale, 2) la biodistribution dans la veine porte hépatique et au foie, et 3) les LNCs intactes restant dans les fèces. L'étude *in vitro* a révélé que les LNC intactes avaient un transport inférieur à 1 % sur le modèle Caco-2/HMEC-1. L'étude *in vivo* a révélé 0 % de biodisponibilité orale et 0 % de LNC intactes a été quantifié dans la veine porte hépatique, le foie et les fèces après 4 heures de gavage oral. Les résultats suggèrent que les LNCs intactes peuvent ne pas être absorbées par la voie GI.

**Title:** Evaluation of lipid nanocapsules for oral absorption using new quantitative FRET technique

**Keywords:** Lipid nanocapsules ; nanomedicines ; FRET ; oral absorption ; cell culture ; Caco-2

**Abstract:** Lipid nanocapsules (LNCs) benefit from their ability to increase the oral bioavailability of the many encapsulated drugs, making them one of the promising oral nanomedicines. However, the oral absorption of the intact LNCs itself has not yet been well studied because of the lack of an appropriate tool. Hence, this thesis aims to characterize the oral absorption of intact LNCs *in vitro* and *in vivo*. LNCs with different sizes (50- and 85-nm) and surface modifications (none, DSPE-mPEG-2000, and stearylamine) were developed for the tests throughout the thesis. For the first part, the new *in vitro* coculture model of Caco-2 epithelium and HMEC-1 endothelium (Caco-2/HMEC-1 model) was developed to investigate the *in vitro* particle transport of LNCs across the epithelium-endothelium membranes.

For the second part, the new quantitative (Förster resonance energy transfer) FRET technique was developed for quantitative analysis of intact LNCs in blood, liver, and feces. Then, the pharmacokinetics of intact LNCs was studied after IV administration using FRET. Finally, *in vivo* oral absorption of intact LNCs was studied in rats by evaluating 1) the oral bioavailability, 2) the biodistribution to hepatic portal vein and liver, and 3) the remaining intact LNC in the feces. The *in vitro* study found that intact LNCs had <1% transportation across the Caco-2/HMEC-1 model. The *in vivo* study found 0% *in vivo* oral bioavailability and 0% of intact LNCs is quantified in the hepatic portal vein, liver, and feces after 4 hours of oral gavage. The evidence suggests that intact LNCs may not be absorbed *via* the GI route.